eman ta zabal zazu
Universidad del País Vasco
Euskal Herriko Unibertsitatea

MnO_X-CeO_2 catalytic formulations for the simultaneous removal of NO_X and PCDD/Fs from exhaust gases of MSWI plants

Juan Alberto Martín Martín

2022

INDEX

Chapter 1

INTRODUCTION

Chapter 1

INTRODUCTION

ABSTRACT

Waste management is one of the most important challenges to be faced in the near future. A sustainable management is encouraged by current legislations, considering waste as raw material that can be still recovered. On this basis, proper waste management promotes waste recovery as raw material or energy instead of landfilling. Incineration is the most widely used process for energy recovery; indeed MSWI plants are considered as waste-to-energy processes, which allow the production of heat and/or electricity from the energy contained in waste.

However, waste incineration process generates a wide variety of pollutants. The present thesis is focused on the removal of two of them, NO_X and PCDD/Fs. Catalytic technology used in some MSWI plants for NO_X abatement has also been reported for PCDD/Fs destruction. The simultaneous removal of both pollutants (dDiNO$_X$ process) has already been successfully assessed with the commercial catalytic formulation currently used to conduct the SCR.

The downsides of commercial SCR catalyst, such as the relatively high operation temperature, are leading to the search for alternative catalysts to perform low temperature SCR. In this context, the feasibility of dDiNO$_X$ process involves the research of these catalytic formulations in the simultaneous removal of NO_X and PCDD/Fs. However, few works have focused on this issue. Thus, the main objective of this thesis is to evaluate the catalytic performance of MnO_X-CeO_2 alternative formulation in dDiNO$_X$ processes.

1. INTRODUCTION.

1.1. THE GLOBAL CHALLENGE OF WASTE PRODUCTION.

Modern society as we know it, based on unrestrained consumption and the promotion of one-time use products with low added value, is continuously creating greater amounts of waste. Thus, future forecasts in this issue are not good considering the likely development of underdeveloped countries [1] and the current trend in developed countries, whose waste production further increases year by year, despite the possession of the latest technologies and the awareness-raising about environmental protection. This is incompatible with the Sustainable Development Goals proposed in the framework of 2030 Agenda, specifically goal 13, related to climate change and its impacts. For this reason, waste management has become one of the global challenges for scientific community that must be faced to achieve the Sustainable Development Goals [2, 3].

Focusing on the municipal solid waste field, the last consolidated version of European directive 2008/98/CE (5/7/2018) defines two types of municipal solid waste: on the one hand, that mixed or separately collected from households (including paper, cardboard, glass, metals, plastics, bio-waste, wood, textiles packaging, electrical/electronic equipment, waste batteries, accumulators and bulky waste such as mattresses and furniture) and, on the other hand, mixed and separately collected waste from other sources, although with similar nature and composition that waste from households.

The European Union (EU) generated 224.5 million tons of municipal solid waste (MSW) in 2019, which corresponds to 502 kg per capita. Table 1.1 reports the amount of MSW per capita for selected years between 1995 and 2019 in the EU 27 and each country [4]. It is worth noting the steady MSW generation in the early 2000s and the decrease in 2012, coinciding with the economic crisis that affected Europe and reduced the consumerist level. Nonetheless, MSW generated per capita is currently on an upward trend, with a 7.5% increase with respect to 1995. The increase in MSW generation is mainly due to the changes in living standard, consumption pattern and food habit of urban population [5].

Table 1.1. Municipal waste generated (kg per capita) in selected years, 1995-2019 [4].

	1995	2000	2006	2012	2016	2019	Change 2019/1995 (%)
EU 27	467	513	513	488	490	502	7.5
Belgium	455	471	485	445	419	415	-8.8
Bulgaria([1])	694	612	577	460	404	407	-41.3
Czechia	302	335	297	308	339	500	65.6
Denmark	521	664	740	806	830	844	62.0
Germany	623	642	564	619	633	609	-2.2
Estonia	371	453	398	280	376	369	-0.5
Ireland ([1])	512	599	792	585	581	598	16.9
Greece	303	412	447	495	498	524	72.9
Spain	505	653	590	468	463	476	-5.7
France	475	514	535	527	530	548	15.3
Croatia	-	262	384	391	403	445	70.0
Italy	454	509	559	504	497	499	9.9
Cyprus	595	628	695	657	633	642	7.9
Latvia	264	271	343	323	410	439	66.3
Lithuania	426	365	405	445	444	472	10.8
Luxembourg	587	654	683	652	815	791	34.8
Hungary	460	446	468	402	379	387	-15.9
Malta	387	533	624	590	641	694	79.2
Netherlands	539	598	597	549	520	508	-5.8
Austria	437	580	597	579	564	588	34.5
Poland	285	320	321	317	307	336	17.9
Portugal	352	457	465	453	474	513	45.9
Romania	342	355	396	251	261	280	-18.0
Slovenia	596	513	516	362	457	504	-15.5
Slovakia	295	254	284	306	348	421	42.9
Finland	413	502	494	506	504	566	36.9
Sweden	386	425	491	454	447	449	16.2

Table 1.1 also shows clear differences in the MSW generated depending on the countries. In 2019, Denmark, with 844 kg per capita, was the one generating the largest amount of MWS, and countries such as Germany, Greece, France, Malta, and Austria were above the EU 27 average, whereas Rumania with 280 kg per capita

was the lowest. Meanwhile, Spain generated 476 kg per capita, which is below the EU 27 average, although with a clear raising trend. These huge variations in the generated MSW reveals different consumption and production pattern in European countries, due to their development and economic wealth [6]. The way in which MSW are collected and managed also affects, because there are differences among the countries regarding the degree in which waste from commercial sector and administration are collected and managed together with waste from household.

Moreover, it is particularly remarkable that 18 out of 27 countries increased the MSW generated from 1995 to 2000, despite the public awareness in this issue and the commitment to reuse and recycle in recent years. This fact provides a disturbing view about the problems arising from uncontrolled and unconscious waste generation, specifically with MSW, and the scale it may reach in the future, if solutions associated to the sustainable management are not applied.

1.1.2. Waste management.

To deal with MSW generation problems in a more sustainable way, the EU adopted, in 2008, Directive 2008/98/CE, which is the main regulatory instrument to change the approach to waste management. This directive establishes a hierarchy for prioritizing an order in waste prevention and management legislation and policy, where prevention is the first step to consider, followed by reuse, recycling, other recovery ways (e.g., energy recovery) and, finally, disposal. To encourage the application of this hierarchy, the last amendment (2018/852) of Directive 2008/98/CE also provides the application of economic instruments and other measures. This is the case of ¨Pay as you throw¨ systems, which charge waste producers according to the actual amount of waste generated and incentivise separation at source, in order to reduce the amount of mixed waste.

Before waste issue became important for society and public administration was committed to appropriate waste management, landfilling was the most used option as waste management. In 1995, more than 60% of MSW generated in EU 27 were landfilled, whereas only 11.6% were recycled [4]. However, landfilling as the only waste management goes against hierarchy established in Directive 2008/98/CE, and landfills present serious structural and environmental problems.

Firstly, landfills have a great environmental impact related to greenhouse gases emission and leachate generation (could pollute nearby aquifers), in addition to the typical odour problems. On the other hand, the use of landfills is limited by their capacity, which implies the need for a new location for the continuation of the activity after filling and sealing. Finally, the use of landfills implies no (or lower) levels of waste recovery compared to other recovery techniques. In this sense, landfilling is currently the last stage of modern waste management systems, after separation and recycling, and after recovery stages, either through biochemical processes (e.g., composting) or energy recovery.

Figure 1.1 shows the amount of MSW in EU 27 by treatment categories: landfill, incineration, material recycling, composting and others. In the last few years, there has been an approach to sustainable waste management as a result of implementation and enforcement of Directive 2008/98/CE. In this way, even though the MSW generation tends to increase, a clear drop of landfilled MSW occurs over time, amounting to 120 kg per capita in 2019 (23.9% of total MSW generated). On the contrary, recycled waste continuously increases over time, reaching in 2019 the value of 152 kg per capita (30.3% of total MSW), 182% more than the MSW recycled in 1995.

Besides recycling, other recovery techniques, such as composting and incineration, also tend to increase, becoming 17 and 27% in 2019, respectively; compared to the 7 and 15% in 1995. Figure 1.1 also shows “in dotted line” the MSW incinerated with energy recovery. In 2019, 99% of MSW incinerated was recovered energetically in comparison to the 56% in 2000 (reported data before this year are not reliable).

MSW management differs across EU from state to state. This is associated to the complex processes and therefore huge upfront investment required for recycling and waste recovery. Thus, technologically developed countries in Northern Europe, such as Denmark, Germany, and Sweden, landfilled around 1% of MSW generated, while practically the remaining 99% was recycled or recovered as compost or energy. However, technologically undeveloped countries, such as, Bulgaria and Rumania, landfilled 61 and 74% of their MSW generated, respectively.

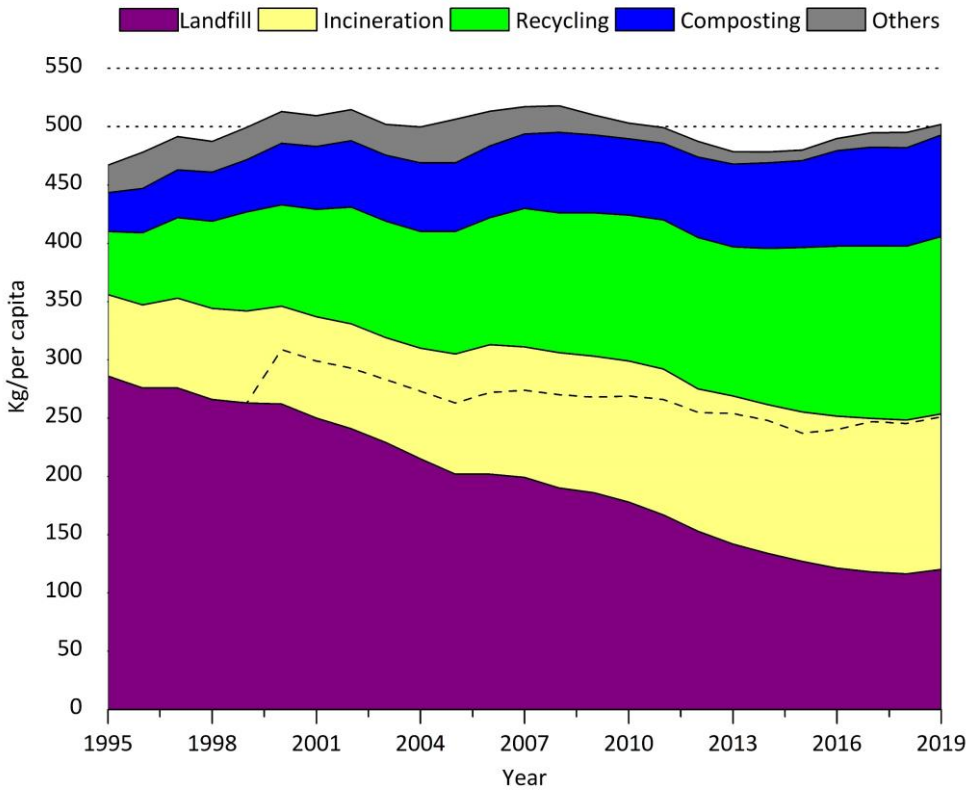

Figure 1.1. Evolution of MSW management in EU 27 over time [4].

In Spain, out of the 224.4 million tons of MSW generated in 2019, 18% was recycled, 17% was recovered as compost, 11% was incinerated with energy recovery and the remaining 54% was landfilled. Figure 1.2 compares the landfilled and incinerated with energy recovery fractions in EU 27 and Spain from 2000 [4]. In EU 27, the fraction of MSW landfilled continuously decreased over time, whereas in Spain, a tiny decrease has been only observed in the last 10 years. On the other hand, both EU 27 and Spain show an upward trend in the energy recovery fraction, although Spain is below the EU 27 average.

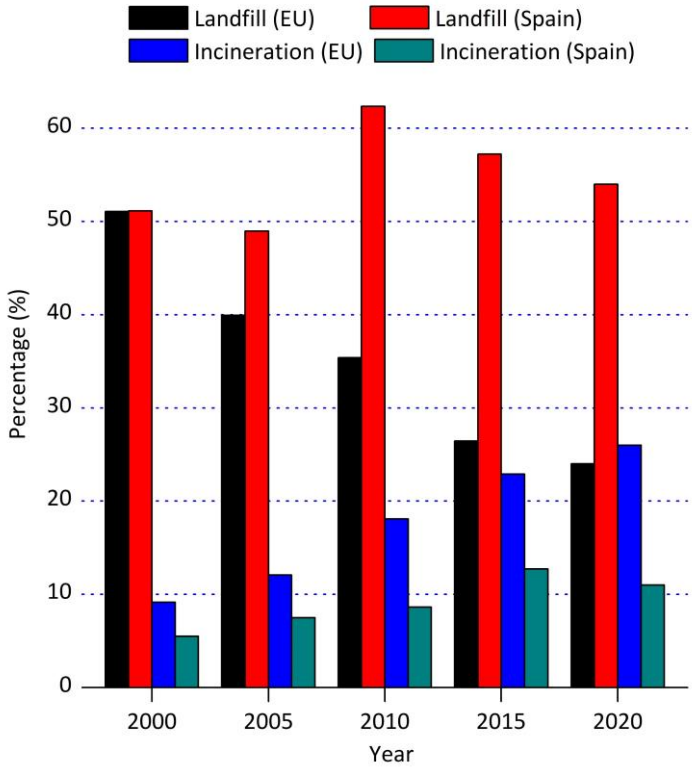

Figure 1.2. Comparison of landfilled and incinerated with energy recovery fractions in EU 27 and Spain in selected years [4].

1.2. ENERGY RECOVERY FROM MSW.

Directive 2008/98/CE [7] defines waste recovery as any operation the principal result of which is waste serving a useful purpose by replacing other materials which would otherwise have been used to fulfill a particular function, or waste being prepared to fulfill that function, in the plant or in the wider economy. Energy recovery is the use of those waste fractions that could not be reused and recycled, nor material recovered through composting, to produce energy, as electricity and/or heat. This recovery contributes to primary energy saving in conventional utility systems. For this reason, nowadays, thermal treatment plants associated to energy production are commonly addressed to as waste to energy (WtE) plants [8].

Energy recovery is supported by scientific community and its evaluation as sustainable alternative to landfilling, progress in solving typical problems, evolution over the years and economic perspective are widely addressed in the literature [2, 3, 9].

There are several technologies for energy recovery of waste through thermal processes: incineration, gasification and pyrolysis. Incineration is a full oxidative combustion in which the waste is used as fuel. Gasification is a partial oxidation of waste at high temperature to generate synthesis gas, which may be used as feedstock for chemical industry and as fuel. Pyrolysis is the thermal degradation of waste in the absence of oxygen to produce a gas, liquid and solid phase. The main difference is that gasification and pyrolysis is used to generate value-added chemicals, whereas incineration only produces energy [10].

Incineration is currently the most widely used process for energy recovery of waste, because it is the least complex and not as much affected by waste nature. Unlike incineration, gasification and pyrolysis processes need waste with certain characteristics to ensure the viability of the process, which involves specific waste pre-treatment that would increase the cost of the process [10].

1.2.1. Incineration as “waste to energy” process.

In the past, incineration process was used to reduce volume (around 90%), weight (80-70%) and hazard of waste [11, 12]. This technique was mainly used by small countries with high population density, where finding lands for landfilling was difficult [13]. However, technological development has made this technique attractive for waste management due to the possibility of recovering the energy released in the combustion of waste.

According to the Confederation of European Waste-to-Energy Plants (CEWEP), there were around 492 municipal solid waste incinerator (MSWI) plants in Europe. France is the country with the highest number of MSWI plants, although countries as Denmark, Finland and Sweden are the ones with the highest fraction of MSW incinerated (above 50% of total MSW amounted) [14]. Figure 1.3 shows the locations of the MSWI plants in Spain and Andorra. There are 12 MSWI plants, although they are unevenly distributed across the country. Thus, MSWI plans are

concentrated in the north, which reveals the backwardness of southern Spain in terms of waste management.

Figure 1.3. Locations of MSWI plants in Spain.

The main stages in a typical MSWI plant are: pre-incineration operations (incoming waste reception, storage and pre-treatment of waste and feeding of waste into the furnace), thermal treatment, energy recovery, flue-gas cleaning and emissions monitoring and control. However, the techniques used for each stage vary depending on the design conditions of the incinerator. According to these stages, Figure 1.4 shows the typical diagram of a MSWI plant and the route taken by the waste and the products of combustion of this waste. Firstly, waste is dumped into the reception trench, where it is stored until a crane-supported grab loads it into the combustion chamber. Here, the waste is incinerated, releasing a large amount of energy, which is used to produce superheated steam in a boiler. The steam is supplied to the energy recovery line. The flue gases produced during the incineration are sent to the gas cleaning systems, where the pollutants are abated, to meet the emission regulations. Finally, purified gases are released in the stack.

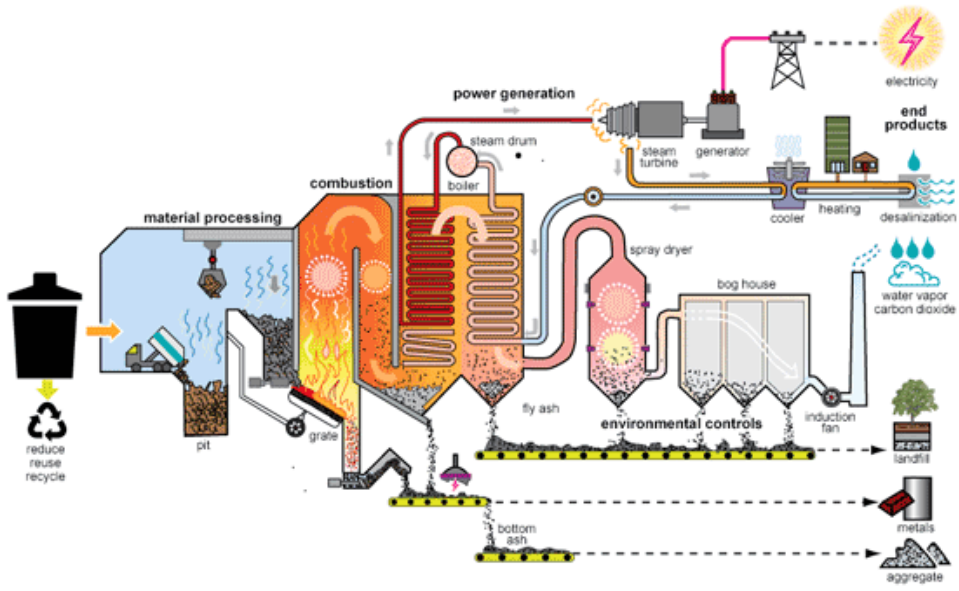

Figure 1.4. Schematic diagram of a MSWI plant.

The incineration process generates and consumes energy, but in most incinerators the energy generated exceeds that consumed. The excess energy is used as thermal energy, electrical energy or both by means of cogeneration systems. The type of energy produced depends on several factors. Generally speaking, in Northern European countries, incinerators usually produce electricity and heat through heating district network to provide heat to homes, schools, hospitals, etc. Conversely, in Southern countries with warm climate, incinerators are designed to produce only electricity. Additionally, approximately 10% of the energy recovered is often used in the plant itself for its operation [15].

Directive 2008/98/CE stablished the R1 parameter as a performance indicator for the level of energy recovery from waste in MSWI plants. Thus, MSWI plants whose R1 value is equal or above 0.65 (for plants authorized after January 1st 2009, or 0.60 if the plant was in operation or authorized before that date [7]) are classified as facilities for the recovery of energy from wastes.

According to CEWEP [16], 65.4% of 314 MSWI plants evaluated from 17 European countries (including Spain) met the R1 criteria. Moreover, the energetic efficiency is strongly related to three parameters: type of energy recovery, size and location

of the MSWI plant. Thus, the most energy efficient MSWI plants are located in Northern European countries because almost all of them have cogeneration. On the other hand, larger MSWI plants tend to be more energetically efficient due to the possibility of installing more efficient systems for energy recovery.

According to the public information provided by each, among all MSWI plants listed in Figure 1.3, only those located in Bilbao and Andorra report official documents confirming the R1 above 0.65. Moreover, the MSWI plants located in Sant Adrià de Besòs and Tarragona also state to meet the required R1 value, although they do not provide any official document accrediting this requirement. The other MSWI plants from Spain do not provide their efficiency parameter R1 in their public information. It was therefore not possible to assess this aspect. In the same way, Grosso and co-workers [17] reported 0.48 as the average R1 in Spain. These data reveal the existence of MSWI plants in Spain with lower values of energy efficiency parameter. Therefore, a commitment is needed to increase the energy efficiency of MSWI plants in Spain in order to promote the maximum waste recovery, as the Directive 2008/98/CE stablished.

1.3. INCINERATION FROM AN ENVIRONMENTAL VIEW.

Since MSW typically has a high degree of heterogeneity with different fractions, the combustion of waste may generate a wide variety of pollutants. The conditions under which waste is incinerated are established in Directive 2000/76/CE of European Parliament [18]. Thus, for the incineration of non-hazardous waste, the minimum temperature must be 850 ^{o}C for 2 seconds at least. These conditions ensure the total oxidation of waste, leading to the maximum energy release and reducing the generation of hazardous compounds. However, the complete suppression of pollutant production during the incineration stage is impossible.

The main environmental problems arising from MSWI plants are associated to pollutant emission to air, although they may also involve emission to water, related with the liquid effluents used in some flue-gas cleaning stages; and to soil, related with the deposition of particulate matter that commonly adsorbs heavy metals and persistent organic compounds on its surface. As a consequence, MSWI plants have faced the public opposition over the years. Nonetheless, the development of control and cleaning technologies, and the tightening of pollutant emission limits have greatly reduced the impact on the environment.

Focusing on air emission pollutants, MSWI plants normally produce between 4500 and 6000 m^3 of flue-gas per tonne of waste [15]. After the furnace, the main components of raw flue gas are nitrogen, oxygen, water vapour and carbon dioxide. Moreover, a wide variety of pollutants may also compose the raw flue gas in lower concentration: particulate matter of different sizes; acid gases such as HCl, SO_2, etc.; nitrogen oxides and ammonia; heavy metals such as Hg, Cd, Ni, etc.; and other carbon-based compounds, such as CO, VOCs, PCDD/F and PCBs.

Currently, Directive 2010/75/CE of the European Parliament stablishes emission limits of the pollutants, operational conditions and technical requirements for incineration of waste [19] (previously regulated by Directive 2000/76/CE). Table 1.2 shows the composition of raw flue gas after the boiler and the emission limit of the pollutants for MSWI plants. Large differences can be observed between both values, especially for particulate matter, acid gases and PCDD/Fs. This fact, added to the above-mentioned huge flue-gas volume produced during the incineration, makes the flue-gas cleaning (FGC) line and control systems as the most important areas of MSWI plants from environmental view. As a consequence, FGC is often a significant contributor to overall incineration cost, approximately between 15 and 35% of the total capital investment [15] and is an important energy consumer (the lower the required emission limits the higher the energy consumption of the FGC line).

FGC line is composed of a combination of single processes that provide a full treatment system for the flue-gas. The selection of these single stages and their position in the FGC line depends on the concentration and the selected emission limit of the pollutants, the investment required for its installation and operation, the effect that certain pollutants may have on the removal efficiency of other subsequent stages and the average operating life. Next, the typical pollutants generated in MSWI plants and the individual units used for their abatement are introduced, highlighting those used for NO_X and PCDD/Fs removal, which are the compounds studied in this work.

Table 1.2 Raw flue gas composition and emission limit for different substances (O_2 reference value 11%) [15].

Substance	Unit	After boiler	Emission limit 2010/75/EU
Total dust	(mg/Nm^3)	1000-5000	10[a]
Total organic compounds (TOC)	(mg/Nm^3)	1-10	10[a]
Hydrogen chloride (HCl)	(mg/Nm^3)	500-2000	10[a]
Hydrogen fluoride (HF)	(mg/Nm^3)	5-20	1[a]
Sulphur dioxide (SO_2)	(mg/Nm^3)	200-1000	50[a]
Nitrogen oxide as NO_2	(mg/Nm^3)	150-500	200[a]
Cadmium and thallium (Cd+Tl)	(mg/Nm^3)	< 3	0.05[b]
Mercury (Hg)	(mg/Nm^3)	0.05-0.5	0.05[b]
Other heavy metals (Sb, As, Pb, Cr, Co, Cu, Mn, Ni, V)	(mg/Nm^3)	< 50	0.5[b]
PCDD/Fs	(ng TE/Nm^3)	0.5-10	0.1[c]
N_2O	(mg/Nm^3)	< 40	–
CO	(mg/Nm^3)	5-50	50[a]
CO_2	(%v)	5-10	–
H_2O	(%v)	10-20	–

[a] Daily average emission limit.

[b] Average emission limit over a sampling period of a minimum of 30 min and a maximum of 8 hour.

[c] Average emission limit value over a sampling period of a minimum of 6 hours and a maximum of 8 hours.

1.3.1. Dust removal.

Dust is mainly ashes generated during MSW incineration. This particulate matter may have different particle size and is also considered as adsorbent of inorganic and organic chemicals, such as metal chlorine and PCDD/Fs. Prolonged exposure to

this matter mainly causes damages in the respiratory systems, as well as the problems associated to the pollutant adsorbed on the ash surface. In the environment, particulate matter is often deposited in soil and water, affecting the health of living beings [20].

Bag filter is the most used technique for dust removal with high efficiency for particle sizes above 0.1 microns (lower particle size is uncommon in MSWI plants). Bag filters must have suitable thermal, physical and chemical resistance. The typical materials used are polyimide, PTFE and fibreglass, which ensure working temperature above 200 ^{o}C. On the other hand, electrostatic precipitators are also selected for dust removal and are based in an efficient retention based on the typical charge of particulate matter. Temperature working windows are between 160-260 ^{o}C, although working in the high limit temperature is recommended to prevent PCDD/Fs generation.

1.3.2. Acid gases removal.

Acid gases group is composed by gaseous halides and sulphur oxides. The most common halogenated hydrides are HCl and HF; whereas SO_2 is the main sulphur oxide, although under appropriate conditions SO_3 can be generated. They are produced by the incineration of chloride, fluoride and sulphur containing waste, such as waste paper, plasterboard, plastic, etc.

Acid gases are irritating and toxic for humans. They have adverse effects on mucus and lungs. In addition, prolonged exposure to HF can cause serious damage to the digestive system and heart. Sulphur oxide released to atmosphere is acid rain precursor because it can react with water generating sulphuric acid. Acid rain causes the acidification of surface water, destruction of forest and wild life [21, 22].

The treatment with alkaline reagents is normally used to remove acid gases. There are different techniques based on the state of sorption agent and the contact between the sorbent and the flue gas: dry, wet and semi-wet processes.

In wet processes, the flue gas goes into a washing solution with the reagent dissolved. This technique leads to reach high efficiencies, although several washing solutions are needed. Thus, the first washing stages are mainly used to remove HCl and HF (with only water), generating extremely acidic solution, whereas in the

subsequent washing stages sulphur oxides are removed, which require conditions close to neutral pH (with sodium hydroxide or limestone slurry).

In dry sorption processes, the adsorption agent is fed into a reactor as dry powder. Typical adsorbents are sodium bicarbonate, hydrated lime and improved hydrated lime with high porosity. The application of this technique generates solid product, which should be subsequently removed in dedusting stages. This technique has lower efficiency than other techniques due to the lower contact between gas and solid phases, and the waste of unreacted sorbent.

In semi-wet processes, the sorption agent is added as a solution or as a suspension by spraying. The solvent is evaporated with the heat of flue gases. The neutralization reaction generates a solid, which must be removed as dust in the same equipment as dry processes. Semi-wet processes increase the contact between flue gas and sorbent agent, saving adsorbent and reaching higher efficiency.

1.3.3. Heavy metals removal (specially mercury).

Mercury, cadmium and thallium are the most restricted heavy metals. Mercury receives the most attention due to its high volatility, passing into the flue gas stream from the furnace. Mercury may be in elemental state and in ionic state, mainly as Hg^{2+}. The main source of heavy metals in the raw flue gas is the incineration of electronic components.

In humans, the prolonged exposure to mercury can affect the nervous system, causing emotional and psychological instability. In the environment, mercury and heavy metals accumulate in the soil and surface water, so they are absorbed by the living beings and can pass to humans through the food chain [23].

Selection of the techniques for mercury removal depends on the mercury state, which in turn depends on the chlorine concentration. Thus, high chlorine contents promote the ionic state, generating $HgCl_2$. Ionic form of mercury can be removed with wet scrubbers [15]. Elemental mercury can be removed from flue gas by adding an oxidizing compound to cause the ionic state of mercury or by deposition on sulphur-doped carbon or zeolites. This process may take place in a fixed-bed or in sorbent injected configuration.

1.3.4. Carbon monoxide and total organic carbon removal.

CO is generated by the incomplete oxidation of carbon containing waste. At low concentrations, CO may cause headache, nausea, weakness and unconsciousness. Continuous exposure may affect the nervous and cardiovascular systems, leading to neurological and cardiac disorder. Regarding the environment, the main problem is its flammability, since it can react with oxygen or other substances creating explosive mixtures. Moreover, CO is ozone precursor when it reacts with other atmospheric pollutants [24].

Together with CO, incomplete oxidation of waste produces a wide variety of unburned hydrocarbons in trace concentrations. The individual determination of these compounds is very difficult, so the TOC parameter (Total Organic Carbon) is usually used to account for these unwanted products. Thus, TOC parameter is an important indicator of the quality of incineration processes.

The generation of CO and compounds included in TOC parameter are mainly prevented by the optimization of chamber conditions, that is, improving the homogeneity in the furnace to avoid the formation of low temperature zones and/or zones with insufficient oxygen.

1.3.5. Nitrogen oxide removal.

Nitrogen oxides (NO_X) include nitrogen oxide (NO) and nitrogen dioxide (NO_2). Nitrous oxide (N_2O) is not measured as NO_X because its formation occurs if temperature of combustion is lower than the stablished or in oxygen deficient conditions. Thus, N_2O is usually considered together with CO emission.

NO_X is one of the most harmful anthropogenic air pollutants and can cause damages in air, soil, water and for living beings. Regarding environmental impacts, NO_X is the cause of photochemical smog, since it may react with other atmospheric pollutants affecting ozone formation. Moreover, NO_2 (emitted or generated from NO oxidation in the environment) is an acid rain precursor. Regarding impact in human beings, long exposure may affect the immune system, reducing the resistance to infections, as well as causing irreversible changes in lung tissue [25, 26].

In MSWI plants, NO_X can be generated by either oxidation of nitrogen contained in the waste (fuel NO_X) or by oxidation of nitrogen in gas the phase (thermal NO_X). The oxidation of molecular nitrogen occurs above 1000 ^oC, so NO_X are mainly formed by the oxidation of nitrogen contained in the waste because the temperature in the chamber is between 850-1000 ^oC and rarely exceeds 1000 ^oC.

There are different techniques to reduce the emission of NO_X. Primary techniques aim to inhibit thermal NO_X production by acting on the furnace conditions to ensure a homogeneous distribution of the primary and secondary air supply and to avoid high temperature zones. Another technique is the recirculation of flue gases in the secondary air supply to reduce the concentration of oxygen. The injection of water steam in primary zone of the chamber is also used to avoid hot spots. On the other hand, secondary techniques aim at reducing the NO_X already generated in order to comply with the emission limits set in the regulation. These techniques use a reducing agent (NH_3 or NH_3 derivatives) to reduce the NO_X in the flue gas to N_2. There are two processes: the selective non-catalytic reduction (SNCR) and the selective catalytic reduction (SCR).

In SNCR, NO_X are reduced by injecting the reduction agent into the furnace, so this process occurs at the temperature of furnace, between 850 and 1000 ^oC. The reducing agent is usually fed as aqueous solution and the most common are ammonia, ammonium hydroxide and urea. An effective SNCR requires a homogeneous mixture of raw flue gases and reducing agent, and a suitable residence time. However, this is extremely complex, and an excess of reduction agent is necessary to reach NO_X removal efficiency above 60-75% [15]. This fact causes the presence of unreacted ammonia (also known as ammonia slip) in the raw flue gas. Moreover, it should be noted the oxidation reaction of ammonia, which generates additional NO_X. According to Best Available techniques (BAT) document, in SNCR systems, NO_X and NH_3 emission ranges for annual average are 70-180 and 1-6 mg/Nm^3, respectively [27]. Moreover, it may also lead to the generation of N_2O as by-product under unfavourable conditions.

In SCR, the reducing agent is added to the flue gas just before it is fed into a catalytic reactor downstream of the incineration chamber. The reaction between NH_3 and NO_X occurs over a catalyst. The commercial catalyst and other alternative formulations that are currently under research will be addressed in Section 1.4.1.

NO_X removal efficiency in SCR process is above 90% [28, 29] with stoichiometric concentration of reduction agent, so, ammonia slip becomes irrelevant [30]. Temperature range at which SCR catalytic unit works depends on several variables, such as the required NO_X limit, the gas flow rate, the position of SCR reactor in the flue gas cleaning line, etc. There are three typical configurations of flue gas cleaning line depending on the location of SCR catalytic unit [31]: high dust, where the SCR reactor is placed at the front of FGC line just after the boiler and before the de-dusting stages; low dust, where the SCR reactor is placed after the de-dusting stages and before the removal of acid gas; and tail end, where the SCR reactor is placed at the end of FGC line after the removal of dust and acid gas.

In most MSWI plants, the SCR process is installed in tail-end configuration in order to prevent the catalytic deactivation caused by particulate matter and acid gas, especially SO_2. For this configuration, the typical operating temperature is between 180-250 ^oC [15, 31, 32]. Since the SCR reactor is located at the end of FGC line, an energy requirement is necessary to reheat the flue gas up to the operating condition of SCR reactor. However, some MSWI plants use high-dust configuration to avoid the reheating step at the expense of limiting the catalyst lifetime due to the higher dust and acid gas concentration.

Years ago, SNCR was the most widely used process to remove the NO_X generated in MSWI plants, because it allowed to reaching the emission limit with lower cost than SCR, since the installation of catalytic reactor and the reheating of flue gas is not necessary. One study estimates that the SNCR operating cost is between 25-40% lower than that of the SCR [33, 34].

However, the regulations on emission of gas pollutants are setting increasingly severe restrictions of emission limits. This is the case of Germany, whose NO_X emission limit is below that established by European regulation [35]. This fact is favouring the use of SCR systems in recent years, because of their higher NO_X removal efficiency and better use of reducing agent. The latter is very important because the impact of reducing agent slip (as in SNCR) is considered to excess the positive effect of NO_X removal [36].

The current increase in the implementation of SCR systems as alternative for NO_X removal is clearly evidenced by the growing number of MSWI plats with SCR reactor in Europe, which has increased from 21% in 2006 to 45% in 2019 [15, 37]. Regarding Spain, more than half of FGC lines have SCR system, which places Spain above

countries with higher rate of MSW incinerated, such as Denmark, Finland and the Netherlands.

1.3.6. Organic carbon compounds. Dioxins and furans.

The incineration of MSW can generate different organic compounds, e.g., benzene, toluene, xylene and polycyclic aromatic hydrocarbons; halogenated aromatic compounds and polychlorinated dibenzo-p-dioxins (PCDD) and polychlorinated dibenzo-p-furans (PCDF). The toxicity of all organic compounds is not the same. Public concern about the toxicity of PCDD/Fs is probably the highest.

PCDDs are composed by two benzenes bonded by two oxygen atoms, each one bonded on adjacent carbons (Figure 1.5). Each of the carbon atoms belonging to benzene structure may be bonded to chlorine instead of hydrogen atoms. PCDFs have similar structure, although the two benzenes are bonded by only one oxygen and a carbon-carbon bond (Figure 1.5). The location and number of chlorine atoms bonded to the carbon atoms belonging to benzene rings determine the different molecules that compose the group of PCDD/Fs as well as their toxicity.

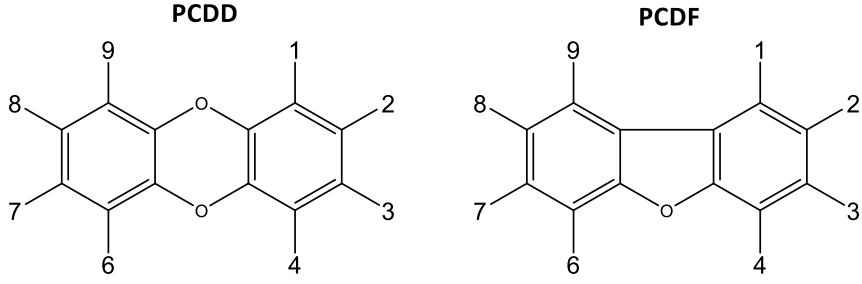

Figure 1.5. Chemical structure of PCDD and PCDF.

The emission limit for PCDD/Fs is established as toxic equivalent (TE) concentration. TE concentration is calculated as the sum of the multiplication of the mass concentration of each PCDD/F listed in the directive 2010/75/CE and its equivalence factor [19]. The equivalence factor, also reported in the above-mentioned directive, determines the relative toxicity of dioxins and furans, with a maximum value of 1 for the most toxic dioxin, which is 2,3,7,8-tetrachlorodibenzodioxin.

Even at low concentrations, PCDD/Fs have high toxicity and may be harmful for the environment and living beings. These compounds accumulate in soils and vegetation. They are degraded very slowly, persisting for many years in the environment and even may accumulate in the living beings, entering the food chain [38]. For humans, the short-time exposure to high PCDD/Fs concentrations may cause skin lesions, as well as liver function disorders. Prolonged exposure has been linked to disturbances of the immune, nervous and endocrine systems, as well as reproductive function [39].

PCDD/Fs contained in waste are efficiently removed at the incineration conditions set by the Directive 2010/75/CE (2 seconds minimum at minimum temperature of 850 ^{o}C). Thus, PCDD/Fs in raw flue gas are generated by the reaction of carbon, oxygen and chlorine compounds after the incineration stage. There are two formation pathways widely accepted [40, 41]. On the one hand the precursor route, in which PCDD/Fs are generated from precursors compounds, such as chlorophenols, chlorobenzenes and polychlorinated byphenils. On the other hand, the novo synthesis, in which PCDD/Fs are generated at low temperature range (200-400 ^{o}C) by means of the reaction between carbon or carbon compounds with inorganic chlorine compounds. The novo synthesis is catalysed by metal oxides, e.g., copper, so it generally occurs on fly ash and de-dusting stages. This fact supports the typical increase in PCDD/Fs concentration in post-combustion zones of MSWI plants throughout the boiler and de-dusting stages.

In order to abate the PCDD/Fs emission, there are different techniques that can be classified in two groups: those focused on preventing the generation of the pollutant (primary techniques) and those that remove the pollutant once it has been generated (secondary techniques).

Primary techniques are related to waste pre-treatment and optimization of combustion stage (to ensure homogeneity, suitable air supply, etc.), as well as control of FGC conditions (to avoid the synthesis novo). The goal is to prevent and/or to reduce the formation of PCDD/Fs and PCDD/Fs precursors. Moreover, the inhibition of PCDD/Fs by injecting chemical compounds in the flue gas is also used to prevent the generation of the pollutant. This technique aims to inhibit the catalytic function of metal oxide in the PCDD/Fs formation reaction. There are two typical inhibitor groups [25, 40, 42]: S-containing compounds, e.g., elemental sulphur, sulphur dioxide, carbon sulphide, pyrite, etc.; and N-containing

compounds, e.g., urea, ammonia, ethanolamine, etc. S-containing compounds work poisoning the metals through the formation of sulphates, whereas N-containing compounds cause the irreversible deactivation by the generation of organometallic nitride complexes.

In the case of secondary techniques, several processes are used in the FGC line to remove PCDD/Fs. It should be noted that most of the PCDD/Fs generated in the incineration are adsorbed in the fly ash, and the remaining are suspended in the gas phase. Thus, the removal efficiency of adsorbed PCDD/Fs will be linked to de-dusting removal efficiency. Regarding PCDD/Fs removal from the gas phase, adsorption process is the most widely used because it is simple, low cost and with high PCDD/Fs removal efficiencies. The most commonly used adsorbent is activated carbon, which is usually injected into the flue gas and then filtered in a bag filter [31, 41]. PCDD/Fs removal efficiencies above 90% are reported in the literature for this technique [43, 44]. However, adsorption processes have the drawback of only transferring the pollutant from the gas-phase to the adsorbent and, thus, it generates a waste that needs to be treated or landfilled.

Catalytic technology is an alternative to adsorption processes because it allows the destruction of PCDD/Fs and their precursors through oxidation reactions. In this sense, catalytic filter is a technology in which bag filters are impregnated with catalyst or the catalyst is mixed with the organic material, usually PTFE, that composes the fibres. This technology allows the efficient removal of particulate matter and PCDD/Fs in the gas phase. Tests at pilot scale have shown removal efficiencies of 96 and 99% for the PCDD/Fs gas phase and for the PCDD/Fs adsorbed on particulate matter, respectively [45]. At full-scale, this technology has been introduced in several MSWI plants from France and Belgium, with a PCDD/Fs removal efficiency above 99.5% [15].

As for catalytic technologies, several researches have reported SCR systems as useful stages for the catalytic oxidation of PCDD/Fs. Wang and co-workers [46] evaluated four sinter plants and reported lower PCDD/Fs concentration in those plants in which the flue gas was treated with SCR. In the same way, Sam-Cwan and co-workers [47] reported PCDD/Fs removal efficiencies of 93% in SCR systems in MSWI plants in Korea, whereas Goemans and co-workers [48] reported a PCDD/Fs removal efficiency of 99% in the SCR catalytic unit in the MSWI plant at Ghent (Belgium). These evidences are the starting point of a single-stage process for the

simultaneous removal of NO_X and PCDD/Fs, which are usually removed independently. In fact, PCDD/Fs removal in deNO_X units is already considered even in the BAT Reference Document for Waste Incineration published in 2019 [15].

1.4. INDEPENDENT CATALYTIC REMOVAL OF NO_X AND PCDD/Fs.

This section addresses the most widely used catalytic formulations studied for the removal of NO_X (through SCR), on the one hand, and PCDD/Fs or its model compounds and precursors (through catalytic oxidation), on the other hand.

1.4.1. NO_X selective catalytic reduction with NH_3.

The SCR of NO_X with ammonia involves the reaction between NO and/or NO_2 with NH_3 and oxygen to form harmless N_2 and water. The reaction between NO and NH_3 with equimolar stoichiometry is the ¨standard SCR¨ (Equation 1.1) and the reaction between NO_2 and NH_3 is known as ¨fast SCR¨ (Equation 1.2) because it is much faster than standard SCR. These are the most common reactions in the reduction of NO_X with NH_3, although other may also occur in lack of oxygen (Equation 1.3).

$$4NH_3+4NO+O_2 \rightarrow 4N_2+6H_2O \quad (1.1)$$

$$4NH_3+2NO_2+O_2 \rightarrow 3N_2+6H_2O \quad (1.2)$$

$$4NH_3+6NO \rightarrow 5N_2+6H_2O \quad (1.3)$$

It is widely accepted in the literature that redox and acid properties are fundamental for SCR. Acid function is strongly related to reagents adsorption and subsequent formation of intermediate species on the catalytic surface, whereas the redox function is associated to the re-oxidation ability of the active phase and the formation of intermediate species as well. Thus, active catalysts for SCR should offer a compromise between these two properties.

Vanadium-based catalysts have been widely studied for SCR over the years, indeed, the commercial catalysts used for stationary sources, such as MSWI plants, power plants, combustion processes, etc.; are based on vanadium oxide over titanium oxide and promoted with tungsten oxide or/and molybdenum oxide ($V_2O_5/WO_3/TiO_2$ and $V_2O_5/MoO_3/TiO_2$). In recent years, there has been a significant

increase in the number of publications focusing on the search for alternative catalyst for SCR. This research aims to solve the weakness of vanadium-based catalysts, such as the narrow operating temperature window and low catalytic activity at low temperature, using eco-friendly metal oxide active phases. Among all alternative catalysts, those based in Mn and Ce are interesting due to their high catalytic activity at low temperature. Exchanged zeolites, such as ZSM5 and BETA, with Fe and Cu, have also proved the broadening of working temperature window.

1.4.1.1. Vanadium-based catalysts for SCR.

The typical support for vanadium-based catalysts is TiO_2 in anatase phase, because it provides resistance to sulphate and favours the dispersion of vanadium, which leads to different vanadium species. In addition, this formulation is usually promoted with WO_3 and/or MoO_3 in order to obtain better catalytic performance and to improve structural properties [29].

The catalytic activity of vanadium-based formulations mainly depends on the vanadium content and its dispersion, that is, the vanadium species generated over the TiO_2 support. Below the monolayer coverage (<8 V atoms/nm^2), isolated species are firstly generated and the increase in vanadium content leads to polymeric species. Above monolayer coverage (>8 V atoms/nm^2), crystalline V_2O_5 nanoparticles are generated [28]. Polymeric species are considered as the most active because they lead to the fastest re-oxidation of the active sites [49, 50].

Regarding catalytic performance, V-based formulation has been extensively studied over the years. At lab-scale, NO conversions below 80% have been reported [51], although subsequently an increase in catalytic activity was found by Lietti and co-workers [52] with NO conversion above 90% in the temperature range of 350-500 ^oC. The promotion with MoO_3 leads to NO conversions above 90% between 250-300 ^oC, although selectivity to N_2 strongly decreases from 450 ^oC [52]. The use of WO_3 as promotor is reported to keep the N_2 selectivity above 95% below 500 ^oC and to broaden the operating temperature window (NO conversion above 90%) between 300-500 ^oC [53, 54]. On the other hand, working with an ammonia slip has also been reported to achieve high NO conversion at low temperature, although it decreases the selectivity to N_2 [55].

On the other hand, two reaction pathways are accepted for SCR over V-based catalysts. The NH_3 adsorbed species react either with adsorbed NO species, through Langmuir-Hinshelwood mechanism, or with gaseous NO, through Eley-Rideal mechanism [56, 57].

However, the main drawback of V-based catalysts is the high operating temperature, which would imply high reheating costs at full scale, since the SCR reactor is normally placed in tail-end configuration (at the end of FGC line). Moreover, this catalytic formulation has high SO_2 oxidation activity and N_2O generation at high temperature. These drawbacks greatly restrict the application of V-based catalysts in deNO_X processes. For this reason, currently, many works study how to overcome these negative aspects doping the V-based catalysts or using catalytic formulations based on metal oxides other than vanadium.

The doping with Ce leads to broadening of the operating temperature window of V_2O_5-WO_3/TiO_2, with NO conversions above 90% between 200-500 ^oC, because the increase of oxygen mobility promotes NO oxidation to NO_2. Moreover, Ce increases the acid properties, more specifically Brønsted acidity [58, 59]. CeO_2 doping of TiO_2 support also leads to the improvement of catalytic activity by means of the more labile surface oxygen, as a result of Ce and Ti interaction [59]. In the same way, Sb and Nb co-doping of V_2O_5/TiO_2 catalysts greatly increases NO conversion, which is associated to enhancement of redox properties and the promotion of surface hydroxyl group, as a consequence of water dissociation [60]. Zr doped V_2O_5/WO_3-TiO_2 increases the activity and N_2 selectivity at high temperature because of the improvement of thermal stability [61].

1.4.1.2. Manganese and cerium oxide-based catalysts for SCR.

Single MnO_X has been extensively studied because of its excellent catalytic performances for low temperature SCR. This fact is associated to the variable oxidation state of Mn and to its excellent redox properties. The high number of oxidation states of Mn is the precursor of the different existing Mn oxides. According to literature, MnO_2 exhibits the highest catalytic activity, although it also promotes a higher N_2O selectivity than, for example, Mn_2O_3 [62, 63].

Despite the good catalytic performance for low temperature SCR, MnO_X has several drawbacks, such as the high selectivity to N_2O above 150 ^oC and the deactivation in

the presence of SO_2 and chlorinated organic compounds (both of which are present in FGC line of MSWI plant) at low temperature. Two modifications are usually made to avoid the disadvantages of single MnO_X: on the one hand, supporting MnO_X over a metal oxide and, on the other hand, the preparation of multi-metal oxide catalysts by mixing or doping MnO_X with other metal oxides.

Al_2O_3 and TiO_2 are the most reported supports for the immobilization of transition metal or multi-metal oxides. Al_2O_3 provides excellent mechanical properties, high temperature resistance and high surface area to the catalyst. Kapteijn and co-workers [62] studied NO and NH_3 adsorption over MnO_X/γ-Al_2O_3 and Singoredjo and co-workers [64] the effect of Mn precursor on the catalytic activity of MnO_X/γ-Al_2O_3 in SCR. However, Al_2O_3 has poor resistance to SO_2. In this sense, a superior SO_2 resistance is provided by TiO_2 because sulphate species are easily decomposed on its surface [65].

On the other hand, MnO_X doping with CeO_2 has been widely reported [66, 67], since Ce can act as modifying agent of the bulk structure improving the catalytic performance. The benefits of CeO_2 come from its capacity to store oxygen, its redox properties and its characteristic structure, which can incorporate other metals, such as Mn, generating a solid solution with structural defects that favours the generation of oxygen vacancies. In this sense, MnO_X-CeO_2 composite is reported as an excellent catalyst for low temperature SCR. Qi and co-workers [68] observed total NO conversion at temperatures below 150 ^oC for catalysts with low Mn contents. The increase of Mn contents leads to broadening the temperature range in which the NO conversion is above 95% [69].

Regarding reaction pathway, NO adsorption is generally stronger in metal oxide catalysts, such as MnO_X-CeO_2 catalysts. On the other hand, there is no agreement about the active sites where NH_3 adsorption occurs. The stronger adsorption of both NO and NH_3 involves a higher contribution of Langmuir-Hinshelwood mechanism in comparison to V-based catalysts.

Preparation method is a key factor for MnO_X-CeO_2 formulation because it affects the interaction between Mn and Ce, and consequently the final structure of the catalyst. There are several methods reported in the literature to prepare the MnO_X-CeO_2 composites: impregnation, co-precipitation, sol-gel, hydrothermal, etc. Table 1.3 lists a short summary of NO conversion obtained in the literature with Mn and Ce based catalysts prepared by different methods. However, no agreement is

found about which one is the most appropriate for a SCR purpose. Yao and co-workers [70] reported excellent catalytic performance for MnO_x-CeO_2 catalysts prepared by hydrothermal method due to the higher amount of oxygen vacancies, surface adsorbed oxygen species and acidic sites. Qi and co-workers [68] compared the catalytic performance of catalysts prepared by citric acid, co-precipitation and impregnation methods. Higher NO conversion levels were observed with the catalysts prepared by citric-acid method. On the other hand, Qi and co-workers [69] reported the preparation of catalysts with superior performance in low-temperature SCR by redox-precipitation method.

Table 1.3 Short review of Mn and Ce based catalysts and catalysts performance in SCR at low temperature.

Catalysts	Preparation Method	Reaction conditions	NO conversion	Ref.
Mn-Ce	Citric acid	1000 ppm NH_3, 1000 ppm NO, 2%O_2, 42000 h^{-1}	>90% (100-150 ^oC)	[71]
Mn-Ce	Co-precipitation	1000 ppm NH_3, 1000 ppm NO, 2%O_2, 84000 h^{-1}	100% (100-180 ^oC)	[72]
Mn-Ce	Citric acid	500 ppm NH_3, 500 ppm NO, 2%O_2, 42500 h^{-1}	>90% (160-200 ^oC)	[73]
Mn-Ce	Surfactant-template	500 ppm NH_3, 500 ppm NO, 5%O_2, 64000 h^{-1}	100% (100-200 ^oC)	[74]
Mn-Ce	Redox-precipitation	800 ppm NH_3, 715 ppm NO, 3%O_2	100% (100-170 ^oC)	[69]

1.4.2. Catalytic oxidation of PCDD/Fs.

Catalytic oxidation aims to the complete oxidation of PCDD/Fs to CO_2, water and other compounds, such as HCl (Equation 1.4). The use of catalysts allows to perform the reaction in a more efficient way. The main advantage of PCDD/Fs catalytic oxidation over the typical separation processes, such as adsorption on activated

carbon, is the complete destruction of the pollutant, which avoids the generation of a waste that further needs to be treated.

$$C_{12}H_nCl_{8-n}O_2+(9+0.5n)O_2 \rightarrow (n-4)H_2O+12CO_2+(8-n)HCl \quad (1.4)$$

Due to the high toxicity and difficult handling of PCDD/Fs, many works use PCDD/Fs model compounds, such (poly)chlorobenzenes and (poly)chlorophenols, to study the catalytic oxidation at lab-scale. This fact may seem to distance the research from the real conditions, although it must be taken into account that PCDD/Fs model compounds have similar structure than PCDD/Fs, so their use is justified and widely reported in the literature [31, 75, 76].

The catalytic oxidation of VOCs involves textural properties (availability of active sites), redox properties (related with oxygen mobility and the dissociation of gas phase oxygen in the catalytic surface) and acid properties (involved in the adsorption of the reactants). Thus, the catalytic formulation for this purpose must have a synergy between these properties. There are generally two groups of catalysts to perform the catalytic oxidation of VOCs: noble metal catalysts and transition metal oxide catalysts.

Noble metal catalysts receive special attention in VOCs oxidation due to their high efficiency. The most reported noble metal catalysts are based on Pt and Pd and supported over different metal oxides. In this sense, Scire and co-workers [77, 78] found higher catalytic activity and lower by-product production with Pt-based catalysts than zeolite-based catalysts, whereas Giraudon and co-workers [79, 80] observed higher catalytic activity using TiO_2 as support, due to excellent reducibility. However, noble metal catalysts are rather restricted due to their high cost and also their deactivation by chlorine adsorption [81].

Regarding transition metal oxides, V-based catalysts have been attractive for the catalytic oxidation of chlorinated VOCs in the last years because they have excellent catalytic activity and selectivity. In this sense, vanadyl species play an important role both in oxidation and SCR. The vanadium with the highest oxidation state (V^{5+}) is the most active species, which becomes prominent in polymeric and crystalline species [82-84].

Despite the extensive study of V-based formulation over the years for the catalytic oxidation of chlorinated VOCs at lab-scale, few experiments have been conducted

with PCDD/Fs [85, 86]. On the contrary, the number of works that have studied the catalytic oxidation of PCDD/Fs model compounds is much larger. In this sense, Corella and co-workers [87] compared the catalytic activity of V_2O_3-WO_3/TiO_2 commercial catalysts and Pt based catalysts in the ortho-dichlorobenzene (o-DCB) oxidation. The results showed o-DCB conversions of 57% at 330 ^oC for deNO_X catalyst, which were higher than those obtained by the noble metal catalyst. In the same way, Lichtenberger and co-workers [75] reported minimum temperatures of 350 ^oC to reach 90% of o-DCB conversion with a V_2O_5/TiO_2 catalyst with polymeric species, whereas Cho and co-workers [88] reported that lower temperatures (around 300 ^oC) allow to reach similar values of o-DCB conversion, although their experiments were carried out in the presence of water.

Currently, many works are focusing on the search for alternative catalysts that lead the efficient removal of PCDD/Fs and chlorinated VOCs with higher conversion at lower temperatures. In this sense, transition metal oxide catalysts based on cobalt, manganese, cerium and iron oxides, etc., are reported in the literature [41, 81]. Among them, Mn-based catalysts show high catalytic activity and selectivity in the oxidation of chloroaromatic compounds at low temperature.

1.4.2.1. Manganese and cerium oxide-based catalysts for PCDD/Fs catalytic oxidation.

The use of Mn-based catalysts is justified due to their high efficiency in oxidation reactions and low toxicity. Their excellent oxidizing properties are associated to the possibility of hosting different oxidation states of Mn in the same structure, which are mainly Mn^{3+} and Mn^{4+}, and the high oxygen content on its structure [89]. It should be noted that no works have been found in the literature that study PCDD/Fs removal with Mn-based catalysts at lab-scale. The majority of them focus on the removal of VOCs and chlorinated organic compounds, such as mono and dichlorobenzene.

Several works have studied supported MnO_X catalyst performance in the catalytic oxidation reaction. The dispersion of MnO_X and its interaction with the support seems to be a key factor in oxidation reactions. Nevertheless, the support also affects catalytic activity. Liu and co-workers [90] studied the MnO_X active phase over different supports in chlorobenzene oxidation. They reported the highest

activity for MnO_X/TiO_2, due to the promotional effect of TiO_2 in the dispersion of the active phase. Al_2O_3 support has also been reported to provide a good dispersion of MnO_X active phase, which leads to total and selective conversion of o-DCB on MnO_X/Al_2O_3 at low temperature.

On the other hand, catalytic behaviour of Mn-based catalysts can be improved by the addition of one or several transition metals, such as Ti, due to the synergy effect generated [91]. Moreover, Mn mixed oxide composites based on Cu, Ce, Co, etc., have been reported in the literature [81, 92, 93]. Interestingly, as in SCR, MnO_X-CeO_2 mixed oxide is the most researched formulation due to the excellent oxygen mobility and storage provided by Ce. Indeed, MnO_X-CeO_2 formulation has been extensively tested in the oxidation of both VOCs, such as hexane, phenol and toluene [94-96], and chlorinated organic compounds, such as (poly)chlorobenzenes and trichloroethylene [97, 98].

The metal content is a key factor, and most authors agree that the best catalytic performances are obtained with Mn-rich formulations. Delimaris and co-workers [96] observed that Mn/(Mn+Ce) with an atomic ratio around 0.75 was the most active catalyst in the catalytic oxidation of ethanol, ethyl acetate and toluene. Similar results were reported by Wang and co-workers [98], who concluded that a Mn atomic ratio around 0.86 was the optimum in chlorobenzene oxidation. The preparation method has also been studied. These mixed oxide catalysts are mainly prepared by sol-gel and co-precipitation, which provide high Mn and Ce interaction both at the catalytic surface and bulk structure.

1.5. SIMULTANEOUS REMOVAL OF NO_X AND PCDD/Fs.

The simultaneous removal of NO_X and PCDD/Fs, proposed for MSWI plants, is an operation that would allow the removal of two different pollutants, which are normally removed separately, in single stages. The implementation of this process on a large scale would cause minor changes in the FGC line, but it would improve cleaning efficiency and even reduce operating costs. In the literature, this process has been proposed on the basis of two pathways: non-catalytic and catalytic pathway.

Non-catalytic pathway is based on the ability of ammonia precursors used for SNCR, such as urea, ammonia solution, ammonium hydroxide, etc., to act as inhibitor of

novo synthesis. Thus, the use of these chemical compounds in SNCR process would simultaneously reduce NO_X and PCDD/Fs emissions. However, this process has limitations associated with the degradation and consumption these ammonia precursors may suffer, since they are added in the combustion stage at high temperature [25, 42].

On the other hand, the catalytic pathway is based on the fact that the catalyst used to abate NO_X emissions in the SCR unit is also active to perform the catalytic oxidation of PCDD/Fs. The simultaneous catalytic removal of NO_X and PCDD/Fs is referred to as $dDiNO_X$, and several evidences in MSWI plants have corroborated its feasibility [46, 48].

1.5.1. State of the art of the catalytic simultaneous removal of NO_X and PCDD/Fs.

The feasibility of simultaneous removal of NO_X and PCDD/Fs has been reported by several authors and at different scales. At full scale, Goemans and co-workers [48] reached PCDD/Fs removal efficiencies below the emission limit after the SCR unit, with NO conversion of 90% in a MSWI plant of Belgium. At pilot-scale, Liu and co-workers [99] reported removal efficiencies above 90% of both pollutants at temperatures higher than 300 ^{o}C. At lab-scale, Debecker and co-workers [100] evaluated the PCDD catalytic oxidation over V_2O_5/TiO_2 catalysts promoted with WO_3 and MoO_3.

The first reference to the simultaneous removal of NO_X and chlorinated hydrocarbons date back to the 1990s. Jones and Roses [101] evaluated the simultaneous removal of NO and o-DCB or ethyl chloride over V_2O_5 supported over Zr-modified Al_2O_3. The results showed high conversions of both pollutants in a moderate temperature range. Subsequent works on this issue are scarce and mainly focused on catalytic oxidation of chlorinated organic compounds with SCR active catalysts, but in the absence of NO and NH_3. The most important contributions in this field in the late 1990s and early 2000s were made by Busca and co-workers and Amiridis and co-workers.

The early studies of Busca and co-workers aims to evaluate $V_2O_5/WO_3/TiO_2$ in the catalytic oxidation of VOCs, such as propane, propene, isopropanol, o-DCB, etc. [102, 103]. Afterwards, they also contributed to the elucidation of active species

formed after chlorinated organic compounds over V_2O_2-MoO_3-TiO_2 catalyst [104]. Similarly, Amiridis and co-workers focused on the study of catalysts using o-DCB as model compound. They evaluated TiO_2 and Al_2O_3 as support and, then, they also compared the catalytic behaviour of different active phases (Fe_2O_3, Co_3O_4, MoO_3, etc.) and perovskite [105-108]. Moreover, they studied other chlorinated benzenes and trichlorophenol as model compounds, as well as the effect of the presence of other compounds, such as water and m-naphthalene [75, 109-111].

The modification of V-based catalysts with promotors or doping agents and the preparation methods of these formulations were further studied by different authors. In this sense, Albonetti and co-workers studied the catalytic oxidation of chlorinated organic compounds with an alternative V_2O_5/TiO_2 catalyst prepared by polyol-mediated synthesis and with a SiO_2 modified V_2O_5/TiO_2 catalyst [112]. In the same way, Debecker and co-workers compared the catalytic behaviour between catalysts prepared by impregnation and flame-made methods in the chlorobenzene oxidation [84]. Furthermore, they analysed V_2O_5/TiO_2 catalysts prepared by sol-gel and MoO_3 and WO_3 doping by non-hydrolytic sol-gel route [113, 114].

These works have mainly extended the knowledge of catalytic oxidation of chlorinated organic compounds over V-based catalysts. However, as mentioned above, they were conducted in the absence of typical SCR feeding. In this sense, Bertinchamps and co-workers [115, 116] evaluated the effect of NO on o-DCB oxidation. They concluded NO causes a positive effect at low temperature due to NO_2 formation, which oxidizes in a faster way the vanadium oxide active sites.

Recently, Gallastegi-Villa and co-workers have reported several works about the simultaneous removal of NO_X and o-DCB. These works have demonstrated the feasibility of dDiNO_X process with V-based formulations [117, 118]. Moreover, they have reported a dependence between NO reduction and o-DCB oxidation. Thus, NO and NH_3 have a positive effect at low temperature in o-DCB oxidation due to the formation of NO_2, whereas at high temperature there is a competition between NH_3 and o-DCB for the Brønsted acid sites. On the other hand, o-DCB has a minor effect on SCR, decreasing NO conversion in the medium-high temperature range [119].

The effect of WO_3 as catalytic promoter in dDiNO_X process was also addressed by Gallastegi-Villa and co-workers [119]. They elucidated an increase of promotional effect of WO_3 at low vanadium loading. This fact is associated to the interaction

between vanadium and tungsten oxides, which promotes a polymerization of both species leading to polymeric structures but with different acidity degree than polymeric vanadium species.

Currently, in order to operate in a more efficient way, the trend is to search for more active catalysts to implement the low temperature SCR, which would decrease the high operating temperature needed by actual SCR units in tail-end configuration in MSWI plants. In this context, the viability of $dDiNO_X$ process depends on catalytic activity of these SCR alternative catalysts in the catalytic oxidation of PCDD/Fs or PCDD/Fs model compounds.

MnO_X-CeO_2 catalytic formulation proposed in this thesis has been reported for its high catalytic activity in low temperature SCR, as described in Section 1.4.1. In the same way, there are several works reporting its high catalytic activity in the catalytic oxidation of VOCs and chlorinated organic compounds, such as PCDD/Fs model compounds. The good catalytic behaviour of this formulation in both reactions is associated to its excellent redox and acid properties, as well as the high oxygen storage and mobility provided by Ce. However, there are no works yet studying the simultaneous removal of NO_X and PCDD/Fs in the same catalytic reactor. Since it has already been proven that SCR and o-DCB oxidation do not occur independently of each other, it is important to progress in the study of both reactions performed simultaneously.

Therefore, this thesis is considered necessary to assess the MnO_X-CeO_2 catalytic formulation, which is currently being postulated for low temperature SCR as alternative to the traditional VO_X-WO_3/TiO_2 catalyst, for the simultaneous removal of NO_X and PCDD/Fs.

1.6. OBJECTIVES AND LAYOUT.

Due to the huge generation of waste, European institutions are currently encouraging a series of policies in accordance with the framework of Directive 2008/98/CE, to promote a sustainable waste management. This directive stablishes a hierarchy for prioritizing an order in waste prevention and management, where any form of waste recovery takes priority over disposal. Energy recovery allows the use of waste fractions that cannot be reused nor recycled to produce energy, in the

form of electricity and/or heat. Incineration is the most widely used process for the energetic recovery of waste.

Although the conditions laid down in the regulations for carrying out the incineration of waste ensure the complete oxidation of waste and the reduction in the generation of hazardous compounds, the complete suppression of pollutants during incineration is impossible. As aforementioned, the gas cleaning system of a MSWI plant is the most important part from an environmental view because it allows to abate the hazardous compounds generated during waste incineration. According to the conventional processes included in the gas cleaning system, the use of SCR catalytic technology to perform the simultaneous removal of NO_X and PCDD/Fs ($dDiNO_X$) is an alternative that allows to operate in a more efficient way, since it promotes the abatement of two pollutants in the same stage with the high efficiency derived from catalytic technologies.

$dDiNO_X$ process has the difficulty of removing two compounds simultaneously by means of two totally different reactions (NO_X through a reduction and PCDD/Fs though an oxidation reaction). The results obtained by the typical SCR catalyst, based on vanadium, show some negative aspects. Currently, the MnO_X-CeO_2 formulation is widely reported as an alternative to perform SCR at low temperature. Thus, this thesis aims the assessment of MnO_X-CeO_2 catalytic formulations in $dDiNO_X$. In order to meet this main goal, several specific objectives have been proposed:

- Optimization of the synthesis of MnO_X-CeO_2 formulations to obtain the best catalytic performance.
- Detailed analysis of activity and selectivity of $dDiNO_X$ process, as well as possible side reactions and effects of feed composition.
- Proposal of a reaction pathway for SCR and oxidation reaction over MnO_X-CeO_2 catalyst.
- Improvement of the catalytic performance through modifications of MnO_X-CeO_2 formulation.

These specific objectives are addressed to in the different chapters that compose this thesis. Chapter 2 deals with the methodology of catalytic synthesis and the description of characterization techniques, as well as the equipment used for this

purpose. In addition, Chapter 2 includes a section where the experimental set-up and the different protocols used to perform the catalytic activity tests are described. This section also includes the results obtained from a repeatability analysis of experimental set-up and the conclusions of applying the plug flow conditions and mass transfer limitations.

Chapter 3 addresses an optimisation of the synthesis of MnO_X-CeO_2 formulations in order to obtain the best catalyst. The chapter is structured in three sections that study the effect of the preparation method, the effect of Mn and Ce composition and the effect of some of the variables involved in the best preparation method. Each of these sections describes the results obtained from the characterization analysis and the catalytic activity tests. This allows to conclude which catalytic properties and active species are the most important to improve the efficiency in $dDiNO_X$. Regarding catalytic activity, SCR and oxidation reactions were performed simultaneously, although each of them has been discussed separately to make it easier for the reader to understand.

After concluding which is the optimal catalyst (preparation method, composition and variables of preparation), a detailed analysis of $dDiNO_X$ process is made in Chapter 4. For this purpose, the results obtained after operating simultaneously and independently are compared. Moreover, different catalytic tests are also performed in order to understand the origin of by-products and to corroborate several hypotheses derived from the analysis of the light-off curves. Chapter 4 also studies the effects that changes in the concentration of the reagents associated to the $dDiNO_X$ process cause on catalytic activity. This issue allows for a deeper understanding of the effect that each of these components has on the process. Additionally, the effect of other compounds that would be present in real conditions, such as water, is evaluated.

In Chapter 5, the species formed after adsorption of the reagents involved in $dDiNO_X$ are evaluated by FTIR. For this purpose, experiments with different feeding and at different temperatures were carried out. Based on the adsorbed species identified; their evolution with time, temperature and the presence of other reagents; and the results obtained from catalytic activity tests in previous chapters, a reaction pathway is proposed for each of the reactions involved in $dDiNO_X$.

Chapter 6 evaluates different strategies followed to improve the catalytic performance of MnO_X-CeO_2 formulations. Two strategies have been followed. On

the one hand, support of the MnO_X-CeO_2 formulation over several supports with different structural, morphological and chemical properties. On the other hand, surface doping of the MnO_X-CeO_2 formulation with different metals. All the catalysts studied in this chapter are characterized and evaluated in the catalytic activity tests. The results are compared to the optimum MnO_X-CeO_2 catalyst in order to know whether the predicted improvements the catalytic properties have a positive effect on catalytic performance.

Although a section with the global view is included at the end of each chapter, Chapter 7 describes the main conclusions of this thesis, thus giving an overview of the whole work. In addition, future works are proposed in order to progress on the aspects that could not be addressed during the period in which this research was carried out.

Finally, Chapters 8 and 9 include the nomenclature and bibliography employed throughout this thesis work.

Chapter 2

MATERIALS, METHODS AND EQUIPMENT

Chapter 2

MATERIALS, METHODS AND EQUIPMENT

ABSTRACT

This chapter provides general information about materials, procedures and experimental set-up used in this thesis for catalyst preparation, characterization and catalytic testing. Firstly, materials and preparation methods for catalytic synthesis are introduced. Subsequently, techniques, equipment and protocols followed in catalyst characterization are summarized. Then, the reaction system and the protocols for catalytic tests are exposed, as well as a repeatability analysis of experimental set-up and the criteria followed to corroborate the absence of diffusional limitations. Finally, the equipment and protocols utilized for in situ FTIR experiments are detailed.

2. MATERIALS, METHODS AND EQUIPMENT.

2.1. CATALYSTS PREPARATION.

For the development of this work, different catalysts have been prepared using several methods. The type of catalysts, the preparation methods and the section in which these catalysts appear are listed below.

- Bulk MnO_X-CeO_2 prepared by co-precipitation (Chapter 3, Chapter 4 and Chapter 5).
- Bulk MnO_X-CeO_2 prepared by sol-gel (Section 3.1 and Section 3.2).
- Supported MnO_X/CeO_2 prepared by impregnation (Section 3.1).
- Mixed MnO_X-CeO_2 prepared by mechanical mixing (Section 3.1).
- Supported MnO_X-CeO_2/(TiO_2, Al_2O_3, H-ZSM5 and H-BETA) prepared by co-precipitation-deposition (Section 6.1).
- Supported metal oxide (Fe, Zr, Co, Sr and W)/MnO_X-CeO_2 prepared by impregnation (Section 6.2).

2.1.1. Materials and reagents.

A great number of catalysts have been synthesized using several preparation procedures and methodologies. The main specifications of all reagents used in catalytic preparation are listed in Table 2.1.

Commercial supports are also included in Table 2.1. ZSM5 and BETA zeolites were supplied in ammonium exchanged form (NH_4-ZSM5 and NH_4-BETA). All supports were calcined at 550 ^oC for three hours with a heating ramp of 1 ^oC/min to provide thermal stability. In the case of zeolites, the calcination step also allowed to transform them into their protonic form (H-ZSM5 and H-BETA).

Table 2.1. Specifications of the reagents used for catalytic preparation.

Name	Chemical formula	Supplier	Assay
Precursors			
Manganese(II) nitrate tetrahydrate	$Mn(NO_3)_2{\cdot}4H_2O$	Merck	>98.5%
Cerium(III) nitrate hexahydrate	$Ce(NO_3)_3{\cdot}6H_2O$	Sigma Aldrich	99%
Iron(III) nitrate nonahydrate	$Fe(NO_3)_3{\cdot}9H_2O$	Alfa Aesar	>98%
Cobalt(II) nitrate hexahydrate	$Co(NO_3)_2{\cdot}6H_2O$	Fluka	>98%
Strontium nitrate hexahydrate	$Sr(NO_3)_2{\cdot}6H_2O$	Sigma Aldrich	>99%
Zirconium(II) nitrate hexahydrate	$Zr(NO_3)_2{\cdot}6H_2O$	Sigma Aldrich	>99%
Ammonium metatungstate hydrate	$(NH_4)_6H_2W_{12}O_{40}{\cdot}xH_2O$	Sigma Aldrich	>99%
Precipitating agents			
Ammonium carbamate	$H_2NCOONH_4$	Sigma Aldrich	99%
Ammonium hydroxide	NH_4OH	Acros Organics	28-30% in water
Sodium carbonate	Na_2CO_3	Fluka	>99%
Sodium hydroxide	NaOH	Acros Organics	98%
Chelating agent			
Citric acid	$C_6H_8O_7$	Sigma Aldrich	99%
Commercial supports			
Titanium dioxide	TiO_2	Millenium Inorg.Global C	>99.5%
Gamma-alumina	γ-Al_2O_3	Saint-Gobain N.	>99.5%
NH_4-ZSM5	NH_4-ZSM5	Zeolyst I.	>99%
NH_4-BETA	NH_4-BETA	Zeolyst I.l	>99%

2.1.2. Preparation methods.

2.1.2.1. Co-precipitation.

Precipitation is the formation of a solid as a result of the saturation of a solution. This process has a first nucleation step, followed by a growth of the particle size. The saturation can be promoted by changes in solute concentration, pH and/or temperature. On the other hand, co-precipitation is based on the precipitation of more than one component, leading to a solid precursor with all components. The catalysts prepared by this technique can have a high content of the metals in small particle sizes. In this work, co-precipitation was induced by changing the pH of precursor solution by means of the addition of a pH-modifying agent, also known as precipitating agent.

Co-precipitation was carried out in a 500 mL beaker equipped with a magnetic stirrer. The proper amounts of manganese nitrate ($Mn(NO_3)_2{\cdot}4H_2O$) and cerium nitrate ($Ce(NO_3)_3{\cdot}6H_2O$) were dissolved in distilled water at room temperature, to obtain a precursor solution with Mn and Ce concentrations of 0.55 and 0.35 M, respectively. Subsequently, precipitation of the metal cations was promoted by adding a 1.3 M solution of ammonia carbamate ($H_2NCOONH_4$) drop by drop with a burette, until a pH value of 9 is reached. The resulting suspension was aged for 2 hours and, then, filtered and washed with distilled water. Finally, the obtained solid was dried over night at 100 ^oC and calcined in static air at 500 ^oC for 3 hours by heating the sample at a rate of 1 ^oC/min in an oven (Nobertherm 30-3000). Additionally, the catalysts were pelleted, powdered and sieved to 0.3-0.5 mm.

Catalysts prepared by this synthesis method are discussed in Chapters 3, 4 and 5. Moreover, in Section 3.3, the effect of precipitating agent, pH, ageing time and calcination temperature on activity and selectivity was analysed.

Co-precipitation-deposition

This method involves the deposition of the active metals, Mn and Ce, from a precursor solution on a support by means of a precipitation process. Accordingly, the proper amount of support, with a particle size below 0.25 mm, was first mixed with 100 mL of distilled water at room temperature in a beaker with magnetic

stirrer in order to obtain a homogeneous suspension. After that, the precursor solution with Mn and Ce was added to the suspension. Finally, co-precipitation of Mn and Ce over the support was promoted by adding the precipitating agent following the same procedure as for bulk MnO_X-CeO_2 catalysts. The catalysts prepared by co-precipitation-deposition are discussed in Section 6.1.

2.1.2.2. Sol-gel.

Sol-gel method produces porous solids with excellent morphological properties that can also have high content of the active metals. It is characterised by the formation of a colloidal solution generated by the condensation of dissolved molecular precursors. Subsequently, a gelation stage promotes the merging of these colloids into polymeric chains through bonding with active metals.

The preparation of bulk MnO_X-CeO_2 catalysts is carried out as follows. The proper amount of $Mn(NO_3)_2{\cdot}4H_2O$ and $Ce(NO_3)_3{\cdot}6H_2O$ were solved at room temperature in a 250 mL beaker equipped with magnetic stirring. Then, citric acid ($C_6H_8O_7$) was added as chelating agent (CA) with a CA/(Mn+Ce) molar ratio of 0.3. The formation of the gel occurred by the progressive evaporation of the solvent at 80 ^oC in continuous stirring. The obtained gel was dried over night at 100 ^oC and calcined in static air at 500 ^oC for 3 hours and with a heating ramp of 1 ^oC/min. Finally, the catalysts were pelleted, powdered and sieved to 0.3-0.5 mm. The catalysts prepared by sol-gel method are discussed in Sections 3.1 and 3.2.

2.1.2.3. Impregnation.

Impregnation is a simple method to prepare supported catalysts. Firstly, an insoluble solid (support) is put in contact with a precursor solution. Then, the solvent of this solution is progressively evaporated. In this work, a volume of precursor solution larger than the pore volume of the support has been used in order to favour a good distribution of the active phase in all the particles of the support (wet impregnation).

All the impregnations of this work were carried out in a rotary evaporator (Büchi R-114) equipped with vacuum system and thermostatic bath, as follows. The catalysts prepared by impregnation method are discussed in Section 3.1 and 6.2.

Firstly, CeO_2 support was prepared by precipitation in the same way as for bulk MnO_X-CeO_2 catalysts, although the obtained solid was calcined at 550 ºC for 3 h in order to ensure its thermal stability in the second calcination step after introducing the active phase. Then, the proper amount of CeO_2 support was weighted and placed in an evaporating flask and, subsequently, it was subjected to vacuum conditions at 40 ºC for approximately 1 hour in order to remove the molecules superficially adsorbed. Next, the evaporating flask, still in vacuum conditions, was immersed in a cold bath (around 5 ºC) to avoid spontaneous evaporation of the precursor solution.

Secondly, the precursor solution with the proper amount of $Mn(NO_3)_2{\cdot}4H_2O$ in distilled water was added to the support. The resulting slurry was continuously stirred for 1 h to ensure a complete homogeneity between precursor solution and support. After that, the temperature of the thermostatic bath was increased to 40 ºC in order to promote the complete evaporation of the solvent, maintaining the rotation of the evaporating flask. Finally, the obtained solid was dried over night at 100 ºC and calcined in air at 500 ºC for 3 hours with a heating ramp of 1 ºC/min. Additionally, the catalysts were pelleted, powdered and sieved to 0.3-0.5 mm.

Metal oxide samples based on Fe, Zr, Co, Sr and W and supported over MnO_X-CeO_2 were also prepared by impregnation. First of all, the MnO_X-CeO_2 (with a role of support in this case) was prepared by co-precipitation following the procedure described above, although the solid obtained by co-precipitation was calcined at 550 ºC for 3 h in order to ensure its thermal stability in the second calcination step after introducing the active phase. Then, the proper amount MnO_X-CeO_2 support was weighted and placed in an evaporating flask and, subsequently, it was subjected to vacuum conditions at 40 ºC for approximately 1 hour in order to remove the molecules superficially adsorbed. Next, the evaporating flask, still in vacuum conditions, was immersed in a cold bath (around 5 ºC) to avoid spontaneous evaporation of the precursor solution.

Once the support was pre-treated and cold, the precursor solution was added in continuous stirring for 1 h. After that, the temperature of the thermostatic bath was increased to 40 ºC in order to promote the complete evaporation of the solvent, maintaining the rotation of the evaporating flask. The obtained solid was dried over night at 100 ºC, calcined in air at 500 ºC for 3 hours with a heating ramp

of 1 ^{o}C/min, and finally, the samples were pelleted, powdered and sieved to 0.3-0.5 mm.

2.1.2.4. Mechanical or physical mixing.

Mechanical mixing method is a very simple process. As its name indicates, it is based on the physical mixing of the pure oxides that make up the final catalyst. In this case, for MnO_X-CeO_2 catalysts, pure CeO_2 and pure Mn_2O_3 were mixed. Pure CeO_2 and pure Mn_2O_3 were prepared separately by precipitation of pure precursors, as detailed above. The resulting catalyst prepared by this method is discussed in Section 3.1.

2.2. CHARACTERIZATION TECHNIQUES.

Characterization is essential to discern the catalytic properties involved in a chemical reaction. This section presents the characterization techniques used to determine the physical-chemical properties of the catalysts evaluated in this work.

2.2.1. Inductively coupled plasma atomic emission spectroscopy (ICP-AES).

Atomic emission spectroscopy is based on the radiation emitted by a single atom or ion in excited state. Each element emits radiation with a characteristic wavelength and its intensity is proportional to the amount of the element, so this technique allows to identify and quantify. Single and exited states of the containing components of the sample are obtained by passing the sample, previously dissolved and nebulised, through the centre of a toroidal plasma stream. Plasma is generated by the action of an oscillating magnetic field, generated by a high-frequency electric current on a gas. Ar is the most common gas [120].

This technique has been utilised to determine the metal components in the bulk samples and the concentration of these components. Additionally, this technique has provided information about the possible impurities present in the catalysts, such as those that might come from the use of Na-based precipitating agents.

Experimental procedure.

The analysis was done in a Horiba Yobin Yvon Activa equipment, where the sample, previously dissolved in acid solution, was nebulised and excited using Ar as precursor gas to produce the stream of plasma. The analysis was carried out by the General Services of Analysis (SGIker) of the University of the Basque Country (UPV/EHU).

Prior to the analysis, the samples were dissolved by acid digestion. In this procedure, a small amount of powdered sample (around 50 mg) was mixed with a solution of HCl and HNO_3 with 3:1 molar ratio in a Teflon tube, which was placed in a microwave digester. Once the sample was dissolved, the remaining liquid in the Teflon tube was poured and set to a fixed volume in a volumetric flask.

2.2.2. Wavelength dispersive X-ray fluorescence (WDXRF).

Wavelength Dispersive X-Ray Fluorescence (WDXRF) is based on analysing the X-ray fluorescence emitted by a sample previously ionised with X-rays. The excitation of the sample leads to a fall of the electrons between the different electronic levels of the atoms. These electronic transitions generate some specific energies that are emitted in the form of radiation and are characteristic of each element composing the sample. The use of a monochromator crystal allows to disperse and select the wavelengths that compose the radiation emitted by the sample.

This technique has been used to obtain additional information about the metal components in the bulk samples and the concentration of these components. Moreover, it was used to evaluate the concentration of deactivating species.

Experimental procedure.

The analysis was performed in a PANalytical AXIOS model sequential wavelength dispersive X-ray fluorescence spectrometer, equipped with rhodium tube and three detectors (gas flow, scintillation and Xe sealing). The analysis was carried out by the General Services of Analysis (SGIker) of the University of Basque Country (UPV/EHU).

A semi-quantitative analysis of each powdered sample was done using the standardless software. For this purpose, a small amount of the sample was crushed and placed on a holder with a mylar designed to measure powdered samples in vacuum conditions. The semi-quantitative software is based on the measurement of a set of scans with different crystal analyser, to determine the presence of the different components of the samples. The semi-quantitative assessment was made on the basis of fundamental parameters and an instrumental calibration provided by the software.

2.2.3. Nitrogen physisorption.

Physisorption is defined as the weak interactions between the surface of a solid (adsorbent) and an adsorbable gas (adsorbate). These weak interactions are promoted by low energy forces (Van deer Waals forces), which are independent of the type of the solid studied [121].

At low temperature, adsorbate gas tends to create a monolayer on the solid surface. The amount of adsorbate necessary to form the monolayer depends exclusively on the size of the adsorbate molecule. Thus, specific surface area of a solid is directly related to cross sectional area of the adsorbate molecule and to the number of molecules needed to generate the monolayer. N_2 is the most widely used adsorbate, with a cross sectional area of $0.162\ nm^2$ at the operating temperature of –196 ^{o}C.

The results of physisorption experiments are expressed as isotherm curves, which represent the volume of adsorbate adsorbed at equilibrium conditions as a function of pressure at constant temperature. Depending on the morphological properties of solids, Brunauer, Emmett and Teller proposed different type of isotherms [122], which were modelled on the basis of several parameters, leading to BET equation. The linearized and simplified form of BET equation is expressed in Equation 2.1, where V_{ads} is the volume of adsorbed gas per mass unit of solid at a given pressure (P), P_0 is the saturation pressure of the adsorbate in the analysis conditions, V_m is the volume of adsorbing gas needed to generate the monolayer and C is a parameter related to adsorption and desorption enthalpies.

$$\frac{P}{V_{ads}(P_0 - P)} = \frac{1}{V_m C} - \frac{C-1}{V_m C}\frac{P}{P_0} \quad (2.1)$$

BET equation is the most used one for the calculation of specific surface areas. For this purpose, firstly, it is necessary to fit the results of adsorption isotherm in the relative pressure range between 0.05-0.25, in order to calculate the V_m parameter. Then, S_{BET} can be calculated using Equation 2.2, where N_A is the Avogadro number, V_{mol} is the nitrogen molar volume, A_s is the cross-sectional area of adsorbate gas and m is the mass of solid used in the experiment.

$$S_{BET} = 10^{-18}\frac{V_m N_A}{m V_{mol}} A_s \quad (2.2)$$

The pore volume of the sample is associated to the maximum volume of adsorbate that can be adsorbed on the solid without the appearance of condensation effects. It was estimated from the total adsorbed volume of N_2 at 0.99 of relative pressure.

As for pore size distribution, the method proposed by Barret, Joyner and Halenda (BJH method) for mesoporous samples was used [123]. This method, which is mainly applied to the desorption branch of the isotherm in the relative pressure range between 0.14 and 0.99, estimates the pore radius at different relative pressures according to Equation 2.3, where r_p is the pore radius (nm), Ψ is the surface tension of the adsorbate (N/m), σ is the contact angle between the condensed phase and the surface of the solid (rad), T is the temperature (K), R is the universal gas constant (8.314 J/(mol K)) and t is the thickness of the adsorbed layer (nm).

$$r_p = 10^3 \frac{2\Psi V_{ads}\cos\sigma}{RTln(P/P_0)} + t \quad (2.3)$$

Regarding microporous materials, total pore volume was estimated according to t-plot method in which the adsorbed volume is represented as a function of a "t" parameter. “t” parameter was calculated by using the correlation of de Boer and co-workers [124], which is normally used for zeolite materials [125]. Additionally, pore size distribution was determined by applying the Horvarth-Kawazoe method at relative pressures below 0.01.

Experimental procedure.

Textural properties were measured at boiling temperature of N_2 (–196 ºC) and in different Micromeritics equipment, TriStar II for mesoporous materials and ASAP 2020 for microporous materials. The latter allows to reach higher accuracy at low relative pressures, in which information of microporosity is obtained.

Prior to the analysis, the sample was treated in order to remove the molecules adsorbed over the surface. In the case of mesoporous samples, the pre-treatment was performed at 350 ºC for 5 h with a constant flow of nitrogen. In the case of microporous materials, the pre-treatment was carried out under vacuum conditions at 400 ºC for 10 h.

The experiments are totally automated and controlled by the equipment. Thus, the equipment sequentially adds nitrogen volumes and records the equilibrium pressure to obtain the adsorption branch of the isotherm. After reaching saturation, the equipment removes certain volumes of N_2 recording the equilibrium pressure, in order to obtain the desorption branch of the isotherm. In the experiments, the operating range of pressure is wide, from 10 Pa up to the saturation pressure of N_2, around 101.3 kPa, in mesoporous samples; and from $6.9 \cdot 10^{-4}$ Pa to 101,3 kPa in microporous samples.

2.2.4. X-ray diffraction (XRD).

XRD provides information about crystalline phases of the catalysts, and other structural parameters, such as crystallinity, structural defects, grain size, etc. It is based on the ability of crystalline structures to diffract X-ray. This ability is due to the distance between the crystal planes is the same order of magnitude as the wavelength of the X-ray (0.1-10 Å). Bragg's law, Equation 2.4, relates X-ray wavelength (λ), interplanar spacing in the crystal (d), and glancing angle of incidence (Θ).

$$n\lambda = 2d \sin\theta \tag{2.4}$$

In this work, since the analysis was performed with powdered samples with random orientation of the particles, all orientations of crystalline planes in the sample are

exposed to the X-ray beam, so the results are representative. In the analysis, theta angle between X-ray source and detector varies during the experiment, which provides different values of 2Θ while the radiation is recorded by the detector.

The results are shown as a diffractogram, in which the intensity of radiation is represented as a function of 2Θ. Identification of phases is achieved by comparing the diffractogram obtained from an unknown sample with patterns of a reference database, which are collected by the ICDD (International Centre for Diffraction Data) database.

Moreover, the size of crystalline phases that compose the sample can be estimated from the intensity and the width of the peaks, by applying Scherrer equation (Equation 2.5), where K is a shape factor, λ is the wavelength of X-ray radiation, Θ is the angle position of the signal and β is the corrected broadening at half the maximum intensity (FWHM). In turn, β is calculated from Equation (2.6), where B is the experimental FWHM and b is a correction parameter associated to the device.

$$\tau = \frac{K\lambda}{\beta \cos\theta} \tag{2.5}$$

$$\beta = \sqrt{B^2 - b^2} \tag{2.6}$$

Experimental procedure.

The analysis was performed in a PANalytical X'Pert PRO automated diffractometer equipped with a graphite secondary monochromator and a PixCel detector in a Bragg-Brentano geometry, and operating Cu Kα radiation (λ=1.5418 Å). The samples were analysed in the 2Θ range of 10-80º, with a step size of 0.026º and a counting time of 1 s. The equipment was controlled with the PANalytical Data Collector software. The analysis was carried out by the General Services of Analysis (SGIker) of the University of the Basque Country (UPV/EHU).

Treatment and processing of XRD data was carried out with WinPLOTR software. In addition, the full profile matching without structural model done for some samples to obtain information about the lattice parameter of crystalline phases was performed with the FullProf.2k software.

2.2.5. Raman spectroscopy.

Raman is based on the analysis on the light scattered by a sample after being irradiated with a monochromatic light with a certain frequency. As a result of the interaction with the matter, a small fraction of scattered light presents a shift in its frequency (Raman scatter). This dispersed light with different frequency provides chemical information about the composition of the matter, because the difference in the frequency between the incident radiation and Raman scattering is independent of the frequency of incident radiation and only depends on the molecular composition and chemical structure [126]. The results are presented as the optical intensity as a function of the normalized Raman shift in wavelength.

Experimental procedure.

The analysis was performed in a Renishaw InVia Raman confocal microscope with a Leica DMLM microscope. The used laser presents an excitation wavelength of 514 nm (ion-argon laser, Modu-Laser). The analysis was carried out at Multispectroscopy Singular Laboratory (Raman-LASPEA) of the General Services of Analysis (SGIker) of the University of the Basque Country (UPV/EHU).

2.2.6. Skeletal Fourier transform infrared (Skeletal-FTIR).

Infrared spectroscopy is based on the analysis of the interaction between an infrared radiation and the matter. When infrared radiation irradiates the matter, part of this radiation is absorbed by exciting the vibrational states of the molecules. An infrared spectrum is obtained by determining the fraction of the incident radiation that is absorbed by the sample at a particular energy value. The appearance of peaks at a certain value of energy, corresponds to the vibrational frequency of the bonds that form the molecules of the sample.

In a FTIR spectrometer, the infrared beam passes through an interferometer. A mirror inside the equipment alters the distribution of the light, changing its position periodically. The signal measured in the detector, called interferogram, represents the fraction of non-absorbed radiation as a function of the position of the mirror (spatial or time domain). The Fourier transform is a mathematical treatment that allows to convert the original data to other to the frequency domain.

Experimental procedure.

Skeletal FTIR analysis of the catalysts were performed in a Nicolet 380 ThermoNicolet Nexus Fourier transform instrument in the range of 4000-400 cm^{-1}. For the analysis, all samples were diluted to 1 wt.%. in KBr and pelletized in discs of 0.7 g approximately. The spectra were collected by 100 scans with a resolution of 4 cm^{-1}. The analysis was performed at the Department of Civil, Chemical and Environmental Engineering (DICCA) of the University of Genova.

2.2.7. Ultraviolet-visible-near infrared diffuse reflectance spectroscopy (UV-Vis-NIR DRS).

Diffuse reflection is the reflection of light in all directions when it is incident on a surface. This technique is based on the ability of some materials to absorb certain wavelength of diffused light while it goes along the material. Thus, the wavelengths absorbed by the material do not appear in the reflected light.

For this type of analysis, a monochromatic light is used to irradiate the sample and the reflected radiation is detected by a photosensitive cell. The comparison between the intensity measured and that of a reference standard, allows to determine the percentage of reflectance. The results were treated according to Kubelka-Munk model and represented as a function of wavelength.

Experimental procedure.

Diffuse reflectance analysis of pure powders was conducted in a Jasco V-570 in the wavelength range of 2300-200 nm at ambient conditions. The analysis was performed at the Department of Civil, Chemical and Environmental Engineering (DICCA) of the University of Genova.

2.2.8. X-ray photoelectronic spectroscopy (XPS).

XPS is based on photoelectric effect promoted by an incident beam of X-ray over the surface of a material. In this sense, the X-ray incident on the material causes the excitation of surface atoms, which results in the emission of photoelectrons. These electrons are collected and characterized by their kinetic energy. In order to

avoid the loss of energy in the travel of the electron between the sample and the detector, as a consequence of collisions or interactions with other atoms, the irradiation must be done in high vacuum condition.

According to the energy balance from the emitted electron, Equation 2.7, the kinetic energy (EK) of the electron is the difference between the energy of the absorbed photon (hv) and the binding energy of the electron in the atom (BE). ϕ is a parameter function of the spectrometer and the analysed material. Since the binding energy is characteristic of the element and the orbital from which the electron was emitted, it allows to obtain information about chemical composition and oxidation states.

$$EK = h\nu - BE - \phi \tag{2.7}$$

Experimental procedure.

The analysis was performed in a SPECS spectrometer with a Phoibos 150 1D-DLD analyser and a monochromatic radiation source Al Kα (1486.7 eV). The pelletized sample in a disc was degassed and introduced into an ultra-high vacuum chamber (10^{-6} Pa). Firstly, an initial analysis of the present elements in the sample was made (time 0.1 s and pass energy of 80 eV) and, then, the detailed analysis of the previously evidenced components was carried out (time 0.1 s and pass energy of 30 eV) with an exit angle of 90^{o}. All spectra were referenced to C 1s. The CASA XPS software was used to treat the obtained results, which mainly involved a Shirley background subtraction and a deconvolution of the spectra using mixed Gaussian-Lorentzian function. The analysis was carried out at the General Services of Analysis (SGIker) of the University of the Basque Country (UPV/EHU).

2.2.9. Scanning electron microscopy (SEM), transmission electron microscopy (TEM) and scanning transmission electron microscopy (STEM).

Scanning Electron Microscopy (SEM) is based on imaging a sample by irradiating it with a focused electron beam. The interaction between electrons and the sample results in the emission of secondary and backscattered electrons, whose intensity depends, among other factors, on morphology of the sample. Thus, the analysis of

these electrons allows the creation of an image resulting from the intensity map of electrons detected.

Similarly, Transmission Electron Microscopy (TEM) uses a beam of high-energy electrons, which is focused on a very small region of the sample. Nonetheless, in this case, the electrons analysed are those transmitted, that is, those that go through the sample. The images obtained by this technique provide information about morphological and structural properties, and allow to differentiate between metallic particles. In fact, with high resolution TEM (HRTEM), information about lattice fringes can be obtained. In the case of SEM, the information obtained is associated to the surface of the sample and more concerned to its morphology.

Scanning Transmission Electronic Microscopy (STEM) is based on irradiating the sample with a focalised beam, which is then analysed over the sample. In STEM mode, several techniques can be coupled to ensure a more accurate analysis of the materials. This is the case of High-Angle Annular Dark Field imaging (HAADF), which only collects the scattered electrons rather than those from the beam; Dispersive X-Ray spectroscopy (EDX), which is based on the analysis of X-rays released by irradiated atoms; and Electron Energy Loss Spectroscopy (EELS), which analyses the energy loss by electrons of the beam due to inelastic scattering.

Experimental procedure.

SEM images were obtained with a Hitachi S-4800 scanning electron microscope with cold cathode field emission gun (FEG). The equipment operated with a voltage of 10 kV and 5 A. The analysis was carried out in the area of analytical and high-resolution microscopy in biomedicine of the General Services of Analysis (SGIker) of the University of the Basque Country (UPV/EHU).

Additionally, SEM-EDS was used to obtain information about surface concentration of deactivated catalysts. It was performed on a Carl Zeiss EVO-40 scanning electron microscope coupled with X-Max EDS from Oxford Instruments. The operating conditions during the measurements were 30 kV and 180 pA. The analysis was carried out at Multispectroscopy Singular Laboratory (Raman-LASPEA) of the General Services of Analysis (SGIker) of the University of the Basque Country (UPV/EHU).

HRTEM and STEM-HAADF images with elemental maps of MnO_X-CeO_2 catalysts in Chapter 3 was performed in a FEI Titan Cubed G2 60-300 electron microscope working at 200 kV and equipped with a Super-X EDX system, high-brightness X-FEG Schottky field emission electron gun, monochromator and CEOS GmbH spherical aberration corrector (Cs). All these components operate under a HAADF detector in STEM mode (camera of 180 mm). HRTEM images were obtained with a Gatan UltraScan 100 2kx2k CCD camera. The analysis was carried out at the General Services of Analysis (SGIker) of the University of the Basque Country (UPV/EHU).

On the other hand, STEM-HAADF images with elemental maps of MnO_X-CeO_2 over different supports (Chapter 6) were obtained in a ThermoFisher Scientific/FEI Titan electron microscope working at 200 kV and equipped with a CEOS CESCOR Cs corrector, EDX Oxford Instruments Ultim Max detector. All these components operate under a HAADF Fischione detector in STEM mode. The analysis was carried out by the Advanced Microscopy Laboratory of the University of Zaragoza.

The samples for HRTEM and STEM-HAADF was dispersed in ethanol with an ultrasonic bath for 30 min. Then, a small volume of the suspension was poured over a copper grid. Ethanol was dried in vacuum conditions.

2.2.10. Temperature programmed reduction (TPR).

TPR allows to assess the susceptibility of a solid to be reduced. It is based on reducing the sample with a reducing gas as the temperature is increased. The monitorization of reducing gas concentration allows to know the temperature at which the reduction of the sample occurs.

The most commonly used reducing agent is H_2, normally diluted in an inert gas. The integration of H_2 flow versus time gives an idea of the reduction capacity of the catalyst. The temperature at which the reduction occurs is related to how easy it is for the sample to be reduced [127]. The H_2 consumption profile also provides information about the metal species that make up the sample, such as their amount and distribution and, in the case of supported catalysts, about the interaction between metal oxide and the support.

Experimental procedure.

H_2-TPR experiments were performed in a Micromeritics AutoChem 2920 with a thermal conductivity detector (TCD) and mass flow controllers for gas feeding. The sample (around 0.15 g) is placed in a U-shaped reactor, which in turn is introduced into the furnace of the apparatus.

Prior to the analysis, the samples were treated in the same equipment to remove adsorbed surface molecules. The pre-treatment was carried out with a 50 cm^3/min flow of a stream of 5% O_2/H_2, while the temperature was increased with a heating ramp of 10 ^oC/min from room temperature to 500 ^oC. The temperature was kept constant at 500 ^oC for 45 min. Then, the temperature of the sample was cooled down to 50 ^oC in He flow. After this, the reduction stage was performed by passing through the samples a 50 cm^3/min flow of a 5% H_2/Ar stream, while increasing the temperature at a rate of 10 ^oC/min up to 900 ^oC. Then, the temperature was kept constant at 900 ^oC for 45 min.

A cold trap just before the TCD condenses the possible water formed in the reduction of the sample and avoids interferences in the TCD.

2.2.11. Temperature programmed desorption (TPD).

Temperature programmed desorption is used to quantify the acidity of the surface of a solid. It is based on the adsorption of a basic gas, which is subsequently desorbed with a carrier gas flow by means of a progressive increase in temperature. The monitorization of desorbed gas allows to know the temperature at which desorption occurs.

The gas most commonly used in this type of experiment is ammonia, due to its high thermal stability and relatively strong basicity, which promotes NH_3 adsorption in all acid centres [128]. The integration of desorbed ammonia flow versus time reveals total acidity. The temperature at which NH_3 desorption occurs is associated to the strength of the acid sites.

Experimental procedure.

The NH_3-TPR experiments were performed in a Micromeritics AutoChem 2920 with a TCD and mass flow controllers for gas feeding. The sample (around 0.15 g) is placed in a U-shaped reactor, which is placed in the oven of the equipment.

Prior to the analysis, the samples were treated in the same equipment to remove adsorbed surface molecules. The pre-treatment was carried out with a 50 cm^3/min flow of a stream of 5% O_2/H_2 and increasing temperature with a heating ramp of 10 ^oC/min from room temperature up to 500 ^oC. The temperature was kept constant at 500 ^oC for 45 min. Then, the samples were cooled down to 40 ^oC in He flow.

For the analysis, firstly, the sample was saturated with a flow of 130 cm^3/min of 1% NH_3/He at 40 ^oC for 60 minutes. Then, the sample was exposed for 60 minutes to a flow of 130 cm^3/min of He, in order to remove the NH_3 weakly adsorbed. Finally, the desorption of chemisorbed NH_3 was promoted by increasing the temperature up to 500 ^oC at a rate of 10 ^oC/min and with a He flow of 130 cm^3/min.

Additionally, due to oxidizing capacities of surface oxygen species, NH_3 adsorbed may be oxidized and desorbed as nitrogen oxides in NH_3-TPD experiments. In order to check whether this fact occurs in the NH_3-TPD experiments, the outlet stream of TDC was further analysed with a MKS mass spectrometer.

2.2.12. FTIR spectroscopy of adsorbed pyridine (PY-FTIR).

This technique is used to discern the nature of the acid sites (Lewis and Brønsted). It is based on the ability of some probe molecules to adsorb differently depending on the nature of the acid site. Pyridine is the most common probe molecule. This molecule can coordinate through its electronic lone pair over Lewis acid sites, or subtract the hydrogen atom from a surface hydroxyl groups to form the pyridinium cation in Brønsted acid sites. Moreover, pyridine may also weakly interact with surface hydroxyl groups through H-bonds, but not forming pyridinium cations [129].

The use of IR spectroscopy makes it possible to observe the vibrational perturbations that appear in the probe molecule spectrum when it is adsorbed on

different acid sites. In addition, the strength of the acid sites is evidenced by shifting the position of the bands towards higher wavenumbers.

Experimental procedure.

FTIR spectra of adsorbed pyridine were recorded in a Nicolet 380 Thermo Nicolet Nexus Fourier transform instrument. The spectra were collected by 100 scans with a resolution of 4 cm^{-1}. The powdered samples were compressed into a disc of about 50 mg. Before pyridine adsorption, each disc was activated at 480 ^{o}C in air for 30 min, and then in vacuum ($1.3 \cdot 10^{-1}$ Pa) for 30 min. The conditions of activation in vacuum were chosen in order to limit a possible surface reduction. Pyridine adsorption was performed at a pressure of 263.4 Pa and at room temperature. Several spectra of the adsorbed species were recorded following outgassing at room temperature, 150, 200, 250, 300 and 350 ^{o}C. The technique was performed at the Department of Civil, Chemical and Environmental Engineering (DICCA) of the University of Genova.

2.2.13. Thermogravimetric analysis (TGA).

This method is based on the measurement of the changes in weight of a sample when it is subjected to changes in temperature and in controlled atmosphere. This technique gives information about compounds adsorbed or chemisorbed over the sample, physical and chemical transformations of the sample, thermal stability, etc.

Experimental procedure.

This technique was used to analyse the deactivating species adsorbed on the catalysts. The experiments were performed in a Setaram Setsys Evolution thermobalance with a cylindrical graphite furnace and an alumina crucible. This equipment was coupled with a mass spectrometer Pfeitffer Vacuum DUO 2.5 in order to identify the gaseous products of the experiment.

To avoid the desorption of deactivating species and only remove ambient adsorbed molecules, the sample was subjected to a low temperature pre-treatment, 120 ^{o}C, with a 50 mL/min of 5% O_2/He stream for 30 min. Then, the experiment was carried

out with the same stream and increasing temperature with a heating rate of 5 ^{o}C/min up to 500 ^{o}C, temperature which was kept constant for 3 hours.

2.3. CATALYTIC ACTIVITY TESTS.

2.3.1. Gas feeding composition.

As mentioned in Chapter 1, the composition of the raw flue gas from MSW incineration is not constant, and it depends on the waste composition. At the same time, the composition of the inlet stream to the catalytic reactor can be different depending on the gas cleaning systems implemented to abate other pollutants and their relative position.

In this thesis, a catalytic reactor in tail-end configuration has been selected. Table 2.2 lists the typical gas composition after the incineration stage and the composition of the inlet stream to the catalytic reactor in tail-end configuration. As can be seen, NO_X concentration after the incineration stage is similar to that at the inlet of catalytic reactor, so the most suitable concentration of NO_X for base experiments in this thesis should range between these two values. PCDD/Fs content should be also similar to that after the incineration stage, because this work proposes the elimination of the actual systems for PCDD/Fs abatement. In the case of other pollutants, their concentration should be defined by the efficiency of the respective cleaning stages.

Unfortunately, it should be noted that the use of PCDD/Fs at lab-scale is difficult and, in our case, unfeasible, because of their high toxicity, difficult handling, commercial unavailability and impossibility to measure their concentration in a relatively rapid way. Other researchers use model compounds with some similarities to PCDD/Fs, e.g., polychloroaromatic compounds with different degrees of chlorination. The most common one is 1,2-dichlorobenzene (o-DCB), because it has an aromatic ring and two chlorine atoms in the position corresponding to the most toxic molecule among PCDDs [107, 131, 132].

Table 2.2. Mean gas composition after the boiler [15] and before the catalytic reactor in tail-end configuration [130] in MSWI plants.

Substance	Unit	After boiler[a]	Tail-end configuration
Water	%	10-20	15-20
O_2	%	---	9-11
CO_2	%	5-10	6-8
CO	ppm	5-50	< 5
Metals	ppm	< 53	< 0.05
Particulate matter	ppm	1000-5000	< 1
HCl	ppm	500-2000	< 2
SO_X	ppm	200-1000	< 10
HF	ppm	5-20	< 0.2
NO_X	ppm	250-500	70-170
PCDD/Fs	ng/Nm^3	0.5-10	0.2-0.5

[a] Calculated considering O_2 reference value as 11%.

According to the facts stated above, the gas feeding composition for the base catalytic tests of this thesis has been fixed as shown in Table 2.3. The decision is based on the following considerations:

- The efficiencies of cleaning stages of FGC line before the catalytic reactor are very high, so the concentration of particulate matter, metals, acid gases (HCl and SO_X), etc., is practically negligible.
- The feeding stream to the catalytic reactor is completely dry. This is not true according to real conditions (Table 2.2), but the presence of water may cause corrosion in the experimental set-up. For this reason, it was decided not to feed water in the base experiments. Nonetheless, the effect of water has been studied with a specific experiment in Chapter 4.
- The feeding stream is free of CO_2. This is not true if it compares to the real conditions (Table 2.2). CO_2 was not fed in order to be able to calculate the CO_2

selectivity in oxidation reaction. Moreover, the effect of CO_2 concentration has been studied with a specific experiment in Chapter 4.

- NO_X from MSW incinerations is exclusively composed by NO. The reason lies on NO_X is mainly composed by NO and NO is the difficult to remove.
- o-DCB is used as model compound of PCDD/Fs. A concentration of 100 ppm has been selected. This concentration is higher than that of PCDD/Fs produced in a MSWI plant due to the detection limit of analytical technique.
- Ar was used as gas balance instead of N_2. N_2 is the most abundant gas in flue gases of MSWI plants; however, it was not used to facilitate the assessment of NO reduction selectivity towards the different products.

Table 2.3. Gas feeding composition for base catalytic tests.

Compound	Unit	Concentration
NO	ppm	300
NH_3	ppm	300
o-DCB	ppm	100
O_2	%	10
Ar	balance	

2.3.2. Reaction system.

Catalyst activity, selectivity and durability have been measured in a bench scale reaction system. It allows simulating the reaction conditions of the SCR unit found in the FGC line of a MSWI plant and, at the same time, reducing the gas flow and the amount of catalyst in comparison to full-scale conditions. It was designed and built by the research group Chemical Technologies for Environmental Sustainability (TQSA) in collaboration with the company PROINCON PIRINEO. The flow diagram is shown in Figure 2.1

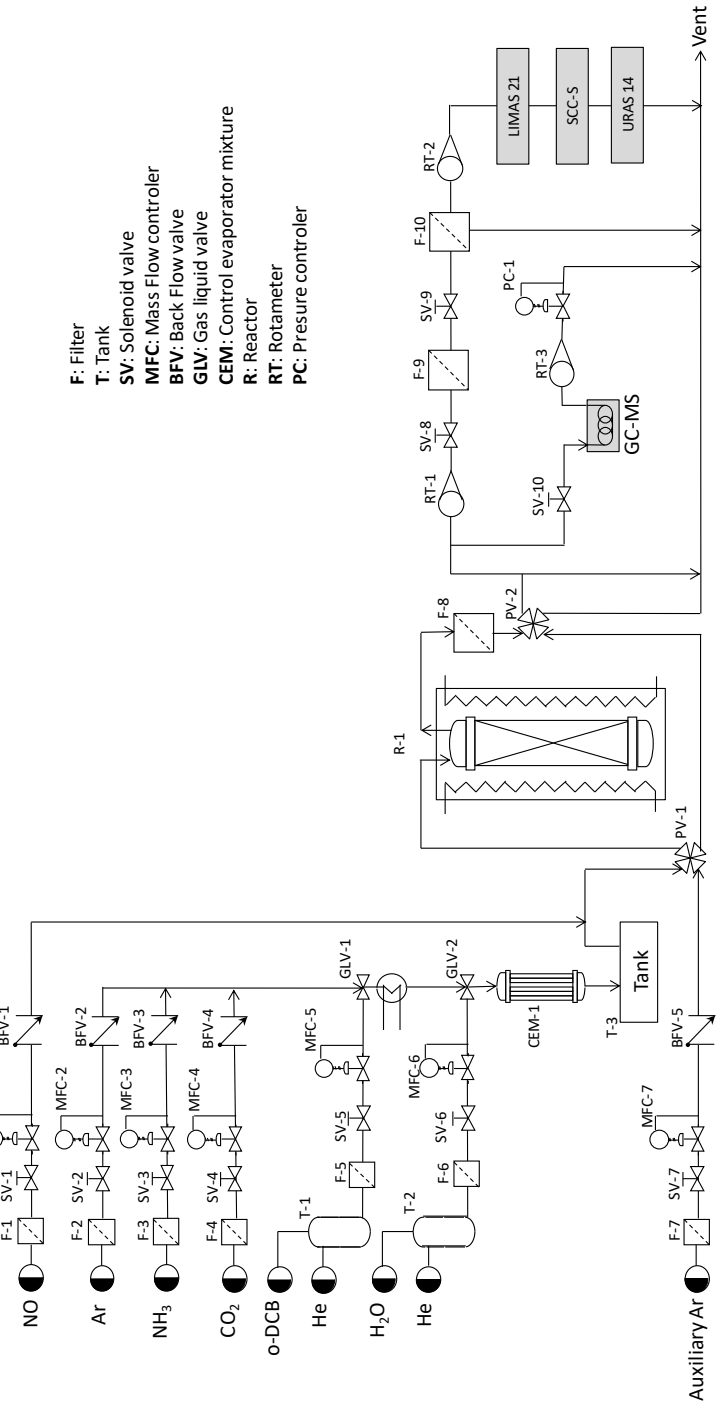

Figure 2.1. Experimental set-up for the catalytic tests.

The experimental system operates in a quasi-automatic mode, by using a Programmable Logic Controller (PLC) connected to a computer equipped with a customized SCADA (Supervisory control and data acquisition) system. This software allows to control and monitor the operating variables, that is, opening and closing of the valves, gas flows, temperature of the different areas and the concentrations of reagents.

The pipelines are made of AISI-316 stainless steel in order to avoid the corrosion that would come from the generation of acid gases such as HCl, and the adsorption of chlorinated organic compounds. The bench scale reaction system can be divided into three different zones: feeding, reaction and analysis zone.

2.3.2.1. Feeding zone.

The feeding system is designed to generate a stream with the reagents and concentrations selected in Section 2.3.2. The feeding stream is obtained synthetically from mixing the pure compounds.

The feeding zone has five gas feeding lines for Ar, O_2, CO_2, NO and NH_3 and two liquid feeding lines for o-DCB and water. Each gas feeding line is equipped with a filter (F, Figure 2.1), a solenoid valve (SV, Figure 2.1), a Bronkhorst F-201CV mass flow controller (MFC, Figure 2.1) and a backflow valve (BFV, Figure 2.1). The liquid feeding lines have the same components, except for the backflow valve, which is replaced by a liquid-gas mixing valve (GLV, Figure 2.1). The mass flow controllers of liquid reagents are Bronkhorst L01-AGD for o-DCB and Bronkhorst L13-AGD for water.

All gas feeding lines except for that of NO discharge into a gas collector. Then, o-DCB is incorporated to the gas stream in the corresponding gas-liquid mixing valve. From this point, the pipe is heated up to 190 ^{o}C in order to avoid o-DCB condensation. Next, and in the case that the experiment is performed in wet conditions, water is incorporated in the respective gas-liquid mixing valve. After the addition of liquid reagents, the resulting gas stream goes through a controller-evaporator-mixer (CEM, Bronkhorst W-102A-111-K) that allows temperature control and homogenisation of the gas stream. In addition, the gas stream passes through a tank (T-3, Figure 2.1) of 25 L in order to buffer the oscillation of the mass flow controllers, especially that of o-DCB and water. After the tank, NO feeding

stream is incorporated, as there is evidence that some of NO fed is oxidized to NO_2 inside the tank.

An auxiliary line of Ar is used for cleaning pipelines, reactor and analyser, and to remove possible adsorbed compounds over the catalyst before the reaction.

Feeding and auxiliary Ar lines converge in a four-port pneumatic valve (PV-1, Figure 2.1), which allows to carry the feeding stream to the reactor and the Auxiliary Ar to the by-pass line (line that by-passes the reactor), or vice versa.

2.3.2.2. Reaction zone.

The reaction system is composed of a U-shaped tubular quartz reactor located in the centre line of a cylindrical shaped convective-flow furnace, which allows an accurate temperature maintenance and the programming of heating ramps.

The U-tube reactor is introduced into the furnace from the top, through a hole opened for this purpose, and a support holds the body of the U-tube reactor hanging inside the furnace. In turn, this support acts as a seal for the furnace opening. The heating coils with an output of 1000 W are housed in the annular space of the furnace. The bottom of the furnace is fitted with a fan in order to homogenise the heating. A hollow cylinder of refractory material is also interposed between the heating coils and the U-tube to prevent the catalyst from being heated by radiation. Several openings in the upper part of this cylinder facilitate the circulation of air from the annular zone to the inner zone of the furnace, and vice versa. The oven has a control panel with two indicators of temperature and a ramp/soak PID controller (ASCO X5), connected to the below-described thermocouple.

To ensure appropriate fluid-dynamic conditions and absence of diffusional control, which will be discussed below, the reactor has a defined inner diameter of 13.6 mm [119]. The outer diameter is 16 mm and the total length of each branch is 620 mm. The catalytic bed is placed over quartz wool, at 15 mm above the bottom or U-bend of the reactor, while the quartz wool is positioned over three notches in the wall of the reactor. At this position, the absence of longitudinal temperature gradients has been proven.

The branch with the catalyst bed (inlet branch) has on its top a stainless-steel pipe tee connector, that allows inserting a type K thermocouple through one of its openings. The reaction temperature is measured as close as possible to the top of the catalyst bed. The remaining opening of tee connector is used to feed the gas stream to the reactor. This stream flows downward, while heating, through the annular space between the thermocouple and the reactor inner wall.

The gaseous products leave the U-tube through the other branch (outlet branch) upward. This stream and the by-pass line converge to a second four-port pneumatic valve (PV-2, Figure 2.1) that allows to send the reactor outlet stream to the analysis system and the by-pass stream to vent, or vice versa.

2.3.2.3. Analysis zone.

The analysis area is composed by three analysers that allow to detect and quantify the majority of the compounds involved in the reactions, either products or reactants.

As shown in Figure 2.1, the reactor outlet stream or the by-pass stream is divided in two lines. One is used to analyse chlorinated organic compounds by Gas Chromatography coupled to a Mass Spectrometer (GC-MS), and the other is used to analyse inorganic compounds by a Non-Dispersive Infrared (NDIR) analyser and an Ultraviolet (UV) analyser, located one after the other.

Flow division of the stream to be analysed is adjusted by a rotameter (RT-1, Figure 2.1). This division sends 20 mL/min to the GC-MS. The remaining flow goes to NDIR and UV analysers. Additionally, after the GC-MS there is a pressure controller Bronkhorst P-502 (PC-1, Figure 2.1) to ensure a constant pressure of 1.4 bar in the sample loop of GC-MS.

Just before the NDIR and UV analysers, particulate matter and acid gases are removed with a particulate filter, two Teflon filters with pore of 0.4 and 0.2 µm and an adsorbent unit. Additionally, the flow is again split and adjusted by a rotameter (RT-2, Figure 2.1) to ensure a constant flow of 80 L/h, as recommended by the manufacturers of analysers.

Next, the characteristics of the techniques and the analysers used are described.

Gas Chromatography coupled to Mass spectrometer (GC-MS).

In chromatographic technique, a mobile phase, usually an inert gas, flows and carries the components of the sample through a separation column, which contains a stationary phase. Due to the different affinity of each component of the sample for the stationary phase, their retention time within the column is different, so that they are separated from one another. A detector measures the amount of each component at the outlet of the column as a function of time.

The analysis was performed in an Agilent Technologies 7890-5975C GC-MS. The mobile phase (carrier) was He and the stationary phase was a HP-VOC column. The volume of sample injected to the column (loop volume) was 0.25 mL.

The detector is a mass spectrometer. It consists of an ionization chamber, where the ions are formed and focused towards the quadrupole. In the quadrupole, the ions are separated by means of an electric field according to their masses and charges (m/z). The electric current of these ions is measured in an electro multiplier.

The detector can operate as universal detector, acquiring ion current (SCAN), or as selective detector (SIM). Both modes have been used simultaneously in this work: the SCAN mode has been used to identify and monitor the mass spectra of the different chlorinated organic compounds, and the SIM mode has been used for quantification, because it only analyses one selected ion.

Table 2.4 lists the characteristics of the operating method designed for the GC-MS. The goal of this method is to obtain as much information as possible in the shortest time, in order to perform as many analyses as possible during the same catalytic test.

Table 2.4. Description of the chromatographic method.

Parameter	Value
Loop volume	0.25 mL
Injector temperature	150 ^{o}C
Split	1/30
Column flow	1 mL/min
Press in the column	8.23 psi
Oven	60 ^{o}C (2 min), ramp 20 ^{o}C/min up to 200 ^{o}C, 200 ^{o}C (0.5 min)
Detector	
Transfer line temperature	280 ^{o}C
Ionic source temperature	230 ^{o}C
Quadrupole temperature	150 ^{o}C
Gain factor	1
Mass range (SCAN mode)	40-200
SIM mass analysed	147

The peaks in the chromatograms were quantified by external standard calibration. The standards were injected directly as liquid with the Agilent 7693A Automatic Liquid Sampler. The right combination of injected volume and split ratio allows to introduce the adequate amounts of each standard into the chromatographic column and elaborate the external calibration curves. In the case of o-DCB calibration, the standard concentration was 5000 µg/mL (Sigma-Aldrich). Injected volumes and split ratios were varied between 0.05-0.3 µL and 170-400, respectively. Equation 2.8 relates the peak area measured in SIM mode to the gas phase analyte concentration (in ppm), where A is the area of the peak, SP is the slope of the calibration line, ρ_I is the analyte density in the injector conditions (150 ^{o}C and 1.4 bar), R_{split} is the split relation and V_{loop} is the loop volume.

$$Concentration = \frac{A}{SP}\frac{\left(R_{split}+1\right)}{\rho_I V_{loop}} \tag{2.8}$$

Non-Dispersive Infrared (NDIR) Analyser.

The NDIR analyser (ABB AO Uras 14) was used for the quantification of CO, CO_2 and N_2O. It is based on resonance absorption of vibration-rotation bands of gas molecules in the mid-infrared spectrum at wavelengths between 2.8 and 8 µm. Each individual gas is identified by its specific absorption bands. The intensity of the infrared radiation absorbed at a certain wavenumber is proportional to the concentration of the component.

The analyser consists of an optical unit, composed by an infrared source, a chopper wheel, an emitter, a sample cell with reference chambers and an infrared detector. The equipment operates in a completely self-contained way. The measured concentrations are directly sent to the PLC controller, which is connected to the main PC.

The calibration of the analyser is carried out every week at the same flow rate and pressure conditions than those used during the catalytic tests. A gas cylinder composed of 1000 ppm CO_2, 1000 ppm CO, 200 ppm N_2O, 2% O_2 and N_2 to balance was used for calibration.

Ultraviolet.

The ultraviolet analyser (ABB AO Limas 21) was used for the quantification of NO, NO_2 and NH_3. However, the measurement of NH_3 is falsified in presence of o-DCB, because of interferences. This method is based on the emission of a characteristic radiation that a molecule emits after returning to its normal state, when it has been previously excited with an ultraviolet radiation with a specific wavelength. The intensity emitted is proportional to the concentration of the component.

The analyser is composed by a beam source that produces UV beam in the 200-500 nm range, two filter wheels, a beam splitter, the sample cell, and the receivers that accept measurement and reference beams. The equipment operates in a completely self-contained way. The measured concentrations are directly sent to the PLC controller, which is connected to the main computer.

The calibration of the analyser is carried out every week at the same flow rate and pressure conditions than those used during the catalytic tests. Two gas cylinders

were used for calibration: (1) composed of 1000 ppm NO and N_2 to balance and; (2) composed of 400 ppm NO_2 and N_2 to balance.

2.3.3. Reaction protocols.

In all experiments, 1.5 g of sieved catalyst with a size between 0.3-0.5 mm was used. The catalyst was mixed with inert quartz, also sieved, to reach a catalytic bed volume of 3 mL. The flow rate in all the experiments was 2 NL/min, which ensures a space velocity of 40000 h^{-1}. These conditions ensure the absence of mass transfer limitations, as will be discussed below.

The catalytic activity tests collected in this work have been performed according to a protocol previously designed [119]. This protocol is composed by four stages: (I) catalyst pre-treatment, (II) feeding stabilization, (III) measurement of feeding concentration and (IV) reaction. The protocol in the three first stages is common in all the catalytic tests, whereas the stage IV was different depending on expected information to be obtained from the experiments.

Catalyst pre-treatment (stage I) aims to remove the adsorbed molecules in the catalyst surface, by flowing 1 NL/min of Ar with the auxiliary Ar stream at 200 ^{o}C for 1 h. Then, the furnace is programmed to heat or cold the catalyst to the reaction temperature.

Simultaneously, the feed stream is generated and stabilized (stage II). First, all heating devices (resistances and CEM) must reach their set points. Then, the mass flow controllers are opened. The positions of the four-port pneumatic valves (PV-1 and PV-2) send this stream to by-pass the reactor and to vent, respectively. At the same time, auxiliary Ar stream flows through the reactor and is also sent to the analysis zone.

Once the mass flow controllers are stabilized at their corresponding set points, concentration of the reagents is measured (stage III). For that purpose, the position of PV-2 is changed. This action directs the auxiliary Ar stream that went through the reactor to vent, and the feed stream that by-passed the reactor to the analysis zone. This stage allows to corroborate the good performance of the experimental set-up and to measure the feed concentration of the reagents.

The chemical reaction test (stage IV) starts when the catalyst temperature and the feed concentrations of all reactants are fully stabilized at their corresponding set points. After that, the positions of the four-port pneumatic valves (PV-1 and PV-2) are simultaneously changed. Thus, the feeding stream is sent to the catalytic reactor and the outlet stream of the reactor is directed to the analysis zone.

In stage IV, four types of experiments have been performed depending on the results to be obtained:

- Light-off. The catalytic activity is measured at different temperatures between 100 and 500 ^{o}C with a heating ramp of 1.5 ^{o}C/min. This type of experiments has been used to choose the most active catalyst among a large number of catalysts, because it is a fairly fast way of operating (one daily test). The results of this type of experiments are those reported in Chapter 3, a small part of Chapter 4 and Chapter 6.

- Light-off until the steady state. The catalyst temperature is increased by steps of 25 ^{o}C in the range 100-500 ^{o}C. Once the temperature is stabilised in each step, it is kept constant until steady state is reached. The steady state is assumed when the variation of conversion and by-products concentration is lower than 3%, for 1 hour. The results of this type of experiments are shown in Chapter 4.

- Time on stream. The chemical reactions are performed for a long time (24 h) at stationary or constant conditions. This experiment allows to determine the time dependence of the reactions and the deactivation of the catalyst. Generally, some information about the catalytic behaviour should be known before selecting the operating temperature. The results and the selected temperature for this type of experiment are discussed in Chapter 4.

- Time on stream with change in the composition of the reagents. The reaction is performed at stationary conditions and it consists in changing the concentration of the reagent to be analysed. The concentration of the reagent is changed after reaching the steady state. These experiments were used to study the influence of o-DCB in NO reduction, the influence of NO and NH_3 in o-DCB oxidation and the influence of oxygen in both NO reduction and o-DCB oxidation. The results are shown in Chapter 4.

Catalyst behaviour was evaluated as a function of NO and o-DCB conversion (Equation 2.9). In o-DCB oxidation, the selectivity towards CO_2, CO and chlorinated organic compounds was evaluated by means of Equations 2.10-2.12. In the NO reduction, concentration of N_2O and NO_2 has been evaluated since the presence o-DCB interferes with NH_3 measurement, and thus, selectivity towards the main products of this reaction cannot be calculated.

$$X = \frac{C_{ini} - C}{C_{ini}} 100 \tag{2.9}$$

$$S_{CO} = \frac{C_{CO}}{6C_{ini,o-DCB}X_{o-DCB}} 100 \tag{2.10}$$

$$S_{CO_2} = \frac{C_{CO_2}}{6C_{ini,o-DCB}X_{o-DCB}} 100 \tag{2.11}$$

$$S_{Cl\ org\ comp} = 100 - S_{CO} - S_{CO_2} \tag{2.12}$$

2.3.4. Repeatability of the experimental set-up.

Repeatability assesses the experimental error provided by the experimental set up during a certain period of time. This analysis gives an idea of the reliability and comparability of the experimental data. A high repeatability ensures that experimental data obtained during this time have not been affected by experimental errors and, thus, they can be compared with each other. The repeatability analysis has been performed by repeating light-off experiments with the same catalyst during the whole experimental period. Table 2.5 lists the number of experiments with the corresponding dates at which they were performed.

Table 2.5. Experiments for the repeatability analysis.

Nº experiment	Date
1	October-18
2	March-19
3	October-19
4	October-20

The results of the repeatability test, shown in Figure 2.2, represent the mean value of NO and o-DCB conversion at each temperature and obtained from the different experiments exposed in Table 2.5. In addition, each value of NO and o-DCB conversion is represented with its corresponding error. For the calculation of experimental error, standard deviation was first calculated, Equation 2.13, where N is the number of experiments, X_i is the measured value and X_{mean} the mean of the obtained values. Then, the experimental error at each temperature was calculated using Equation 2.14.

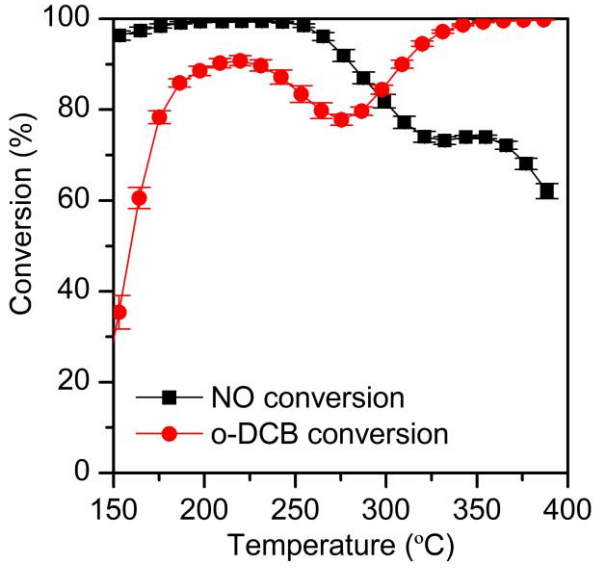

Figure 2.2. Results of repeatability tests in the experimental set-up.

$$SD = \sqrt{\frac{\sum_{i=1}^{N}(X_i - X_{mean})^2}{N-1}} \tag{2.13}$$

$$SE = \frac{SD}{\sqrt{N}} \tag{2.14}$$

The values of the errors obtained at each temperature are very small; in fact, they are an order of magnitude smaller than the measurements. This indicates a high repeatability and, thus, a low contribution of the experimental error provided by

the experimental set-up during the period of time in which this thesis was carried out.

Regarding each reaction, the maximum standard deviation is around 2.5 in SCR. This result has been obtained in the temperature range between 250-300 ^{o}C. In the oxidation reaction, the maximum value is 4.5 between 150-200 ^{o}C. In these temperature ranges, conversions of NO and o-DCB change abruptly.

The fact that the largest deviations are found in the regions where conversions change abruptly with temperature could be due to small delays in the data collection which produce small changes in temperature that result, in turn, in noticeable changes in the measured conversions. These small delays in data collection could be associated to heating and cooling time of the chromatograph, which can be slightly different for each chromatographic analysis.

2.3.5. Plug flow conditions and mass transfer limitations.

2.3.5.1. Plug flow conditions.

In a plug flow reactor, the fluid flow through the catalytic bed is ordered, that is, there is no mix between any elements of fluid. Conditions ensuring plug flow are given by Equations 2.15 and 2.16 [133], where D (m) is the reactor diameter, L (m) is the length of the catalytic bed, d_{pt} (m) is the particle diameter of the catalyst, n is the reaction order and X the conversion.

$$\frac{D}{d_{pt}} > 10 - 15 \tag{2.15}$$

$$\frac{L}{d_{pt}} > \frac{20n}{Bo} ln\left(\frac{1}{1-X}\right) \tag{2.16}$$

For axial condition, it is necessary to calculate the Bodenstein number (Equation 2.17), where u (m/s) is the flow rate and $D_{i,ax}$ (m^2/s) is the axial dispersion coefficient. The axial dispersion coefficient is calculated by means of Wakao equation (Equation 2.18) [134], where the value of m is cero if the Reynolds number of the particle is higher than 5, and 0.5 for lower Reynolds values. Moreover, ε_L and τ_L are porosity and tortuosity of the catalytic bed, respectively, whereas $D_{i,min}$ (m^2/s) is the mixture dispersion coefficient.

$$Bo = \frac{ud_p}{D_{i,ax}} \tag{2.17}$$

$$\frac{D_{i,ax}}{\varepsilon_L} = \frac{D_{i,mix}}{\tau_L} + md_{pt}u \tag{2.18}$$

Since the feeding stream is a multicomponent mixture, the dispersion coefficient of the mixture should be calculated (Equation 2.19) using the $D_{i,j}$ (m^2/s) and the x_i, which are the binary dispersion coefficients and the molar fraction of the component of the mixture, respectively. The binary dispersion coefficients are in turn calculated through the Fuller-Schelter-Giddings equation (Equation 2.20) [135], where T (K) is the temperature, PM (mol/kg) is the molecular weight, P (Pa) is the pressure and v (m^3/mol) is the dispersion volume of the compound.

$$D_{i,mix} = \frac{1 - x_i}{\sum_{j \neq i}^{j=n} x_j / D_{i,j}} \tag{2.19}$$

$$D_{i,j} = 10^{-3} \frac{T^{1.75} \left(\frac{1}{PM_i} - \frac{1}{PM_j}\right)^{1/2}}{P\left({v_i}^{1/3} + {v_j}^{1/3}\right)^2} \tag{2.20}$$

The tortuosity of the catalytic bed is estimated by means of the equation of Puncochar and Drahos (Equation 2.21) [136]. The porosity of the catalytic bed is calculated through Equation 2.22, where ρ_L and ρ_a (kg/m^3) are the density of the catalytic bed and the bulk density of the catalyst, respectively.

$$\tau_L = \frac{1}{\sqrt{\varepsilon_L}} \tag{2.21}$$

$$\varepsilon_L = \left(1 - \frac{\rho_L}{\rho_a}\right) \tag{2.22}$$

2.3.5.2. External mass transfer limitations.

External mass transfer concerns the diffusion of the reactants from the fluid to the surface of the catalysts. This can be negligible when the Mears criterion is met (Equation 2.23). Mears criterion is obtained by applying a steady-state mass balance to a particle of catalyst, and assuming that chemical reaction rate as observable reaction rate.

$$\frac{(-r_A)_{obs}\rho_L rn}{k_c C_A} < 0.15 \tag{2.23}$$

In Equation 2.23, $(-r_A)_{obs}$ is defined as the maximum reaction rate at the inlet of the catalytic bed (Equation 2.24). In addition, r (m) is the radius of the catalytic particle, k_c (m/s) is the mass transfer coefficient and C_A (mol/m^3) is the concentration of the reactant.

$$(-r_A)_{obs} = (-r_A)_{max} = \left(\frac{d(X_A)}{d\left(W/F_{A0}\right)}\right)_{X_A=0} \tag{2.24}$$

The mass transfer coefficient (k_c) is calculated according to Ranz-Marshall equation (Equation 2.25), where Sh is the Sherwood number (Equation 2.26), Re_p is the Reynolds number of the particle (Equation 2.27) and Sc is the Schmidt number (Equation 2.28). ρ (kg/m^3) is the density of the gas and μ (kg/(m s)) is the viscosity of the gas.

$$Sh = 2 + 0.6{Re_p}^{1/3}Sc^{1/3} \tag{2.25}$$

$$Sh = \frac{k_c d_{pt}}{D_{i,mix}} \tag{2.26}$$

$$Re_p = \frac{u d_p \rho}{\mu} \tag{2.27}$$

$$Sc = \frac{\mu}{\rho D_{i,mix}} \tag{2.28}$$

2.3.5.3. Internal mass transfer limitations.

Internal mass transfer concerns the diffusion of the reactants within the particle of catalyst. This can be negligible when the Weisz-Prater criterion is met (Equation 2.29). Weisz-Prater criterion is obtained by equalling mass transfer and chemical reaction rates, considering that external diffusion is negligible, and thus the concentration of the reactants at the surface of the catalyst is similar to that in the gas.

$$\frac{(-r_A)_{obs}\rho_r r^2}{D_e C_{As}} < 1 \tag{2.29}$$

In Equation 2.29, ρ_r (kg/m$_3$) is the actual density of the catalyst, D_e (m^2/s) is the effective diffusivity and C_{As} is the concentration of the reactant at the surface. Actual density of the catalyst is calculated with Equation 2.30, where V_p (m^3/kg) is the pore volume of the catalyst. Effective diffusivity is calculated with Equation 2.31, where τ is the tortuosity of the catalyst, ε is the porosity of the catalyst and D_k (m^2/s) is the Knudsen diffusivity.

$$\rho_r = \frac{1}{\frac{1}{\rho_a} + V_p} \tag{2.30}$$

$$D_e = \frac{\varepsilon}{\tau\left(\frac{1}{D_{i,mix}} + \frac{1}{D_K}\right)} \tag{2.31}$$

Knudsen diffusivity was estimated by means of Equation 2.32, where d_p (m) is the mean pore diameter of the catalyst and PM_c (mol/kg) the molecular weight of the catalyst. Porosity and tortuosity of the catalyst were calculated according to Equations 2.33 and 34.

$$D_K = 48.5 d_p \left(\frac{T}{PM_c}\right)^{1/2} \tag{2.32}$$

$$\varepsilon = \rho_r V_p \tag{2.33}$$

$$\tau = \frac{1}{\varepsilon} \tag{2.34}$$

2.3.5.4. Application of plug flow conditions, Mears and Weisz-Prater criteria.

The most significant results after applicating plug flow, Mears and Weisz-Prater criteria are briefly discussed below. It should be noted that these criteria were applied considering a temperature of 300 ^{o}C for both NO and o-DCB, at the smallest and largest particle size of the catalyst (0.3 and 0.5 cm). The necessary data and the value of the parameters calculated are shown in Table 2.6.

Regarding plug flow conditions, the values of the D/d_p ratio for the particle size of 0.3 and 0.5 cm are 45.3 and 27.2, respectively. Both results meet the limit proposed by Equation 2.15. In the case of the axial condition (L/d_p), the values obtained for NO and o-DCB agree with the criterion introduced in Equation 2.16 using a conversion for both compounds of 0.85.

Regarding mass external limitation, the Mears criterion increases with particle size, and is also higher in the case of o-DCB. Nonetheless, the results obtained are significantly below the limit of 0.15 (Equation 2.23). In fact, the results are at least one order of magnitude below the limit.

In the case of mass internal limitation, both NO and o-DCB meet the Weisz-Prater criterion (Equation 2.29). It should be noted that the value of Weisz-Prater criterion is higher for o-DCB due to its larger molecular volume. In the case of the largest particle size, the result is close to the limit, so it is not recommended to work in field of catalyst design with larger particle sizes that those used in this work.

Table 2.6. Values of the variables needed for the determination of plug flow, Mers and Weisz-Prater criterion (Equation 2.15-2.34).

Variable	Value	Variable	Value	
D (m)	$13.6 \cdot 10^{-3}$	ε_L	0.89	
L (m)	$2 \cdot 10^{-2}$	τ_L	1.06	
V (mL)	3	ε	0.53	
W (g)	1.5	τ	1.89	
u (m/s)	0.23		**d_p=0.0003 m**	
T (K)	573		**NO**	**o-DCB**
P (Pa)	182385	$D_{i,mix}$ (m^2/s)	$4.8 \cdot 10^{-5}$	$1.4 \cdot 10^{-5}$
Q (NL/min)	2	$D_{i,ax}$ (m^2/s)	$4 \cdot 10^{-5}$	$1.2 \cdot 10^{-5}$
ρ (kg/m^3)	1.5	D_e (m^2/s)	$6.8 \cdot 10^{-6}$	$3.0 \cdot 10^{-6}$
ρ_L (kg/m^3)	500	D_k (m^2/s)	$2.5 \cdot 10^{-6}$	$1.1 \cdot 10^{-6}$
d_p (m)	$0.3\text{-}0.5 \cdot 10^{-3}$	k_c (m/s)	0.45	0.15
V_p (m^3/kg)	$2.5 \cdot 10^{-4}$	L/d_p	66.6	66.6
d_{poro} (m)	$2 \cdot 10^{-8}$	D/d_p	45.3	45.3
ρ_a (kg/m^3)	$4.5 \cdot 10^{3}$	C_{Mears}	0.004	0.009
n	1	$C_{Weisz\text{-}Prater}$	0.156	0.435
μ (kg/(m s))	$3.79 \cdot 10^{-5}$		**d_p=0.0005 m**	
x_{Ar}	0.8995		**NO**	**o-DCB**
x_{NO}	0.0003	$D_{i,mix}$ (m^2/s)	$4.8 \cdot 10^{-5}$	$1.4 \cdot 10^{-5}$
x_{NH3}	0.0003	$D_{i,ax}$ (m^2/s)	$4 \cdot 10^{-5}$	$1.2 \cdot 10^{-5}$
$x_{o\text{-}DCB}$	0.0001	D_e (m^2/s)	$6.8 \cdot 10^{-6}$	$3.0 \cdot 10^{-6}$
x_{O2}	0.1000	D_k (m^2/s)	$2.5 \cdot 10^{-6}$	$1.1 \cdot 10^{-6}$
v_{Ar}	16.1	k_c (m/s)	0.29	0.10
v_{NO}	11.2	L/d_p	40.0	40.0
v_{NH3}	14.9	D/d_p	27.2	27.2
$v_{o\text{-}DCB}$	125.7	C_{Mears}	0.006	0.013
v_{O2}	16.6	$C_{Weisz\text{-}Prater}$	0.270	0.790

2.4. ASSESMENT OF REACTIVE SPECIES ON THE SURFACE CATALYST BY IN SITU FTIR.

This technique has been used to identify the species formed on the catalyst after the adsorption of the reagents involved in both SCR and o-DCB oxidation (Chapter 5). The identification of adsorbed species is made on the basis of the characteristic IR bands (fundamentals of FTIR technique are included in Section 2.2.6) of each adsorbed species.

Experimental procedure.

Experiments were carried out in a Cary 600 Series FTIR spectrometer (Agilent) coupled with a high temperature high pressure (Specac) cell with ZnSe windows, and inlet and outlet for gases and cooling system. The sample (approximately 50 mg), without dilution, is pressed into a disc and placed on a holder inside the cell in a position in which the IR beam passes through the sample. The gas feeding stream is created in the feeding zone of the experimental set-up for catalytic activity tests (described in Section 2.3.2.1). This feeding stream is connected to the inlet of the gas cell. Moreover, the experimental set-up for in situ FTIR experiments has the possibility of generating vacuum in the gas cell, by means of a system with a vacuum pump that works in parallel to the feeding stream.

All experiments were performed with the same protocol, obviously changing feed stream and temperature. The spectra were collected by 48 scans with a resolution of 4 cm^{-1}. Next, the different stages of the procedure are listed:

A. Prior to the experiments, a background spectrum of the empty cell (without sample) is recorded. Afterwards, the sample is placed on the holder and, then, a spectrum of the sample is recorded.

B. Subsequently, the sample is pre-treated with a feeding stream (600 mL/min) composed of 5%O_2 and Ar to balance at 500 ^oC for 30 min. After that time, the feeding stream is by-passed and the gas cell is subjected to vacuum conditions for 30 min. After each pre-treatment step, a spectrum is recorded. Comparison of these spectra with that recorded before pre-treatment (stage A) allows to confirm the removal of surface species on the catalyst.

C. After pre-treatment, the temperature of the sample is decreased to the temperature at which the experiment is to be performed in vacuum conditions. After reaching this temperature, a spectrum is recorded. This spectrum will be subtracted of the following spectra in order to only evaluate the absorbance of the adsorbed molecules and not that resulting from the catalyst.

D. Then, the feeding stream (600 mL/min) is fed to the gas cell for 30 min. Simultaneously, spectra are recorded as a function of exposure time. The feeding stream varies according to the adsorbed species to be analysed. The feeding stream compositions were:

- NO adsorption: 1000 ppm NO and Ar to balance.
- NO and O_2 co-adsorption: 1000 ppm NO, 5%O_2 and Ar to balance.
- NH_3 adsorption: 1000 ppm NH_3 and Ar to balance.
- NH_3 and O_2 co-adsorption: 1000 ppm NH_3, 5%O_2 and Ar to balance.
- NO, NH_3 and O_2 co-adsorption: 1000 ppm NO, 1000 ppm NH_3, 5%O_2 and Ar to balance.
- o-DCB adsorption: 1000 ppm o-DCB and Ar to balance.
- o-DCB and O_2 co-adsorption: 1000 ppm o-DCB, 5%O_2 and Ar to balance.

After 30 min of exposure time, the weakly adsorbed species are removed by passing Ar through the catalyst for 30 min.

E. In transient experiments, after purging, the catalyst is again exposed to another feeding stream for 30 min. The compositions and flows of the second feeding stream are similar to those described in stage D. The transient experiments were:

- NH_3 adsorption over NO adsorbed species.
- NO adsorption over NH_3 adsorbed species.
- o-DCB adsorption over NO adsorbed species.
- o-DCB adsorption over NH_3 adsorbed species.

Finally, the spectra were processed with Agilent Resolution Pro software, which allowed subtracting the spectrum recorded after pre-treatment (stage C) to the other spectra recorded after exposing the catalysts to the feeding stream.

Chapter 3

OPTIMIZATION OF MnO_X-CeO_2 CATALYTIC FORMULATION FOR THE SIMULTANEOUS REMOVAL OF NO_X AND o-DCB

Chapter 3

OPTIMIZATION OF MnO_X-CeO_2 CATALYTIC FORMULATION FOR THE SIMULTANEOUS REMOVAL OF NO_X AND o-DCB

ABSTRACT

This chapter aims to optimise catalytic MnO_X-CeO_2 formulations in order to achieve the highest catalytic performances in $dDiNO_X$ process. For this purpose, all prepared MnO_X-CeO_2 catalysts were characterized and tested in the simultaneous SCR and o-DCB oxidation.

The evaluation of different preparation methods and metal contents concluded that bulk catalysts, and specifically those synthesised by co-precipitation with high Mn content, i.e., 85%Mn and 15%Ce (85Mn15Ce), allows to reach the highest activity in both reactions. The excellent catalytic performances are associated to the co-existence of Mn in different phases both in the surface and the bulk: Mn in high interaction with Ce (solid solution) and Mn segregated as oxide; which improve oxygen mobility, redox and acid properties.

Calcination temperature and several variables involved in the co-precipitation method (pH, ageing time and precipitating agent) were also analysed. Calcination temperature mainly affects active metals segregation. Moreover, ammonium carbamate as precipitating agent leads to the most appropriate morphological catalytic characteristics. pH and ageing time are not key variables for catalytic activity, although they have shown to alter structural properties.

3. OPTIMISATION OF MnO_X-CeO_2 CATALYTIC FORMULATION FOR THE SIMULTANEOUS REMOVAL OF NO_X AND o-DCB.

3.1. INFLUENCE OF PREPARATION METHOD IN MnO_X-CeO_2 CATALYSTS FOR THE SIMULTANEOUS REMOVAL OF NO_X AND o-DCB.

The MnO_X-CeO_2 catalytic formulation has been postulated in recent years as an alternative for low temperature SCR. At the same time, this formulation has been investigated in the catalytic oxidation of PCDD/Fs model compounds. There is a great agreement in the literature on the effect of preparation method on catalytic performance of MnO_X-CeO_2 catalysts. This is mainly associated to the fact that each preparation method promotes different interaction between the active metals, thereby leading to different catalytic properties. Thus, the main objective of this section is to correlate the catalytic performance of several catalysts prepared by different preparation methods with their catalytic properties. For this purpose, four synthesis methods were studied: impregnation, sol-gel, co-precipitation and mechanical mixing. These methods were selected because they lead to different interaction between Mn and Ce, as well as being simple and easy to scale up.

Sol-gel and co-precipitation methods lead to bulk catalysts, in which Mn and Ce can be part of a common structure (mixed oxide phase) or segregate separately in the characteristic structure of their oxides. The difference between both resides in the way in which the solid is generated before calcination: in sol-gel, by the progressive evaporation of solvent in which the precursors and the chelating agent are dissolved, whereas, in co-precipitation, by the change of pH with a precipitating agent that causes the simultaneous precipitation of precursors. On the other hand, impregnation method leads to catalysts in which the active phase is located over the surface of a support. In this case, such loading has been carried out through the suspension of insoluble support in the precursor solution and the subsequent evaporation of the solvent. Finally, mechanical mixing method leads to catalysts in which the metal oxides, previously prepared separately, are physically mixed.

It must be pointed out that, to study the effect of preparation method carried out in this chapter, an equimolar composition of active metals was selected, i.e., $50MnO_X$-$50CeO_2$, for the catalysts prepared by sol-gel and co-precipitation, in order to promote the interaction between Mn and Ce and ensure the presence of both

metal oxides on the catalytic surface. In the case of the catalyst prepared by mechanical mixing, similar equimolar concentration of Mn and Ce was selected. For the catalysts prepared by impregnation, the Mn loading was selected to ensure a coverage of the support (cerium oxide) around half the monolayer, which allows the presence of surface Mn and Ce. For this purpose, the cross-sectional area of MnO_X (one metal atom and its oxygen coordination sphere) [137] was considered as 0.15 nm^2. Taking this into account, a 2% Mn (%wt.) was selected for the catalysts prepared by impregnation.

3.1.1. Characterization of MnO_X-CeO_2 prepared by different methods.

3.1.1.1. Structural and textural properties.

The structural properties of the catalysts were firstly investigated by XRD. Figure 3.1 shows six diffraction patterns, four of them belonging to the samples prepared by different methods and the remaining two corresponding to pure cerium and manganese oxides prepared by precipitation. Pure cerium oxide exhibits diffraction peaks at 28.6, 33.2, 46.7 and 56.5^o associated to fluorite cubic structure characteristic of cerionite (ICDD, 00-004-0593). On the other hand, pure manganese oxide shows several peaks, the strongest one located at 33.1^o, and other less intense at 23.3, 38.4, 45.4, 49.4, and 55.3^o related to α-Mn_2O_3 crystal phase (JPCDS, 01-078-030). No diffraction peaks of other manganese oxide phases, such as MnO_2 or Mn_3O_4, were identified.

The sample prepared by mechanical mixing exhibits peaks related to both fluorite and α-Mn_2O_3 crystal phases, as a consequence of the mixture of the two oxides that had been previously prepared. However, only fluorite diffraction peaks were found in the samples prepared by sol-gel, impregnation and co-precipitation. The absence of diffraction peaks from manganese oxide is associated to the low Mn content (impregnation) and to the Mn insertion on cerium oxide structure (sol-gel and co-precipitation). Moreover, comparing with the pure cerium oxide diffraction profile, it is important to note the broaden of fluorite peaks in the catalysts prepared by sol-gel and co-precipitation, and the slight shift of the strongest peak to higher brag angles in the catalyst prepared by sol-gel.

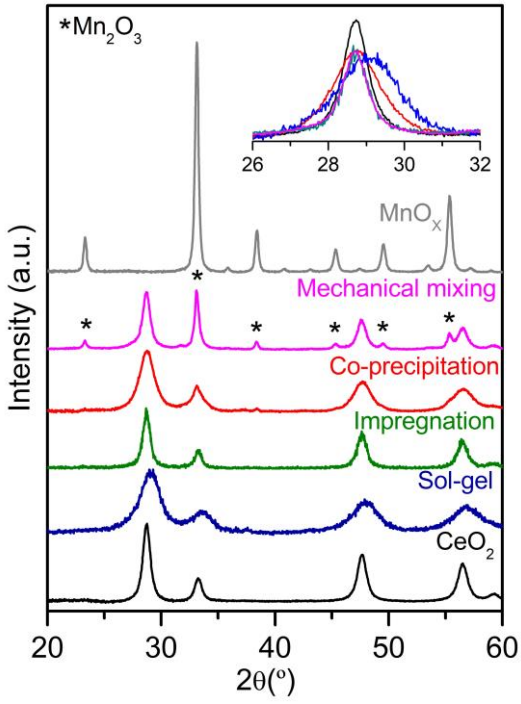

Figure 3.1. XRD patterns of MnO_X-CeO_2 catalysts prepared by different preparation methods. Inset figure: zoom of 2θ region between 26-32º.

The broaden and shift of CeO_2 diffraction peaks in the presence of metal dopant is associated in the literature to the generation of a solid solution phase [138], in this case formed by Mn and Ce oxides. The solid solution phase is promoted by a strong interaction between both metals, so this effect should cause a distortion in the cerium lattice cells. In order to verify the formation of solid solution phase, the lattice parameter of fluorite phase was calculated, and it is reported in Table 3.1.

The values of lattice parameter for the catalysts prepared by sol-gel and co-precipitation are smaller than those calculated for pure cerium oxide. The decrease of lattice parameter is associated to the contraction and distortion of the CeO_2 fluorite structure as a consequence of Mn insertion, due to the lower ionic radius of Mn ions (Mn^{4+}=0.53 Å; Mn^{3+}=0.65 Å; Mn^{2+}=0.83 Å) than Ce^{4+} ion (Ce^{4+}=1.01 Å) [97]. Therefore, this result evidences the high interaction between Mn and Ce, and the formation of solid a solution phase. On the contrary, the lattice parameter for

mechanical mixed catalyst is close to that of pure cerium oxide, which confirms the low interaction between both metals. Similar result is observed for the catalyst prepared by impregnation, although, as in the catalysts prepared by sol-gel and co-precipitation, no MnO_X diffraction peaks were detected. The absence of diffraction peaks is due to the high dispersion of Mn over the CeO_2 support (caused by the low Mn loading). The higher the Mn dispersion, the more the interaction with the CeO_2 surface. However, impregnation method does not provide enough interaction between Mn and CeO_2 bulk to affect the lattice parameter.

Table 3.1. Structural properties of MnO_X-CeO_2 catalysts prepared by different methods.

Sample	Fluorite lattice parameter (nm)	Fluorite crystal size (nm)	F_{2g} position (cm^{-1})	FWHM of F_{2g} (cm^{-1})
CeO_2	5.4135	9	462	19
Sol-gel	5.3854	3	457	56
Impregnation	5.4161	8	460	23
Co-precipitation	5.4035	4	456	41
Mechanical mixing	5.4117	10	462	20
MnO_X	--	--	--	--

Table 3.1 also reports an estimation of fluorite crystal size, calculated with Scherrer equation and applied to its most intense peak located at 28.6º, which corresponds to the (111) plane. The catalysts prepared by mechanical mixing and impregnation exhibit similar crystalline sizes than pure cerium oxide. On the contrary, crystalline size is notably smaller in the catalysts prepared by sol-gel and co-precipitation. This fact is associated to Mn incorporation to the CeO_2 structure, which generates structural defects that prevent the growth of CeO_2 crystalline domains. The lower fluorite crystal size is in accordance with the smaller lattice parameter, which gives a further evidence of solid solution formation.

Raman spectroscopy was also used to characterize the structural properties of the catalysts. This technique analyses metal-oxygen vibrations and is sensitive to alterations in the catalyst structure.

Raman spectra of all samples are shown in Figure 3.2. Pure cerium oxide spectrum exhibits an intense peak at 460 cm^{-1}, associated to F_{2g} mode of CeO_2 [139, 140]. On the other hand, pure manganese oxide shows peaks at 693, 640, and 306 cm^{-1}, related to vibrational modes ν_7, ν_6, and ν_2 of α-Mn_2O_3 [141]. This result is in accordance with XRD, where this crystal phase was the only one identified. All spectra of the catalysts prepared by different methods exhibit the F_{2g} band, although, interestingly, the location of the peak slightly differs depending on the preparation method (Table 3.1). In this sense, the position of the band in the catalyst prepared by mechanical mixing is the same that of pure cerium oxide, whereas in the catalysts prepared by the remaining methods, it is shifted to lower wavenumber, this shift being more noticeable in the catalysts prepared by sol-gel and co-precipitation.

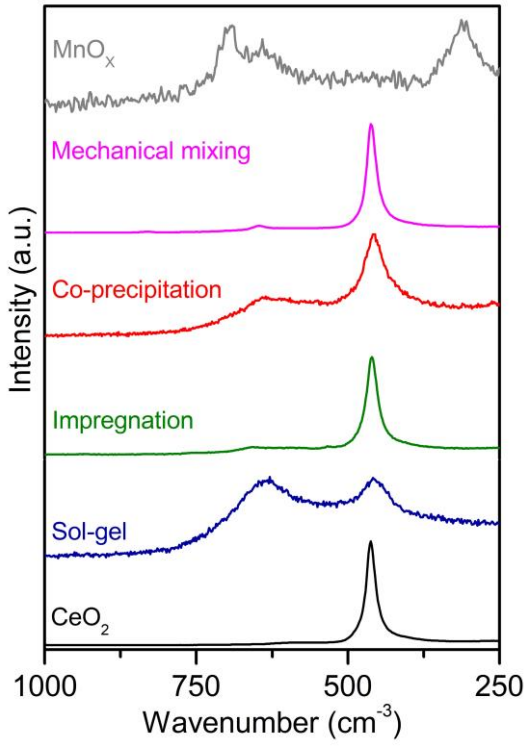

Figure 3.2. Raman spectra of MnO_X-CeO_2 prepared by different methods.

F_{2g} band is related to symmetrical stretching vibration of the atoms belonging to the structure around Ce^{4+} [142], so the variations above mentioned evidence alterations in the environment of sublattice oxygen due to the interaction between Mn and Ce. Thus, the fact that the largest shifts occur in the catalysts prepared by sol-gel and co-precipitation suggests that these methods provide a greater interaction between the active metals, which promotes the formation of mixed oxide phase where both metals are within the same fluorite-type structure.

In addition to F_{2g} displacement, Raman spectra of the catalysts prepared by sol-gel and co-precipitation exhibit a band between 700-600 cm^{-1}. This band may be composed of two contributions: on the one hand, that associated to manganese oxide, since it has been already checked that pure manganese oxide exhibits several bands above 630 cm^{-1}; and, on the other hand, the one associated to the structural defects of fluorite structure, that is, oxygen vacancies, which are reported in the literature around 600 cm^{-1} [142]. Oxygen vacancies appear to compensate the negative charge generated by the incorporation of a doping cation with different nature and oxidation state [138]. In this specific case, the substitution of Ce^{4+} by Mn^{n+} in the CeO_2 lattice.

Since the generation of oxygen vacancies involves the formation of structural defects, the size of the crystalline domains of fluorite-type structure will also be affected. In this sense, Table 3.1 reports the FWHM of the F_{2g} peak. The FWHM of the catalysts prepared by mechanical mixing and impregnation are similar to those measured for pure cerium oxide, whereas they are much larger in the catalysts prepared by sol-gel and co-precipitation. These results evidence similar crystalline domain sizes to those of cerium oxide in the samples with low interaction between Mn and Ce, unlike the catalysts with high interaction, where the crystalline domains are smaller. These results are in line with the conclusions obtained from the crystal size analysis in XRD.

Textural properties of the samples were evaluated by N_2-physisoprtion. N_2 adsorption/desorption isotherms are shown in Figure 3.3A. According to International Union of Pure and Applied Chemistry (IUPAC) classification, all catalysts show type IV isotherms with H3 hysteresis loop in the relative pressure (P/P_0) from 0.4 to 1, so all samples can be classified as mesoporous materials.

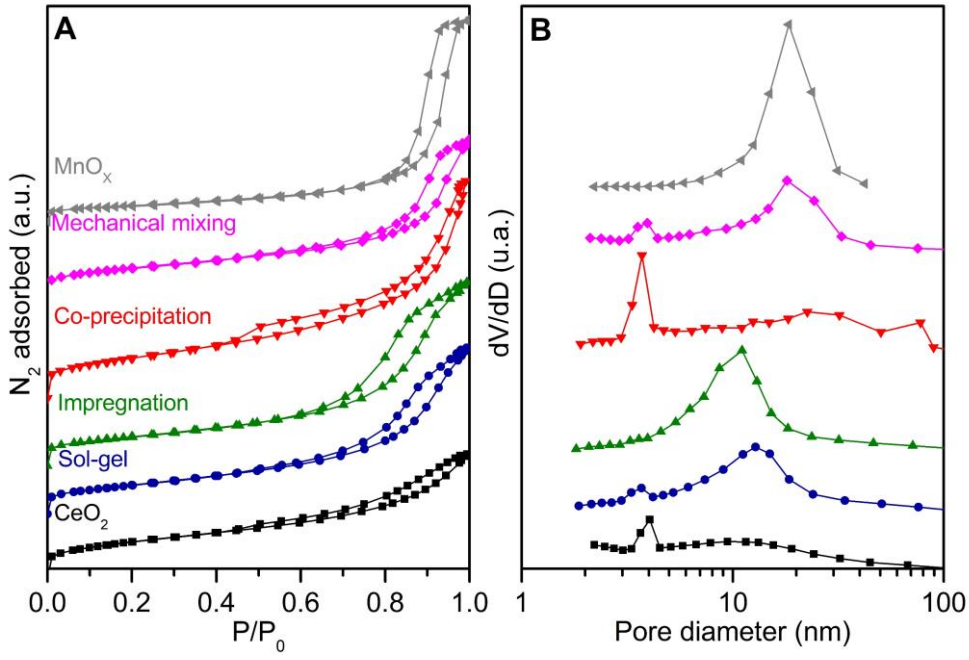

Figure 3.3. A) N_2 physisorption isotherms and B) pore size distribution of MnO_X-CeO_2 catalysts prepared by different methods.

Table 3.2 reports specific surface area, pore volume and mean pore diameter of the catalysts. The specific surface areas of bimetallic samples are ranged between those obtained for pure cerium oxide and pure manganese oxide, except the one prepared by co-precipitation. In the case of the catalyst prepared by mechanical mixing, the value agrees with the weighted sum of the surface area of the pure oxides. The lower surface area obtained for the catalysts prepared by impregnation compared to cerium oxide support can be associated to blocking of pores by MnO_X particles. Interestingly, despite their similar structural properties, a large difference in the surface area has been found for the catalysts prepared by sol-gel and co-precipitation, the latter being even higher than that of pure cerium oxide. In the same way, pore volume of bimetallic samples is ranged between the values of pure oxides, except for the catalyst prepared by co-precipitation, which could be linked with the higher surface area measured for this sample.

Table 3.2. Textural properties of MnO_X-CeO_2 catalysts prepared by different methods.

Sample	Mn (mol.%)	S_{BET} (m^2/g)	V_P (cm^3/g)	d_P (nm)
CeO_2	0.0	80	0.12	6.3
Sol-gel	49.4	63	0.16	8.5
Impregnation	2.0[a]	63	0.17	9.1
Co-precipitation	47.9	88	0.21	8.0
Mechanical mixing	48.6	67	0.14	9.4
MnO_X	100	34	0.19	16.6

[a] Mn composition in wt.%.

On the other hand, the mean pore diameter is larger for the catalysts with less interaction between Mn and Ce, those prepared by impregnation and mechanical mixing. In this regard, Figure 3.3B shows the pore size distribution of the samples. Pure manganese oxide exhibits only a single pore size of approximately 19 nm, whereas cerium oxide shows two well-defined pore sizes, one around 4 nm and the other between 7 and 17 nm. Pore distribution differs for the catalysts prepared by different methods; the one prepared by mechanical mixing exhibits the typical pore size of pure oxides and the pore size of the catalyst prepared by impregnation is centred around 10 nm. In the case of the catalysts prepared by sol-gel and co-precipitation, two different pore sizes were observed similarly to cerium oxide pore distribution, although with some differences. Thus, additional pores with a size around 30 nm were observed in the catalyst prepared by co-precipitation, whereas in that prepared by sol-gel a higher number of pores with size of 10 nm were measured in comparison to pure cerium oxide.

It is important to note there are discrepancies in the literature about the appearance of pores with size around 4 nm in mesoporous materials when the hysteresis loop is abruptly closed in the P/P_0 range around 0.45 [143], as occurs in some of the samples here studied. This phenomenon is usually related to tensile effect strength. Figure 3.4 shows a zoom of the N_2 adsorption and desorption isotherms in the P/P_0 region between 0.3-0.6 for the catalysts characterized by exhibiting pores size around 4 nm (cerium oxide and the samples prepared by sol-gel, co-precipitation and mechanical mixing). By comparing Figure 3.4 and

Figure 3.3B, it can be seen that the more abruptly the isotherm is closed, the more noticeable is the peak associated with pores of 4 nm. Therefore, these results suggest that pores of 4 nm are not representative of the textural properties of the samples.

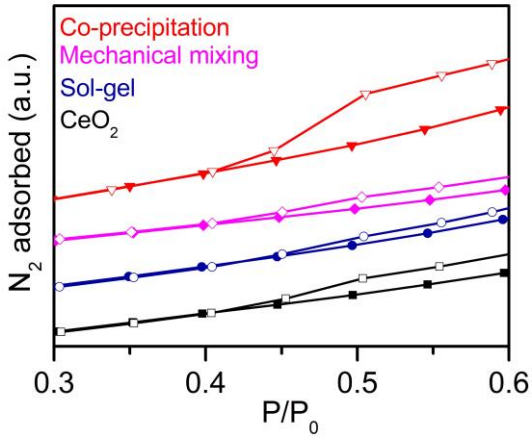

Figure 3.4. A detailed view of the isotherms of selected catalysts in the P/P_0 range 0.3-0.6.

3.1.1.2. Redox and acid properties.

Redox properties were investigated by means of H_2-TPR. Figure 3.5 shows the reduction profiles of all samples. Pure cerium oxide exhibits two reduction peaks at approximately 430 and 830 ^oC, which are associated to surface and bulk cerium oxide reduction, respectively [74]. It should be noted that after reaching the temperature of 950 ^oC in the experiment, the sample is not completely reduced yet (H_2 consumption does not reach the baseline). For this reason, the temperature was kept constant for 30 minutes in order to ensure the total reduction of bulk cerium oxide, as can be seen in the right part of the graph. Obviously, this isothermal stage before finishing the experiment was performed in all the samples to quantify as accurately as possible the H_2 consumption of bulk cerium oxide.

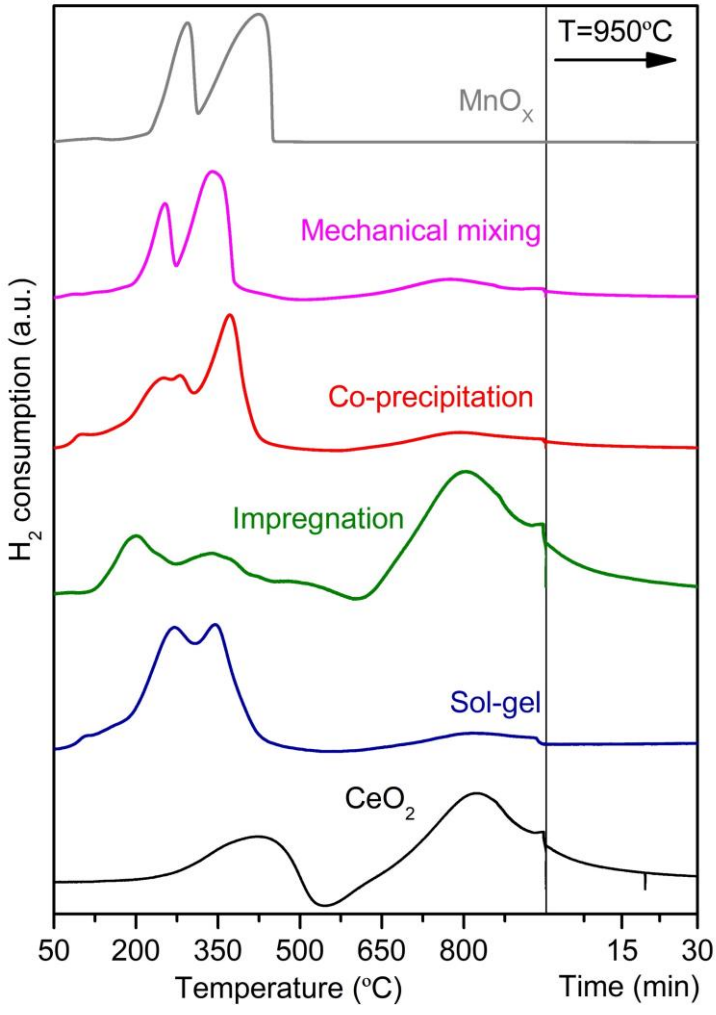

Figure 3.5. H_2-TPR profiles of MnO_X-CeO_2 prepared by different methods.

On the other hand, the reduction profile of pure manganese oxide shows two peaks at 293 and 423 ºC fitting well with the Mn_2O_3 reduction profile reported in the literature [63]. This result agrees with those obtained by XRD and Raman, where α-Mn_2O_3 was the only crystal phase identified for the pure manganese oxide. The first peak corresponds to the reduction of Mn_2O_3 to Mn_3O_4 and the second one to the reduction of Mn_3O_4 to MnO [144]. No reduction peaks were observed above 500 ºC.

Regarding bimetallic catalysts, all TPR profiles show two strong reduction peaks at low temperature, mainly associated to manganese and, to a lower extent, to surface cerium reduction. The latter becomes practically indistinguishable in all catalysts, with the exception of that prepared by impregnation, in which the low manganese content allows this step to be distinguished at approximately 460 ^{o}C. As Table 3.3 reports, these reduction peaks clearly take place at lower temperature in comparison to pure manganese oxide, due to the interaction between Mn and Ce.

At high temperature, all bimetallic catalysts exhibit a similar reduction peak, although slightly shifted to lower temperatures. Moreover, in the catalyst prepared by impregnation, in contrast to the others, H_2 consumption at high temperature is relatively higher than that measured at low temperature. This result is due to the much higher proportion of cerium oxide than manganese oxide in this catalyst.

However, several differences were detected in the H_2 uptake at low temperature, specifically in the shape of the reduction peaks. This result probably corresponds to the different interactions between the active metals observed depending on the preparation method. In this sense, the catalyst prepared by mechanical mixing exhibits similar reduction profile than pure manganese oxide, which reveals the low interaction between Mn and Ce. In the case of the catalyst prepared by impregnation, the two peaks are not well-defined because of the low Mn loading, and they are further separated. Moreover, the first reduction peak takes place even at lower temperatures than in the other catalysts, which suggests a high reducibility of Mn species due to a high dispersion and interaction with CeO_2 support, as was concluded from the analysis of structural properties.

On the other hand, the catalysts prepared by sol-gel and co-precipitation show a higher overlap in the reduction peaks. This fact could be the consequence of the higher interaction between active metals at bulk, which would promote the overlapping of the different Mn reduction steps due to the higher amount of oxygen vacancies (previously evidenced by Raman). Furthermore, an additional reduction peak is observed in both catalysts around 100 ^{o}C. This H_2 consumption at very low temperature is related in the literature to the reduction of surface isolated Mn embedded into the CeO_2 [95, 145]. The structural analysis of the samples revealed the formation of solid solution in the catalysts prepared by sol-gel and co-precipitation; so the fact that this peak appears only on those catalysts agrees with that assignment.

H_2 consumption from TPR analysis has been reported in Table 3.3. Obviously, samples with higher Mn content present larger H_2 consumption. In addition, the average oxidation state of Mn (Table 3.3) has been estimated from the total H_2 consumption, with some assumptions, such as a negligible H_2 consumption of cerium oxide at low temperature and assuming MnO as the final reduction state of Mn.

Table 3.3. Results of H_2-TPR for catalysts prepared with different methods.

Catalyst	Mn reduction peaks (°C)		H_2 consumption (mmol H_2/g)	Mn oxidation state
	Peak I	Peak II		
CeO_2	--	--	1.3	--
Sol-gel	271	345	4.2	3.8
Impregnation	200	332	1.4	2.8
Co-precipitation	264	371	3.1	3.5
Mechanical mixing	252	340	3.6	3.3
MnO_X	293	423	6.6	3.1

The oxidation state of pure manganese oxide is very close to 3, which is in agreement with the structural analysis that corroborated the presence of only the Mn_2O_3 phase. In addition, the H_2 consumed in the first peak is half that of the second, which is in accordance with the previous reduction step assignment for each peak. In the case of the catalyst prepared by mechanical mixing, a manganese oxidation state between 4 and 3 was estimated by TPR, whereas the average oxidation state of Mn in the catalyst prepared by impregnation is very low compared to the others. This is associated to the calculating error as a consequence of the low Mn loading. On the other hand, the average oxidation state of Mn is significantly higher in the catalysts prepared by sol-gel and co-precipitation, being between 3 and 4. This result supports the presence of Mn in different oxidation states (Mn^{3+} and Mn^{4+}).

Since the analysis of Mn oxidation state has evidenced that the interaction between Mn and Ce leads to the formation of Mn species with oxidation state higher than 3, it would not be appropriate to use the same assignment of reduction peaks for the bimetallic catalysts as for the sample composed by only manganese oxide, because

the reduction of Mn species with oxidation state higher than 3 would not be taken into account. In this sense, several works in the literature agree that Mn^{4+} reduction is practically indistinguishable from that of Mn^{3+}; so many authors relate the H_2 uptake in peak I with the MnO_2/Mn_2O_3 to Mn_3O_4 reduction stage, and the H_2 uptake in peak II, at higher temperature, with the reduction of Mn_3O_4 to MnO [97, 146, 147]. However, the assignment of Mn reduction peaks in bimetallic samples will be discussed in more detail during the analysis of the effect of Mn and Ce content in Section 3.2.

Therefore, TPR results have shown that the combination of Mn and Ce improves the reducibility of the samples with respect to the pure oxides, independently of the interaction degree between both metals. However, this variable affects the way in which the different reduction stages take place, promoting their overlapping in the catalysts prepared by sol-gel and co-precipitation. This effect is associated to the presence of different Mn species with high oxidation state.

It is well known that acid properties take part in the adsorption and activation of the compounds that participate in both SCR and catalytic oxidation reactions. The influence of preparation method in acid properties was evaluated by NH_3-TPD and the NH_3 desorption profiles are showed in Figure 3.6A. The strength of the acid sites is related with the position of the NH_3 desorption peak. NH_3 adsorbed over weak acid sites is less thermally stable than that adsorbed over strong acid sites, so contributions located at low temperature correspond to weak acid sites, whereas those located at higher temperatures correspond to strong acid sites [70, 148]. The amount of acid sites is related with the integrated area of the peaks.

Pure cerium oxide shows a NH_3 desorption peak around 100 ^oC, followed by a broad shoulder between 150 and 250 ^oC. Pure manganese oxide exhibits two NH_3 desorption peaks, one similar to that shown by cerium oxide and the other located around 180 ^oC along with a tiny NH_3 desorption above 300 ^oC. Therefore, pure oxides mainly present two NH_3 desorption zones: that located at low temperature would be attributed to NH_3 weakly adsorbed on the catalytic surface, and that located at intermediate temperature could be related to strongly adsorbed NH_3.

All bimetallic samples, prepared by different methods, show a similar NH_3 desorption peak at low temperature, which corroborates the presence of weak acidity. However, several differences are observed at medium and high temperatures. The sample prepared by mechanical mixing exhibits larger NH_3

desorption than cerium oxide, although lower than pure manganese oxide. On the other hand, in the catalysts prepared by impregnation, sol-gel and co-precipitation, NH_3 desorption at medium temperature is higher than that at low temperature. The increase of NH_3 desorption in the medium temperature range for catalysts prepared by impregnation, sol-gel and co-precipitation, is obviously related to the interaction between manganese and cerium, since no such remarkable peak is observed in the catalyst prepared by mechanical mixing, in which the interaction between both metals is minimum.

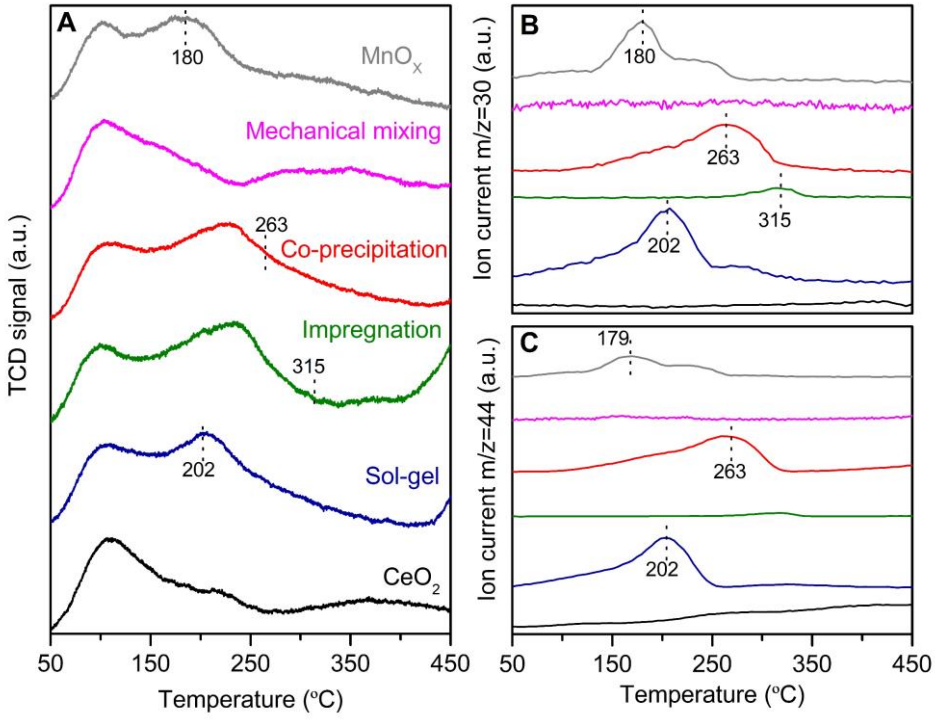

Figure 3.6. A) NH_3-TPD profiles, B) NO desorption profile and C) N_2O desorption profiles of MnO_X-CeO_2 catalysts prepared by different methods.

It is important to note the remarkable NH_3 desorption peak at medium temperature in the catalyst prepared by impregnation, despite having a lower manganese content, compared to the catalysts prepared by sol-gel and co-precipitation. This is due to the fact that acidity is a property entirely related with the catalytic surface; so the interaction between Mn and Ce in the lattice structure (provided by methods

such as sol-gel and co-precipitation) tends to be of minor relevance compared to the interaction between both active metals in the surface. In this sense, XRD and Raman results evidenced the excellent dispersion of manganese on the cerium oxide support in the impregnated catalyst. This fact ensures high surface interaction between Mn and Ce, which greatly improves strong acidity.

Due to the excellent oxidizing properties of some samples, provided by their oxygen vacancies, NH_3 adsorbed in the TPD may react with surface oxygen of the catalysts leading to nitrogen oxides generation. In order to check this issue, a mass spectrometer was used. NO and N_2O were the only nitrogen oxides detected through their corresponding m/z=30 and m/z=44, respectively. Figure 3.6B and 3.6C show the NO and N_2O generation with temperature in the same range as TPD. The production of both nitrogen oxides mainly occurs at medium temperatures and in the catalysts composed by only manganese oxide and those bimetallic prepared by sol-gel and co-precipitation.

Since NO and N_2O in NH_3-TPD appear at medium temperature, their production is associated to strong acidity. However, strong acidity is not the only property involved in further oxidation of adsorbed NH_3. High differences in by-product generation have been found among the catalysts prepared by impregnation, sol-gel and co-precipitation. This means oxygen mobility plays a key role in the subsequent oxidation of adsorbed NH_3, and this property is greatly favoured in those catalysts in which the interaction between the two active metals is in the bulk structure and not only on the surface. Hence the great difference in NO and N_2O production between the different preparation methods.

Total acidity of the samples is summarized in Table 3.4. The nitrogen oxides generated at medium temperature, as shown in Figures 3.6B and 3.6C, were not considered in acidity estimation. So, the acidity values of the samples were only expressed as NH_3 desorbed.

Pure cerium oxide exhibits higher total acidity than pure manganese, although this result is strongly affected by specific surface area. If acidity is calculated per unit area instead of per unit mass, as shown in the last column of Table 3.4, manganese oxide becomes the most acidic sample. Regarding bimetallic samples, the catalyst prepared by co-precipitation is the most acidic, followed by those prepared by sol-gel and impregnation. Table 3.4 also summarizes the ratio between strong and weak acidity. Weak acidity was considered to be that related to NH_3 desorbed

below 170 °C, while NH_3 desorption above that temperature was associated to strong acidity. Interestingly, higher ratios are obtained for bimetallic catalysts in comparison to pure oxides. The highest value was obtained for the catalysts prepared by co-precipitation, followed by impregnation and sol-gel. This result corroborates that the interaction between Mn and Ce favours strong acidity, as observed in the NH_3 desorption profiles.

Table 3.4. Results of NH_3-TPD analysis.

Catalyst	Acidity (μmol NH_3/g)		Acidity (μmol NH_3/m^2)
	Strong/weak	Total	Total
CeO_2	1.1	204.1	2.5
Sol-gel	1.6	200.7	3.2
Impregnation	1.7	160.2	2.5
Co-precipitation	2.0	304.5	3.4
Mechanical mixing	1.4	80.8	1.2
MnO_X	1.1	171.0	5.0

3.1.2. Catalytic performance of MnO_X-CeO_2 prepared by different methods.

3.1.2.1. Analysis of NO and o-DCB conversions.

Once the most important aspects of characterization have been addressed, this section aims to focus on the study of the catalytic activity in the simultaneous NH_3-SCR and o-DCB oxidation.

Figure 3.7 shows NO and o-DCB conversion profiles of the above characterized samples. Pure CeO_2 exhibits a negligible NO conversion (< 20%) below 200 °C. Higher temperatures promote an increase of NO conversion to over 80% at 350 °C, temperature above which NO conversion strongly drops. On the other hand, pure manganese oxide leads to NO conversion above 80% at temperatures lower than 175 °C. However, further temperature increase causes a small drop down and then

a new peak of NO conversion, although above 250 ºC NO conversion sharply drops again.

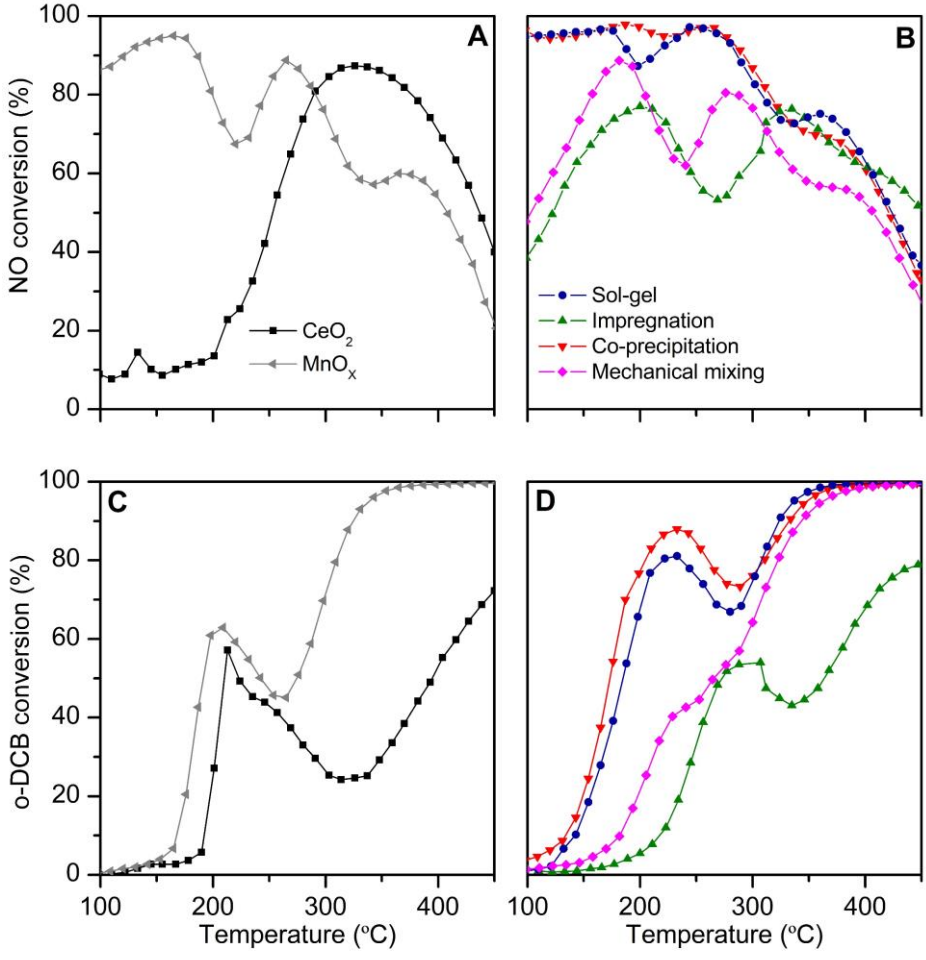

Figure 3.7. NO conversion obtained with A) pure oxides and B) bimetallic catalysts prepared by different methods. o-DCB conversion obtained with C) pure oxides and D) bimetallic catalysts prepared by different methods.

Bimetallic catalysts (Figure 3.7B) improve in some cases the catalytic activity of pure oxides. The catalyst prepared by mechanical mixing shows an intermediate NO conversion profile between the two pure oxides, i.e., similar shape to that of pure manganese oxide, although with lower conversion values over the whole

temperature range, as a consequence of cerium oxide. In the case of the catalyst prepared by impregnation, lower NO conversion is obtained in the low temperature range respect to pure manganese oxide, although NO conversion becomes higher above 300 ^{o}C. It should be noted that, although neither of the two catalysts improve the catalytic results obtained by pure manganese oxide, they do the pure cerium oxide results in the low temperature range.

The results obtained by impregnated catalyst at low temperature are interesting, since NO conversions are somewhat lower than those obtained with the catalyst prepared by physical mixing, despite its much lower Mn content. This result denotes that NO conversion at low temperature can be greatly improved due to surface Mn and Ce interaction. Indeed, surface interaction between active metal provides to the impregnated catalyst lower Mn reduction temperature and higher total acidity than physical mixed catalyst.

Regarding the catalysts prepared by sol-gel and co-precipitation, similar NO conversion profiles are obtained for both. These catalysts show NO conversion above 95% at temperatures below 275 ^{o}C, so they exhibit the best catalytic performances in SCR among studied samples. In these catalysts, a high interaction between Mn and Ce was evidenced. Solid solution was corroborated by the modification of lattice parameter and the shift of F_{2g} mode with respect to pure CeO_2 in XRD and Raman. Therefore, this corroborates the results observed in the impregnated catalyst: that the interaction between active metals leads to improving NO conversion at low temperature.

The high interaction between Mn and Ce in the catalysts prepared by sol-gel and co-precipitation not only favours high oxygen mobility (due to structural defects), but it has also been corroborated that provides Mn species with different high oxidation states (Mn^{4+} and Mn^{3+}), which enhance redox properties, essential for SCR. The presence of these species was corroborated by the estimation of the mean oxidation state of Mn by H_2-TPR. Moreover, acid properties, and specifically strong acidity, which are involved in the adsorption and subsequent reaction of adsorbed species, are also improved.

The same way than in pure oxides, NO conversion in bimetallic catalysts sharply drops down around 275 ^{o}C. This fact is associated to side-reactions, specifically NH_3 oxidation, that leads to the consumption of a reagent involved in the SCR. The influence of SCR side reactions will be addressed in Chapter 4.

Regarding o-DCB oxidation reaction (Figure 3.7C and 3.7D), all catalysts exhibit an S-shape conversion profile in which o-DCB conversion sharply increases with temperature. However, in the medium temperature range, o-DCB conversion drops down and then up again with temperature (the analysis of this interesting fact will be dealt in Chapter 4, where further experiments will allow to draw more accurate conclusions). Obviously, the temperature where maximum o-DCB conversion is reached and the value of maximum o-DCB conversion depend on the catalyst.

In the pure oxides, similar o-DCB conversion, around 60%, is reached at 225 ^{o}C, but the subsequent drop is more noticeable for cerium oxide. For pure manganese oxide, total conversion is obtained at 350 ^{o}C. In the case of bimetallic catalysts, the one prepared by impregnation shows the worst results; in fact, it hardly improves those obtained with cerium oxide, and does not even exceed 80% of o-DCB conversion over the whole temperature range. On the other hand, the catalyst prepared by physical mixing, despite having less interaction between Mn and Ce, shows higher conversion than the impregnated one, so the amount of Mn seems to be a key factor in the oxidation reaction.

The samples prepared by sol-gel and co-precipitation exhibit the best catalytic performance, mainly at low temperature, where o-DCB conversion above 80% is reached around 200 ^{o}C (in the peak rise of o-DCB conversion). Moreover, these catalysts shift the conversion profiles to lower temperatures compared to the pure oxides. o-DCB conversions above 90% are reached around 325 ^{o}C for both catalysts.

The better catalytic performance of catalysts prepared by sol-gel and co-precipitation suggests an increase in oxidative capability compared to the rest of the catalysts. This fact is favoured by a higher interaction degree between Mn and Ce, as mentioned above in the SCR analysis. This high interaction leads to the formation of mixed oxide phase, generating oxygen vacancies that provide to the catalysts high oxygen mobility and storage capacity in its structure. This feature is fundamental in oxidation reactions, which occur at lower temperatures due to the higher activity of surface oxygen species as well as the faster regeneration of oxygen consumed in the reaction.

Interestingly, it must be pointed out that the comparison between the o-DCB conversion profiles of the catalysts prepared by sol-gel or co-precipitation and that of pure manganese oxide reveals a noticeable difference only at low temperatures (first peak). This difference is obviously associated to the interaction between Mn

and Ce. Therefore, it is proposed that the promotional effect that bimetallic catalysts have on o-DCB conversion at low temperature is mostly associated to the catalytic properties provided by the high interaction between Mn and Ce.

The fact that the interaction between Mn and Ce leads to higher o-DCB conversion at low temperatures (first peak of o-DCB conversion) agrees with the results of the catalyst prepared by physical mixing. This catalyst, despite having the same Mn and Ce content as the catalysts prepared by sol-gel and co-precipitation, exhibits much lower o-DCB conversion at low temperature, around 40%.

Obviously, good catalytic activity in $dDiNO_x$ process involves high conversions in both NO reduction and o-DCB oxidation in the same temperature range. Based on the above results, the catalysts with the best catalytic performance in both reactions have been those prepared by sol-gel and co-precipitation. In this sense, NO and o-DCB conversions above 80% have been obtained within the temperature ranges of 225-235 ^{o}C and 200-261 ^{o}C for the catalysts prepared by sol-gel and co-precipitation, respectively.

As above mentioned during the analysis of catalytic activity, the excellent catalytic performance of the catalysts prepared by sol-gel and co-precipitation is associated to the fact that both methods ensure a good interaction between Mn and Ce in the surface and at the bulk.

3.1.2.2. Analysis of SCR and o-DCB oxidation by-products.

As described in Chapter 1, other reactions involving several or all the reagents that take part in SCR can occur in parallel to the SCR. This fact may generate reaction by-products, promoting an unselective reduction of NO. Similarly, o-DCB oxidation may not be complete, thereby generating unwanted partial oxidizing compounds.

It should be noted that the information below only intends, at this stage, to analyse the influence of preparation method on by-products production, both in SCR and o-DCB oxidation. It is not the objective of this section to go in-depth into the origin (side-reactions involved in the by-product generation) of the by-products, which will be addressed in Chapter 4.

In this sense, N_2O and NO_2 were found to be the only by-products of SCR. Figure 3.8 shows the N_2O and NO_2 production profiles of both compounds. Pure cerium oxide

hardly generates N_2O in the whole temperature range (Figure 3.8A), so its formation is mainly associated to Mn species. In fact, N_2O is formed in pure manganese oxide on the whole range of temperature. Its production profile is a broad peak, which reaches its maximum at 200 ^oC and keeps constant up to 300 ^oC, temperature from which N_2O production decreases.

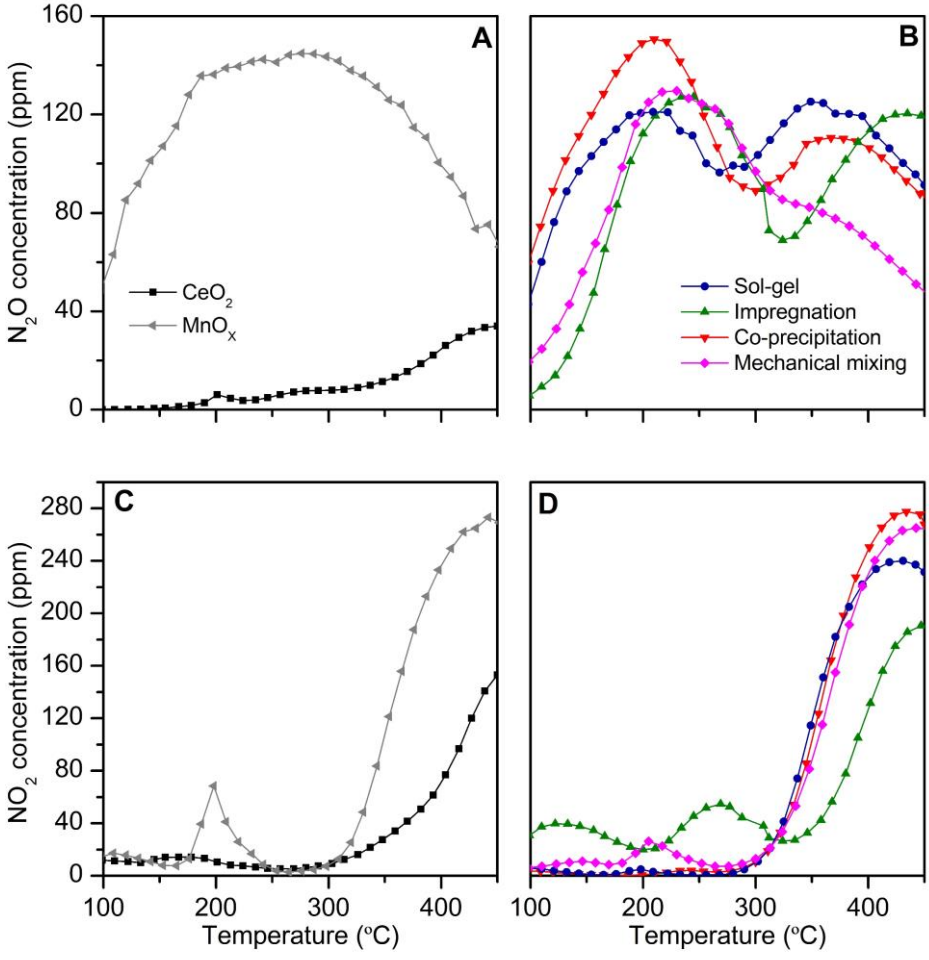

Figure 3.8. N_2O generation with A) pure oxides and B) bimetallic catalysts prepared by different methods. NO_2 generation with C) pure oxides and D) bimetallic catalysts prepared by different methods.

Regarding bimetallic catalysts (Figure 3.8B), N_2O is also generated in the whole temperature range. This behaviour was expected, since N_2O was detected as oxidation product of adsorbed NH_3 oxidation in TPD experiment. However, in TPD, N_2O was only produced between 150-300 ^oC and in the absence of oxygen. These results suggest that under oxidising conditions, such as those in SCR, MnO_X-CeO_2 formulation tends to produce N_2O to a greater extent.

N_2O production profiles of bimetallic catalysts are different than those of pure oxides. They are composed by two peaks, one at 200 ^oC and the other at 350 ^oC, although, in the catalysts prepared by impregnation and mechanical mixing, the N_2O profile shifts to higher temperatures. The co-precipitated catalyst is the one generating more N_2O at low temperature and the sol-gel catalyst is the one generating more N_2O at high temperature.

On the other hand, NO_2 is produced by all catalysts at high temperature (Figure 3.8C and 3.8D), just above 300 ^oC, and its concentration continuously increases with temperature, which is in line with the results of Wang and co-workers [149]. Pure cerium oxide and the bimetallic impregnated sample are those with the lowest NO_2 production, due to the lower Mn content. The remaining bimetallic catalysts exhibit a similar NO_2 production profile than pure manganese oxide.

In the case of oxidation reaction, CO is the main by-product, and it is produced in the whole range of temperatures, although to a different extent depending on the sample. Moreover, chlorinated organic compounds are also generated in specific range of temperature. Figure 3.9 shows the selectivity towards these compounds. It must be pointed out that selectivity of by-products from oxidation reaction are showed above 200 ^oC, due to the low o-DCB conversion below this temperature.

The CO selectivity gradually increases in pure cerium oxide (Figure 3.9A), although it does not overcome values of 20% in the studied temperature range. On the other hand, in pure manganese oxide, CO selectivity profile increases at low temperature until reaching a plateau between 250-350 ^oC, where it is around 30%. CO selectivity strongly decays above 350 ^oC. Bimetallic catalysts exhibit similar CO selectivity profiles than pure manganese oxide, although lower CO selectivity is obtained by the catalysts prepared by impregnation, sol-gel and co-precipitation.

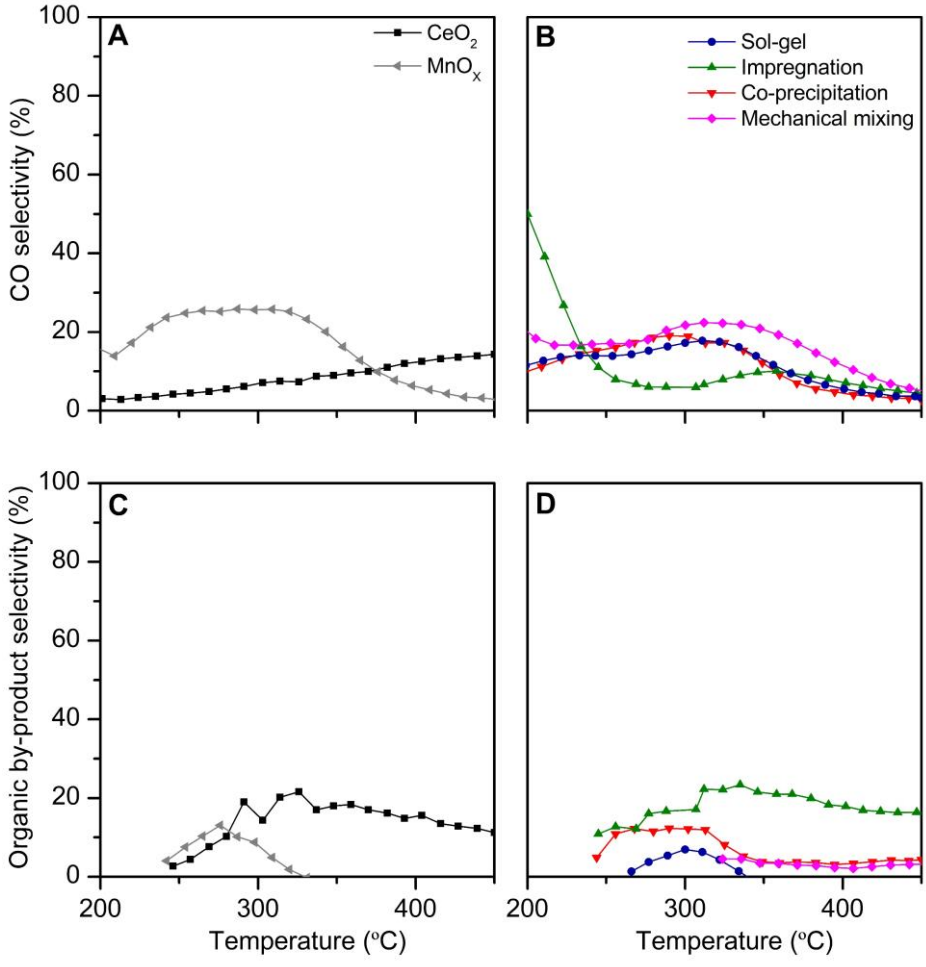

Figure 3.9. CO selectivity obtained with A) pure oxides and B) bimetallic catalysts prepared by different methods. Chlorinated organic by-products selectivity obtained with C) pure oxides and D) bimetallic catalysts prepared by different methods.

The global selectivity towards chlorinated organic compounds is showed in Figure 3.9C and 3.9D. Pure cerium oxide is the catalyst with the highest production of chlorinated organic compounds, with selectivity values around 20% above 300 °C. The formation of chlorinated organic compounds occurs in pure manganese oxide between 250-325 °C; the selectivity profile firstly increases, reaching the

maximum value of 12%, and then abruptly decreases with temperature. Impregnated catalyst exhibits a similar chlorinated organic by-product profile than pure cerium oxide, due to the high Ce content. The remaining catalysts exhibit similar selectivity profiles than manganese oxide, although with lower selectivity values.

The catalysts prepared by sol-gel and co-precipitation produce less oxidation by-products than pure manganese oxide. Since these by-products come from o-DCB partial oxidation, the lower yields indicate that these catalysts favour total o-DCB oxidation, due to their better oxidising capacities.

3.2. INFLUENCE OF Mn AND Ce COMPOSITION IN MnO_X-CeO_2 CATALYSTS FOR THE SIMULTANEOUS REMOVAL OF NO_X AND o-DCB.

The results of Section 3.1 have revealed the effect of preparation method on structural properties and catalytic activity. Bulk catalysts, those prepared by sol-gel and co-precipitation, have showed the best catalytic performance in NH_3-SCR and o-DCB oxidation. This fact has been associated to the higher interaction between Mn and Ce, which not only occurs on the catalytic surface, as in supported catalysts, but also in the bulk.

In addition to the preparation method, the concentration of active metals, that is, Mn and Ce, is a key factor reported in the literature to affect the catalytic activity in SCR and catalytic oxidation reactions. In this sense, molar Mn concentrations below 50% have been reported to lead to high NO conversion at low temperature [71], although there are no works that evaluate high Mn containing catalyst for SCR. In the case of catalytic oxidation reactions, Mn molar concentrations higher than those of Ce are reported to promote high activity in VOCs, trichloroethylene and chlorobenzene oxidations [96, 97]. It should be noted these references have the handicap of operating independently, so the effect of SCR in catalytic oxidation reaction and vice versa is not taken into account.

The aim of this section is to assess the effect of Mn and Ce content in bulk catalysts prepared by sol-gel and co-precipitation, on the simultaneous removal of NO_X and o-DCB. For this purpose, three bimetallic compositions have been selected, one rich in Ce (15%mol Mn and 85%mol Ce, named 15Mn85Ce), a second one with

equimolar concentration of both metals (50%mol Mn and 50%mol Ce, named 50Mn50Ce) and the third one rich in Mn (85%mol Mn and 15%mol Ce, named 85Mn15Ce). Moreover, in order to facilitate the analysis and discussion, characterization and activity results of pure oxides (CeO_2 and MnO_X) have also been studied. Each sample, including even the pure oxides, have been prepared by both methods. Thereby two families of bulk catalysts, each consisting of 5 samples, will be studied.

3.2.1. Characterization of MnO_X-CeO_2 with different composition.

3.2.1.1. Structural and textural properties.

The influence of manganese and cerium contents in the samples was firstly investigated by XRD. Figure 3.10A and 3.10B show the diffraction patterns of the catalysts prepared by sol-gel and co-precipitation, respectively. Both pure cerium oxides exhibit diffraction peaks characteristic of fluorite cubic structure, already described in the previous section. In the same way, the pure manganese oxides prepared by these two methods also show the same crystalline phase, α-Mn_2O_3. Therefore, from a structural view, similar pure oxides are synthesised independently of the preparation method. However, this postulate will be further verified by other characterization techniques.

Regarding bimetallic samples, similar results are obtained by increasing Mn content, which leads to broadening of the fluorite peaks. Moreover, a slight shift to higher Bragg angles of the most intense fluorite peak is promoted with Mn, but it is only clearly observed in the catalysts prepared by sol-gel, as can be seen in the inset graphs of Figure 3.10. However, at high Mn content, in the 85Mn15Ce catalysts, different results are observed depending on the preparation method. Sol-gel method leads to an amorphous sample with tiny diffraction peaks located at 28.8 and 37.4^o and associated to MnO_2 (ICDD, 00-050-0866). On the other hand, co-precipitation method promotes the coexistence of two different crystal phases, evidenced by the appearance of new diffraction peaks at 33.2 and 38.5^o (associated to Mn_2O_3) together with those already present at lower Mn contents, that belong to fluorite phase.

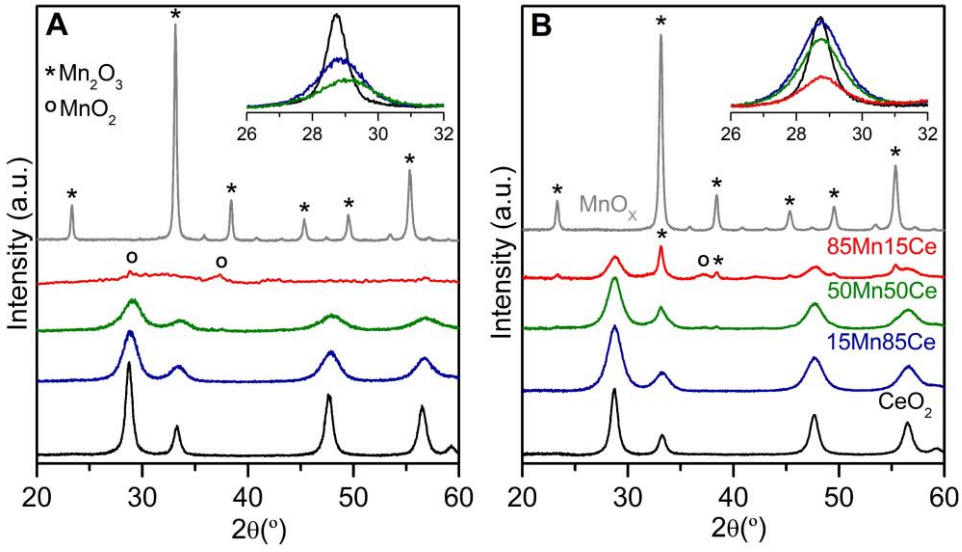

Figure 3.10. XRD patterns of MnO_X-CeO_2 catalysts with different Mn and Ce content prepared by A) Sol-gel and B) Co-precipitation. Inset figures: Zoom of 2θ region between 26-32º.

The broadening and shift of CeO_2 diffraction peaks has already been used as evidence for the formation of the mixed oxide phase, as a consequence of the distortion caused by manganese insertion into fluorite structure. In this sense, Figure 3.11 summarizes the lattice parameter of fluorite structure of the catalysts. The increase of Mn content clearly leads to a decrease of lattice parameter in the catalysts prepared by both methods, although it is more remarkable in those prepared by sol-gel. This result corroborates the formation of a solid solution in all catalysts and suggests a larger distortion of fluorite structure in those prepared by sol-gel, probably caused by a greater manganese incorporation.

In the case of the 85Mn15Ce catalyst, a higher value of lattice parameter has been calculated in the catalyst prepared by co-precipitation, which breaks the downward trend. This result indicates that high Mn contents favour the segregation of MnO_X because of the saturation of fluorite structure, which is in accordance with the Mn_2O_3 diffraction peaks obtained for this catalyst in Figure 3.10. A similar result was observed by Ye and Xu [150], who reported that the amount of Mn species entering the fluorite lattice is limited to 0.7 molar ratio. On the other hand, the

lattice parameter of 85Mn15Ce catalyst prepared by sol-gel could not be calculated due to the disappearance of that crystal phase.

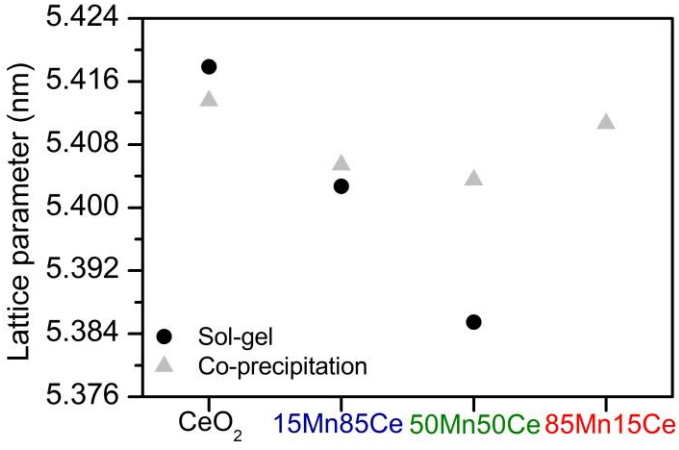

Figure 3.11. Lattice parameter of fluorite phase from XRD data.

The fluorite crystal sizes, estimated by Scherrer equation applied to (111) plane, of the samples with different Mn content are summarized in Table 3.5. The decrease of fluorite crystal phase at higher Mn contents evidences the structural defects associated to Mn incorporation to cerionite structure, which is further evidence of solid solution.

Table 3.5. Crystal size of MnO_X-CeO_2 catalysts with different Mn and Ce content.

Sample	Fluorite crystal size (nm)	
	Sol-gel	Co-precipitation
CeO_2	9	9
15Mn85Ce	4	5
50Mn50Ce	3	4
85Mn15Ce	--	4
MnO_X	--	--

Raman spectroscopy was used to supply further information about the effect of Mn and Ce contents on structural properties. Figure 3.12A and 3.12B show the Raman spectra of samples prepared by sol-gel and co-precipitation, respectively. Both pure cerium oxides exhibit the typical F_{2g} mode of fluorite structure, around 463 cm^{-1}. On the other hand, the Raman peaks of both manganese oxides are associated to Mn_2O_3. In bimetallic catalysts, the increase of Mn content causes a decrease in the intensity and a slight shift of F_{2g} band to lower wavenumber on the catalysts prepared both by sol-gel and co-precipitation. XRD technique only allowed these shifts to be evidenced in the catalysts prepared by sol-gel. Thus, Raman technique has successfully supplemented the XRD results.

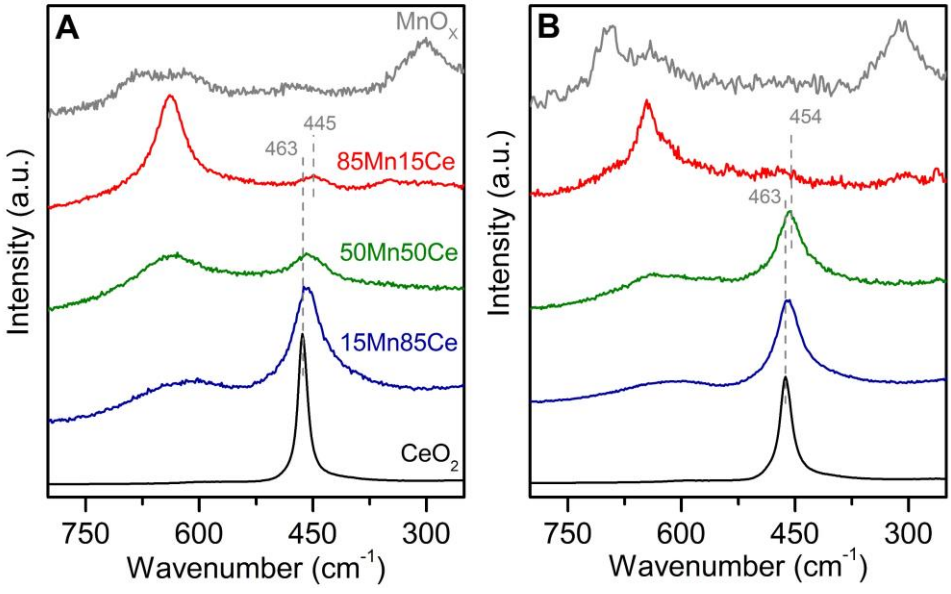

Figure 3.12. Raman spectra of MnO_X-CeO_2 catalysts with different Mn and Ce content prepared by A) Sol-gel and B) Co-precipitation.

As previously discussed, the F_{2g} vibration mode is very sensitive to Ce environment [142], so the changes on its position reveal modification of Ce-O bonding symmetry due to Mn incorporation to cerium oxide. Nonetheless, the F_{2g} shift is more remarkable in the catalysts prepared by sol-gel. This fact highlights the higher distortion degree of fluorite structure in the catalysts prepared by sol-gel when manganese is incorporated. This result agrees with the lower lattice parameter of

catalysts prepared by sol-gel (Table 3.5). Furthermore, the increase in Mn content promotes the appearance of the band located around 600 cm^{-1}, that is associated to oxygen vacancies [151], as a consequence of the structural defects caused by the incorporation and good dispersion of Mn into the CeO_2 lattice.

High Mn content, 85Mn15Ce sample, produces a notable decrease of the F_{2g} band, which practically vanishes. Moreover, an additional peak appears around 640 cm^{-1}, which overlaps with the band associated to oxygen vacancies. This band, also observed in pure MnO_X sample, increases its intensity with Mn content and is related to the formation of MnO_X crystals segregated from fluorite structure.

In order to obtain more structural information to support the XRD results at high Mn concentrations, skeletal FTIR technique has been performed (DICCA, University of Genova). Figure 3.13A and 3.13B show the skeletal FTIR spectra of samples with different Mn and Ce content and prepared by sol-gel and co-precipitation, respectively.

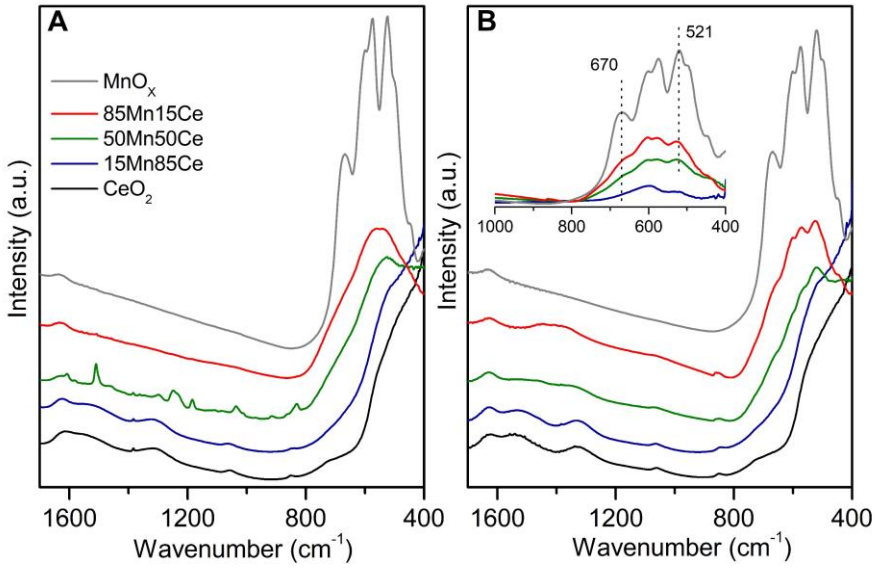

Figure 3.13. Skeletal FTIR spectra of MnO_X-CeO_2 catalysts with different Mn and Ce content prepared by A) Sol-gel and B) Co-precipitation. Inset figure: Subtraction of CeO_2 spectrum in bimetallic samples.

Pure cerium oxides show two broad bands at approximately 700 and 550 cm^{-1}. The latter is associated to the longitudinal optical mode of fluorite structure. At wavenumbers below 500 cm^{-1}, the absorbance profile continuously increases because of the contribution of transverse mode of fluorite structure, reported to be located at 360 cm^{-1} [151]. Other weak bands are also observed at 1060 and 850 cm^{-1} and have been related to vibrations of Ce-O bonds [152, 153]. Additional bands appear at higher wavenumbers related to adsorbed surface species. The band located at 1626 cm^{-1} is associated to stretching vibration of molecularly adsorbed water [152] and the bands located at 1538 and 1327 cm^{-1} are associated to surface carbonates likely formed by reactive adsorption of CO_2 from air over the basic surface sites of CeO_2. Moreover, the cerium oxide prepared by sol-gel exhibits a tiny additional peak at 1380 cm^{-1} related to nitrates not removed in the calcination. On the other hand, similar spectra have been observed for the samples composed by only manganese oxide, with peaks at 670, 600, 571, 500, 524 and 450 cm^{-1} that correspond to the vibrational modes of α-Mn_2O_3 [141]. These results indicate high structural similarities between pure cerium oxides prepared by sol-gel and co-precipitation. The same occurs with the pure manganese oxides prepared with these methods, as observed by XRD.

The increase of Mn content in bimetallic samples promotes a better definition in the shoulder located around 550 cm^{-1} and the slope of the absorbance profile at lower wavenumber decreases almost to a plateau in the 50Mn50Ce catalyst. This can be due to the growth of another contribution in this range, related to the addition of Mn and parallel to the decreasing in cerium oxide content, which leads to the detection of an isosbestic point around 450-430 cm^{-1}. Similar results were observed by Escribano and co-workers [151] in Ce-Zr mixed oxides. Additional bands can be observed only in the 50Mn50Ce catalyst prepared by sol-gel at 1300, 1250, 1200 and 1180 cm^{-1}, which could be associated to residual organic compounds present in the catalyst, since citric acid was used as chelating agent in order to promote the formation of the gel during the synthesis.

The differences observed between low Mn content catalyst spectra with respect to pure cerium oxide are related to a decrease of Ce-O bonds and the modification of the atoms belonging to the original structure of cerium oxide, as a consequence of the high interaction between Mn and Ce. This fact supports the formation of solid solution phase, above evidenced by Raman and XRD.

The increase in Mn content to 85% promotes the appearance of the peaks associated to MnO_X in the range of 800-500 cm^{-1}, although with different degrees of definition. Comparison between the 85Mn15Ce spectra reveals a higher definition of the peaks previously associated to Mn_2O_3 in the spectrum of the catalyst prepared by co-precipitation. Thus, this result highlights that co-precipitation method favours structure order, that leads to an increase of crystallinity of MnO_X phase. This fact is in accordance with XRD results, where a co-existence between fluorite and Mn_2O_3 crystal phase was observed in the catalyst prepared by co-precipitation, unlike the one prepared by sol-gel which resulted in a completely amorphous structure.

Despite the high degree of crystallinity of the Mn_2O_3 phase in the catalysts prepared by co-precipitation, some differences are observed in comparison to pure MnO_X, especially in the 700-450 cm^{-1} region, where, for example, the peak located at 670 cm^{-1} is not well defined in the bimetallic catalyst. This fact could be associated to the modification of Mn_2O_3 vibrational modes due to the interaction with Ce. In order to evidence such differences in the Mn bands of bimetallic catalysts, the subtraction spectra obtained by subtracting pure ceria spectrum from those of bimetallic co-precipitation catalysts was analysed. The results are shown in the inset graph of Figure 3.13B. The subtracted spectra reveal no new peaks, although it evidences that the complex envelop of peaks in the range 800-500 cm^{-1} does not completely correspond, in shape and intensity, to the spectrum associated to pure Mn_2O_3, even in the catalyst with the highest Mn content. Moreover, it has been detected a shift of two peaks related to manganese oxide vibrational modes from 670 and 521 cm^{-1} in pure manganese oxide sample to 660 and 526 cm^{-1} in bimetallic samples. These observations suggest that the presence of cerium affects Mn-O vibrational modes, probably associated to the presence of Ce-O-Mn structure. These results support those observed by XRD for co-precipitated 85Mn15Ce catalyst, where a coexistence of strongly deteriorated fluorite crystal phase was evidenced together with Mn_2O_3 crystal phase.

The effect of metal composition on morphological properties was evaluated by N_2-physisorption. All samples show type IV isotherms (not shown to avoid repetition) according to IUPAC classification, belonging to the group of mesoporous materials.

Table 3.6 summarizes specific surface area, pore volume and mean pore diameter of the catalysts. All bimetallic samples exhibit higher BET surface area and larger

pore volume than the respective pure oxides, so the interaction between Mn and Ce clearly improves textural properties. In addition, the increase of Mn content leads to higher BET surface area, but only up to reach a maximum located at 50% Mn (sol-gel series) or 85% Mn (co-precipitation series). It should be noted that co-precipitation method provides higher BET surface area in comparison to sol-gel, regardless of Mn and Ce content.

Table 3.6. Textural properties of MnO_X-CeO_2 catalysts with different Mn and Ce content.

Sample	Sol-gel			Co-precipitation		
	S_{BET} (m^2/g)	V_P (cm^3/g)	d_P (nm)	S_{BET} (m^2/g)	V_P (cm^3/g)	d_P (nm)
CeO_2	60	0.11	6.2	80	0.12	6.3
15Mn85Ce	67	0.14	7.2	84	0.18	7.8
50Mn50Ce	63	0.16	8.5	88	0.21	8.0
85Mn15Ce	57	0.15	8.0	87	0.25	9.0
MnO_X	15	0.10	23.8	34	0.17	16.6

Pore volume and mean pore diameter (Table 3.6) follow a similar trend: the higher the Mn content, the larger the pore volume and the mean diameter, except for the 85Mn15Ce catalyst prepared by sol-gel. For a detailed analysis, Figure 3.14A and 3.14B show the pore distribution of sol-gel and co-precipitation catalysts, respectively. Apparently, both pore distribution of sol-gel and coprecipitated catalysts show a well-defined peak around 4 nm. However, according to Section 3.1, this pore size is not representative of textural properties of the samples and only appears in the pore distribution as a consequence of tensile effect strength.

Up to equimolar composition, the increase of Mn content shifts the pore distribution to larger diameters. However, at high Mn content (85Mn15Ce) a different trend is observed depending on preparation method. In sol-gel, the pore distribution shifts down to 6 nm, whereas in those prepared by co-precipitation a bimodal distribution is promoted, with pore diameters of 6.5 and 20 nm. The different results for these catalysts could be associated to the differences observed at structural level. In the catalysts prepared by co-precipitation, the bimodal distribution could be related with the two different crystal structures, the lower

pore diameter peak corresponding with the manganese oxide phase since it is promoted at higher Mn content. In sol-gel catalysts, an amorphous structure was evidenced, which would be in accordance with the single peak observed on its distribution.

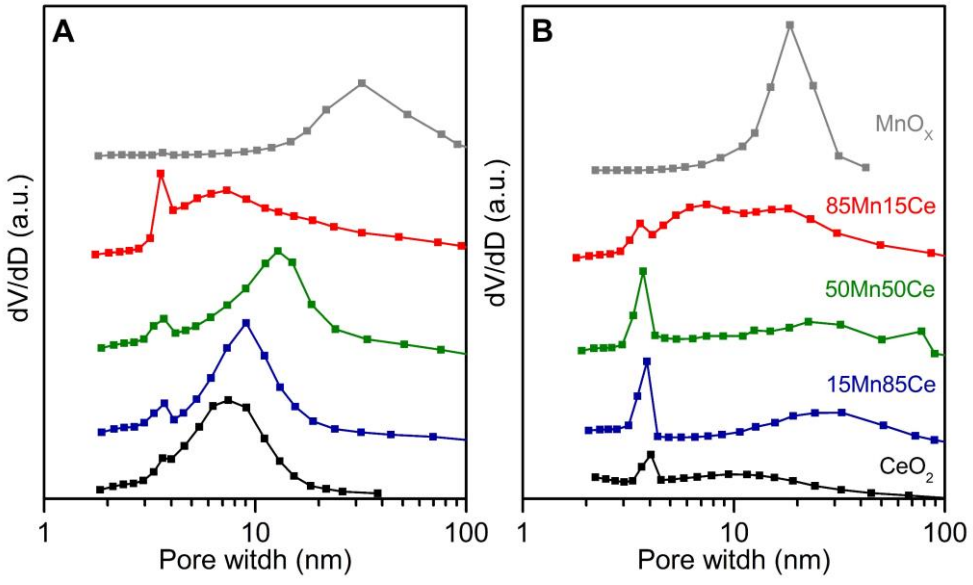

Figure 3.14. Pore size distribution of MnO_X-CeO_2 catalysts with different Mn and Ce content prepared by A) Sol-gel and B) Co-precipitation.

The analysis of Mn and Ce content on catalysts prepared by sol-gel and co-precipitation and the effect of the interaction between both metals on surface composition has been analysed by XPS. All binding energies are referenced to elemental carbon (C 1s) spectrum at 284.5 eV.

Figure 3.15A and 3.15B show the O 1s spectra of the samples prepared by sol-gel and co-precipitation. The spectra have been mainly deconvolved in two peaks associated to different surface oxygen [138, 146]. The peak around 529.5 eV is attributed to lattice oxygen (O^{I}) and that located around 531.2 eV is related to surface oxygen (O^{II}). An additional contribution, which corresponds to molecular water and carbonate species (O^{III}), around 533.2 eV, has been used in some samples. These species were evidenced by skeletal FTIR analysis, especially in the catalysts with high Ce contents (CeO_2 and 15Mn85Ce), which is consistent with the

notable presence of this contribution in these catalysts. All samples exhibit similar spectrum profiles, the contribution of lattice oxygen being the most prominent, while the contribution associated to adsorbed oxygen appears as a broad shoulder. In both sol-gel and co-precipitation catalysts, the presence of either low or high Mn content causes a shift in the whole spectra towards lower binding energies. This fact is due to high interaction between Mn and Ce, as a consequence of solid solution formation at the catalytic surface [154].

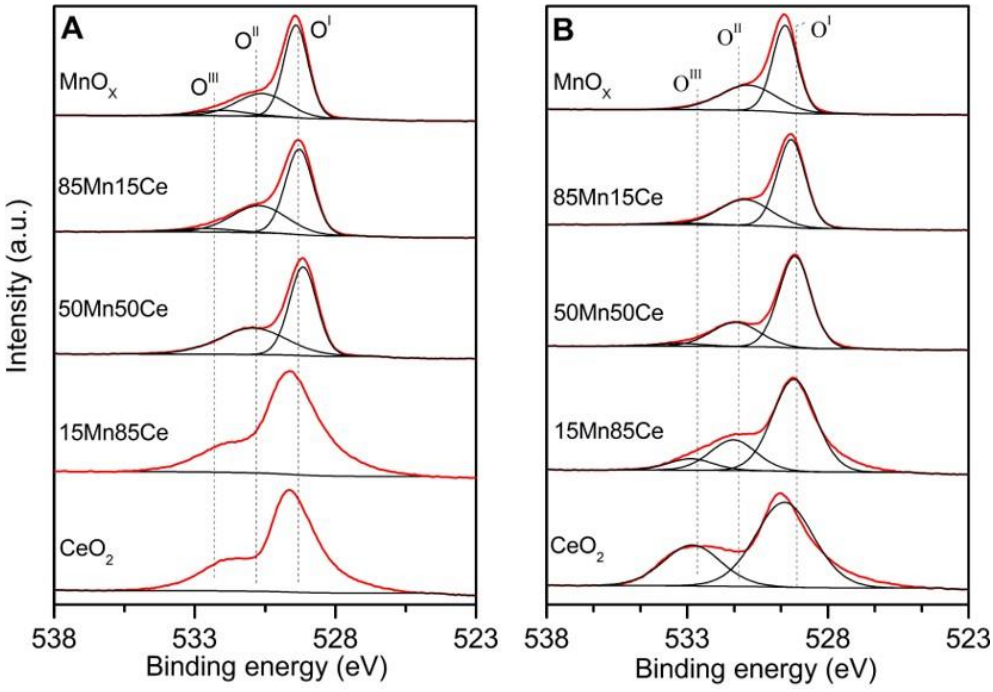

Figure 3.15. O 1s spectra of MnO_X-CeO_2 catalysts with different Mn and Ce content prepared by A) Sol-gel and B) Co-precipitation.

On the other hand, Figure 3.16A and 3.16B show the fitted XPS spectra of Mn 2p of the catalysts prepared by sol-gel and co-precipitation, respectively. The Mn 2p spectrum has two spin-orbit doublets, Mn 2p 3/2 and Mn 2 1/2, which were fitted using three contributions located at 641.1, 642.3 and 644.6 eV for pure manganese oxide samples, attributed to Mn^{3+}, Mn^{4+}, and the shake-up satellite of Mn^{3+} species, respectively [155, 156]. The increase in Mn content leads to the appearance of a tiny shoulder, more noticeable in the Mn 2p 3/2 around 640 eV. Surface Mn^{4+}/Mn^{3+}

ratios were calculated by integration of both spin-orbit doublets for each species and are reported in Table 3.7. The increase of Mn content clearly promotes the presence of surface Mn^{4+} species in the bimetallic catalysts prepared by sol-gel. Similar trend is obtained in the catalysts prepared by co-precipitation, but only up to the 50Mn50Ce catalyst. Thus, higher Mn contents decrease the Mn^{4+}/Mn^{3+} ratio, evidencing a greater presence of surface Mn^{3+} species than at low Mn contents.

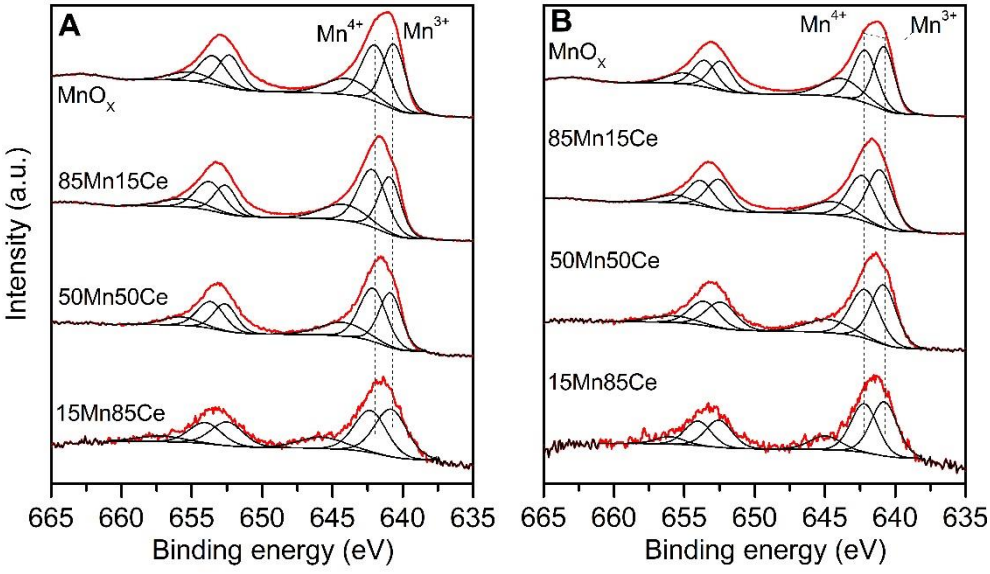

Figure 3.16. Mn 2p spectra of MnO_X-CeO_2 catalysts with different Mn and Ce content prepared by A) Sol-gel and B) Co-precipitation.

Table 3.7. XPS results of MnO_X-CeO_2 catalysts with different Mn and Ce content.

Sample	Mn^{4+}/Mn^{3+}		Ce^{3+}/Ce^{4+}	
	Sol-gel	Co-precipitation	Sol-gel	Co-precipitation
CeO_2	-	-		
15Mn85Ce	0.87	0.90	0.23	0.17
50Mn50Ce	1.16	0.93	0.22	0.18
85Mn15Ce	1.29	0.87	0.20	0.16
MnO_X	1.04	1.00	-	-

Even though active metals content has been proven to affect the presence of surface Mn species, it should be noted that the Mn^{4+}/Mn^{3+} ratios are always close to one. Therefore, the presence of both Mn^{4+} and Mn^{3+} species in the catalytic surface is corroborated.

The Ce 3d spectra of the catalysts prepared by sol-gel and co-precipitation are shown in Figure 3.17A and 3.17B, respectively. Ce 3d spectrum has two spin-orbit 3/2 and 5/2, although in this study the Ce 3d 5/2 was the only one analysed, because of the overlapping of Ce lines with Auger Mn line at high Mn contents. Ce 3d 5/2 spectrum was fitted with five peaks with V notation. According to literature, V, V^{II} and V^{III} are associated to Ce^{4+}, and V^0 and V^I are associated to Ce^{3+} [157, 158].

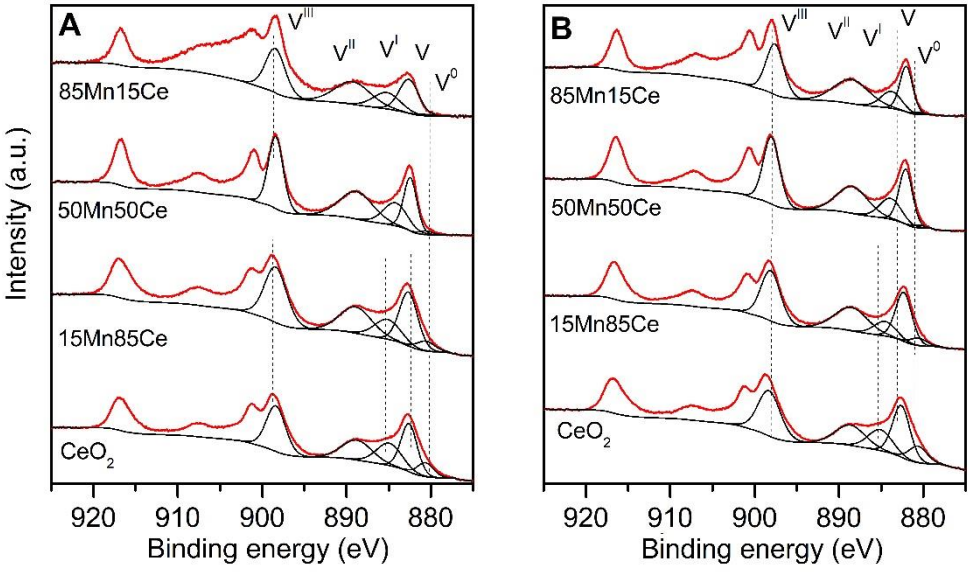

Figure 3.17. Ce 3d spectra of MnO_x-CeO_2 catalysts with different Mn and Ce content prepared by A) Sol-gel and B) Co-precipitation.

Independently of metal content and preparation method, all samples exhibit the clear presence of Ce^{4+} and Ce^{3+} on the surface. The Ce^{3+}/Ce^{4+} ratios, summarized in Table 3.7, were calculated by means of the integration of the contributions used for fitting the spectra. The results corroborate that Ce^{4+} is the main oxidation state. Moreover, in the sol-gel catalysts, the higher the Mn content, the lower the surface

Ce^{+3}. In the co-precipitated catalysts, as it was the case with the ratio of surface manganese, low Mn content (up to 50Mn50Ce catalyst) increases the presence of surface Ce^{3+} species, while further increase has a detrimental effect, decreasing the Ce^{3+}/Ce^{4+} ratio.

The relative surface Ce^{3+} concentration is reported in the literature as an important indicator for structural defects in ceria-based catalysts [139, 159]. In this sense, the direct relationships observed for Mn^{4+}/Mn^{3+} and Ce^{3+}/Ce^{4+} ratios in the co-precipitated catalysts suggests that the increase in surface content of Mn^{4+} species could be linked to the increase in surface defects. This fact will be discussed below together with the analysis of redox properties, in order to verify whether it also occurs in the bulk structure of the catalysts.

In order to have a deep insight of elemental composition on the catalytic surface, the bimetallic samples with the lowest and highest Mn contents, 15Mn85Ce and 85Mn15Ce, were analysed by transmission electron microscopy high-angle annular dark field (STEM-HAADF). Additionally, X-EDS elemental maps were obtained for the samples.

Figure 3.18 shows the HAADF images and the resulting maps corresponding to cerium (green) and manganese (red). Moreover, EDX spectra of certain specific areas of each sample are also provided. The 15Mn85Ce catalysts prepared by both sol-gel and co-precipitation exhibit a good dispersion of Mn and Ce. The presence of Mn and Ce is clearly evidenced by the EDX spectra. Obviously, the peaks associated to Ce are much more intense than those of Mn, due to the low content of the latter. The good dispersion of the active metals suggests that both share a common mixed oxide structure. This result supports those obtained in the structural analysis, that indicate Mn enters fluorite structure of cerium oxide at low Mn contents.

However, in the catalysts with high Mn content, a clear phase segregation is promoted. In the catalyst prepared by sol-gel, two different areas are observed in the metal distribution maps, one with the presence of both metals (Area A) and another one only composed of Mn (Area B). The spectrum of Area A corroborates the presence of both Mn and Ce, although unlike previously observed in the 15Mn85Ce catalysts, Mn is the major metal component. In the Area B, the spectrum corroborates the presence of only Mn, which confirms the presence of manganese oxide aggregates in the catalytic structure. The manganese oxide aggregate

corresponding to Area B has a size around 40 nm. However, the absence of crystallinity in the manganese oxide phase was concluded by XRD, so manganese aggregated in the 85Mn15Ce prepared by sol-gel should have an amorphous structure or be composed of small crystal domains with size in the nanometre range.

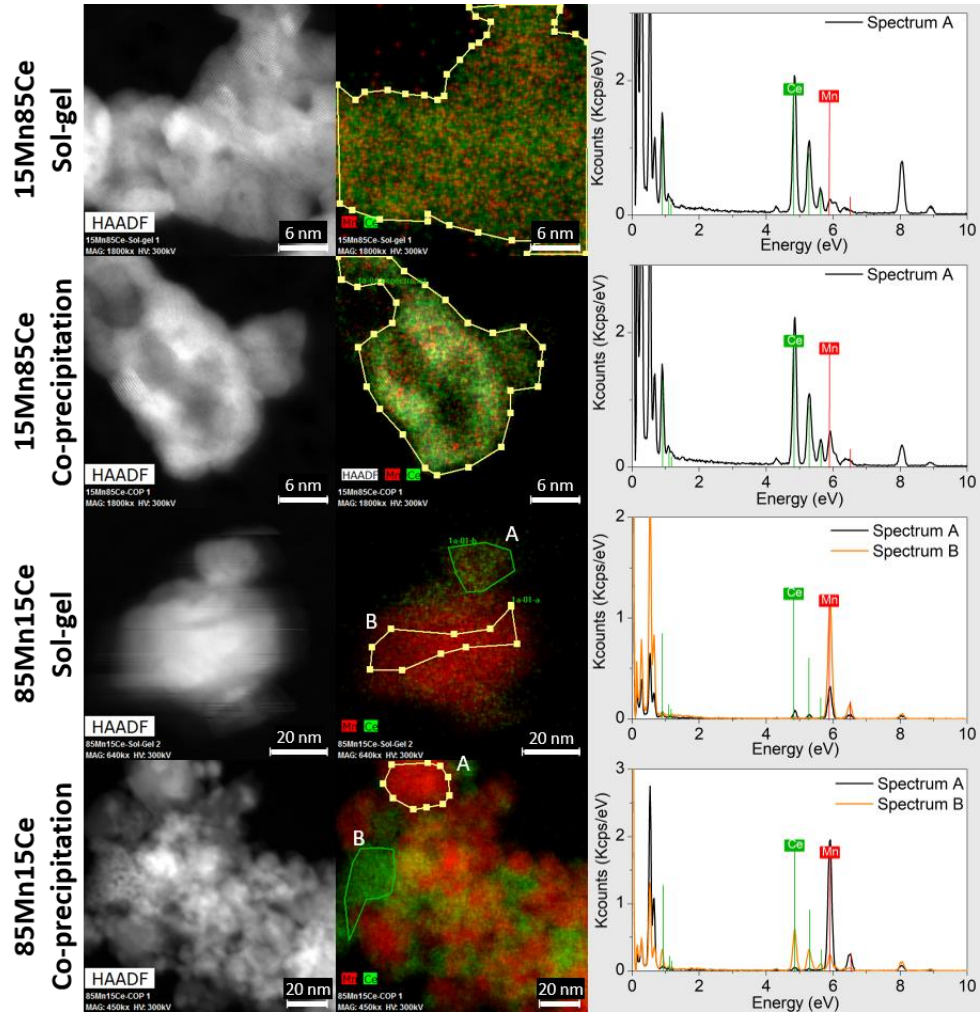

Figure 3.18. STEM-HAADF images and EDX maps of selected MnO_X-CeO_2 catalysts with different Mn and Ce content. Red (Mn) and green (Ce).

On the other hand, in the 85Mn15Ce catalyst prepared by co-precipitation, the elemental map shows the presence of several areas with different interaction between Mn and Ce, as a consequence of the different segregation degree of Mn in the catalytic structure. Thus, the spectrum of Area A reveals the presence of only Mn, that is, manganese oxide completely segregated, whereas the spectrum of Area B denotes a major content of Ce, although Mn is also present. A further view out of the areas marked in the maps (there are no spectra of this region) evidences the different interaction degree of Mn and Ce within the same catalytic particle. This wide variety on the metal interaction degree, which has not been observed in the catalysts prepared by sol-gel, may favour the formation of metal with the same nature but with different oxidation state, beneficial for catalytic performance.

The samples with the lowest and the highest Mn content, 15Mn85Ce and 85Mn15Ce, were analysed by HRTEM as well. Figure 3.19 shows the selected HRTEM images for those catalysts. Both 15Mn85Ce catalysts and the 85Mn15Ce catalyst prepared by co-precipitation display a clear structural order. It can be observed the lattice fringe with interplanar spacing around 0.312 nm associated to {111} of fluorite phase. Interestingly, the presence of fluorite phase was identified by XRD in these catalysts. On the other hand, the image of 85Mn15Ce catalyst prepared by sol-gel shows no structural order, which is in line with its amorphous structure observed by XRD.

It should be noted that fluorite phase is characteristic of both pure cerium oxide and cerium oxide with Mn inserted in its structure. The presence of fluorite phase in the co-precipitated catalyst with the highest Mn concentration suggests the presence of a fluorite structure strongly deteriorated by the high degree of insertion of Mn. This fact is in accordance with the elemental maps for the co-precipitated 85Mn15Ce catalyst, where both cerium oxide and cerium oxide with a high interaction degree with Mn was evidenced.

However, no lattice fringes related to manganese oxide crystal phases have been identified in either low or high Mn content catalysts, even though Mn_2O_3 as bixbyite crystal phase was detected in 85Mn15Ce prepared by co-precipitation.

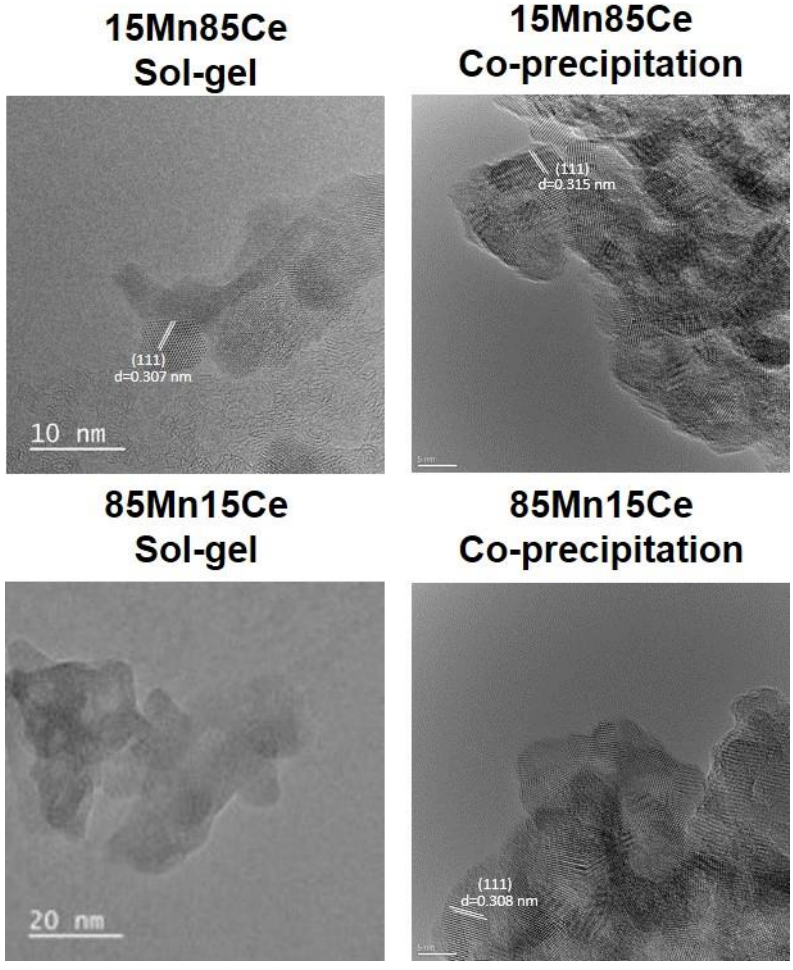

Figure 3.19. HRTEM images of selected MnO_X-CeO_2 catalysts with different Mn and Ce content.

3.2.1.2 Redox and acid properties.

H_2-TPR was used in order to investigate the redox properties of the catalysts with different content of Mn and Ce. Figure 3.20A and 3.20B show the reduction profiles of the samples prepared by sol-gel and co-precipitation, respectively. In this section, unlike Section 3.1.1.2, the reduction profiles have been presented without

the isothermal stage at 950 °C. However, this stage was performed to ensure the total reduction of bulk cerium oxide.

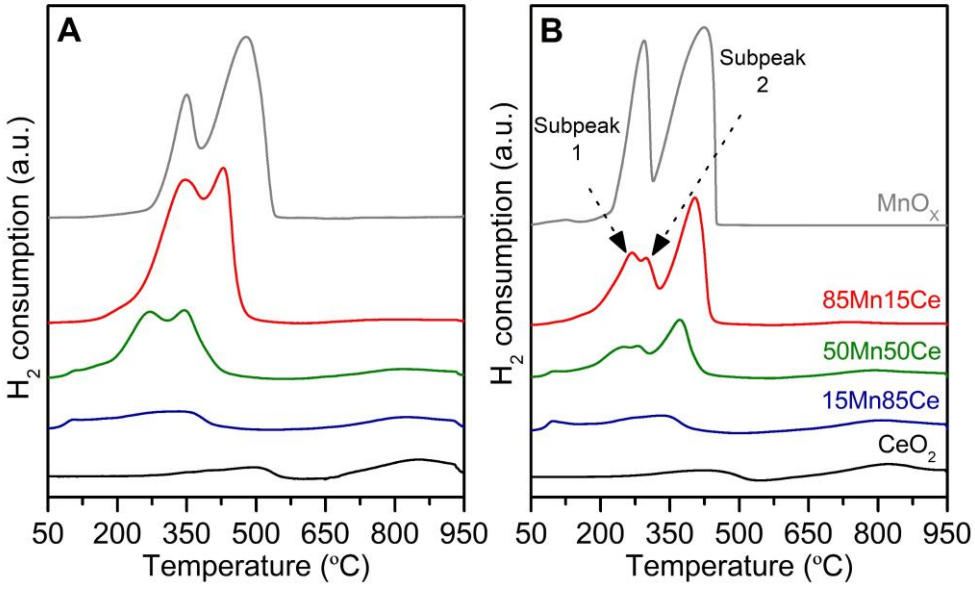

Figure 3.20. H_2-TPR profiles of MnO_X-CeO_2 catalysts with different Mn and Ce content prepared by A) Sol-gel and B) Co-precipitation.

Pure cerium oxides exhibit two reduction peaks. The one located around 450 °C has been previously associated to surface cerium oxide reduction and that located above 800 °C is related to bulk cerium oxide reduction. On the other hand, similar reduction profiles are exhibited by both pure manganese oxides, with two peaks around 300 and 450 °C fitting well with the Mn_2O_3 reduction profile. This result agrees with XRD and FTIR results, where Mn_2O_3 was the only crystal phase identified for the pure manganese oxide. As it was proposed before, the first peak corresponds to the reduction of Mn_2O_3 to Mn_3O_4 and the second to the reduction of Mn_3O_4 to MnO. It should be noted that the reduction temperature of pure oxides prepared by co-precipitation is lower than that of those prepared by sol-gel, so co-precipitation method seems to provide better redox properties.

All TPR profiles of bimetallic samples exhibit H_2 consumption at low and high temperature with few differences in comparison to pure oxides. Low Mn content samples, that is, 15Mn85Ce catalysts, shifts to lower temperatures the reduction of

surface cerium oxide, which suggests an improvement of redox properties due to the increase of oxygen vacancies, generated by structural defects caused by the high interaction between Mn and Ce. Moreover, an additional peak associated to highly dispersed surface Mn species [95] and a broad shoulder related to isolated Mn ion embedded into CeO_2 lattice [145] appear at 100 and 273 ^oC, respectively.

The further increase of Mn content leads to the appearance of two strong reduction peaks in the temperature range of 200-500 ^oC, which are mainly associated to Mn reduction. The reduction of surface cerium oxide is also present in this temperature range, although it is difficult to distinguish. H_2 uptake related to Mn takes place at lower temperatures in the catalysts prepared by co-precipitation, as it occurs with the pure oxides. Many authors report that H_2 consumption located at low temperature (around 300 ^oC) is related to the reduction from MnO_2/Mn_2O_3 to Mn_3O_4, and the H_2 consumption at intermediate temperature (around 400 ^oC) is related to the reduction from Mn_3O_4 to MnO and surface oxygen of cerium oxide [74, 146, 147].

However, there is a difference in the first reduction peak of the 85Mn15Ce catalyst, since it splits into two smaller subpeaks strongly overlapped in the catalyst prepared by co-precipitation, while in the one prepared by sol-gel the peak splitting is not observed. As mentioned above, the first reduction peak is associated with the reduction of Mn with high oxidation state, either Mn^{4+} or Mn^{3+}. These two reduction subpeaks could suggest the reduction of Mn with high oxidation state in different environments: on the one hand, the reduction of Mn with strong interaction with Ce or embedded into cerium oxide lattice and, on the other hand, the reduction of MnO_X crystals. Both phases have been only evidenced in the structural analysis of co-precipitated catalyst (as a highly Mn-substituted fluorite phase and the M_2O_3).

It should be noted that Mn in high interaction degree with Ce should be more easily reduced due to the high oxygen mobility provided by Ce. Therefore, this first subpeak located around 260 ^oC has been proposed to be the reduction of Mn into the CeO_2 lattice or with high interaction with Ce, whereas the second subpeak around 300 ^oC is associated to the reduction of Mn_2O_3 crystal phase.

Table 3.8 summarizes the total H_2 consumption and the average oxidation state of Mn in the samples. The latter has been estimated according to that commented in Section 3.1.1.2. The Mn oxidation state in the catalysts prepared by sol-gel is close

to Mn^{4+}, so these species are clearly promoted by this preparation method. On the contrary, the oxidation state in the catalysts prepared by co-precipitation ranges between Mn^{4+} and Mn^{3+} and decreases at high Mn content, which clearly evidences that it is related to the segregation degree of Mn. Thus, Mn^{4+} is promoted at low Mn concentration, where the interaction between Mn and Ce is strong, whereas high Mn concentrations lead to Mn^{3+} because of the promotion of Mn_2O_3 crystal phase.

Table 3.8. Results of H_2-TPR analysis.

Catalyst	Sol-gel		Co-precipitation	
	H_2 consumption (mmol H_2/g)	**Mn oxidation state**	**H_2 consumption (mmol H_2/g)**	**Mn oxidation state**
CeO_2	1.7	--	1.3	--
15Mn85Ce	2.1	4.3	1.7	4.1
50Mn50Ce	4.1	3.9	3.1	3.5
85Mn15Ce	7.6	3.9	5.3	3.3
MnO_X	8.0	3.3	6.6	3.1

The influence of Mn and Ce content in acid properties was studied by NH_3-TPD and FTIR of adsorbed pyridine. FTIR technique was carried out at DICCA department of University of Genova. Quantitative results of NH_3-TPD calculated by time-integration of TCD signal of desorbed species are summarized in Table 3.9.

Table 3.9. Results of NH_3-TPD.

Catalyst	Acidity (µmol NH_3/g)			
	Sol-gel		Co-precipitation	
	Strong/weak	Total	Strong/weak	Total
CeO_2	1.1	129.1	1.1	204.1
15Mn85Ce	2.9	214.5	1.7	241.3
50Mn50Ce	1.6	200.7	2.0	304.5
85Mn15Ce	0.7	163.8	1.3	299.4
MnO_X	1.1	81.5	1.1	171.0

Acidic properties are notably enhanced by the interaction between Mn and Ce, because total acidity of bimetallic samples is higher than that of their respective pure oxides. The increase of Mn content produces an increase in total acidity, reaching the maximum in the 15Mn85Ce catalyst of the sol-gel family and in the 50Mn50Ce of the co-precipitation. Furthermore, it should be noted that the values of total acidity are higher in co-precipitated catalysts.

NH_3-TPD was also performed to obtain information about acid strength. Figure 3.21A and 3.21B show the NH_3 desorption profiles of the catalysts prepared by sol-gel and co-precipitation, respectively. As mentioned above Section 3.1.1.2, both pure cerium oxides show a main NH_3 desorption zone associated to weak acidity (around 100 ^oC) and a shoulder between 150-250 ^oC, related to strong acidity. In the same way, similar NH_3 desorption profiles are observed for the pure manganese oxides, with two well-defined contributions of weak and strong acidity at 100 and 180 ^oC.

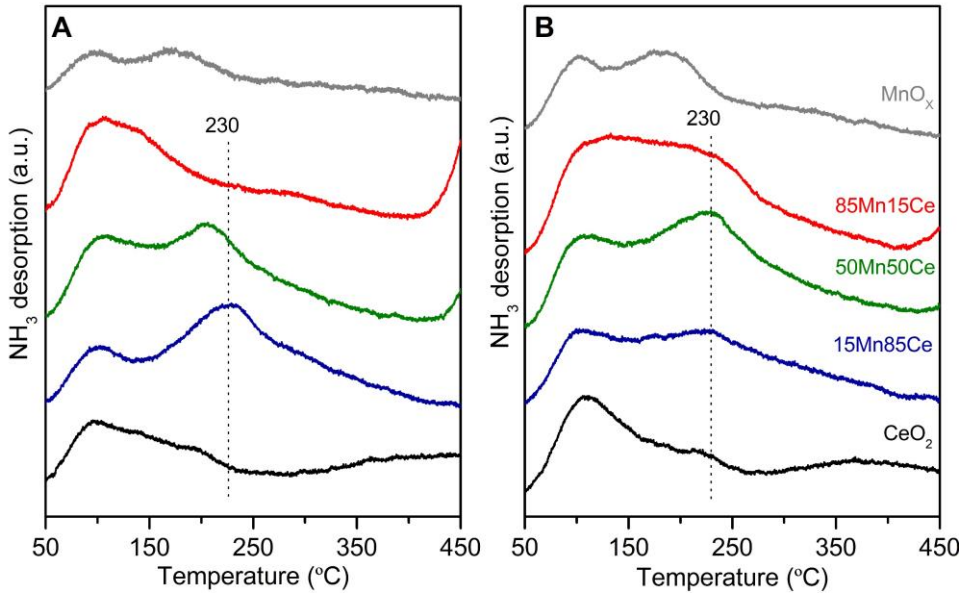

Figure 3.21. NH_3-TPD profiles of MnO_X-CeO_2 catalysts with different Mn and Ce content prepared by A) Sol-gel and B) Co-precipitation.

Regarding bimetallic catalysts, all of them clearly show the NH_3 desorption peak at 100 ^oC, which evidences the presence of weak acidity regardless of Mn and Ce

contents. However, the metal content does affect strong acidity. The increase in Mn content up to 50% promotes strong acid sites. The peak associated to this type of acidity in the bimetallic catalysts is located at higher temperature, around 230 ^{o}C, compared to pure oxides. So, this result evidences the generation of stronger acidic centres as a consequence of the interaction between Mn and Ce.

Strong acidity is negatively influenced by high Mn contents, i.e., 85Mn15Ce catalyst, its contribution disappearing in the catalyst prepared by sol-gel. Table 3.9 reports the ratio between strong and weak acidity, calculated taking into account the same considerations than in Section 3.1.1.2. As it can be seen, in co-precipitated catalysts, the ratio between strong and weak acidity increases with Mn content, although it starts to decrease coinciding with the drop in total acidity. This result suggests that the negative effect of Mn content on total acidity is probably linked to the different crystalline phases composing the co-precipitated catalyst with the highest Mn content (evidenced by the structural analysis), which in turn has a negative effect on strong acidity.

On the other hand, the FTIR analysis of adsorbed pyridine was conducted to obtain information about the nature of the acid sites. Pyridine may coordinate through its electronic lone pair over Lewis acid sites or subtracting the hydrogen atom from a surface OH group forming the pyridinium cation in Brønsted acid sites. This fact allows to distinguish between Lewis and Brønsted acidity. Moreover, pyridine may also weakly interact with surface OH groups through H-bonds, but not forming pyridinium cations [129].

According to the literature, the bands around 1632-1580 cm^{-1} and 1455-1438 cm^{-1} are attributed to ν_{8a} and ν_{19b} vibrational modes of coordinated pyridine over Lewis acid sites, whereas the bands around 1640 and 1540 cm^{-1} are related to ν_{8a} and ν_{19b} vibrational modes of pyridinium cation [160, 161]. Moreover, the shift of ν_{8a} vibrational mode is usually used to compare the strength of Lewis acid sites, so that the higher the wavenumber the stronger the interaction between pyridine and the Lewis acid site [131].

Figure 3.22A shows the FTIR spectra of surface species arising from pyridine adsorption over catalysts with different Mn and Ce contents prepared by co-precipitation and, at room temperature. Spectra of pyridine adsorbed over pure cerium and manganese oxides are also reported. All the catalysts show bands around 1600 and 1572 cm^{-1} associated to ν_{8a} vibrational mode; and around 1482

and 1440 cm^{-1} associated to ν_{19b} vibrational mode of coordinated pyridine over Lewis acid sites. There is no evidence of bands associated to pyridinium ion formation over Brønsted acid sites. It should be noted that the noise in the subtraction spectrum of 85Mn15Ce catalyst and the low intensity of bands in the spectrum of the 50Mn50Ce correspond to the presence of strong bands due to carbonate species in this region, as evidenced by the skeletal FTIR technique.

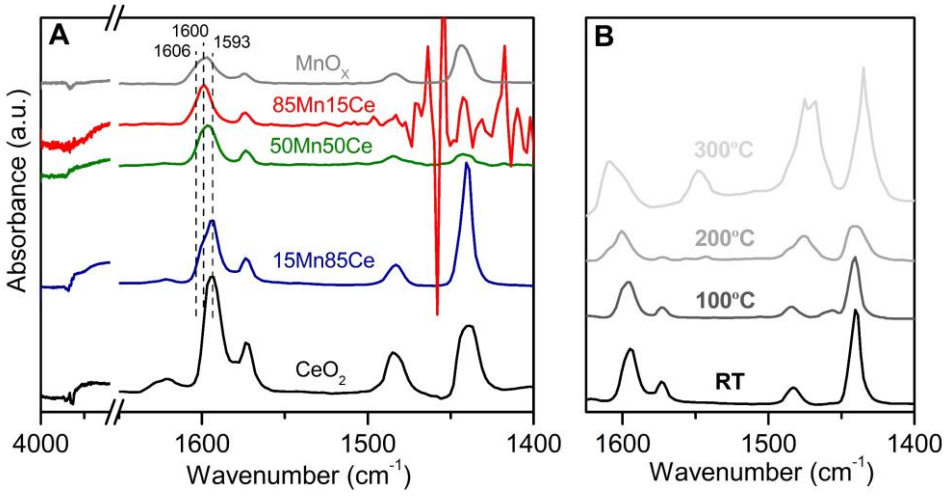

Figure 3.22. A) FTIR spectra from pyridine adsorption and evacuation at room temperature of MnO_X-CeO_2 catalysts with different Mn and Ce content prepared by co-precipitation. B) FTIR spectra of adsorbed species arising from pyridine interaction over 15Mn85Ce catalyst after outgassing at different temperatures.

There are significant differences regarding bands shape and position associated to ν_{8a} vibrational mode depending on Mn content. For pure cerium oxide, a well-defined peak is located at 1593 cm^{-1}, thus at only slightly lower frequency than those reported by Binet and co-workers [162] and consistent with the weak Lewis acidity of ceria surface. Actually, some contribution of H-bonded species can be also expected in this frequency region, as will be discussed below. The increase in Mn content leads to the appearance of a shoulder around 1600 cm^{-1}, which becomes the main contribution above Mn concentrations of 50%. At high Mn content, an additional contribution appears around 1606 cm^{-1}, which is even more noticeable in the pure manganese oxide. A very similar adsorption has been assigned to pyridine coordinated over Mn^{3+}/Mn^{2+} sites [163].

The analysis of the high frequency region of the corresponding spectra shows negative bands around 3630 cm^{-1} in pure cerium oxide and 15Mn85Ce samples. The appearance of these negative bands would be associated with the loss of the characteristic surface hydroxyl groups of cerium oxide as a result of interaction with pyridine. Moreover, a broad band around 3350 cm^{-1} is noticeable in all catalysts, although it is more intense at high cerium oxide content, associated to surface H-bonds. Despite these results, no bands associated to pyridinium ion were evidenced, which suggests these surface sites are not able to protonate pyridine molecule.

The appearance of new contributions at higher wavenumber with Mn content suggests that pyridine interacts differently with the exposed surface sites depending on catalysts composition, and more electron withdrawing sites are formed with increasing Mn content. It is well known that the shift of V_{8a} vibrational mode to higher wavenumber denotes an increase in Lewis acid strength [164]. Therefore, Mn provides stronger Lewis acid sites. This result is in agreement with that observed by NH_3-TPD, where acidic centres with different strength were evidenced, those related with strong acidity being promoted at higher interactions between Mn and Ce.

The fact that the increase in Mn content promotes two contributions at 1606 and 1600 cm^{-1} could be associated with the segregation degree of Mn species in the surface. In this sense, XRD revealed the presence of Mn in crystalline form, as Mn_2O_3, and Mn embedded into the CeO_2 structure. Since the contribution at 1606 cm^{-1} is more noticeable in the 85Mn15Ce sample, where Mn_2O_3 segregation was detected, this contribution can be assigned to pyridine adsorbed over crystalline species, whereas the one located at 1600 cm^{-1} is related to the adsorption over Mn species with high Ce interaction.

In order to study the strength of the interaction and the thermal stability of adsorbed pyridine, a thermal evolution of adsorbed species has been performed for 15Mn85Ce and the results are shown in Figure 3.22B. The increase of temperature clearly decreases the intensity of the main pyridine bands. Moreover, new bands appear at 1610, 1547, 1475 and 1435 cm^{-1} at temperature above 200 ^oC. These new bands suggest that pyridine is transformed, leading to other intermediate oxidized products. On the other hand, V_{8a} vibrational mode of adsorbed pyridine is shifted toward higher wavenumber with the increase of

outgassing temperature. This fact would be associated to pyridine desorption of weak acid sites (the weaker the interaction the lower the desorption temperature), which also denotes the presence of Lewis acid sites with different strength. Additionally, the desorption of H-bonded pyridine molecule, whose characteristic bands fall in this range, can contribute to this effect [151].

It should be noted that it would have been interesting to compare these results, obtained with a catalyst rich in cerium, with those obtained with another one rich in Mn, such as 85Mn15Ce. However, the excessive noise in the region below 1500 cm^{-1} for this catalyst, already observed in Figure 3.22A, made it impossible to obtain relevant results.

In summary, the analysis of acidic properties has shown the presence of only Lewis acid sites in the studied catalysts. However, Mn content promotes the presence of acidic sites with different strength. In this way, the increase of Mn content leads to stronger acid sites. This fact has been proven both by NH_3-TPD, by means of the larger amount of NH_3 desorbed at high temperature with respect to that desorbed at low temperature, and by the FTIR analysis of adsorbed pyridine, through the shift of V_{8a} vibrational mode at higher Mn contents. In addition, the thermal analysis of pyridine adsorbed species has also corroborated the presence of acid sites with different strength because of the shift of V_{8a} vibrational mode to higher wavenumber with temperature.

The promotional effect of strong acidity with the increase of Mn content could be associated to promotion of high interaction between Mn and Ce (solid solution phase). Nonetheless, NH_3-TPD has evidenced that high Mn content (for example, in 85Mn15Ce catalyst) has a detrimental effect on strong acidity, simultaneously decreasing total acidity, due to the formation of another crystal phase associated to segregated manganese oxide.

3.2.2. Catalytic performance of MnO_X-CeO_2 with different composition.

3.2.2.1. Analysis of NO and o-DCB conversions.

After analysing the effect of Mn and Ce content on catalytic properties, the effect of this variable on catalytic activity in the simultaneous NH_3-SCR and o-DCB oxidation will be studied. Figure 3.23 shows NO conversion of samples prepared by

(A) sol-gel and (B) co-precipitation; and o-DCB conversion of samples prepared by (C) sol-gel and (D) co-precipitation.

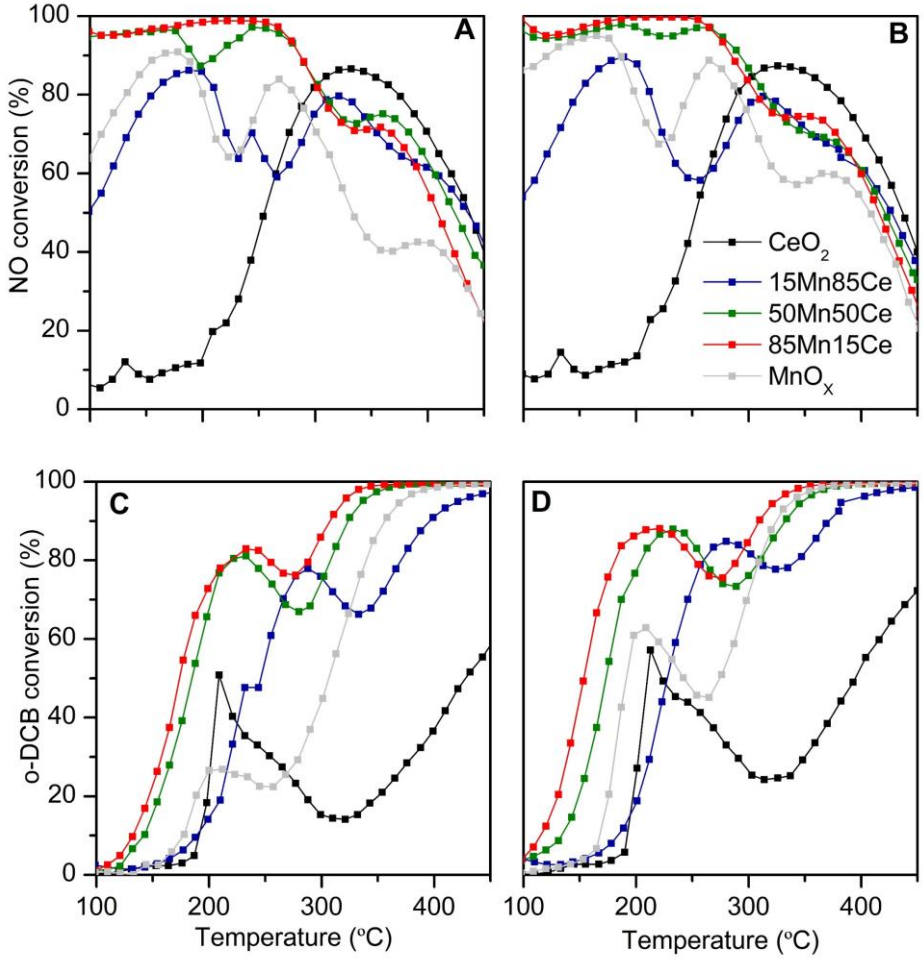

Figure 3.23. NO conversion of MnO_X-CeO_2 catalysts with different Mn and Ce content prepared by A) Sol-gel and B) Co-precipitation. o-DCB conversion of the same catalysts prepared by C) Sol-gel and D) Co-precipitation.

Regarding NO conversion over pure oxides, there is no significant differences between samples prepared by sol-gel and co-precipitation. Thus, cerium oxide is only active at high temperature, above 300 °C, whereas manganese oxide leads to

high NO conversions at low temperatures. Nevertheless, higher NO conversions are reached with the pure manganese oxide prepared by co-precipitation.

Bimetallic catalysts exhibit different NO conversion depending on Mn and Ce content, although there are no remarkable differences between the preparation methods. Low Mn content, i.e., 15Mn85Ce catalyst, promotes a similar NO conversion profile than pure manganese oxide. However, for this catalyst, the Mn content and/or the interaction between Mn and Ce is not enough to overcome the NO conversion obtained by pure manganese oxide at low temperature.

Bimetallic catalysts with Mn contents higher than 50% allow higher NO conversion than pure manganese oxide, and nearly total conversion is reached below 275 ^{o}C. On the other hand, NO conversion strongly decays at high temperature in all catalysts due to SCR side-reactions, as it was also observed in Section 3.1.2.1. Interestingly, the higher the Mn content the more noticeable the drop of NO conversion.

Therefore, the catalysts with high Mn contents allow to reach the best catalytic activity in SCR. This result derivates from the excellent properties provided by the interaction between Mn and Ce and from the fact that Mn is the most active metal for low temperature SCR. The high interaction between Mn and Ce generates a common fluorite structure, that was corroborated by the change in the lattice parameter (XRD), the shift of F_{2g} mode (Raman) and the modification in the slope of Ce-O bands (Skeletal-FTIR). In fact, the mixed oxide phase with different substitution degree was clearly observed at nanoscale by the EDS elemental mapping of STEM-HAADF images.

One of the most important aspects of the formation of the mixed oxide phase is the creation of structural defects, which in turn are related to the amount of oxygen vacancies whose presence was confirmed by Raman. Oxygen vacancies greatly improve the oxygen migration abilities and allow for faster replacement of surface oxygen species involved in the SCR. This feature is considered as a key factor for the improvement of SCR performance at low temperature. Moreover, the oxygen storage capacity is enhanced by oxygen vacancies.

On the other hand, the interaction between Mn and Ce also provides a wide variety of both Mn, as Mn^{4+} and Mn^{3+}, and Ce species, as Ce^{3+} and Ce^{4+}. The presence of these species in the catalytic surface was corroborated by XPS, and in the bulk, by

H_2-TPR. The electronic interaction between Mn^{4+}/Mn^{3+} and Ce^{3+}/Ce^{4+} is essential for both molecular oxygen uptake from the gas phase to replace adsorbed oxygen consumed in the reaction, and adsorption and subsequent reaction of reactants.

XPS results have shown that Mn^{4+} species are promoted in the catalysts prepared by sol-gel at higher Mn content. Similar trend is obtained for the catalysts prepared by co-precipitation, but only up to 50% Mn, because the further increase of Mn content promotes Mn^{3+} species, as a consequence, the Mn^{4+}/Mn^{3+} ratio decrease. In the bulk structure, similar conclusion was obtained from H_2-TPR by means of the estimation of mean oxidation state of Mn. However, despite this promotion of one or the other Mn species depending on the preparation method, similar NO conversions have been obtained. Therefore, this fact suggests that no Mn species is more active than the other, but it is the presence of both species, in high interaction with the Ce^{3+}/Ce^{4+} redox pair (to get a faster electron transfer), what promotes the high catalytic performance in low temperature SCR.

In the case of o-DCB oxidation reaction (Figure 3.23C and 3.23D), similar o-DCB conversion profiles with a S-shape with two steps are obtained for all catalysts. In the same way than in Section 3.1.2.1, o-DCB conversion increases in the first step up certain value, which is different depending on the sample. In the second step, o-DCB conversion increases with temperature until reaching total conversion. Between these two steps, o-DCB conversion decays.

In bimetallic catalysts, the increase in Mn content shifts the o-DCB conversion profile to lower temperatures in both the catalysts prepared by sol-gel and co-precipitation. This result denotes an improvement of oxidative capability with Mn content. Obviously, this fact is associated to the increase in the oxygen mobility caused by the high interaction between Mn and Ce, as a result of solid solution phase. The enhancement of oxidising capacities could be verified by NH_3-TPD, in which high Mn contents, up to a certain value, promote strong acidity. This type of acidity was characterized as being able to oxidize the NH_3 adsorbed over the catalysts in the absence of oxygen, hence its greater oxidizing power.

Figure 3.24 shows the T_{90} (temperature at which 90% o-DCB conversion is reached) for each catalyst. As can be seen, T_{90} decreases gradually at higher Mn contents (with the exception of pure manganese oxide), due to the above-mentioned shift of o-DCB conversion profiles to lower temperatures. Interestingly, this result evidences that solid solution is not the only factor that improves catalytic

performance in o-DCB oxidation, since the bimetallic catalysts with the highest Mn content (85Mn15Ce) present lower values of T_{90}, although the solid solution is not the main phase. Indeed, in the 85Mn15Ce a promotion of amorphous structure and a high Mn_2O_3 segregation degree was observed by XRD prepared by sol-gel and co-precipitation, respectively.

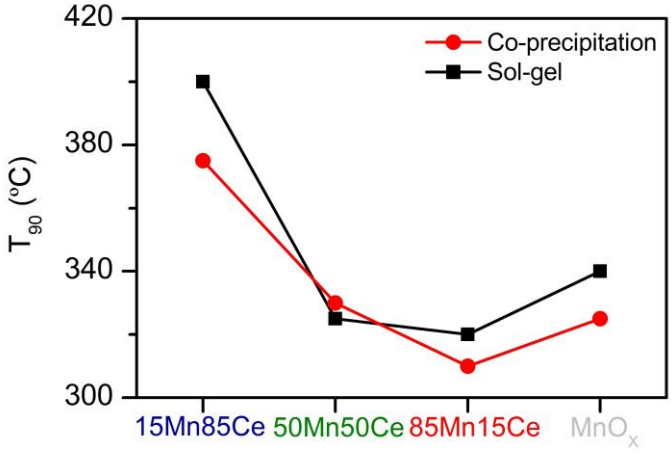

Figure 3.24. T_{90} in o-DCB oxidation of MnO_X-CeO_2 catalysts with different Mn and Ce content.

According to literature, the value of Mn/(Mn+Ce) that limits the incorporation of Mn species into fluorite lattice is between 0.6-0.75 [150]. Thus, when Mn/(Mn+Ce) is below 0.6, almost all Mn species are into the fluorite structure, forming the solid solution, whereas values above 0.75 lead to Mn segregation due to saturation of the structure. These facts have been evidenced by XRD and Skeletal FTIR, where the peaks associated with manganese oxide phases only appeared in 85Mn15Ce samples. Moreover, Mn segregation was observed through EDS mapping of STEM-HAADF images of 85Mn15Ce prepared by both sol-gel and co-precipitation. Therefore, it is proposed that the synergistic effect between the solid solution phase and the manganese oxide is what provides the best catalytic performance in the bimetallic catalysts with high Mn content.

Nonetheless, it should be pointed out that, unlike SCR, where no difference in the catalytic performance was observed between the catalysts prepared by sol-gel and co-precipitation, in the oxidation reaction, the catalysts prepared by co-precipitation allow to obtain the same o-DCB conversion at lower temperatures

than those prepared by sol-gel (lower T_{90} for co-precipitated catalysts). This may be associated to two key factors: higher surface area and synergy between mixed oxide phase and segregated manganese oxide in the co-precipitated catalysts.

On the other hand, as well as the shift of the o-DCB conversion profiles, it should be noted that bimetallic catalysts, independently of Mn and Ce contents, promote a great increase in o-DCB conversion at low temperature, in comparison to pure oxides.

In the analysis about the effect of preparation method on catalytic activity of Section 3.1, the o-DCB conversion rise in bimetallic catalysts at low temperature was mostly associated to the promotional effect provided by the interaction between Mn and Ce. The fact that there are not remarkable differences between the catalysts with high and low Mn content indicates that segregated manganese oxide in the catalysts with the highest Mn content is not involved to a great extent in the oxidation reaction at low temperature, since, if it were, o-DCB conversion in the first rise would gradually increase with Mn content.

Based on the above results, the bimetallic catalyst with the highest Mn content, i.e., 85Mn15Ce, has shown the best catalytic performance in the experimental conditions. This composition allows to obtain total conversion of NO below 275 ^{o}C and total conversion of o-DCB above 325 ^{o}C. As mentioned before, good catalytic performance in $dDiNO_X$ process requires high conversion of both compounds in the same temperature range. Therefore, as in the analysis of the preparation method, the selection of the catalyst with the best catalytic performance is based on reaching conversion of both pollutants above 80%. This condition is fulfilled, for the 85Mn15Ce composition, between 210-250 ^{o}C (working window of 30 ^{o}C) for sol-gel catalyst, and between 180-250 ^{o}C (working window of 70 ^{o}C) for co-precipitation catalyst.

Therefore, the 85Mn15Ce prepared by co-precipitation shows the best catalytic activity. This is mainly due to the higher activity in the oxidation reaction, since in SCR both sol-gel and co-precipitated samples showed similar NO conversions. The excellent catalytic performance is related to the coexistence of a mixed oxide phase with a fluorite structure, strongly distorted by the interaction of Mn and Ce, and a segregated Mn_2O_3 phase. This structure provides to the catalysts a high oxygen mobility in both surface and bulk structure and high variability of Mn and Ce species, which greatly improves redox and acid properties.

3.2.2.2. Analysis of SCR and o-DCB oxidation by-products.

As previously observed in Section 3.1.2.2, several by-products are generated in both SCR and o-DCB oxidation reactions. In the same way, the goal of this section is just to analyse the influence of Mn and Ce content in by-products distribution, and not to go in-depth into the origin of these by-products.

In SCR, N_2O and NO_2 are the main by-products and their production profile is shown in Figure 3.25. Similar results were obtained for both by-products as in Section 3.1.2.2. Regarding N_2O (Figure 3.25A and 3.25B), cerium oxide is the catalyst with the lowest N_2O production, whereas pure manganese oxide exhibits a high N_2O generation in the whole temperature range, with the maximum production between 200 and 300 ^oC. There are no remarkable differences between the catalysts prepared by sol-gel and co-precipitation concerning N_2O production.

In bimetallic samples, N_2O production profile is composed by two contributions: one around 200 ^oC and the other around 350 ^oC, although the exact temperature depends on the catalyst. Thus, the higher the Mn content, the more shifted the N_2O production profiles to lower temperatures, especially the second contribution. Moreover, the N_2O generated comparing the catalysts prepared by different methods is similar, although slightly higher for those prepared by co-precipitation. This fact could be associated with the higher oxidising capacity of the catalysts prepared by this method, as they performed the o-DCB oxidation at lower temperatures than those prepared by sol-gel.

It must be pointed out that the catalysts with the lowest Mn content (15Mn85Ce), despite their high Ce content, promote a significant production of N_2O compared to pure cerium oxide. This fact suggests Mn as the main precursor of side-reactions that generate N_2O, as it was proposed in Section 3.1. According to literature, there are divergences about how Mn is involved in N_2O formation. Some authors consider that N_2O formation is related to well-ordered MnO_X crystalline phase due to the presence of highly-reactive oxygen [165-167], whereas other researchers support that the highest N_2O production takes place at high temperatures and catalysts with larger Mn contents [168]. The results in Figure 3.25 show no remarkable differences between the catalysts with low and high Mn content in N_2O production, so N_2O formation is probably associated to the catalytic properties provided by Mn,

instead of its crystalline phase and the reaction temperature. Later, in Chapter 4, the side reactions involved in N_2O generation will be discussed.

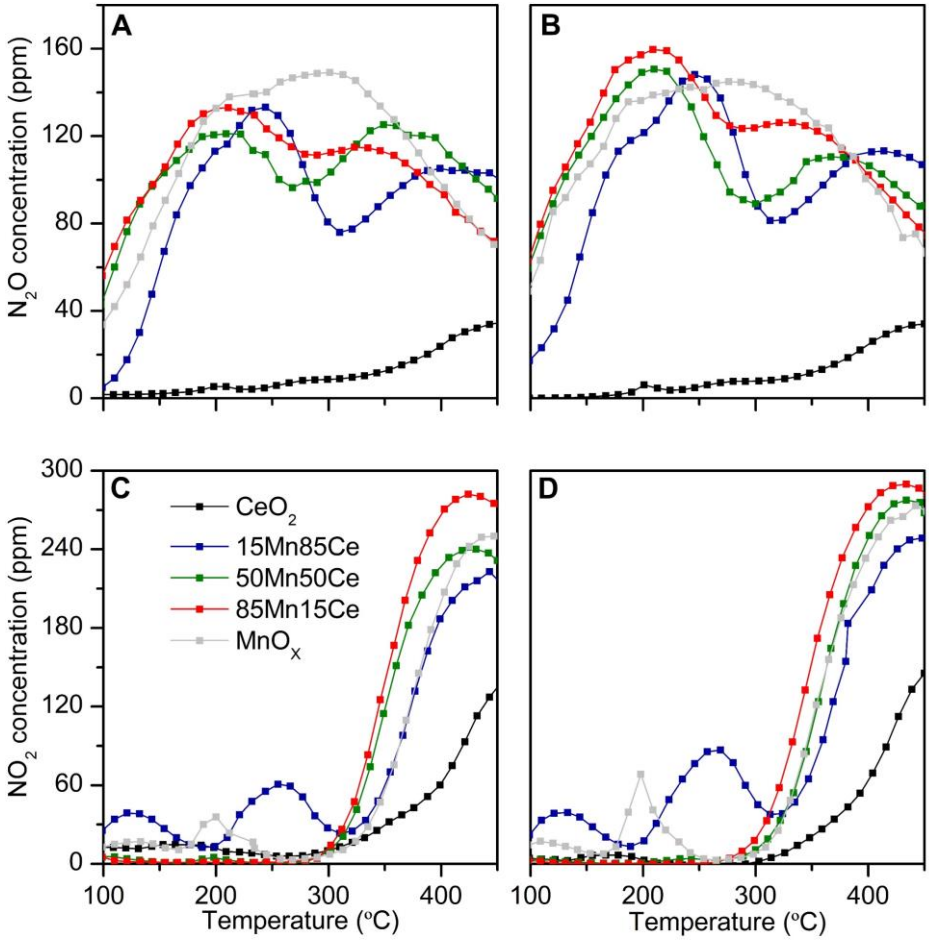

Figure 3.25. N_2O generation with MnO_X-CeO_2 catalysts with different Mn and Ce content prepared by A) Sol-gel and B) Co-precipitation. NO_2 generation with the same catalysts prepared by C) Sol-gel and D) Co-precipitation.

On the other hand, NO_2 production occurs above 300 °C and it sharply increases with temperature for all catalysts, in line with that discussed in Section 3.1. Higher Mn content slightly shifts NO_2 profiles to lower temperatures, which denotes a promotional effect of Mn content in the oxidation reactions involved in NO_2

formation. In the same way, the higher the Mn content, the greater the NO_2 production. Both facts are in accordance with the increase in NO_2 production with Mn content, and are associated to the higher oxidizing capacity promoted by Mn.

In addition to NO_2 generation at high temperature, 15Mn85Ce and pure manganese oxide samples exhibit a NO_2 production peak at 250 and 200 ^oC, respectively. Interestingly, only these catalysts showed a drop of NO conversion in the same temperature range. These facts suggest that NO conversion drop could be related to NO_2 production, specifically from NH_3 oxidation side reaction, as proposed above; since it comes from NO oxidation, NO conversion would not be affected.

In the case of oxidation reaction, CO_2 is the main product, although its selectivity is not showed. This fact reveals the selective character of MnO_X-CeO_2 formulation towards total oxidation. On the other hand, CO is the main by-product, although chlorinated organic compounds are generated as well. Figure 3.26 shows the selectivities for both CO and all the organic compounds detected during the reaction. In the same way than in Section 3.1, the selectivity to oxidation by-products is shown above 200 ^oC, due to the low o-DCB conversion below this temperature.

Similar profiles of CO selectivity are obtained for the catalysts prepared by sol-gel and co-precipitation (Figure 3.26A and 3.26B). In this regard, CO selectivity of cerium oxides gradually increases with temperature, whereas manganese containing catalysts show a profile with a plateau from 200 to 350 ^oC, temperature above which CO selectivity strongly decays.

The values of CO selectivity in the plateau at medium temperatures increase with Mn content. Thus, at 300 ^oC, CO selectivity increases from 6 to 27% from the 15Mn85Ce to pure manganese oxide samples, in both those prepared by sol-gel and co-precipitation. These results denote a small negative effect of Mn content over total o-DCB oxidation, in spite of the clear effect higher Mn contents have on the oxidising capacity of the samples discussed above. These two facts, that seem beforehand to be opposed, are compatible because, at these conditions, the increase of Mn content may favour o-DCB oxidation (increasing o-DCB conversion at lower temperatures) but, at the same time, decreasing the selectivity of oxidation reaction towards CO_2.

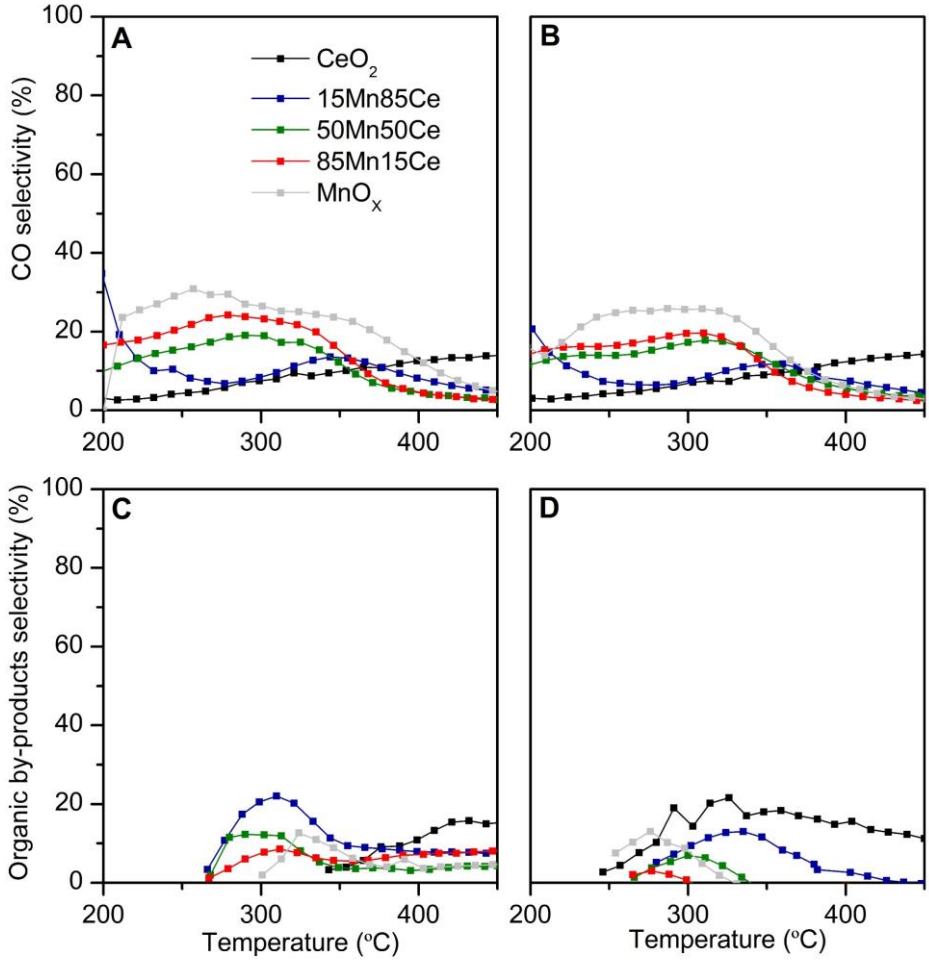

Figure 3.26. CO_2 selectivity obtained with MnO_X-CeO_2 catalysts with different Mn and Ce content prepared by A) Sol-gel and B) Co-precipitation. Chlorinated organic by-product selectivity obtained with the same catalysts prepared by C) Sol-gel and D) Co-precipitation.

Chlorinated organic by-products are originated from partial oxidation of o-DCB. They are mainly produced above 250 ºC. Pure cerium oxide prepared by sol-gel has a lower production and shifted to at higher temperatures compared to the one prepared by co-precipitation. Similarly, in pure manganese oxides, by-products are formed at higher temperatures in the one prepared by sol-gel than in the co-

precipitated one. For bimetallic catalysts, the increase in Mn content decreases the selectivity towards chlorinated organic by-products, contrarily to the trend followed by CO selectivity. This fact supports the above proposal, that the increase of Mn leads to higher oxidising capacity, which allows for o-DCB and even chlorinated organic by-products oxidation. In addition to decreasing the production of chlorinated organic by-products, the increase in Mn content shifts their production to lower temperatures in bimetallic co-precipitated catalysts.

3.3. INFLUENCE OF VARIABLES INVOLVED IN CO-PRECIPITATION METHOD FOR THE PREPARATION OF MnO_X-CeO_2 CATALYST FOR THE SIMULTANOUS REMOVAL OF NO_X AND o-DCB.

The results of the previous sections have evidenced the higher catalytic activity of bulk catalysts with high Mn content in the simultaneous removal of NO_X and o-DCB. Among the two preparation methods analysed for the preparation of bulk catalysts, co-precipitation leads to the highest conversion of both pollutants at lower temperatures, especially because of its good activity in the oxidation reaction. Moreover, co-precipitation method has other advantages, such as simplicity and ease to scale up.

The excellent catalytic result of high Mn content co-precipitated catalysts is related to several factors, which have been discussed above. Firstly, co-precipitation method produces bulk catalysts that favour the interaction between Mn and Ce in all the catalytic structure, not only on the surface. Secondly, high Mn contents promote the presence of different species of Mn, which is the most important metal, such as manganese with higher and lower interaction with Ce (solid solution with different interaction degrees) and manganese oxide aggregates. This fact allows to improve morphological, redox and acid properties, thereby improving catalytic activity.

Several works have reported the variables involved in preparation method may promote significant changes in morphological and chemical properties of the catalysts and, consequently, the catalytic behaviour [169]. Thus, the aim of this section is to study the effect of three variables involved in co-precipitation method: ageing time, pH and precipitating agent, as well as calcination temperature, in

catalytic properties and activity. For this purpose, co-precipitated 85Mn15Ce catalyst, as the best performing catalyst from the above sections, has been chosen.

The values of the variables to be analysed are as follows (the underlined values of each variable were those set when the variable in question was not analysed):

- Calcination temperature: 500, 600, 700 and 800 ºC.
- Ageing time: 0, 2, 6 and 24 h.
- pH: 7, 8 and 9.
- Precipitating agent: sodium hydroxide, ammonia, sodium carbonate and ammonium carbamate.

3.3.1. Characterization of MnO_X-CeO_2 catalysts prepared modifying the variables involved in co-precipitation.

3.3.1.1. Structural and textural properties.

The influence of the different variables in the distribution of crystal phases was studied by XRD. Figure 3.27 shows the diffraction patterns of the catalysts.

Regarding calcination temperature (Figure 3.27A), α-Mn_2O_3 and fluorite are the main crystal phases. The catalyst calcinated at 500 ºC also exhibits a small diffraction peak at 37.1º related to MnO_2. The higher the calcination temperature, the more intense and narrower the diffraction peaks of the main crystal phases are. This result denotes an increase in the crystallinity degree of the samples with calcination temperature. Table 3.10 reports α-Mn_2O_3 and fluorite crystal sizes of all samples. The higher crystallinity is also evidenced by the increase in crystal size from 4 to 17 for fluorite phase and from 14 to 35 for α-Mn_2O_3.

In the case of the catalysts with different ageing time, Figure 3.27B, well defined diffraction peaks were identified associated to CeO_2 (fluorite phase), Mn_2O_3 and MnO_2. Longer ageing time does not affect fluorite diffraction peaks. However, the peaks associated to Mn_2O_3 become less intense. This trend is also evidenced through the crystal size of both phases (Table 3.10). Thus, while fluorite crystal size remains constant, the Mn_2O_3 crystal size starts to decrease at above 6 hours.

The negative effect of ageing time in the crystallinity degree of Mn_2O_3 could be associated to a promotion of Mn and Ce interaction that would lead to a deteriorated fluorite phase and/or to the promotion of amorphous manganese oxide phase (or manganese oxide phase with very small crystal domains). The latter hypothesis is more feasible, since the fluorite diffraction peaks are not modified with different ageing times.

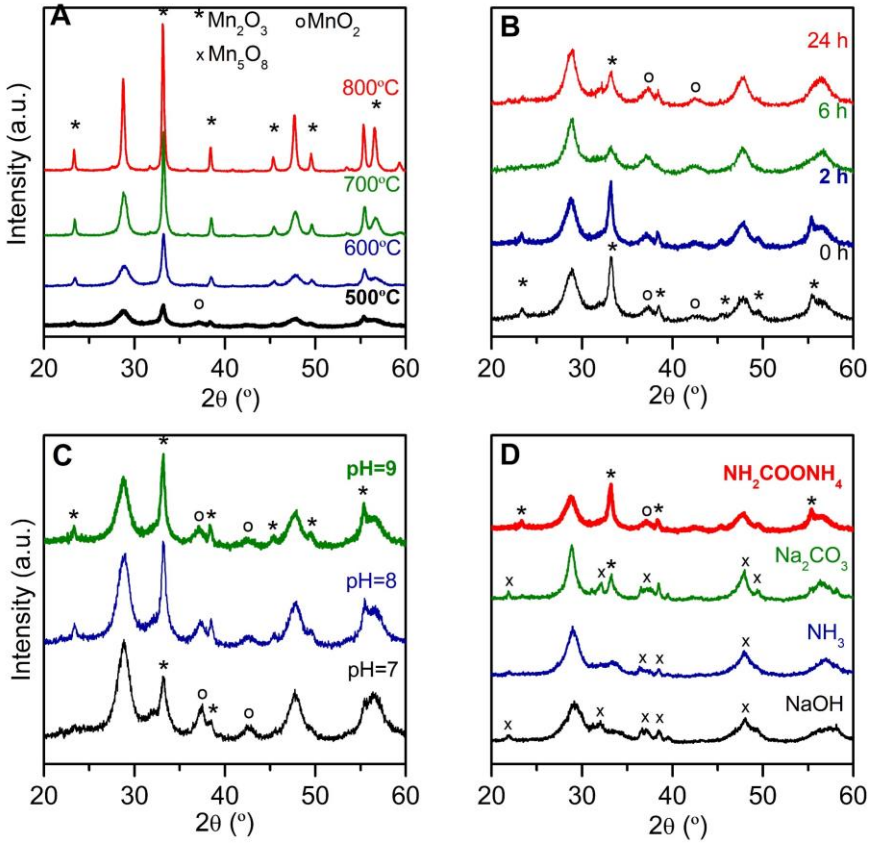

Figure 3.27. XRD patterns of co-precipitated 85Mn15Ce catalyst. Variable analysed: A) calcination temperature, B) ageing time, C) pH and D) precipitating agent. Thick line: base sample.

Similarly, diffraction peaks associated to CeO_2, Mn_2O_3 and MnO_2 are detected in the samples prepared at different pH (Figure 3.27C). No noticeable changes are observed in the fluorite diffraction peaks. Indeed, similar crystal sizes have been

estimated for the catalysts with different pH values. On the other hand, the increase of pH leads to larger Mn_2O_3 crystal size, whereas the peaks associated to MnO_2 become less intense in comparison to those of Mn_2O_3. Therefore, pH affects crystallinity of manganese oxide favouring the presence of Mn^{3+} species (Mn_2O_3) at higher values.

Table 3.10. Structural data obtained from XRD for co-precipitated 85Mn15Ce prepared modifying calcination temperature, ageing time, pH and precipitating agent.

Sample	Fluorite crystal size (nm)	Mn_2O_3 crystal size (nm)
Calcination temperature		
500 ^oC	4	15
600 ^oC	7	19
700 ^oC	12	30
800 ^oC	27	36
Ageing time		
0 h	5	15
2 h	4	15
6 h	6	7
24 h	6	7
pH		
pH=7	5	9
pH=8	5	15
pH=9	4	15
Precipitating agent		
NaOH	4	--
NH_3	5	--
Na_2CO_3	9	--
NH_2COONH_4	4	15

Regarding the catalysts prepared with different precipitating agents, Figure 3.27D shows the presence of fluorite diffraction peaks in all samples. The crystallinity of this phase is similar in all samples (crystal size around 5 nm), except for the catalyst co-precipitated with Na_2CO_3, in which it is even larger. Interestingly, different manganese oxide phases are promoted by different precipitating agents. Thus, Mn_5O_8 crystal phase is the only one detected in the samples co-precipitated with NH_3 and NaOH, whereas Mn_2O_3 is the main phase in that precipitated with NH_2COONH_4. In the catalyst co-precipitated with Na_2CO_3, diffraction peaks associated to both manganese oxide phases were detected.

The influence of variables involved in co-precipitation method on the structural properties of the catalysts was further studied by skeletal FTIR (DICCA, University of Genova). Figure 3.28 shows the skeletal FTIR spectra of the samples, ordered according to the variable analysed.

Regarding the catalysts calcinated at different temperatures (Figure 3.28A) the one calcinated at 500 ^{o}C presents a strong adsorption below 800 cm^{-1} with bands at 523, 574 and 602 cm^{-1} and shoulders at 446, 500 and 656 cm^{-1}. These bands are associated to Mn-O vibrational modes of α-Mn_2O_3 [141, 147]. Another weak band is also observed around 850 cm^{-1} related to Ce-O bond [152, 153]. Additional bands appear at high wavenumber, usually associated to surface species. Thus, the band located at 1630 cm^{-1} is associated to stretching vibration of molecularly adsorbed water [152], whereas the assignation of the broad and complex band at 1400 cm^{-1} is not straightforward but it could be due to a form of carbonate species (for instance, some bulk carbonate). These carbonates would result from incomplete calcination of the precipitating agent, since their bands disappear at higher calcination temperature.

The increase of calcination temperature leads to well-defined bands located at low wavenumber, the spectra becoming similar to pure manganese oxide spectrum (reported in the previous sections). These results could evidence an increase of crystallinity degree of Mn_2O_3 phase at higher calcination temperatures. In this sense, XRD evidenced the higher the calcination temperature, the larger the Mn_2O_3 crystal size, which supports FTIR results.

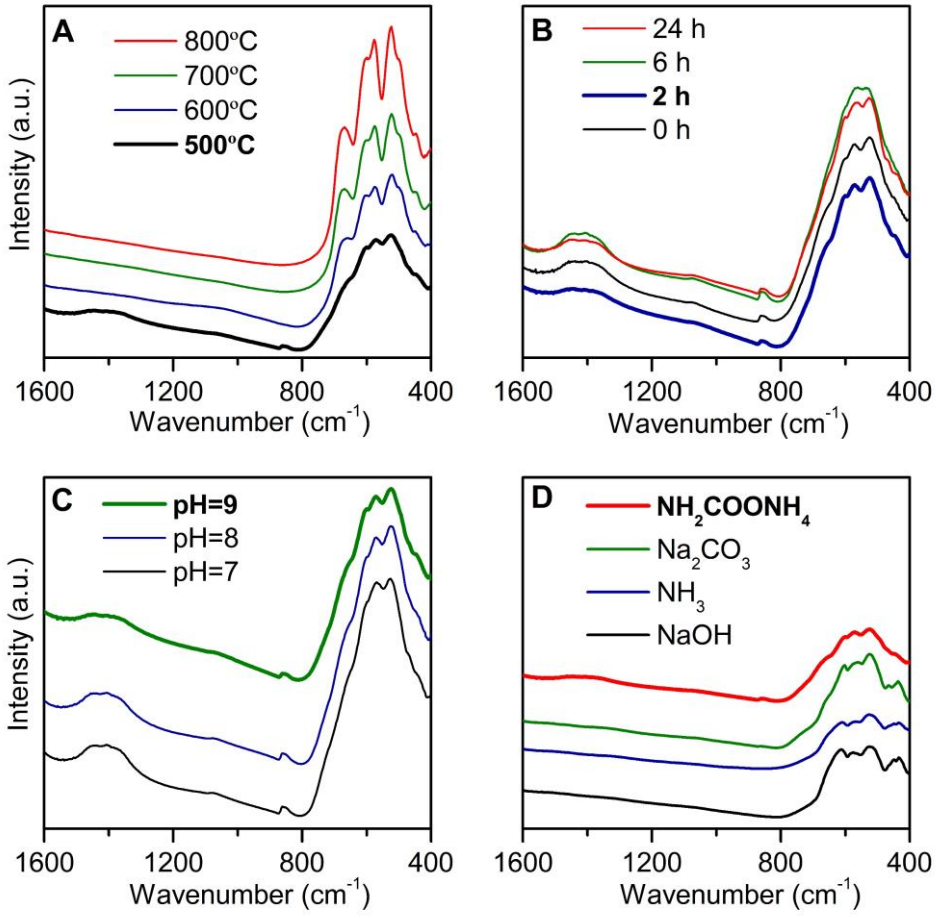

Figure 3.28. Skeletal FTIR spectra of co-precipitated 85Mn15Ce catalyst. Variable analysed: A) calcination temperature, B) ageing time, C) pH and D) precipitating agent. Thick line: base sample.

Additionally, the increase of calcination temperature slightly shifts the shoulder located at 656 to 670 cm^{-1} (same position than in pure manganese oxide) in the catalyst calcinated at 700 ºC. The slight shift of some bands in the spectra of mixed catalysts with respect to those observed in pure manganese oxide is related to modifications of Mn-O vibrational modes caused by the interaction between Mn and Ce, which would evidence the presence of solid solution phase. However, the fact that the increase of calcination temperature shifts the position of these bands

towards the position of those observed in pure manganese oxide sample, denotes that higher calcination temperature has a detrimental effect on the solid solution phase, promoting the segregation of Mn and Ce in their metal oxides. This is also in accordance with the higher crystallinity promoted by calcination temperature.

FTIR spectra of samples with different ageing time and pH (Figure 3.28B and 3.28C) exhibit similar bands previously assigned to Mn_2O_3 and Ce-O bonds. At higher wavenumber, the broad band at 1400 cm^{-1}, related to bulk carbonates, is also present. As discussed before, the bands related to Mn_2O_3 are broader than those in pure manganese oxide. This effect evidences the modification of Mn-O vibrational modes due to the interaction between Mn and Ce, which suggests the presence of solid solution phase in the catalyst structure. However, the fact that ageing time and pH do not modify the position and definition of the peaks suggests that both parameters do not greatly affect the final structure of the catalysts or the effect caused is not so clear to be observed by FTIR, since XRD technique allowed to evidence the effect of both variables on manganese oxide phase.

In the case of the catalysts co-precipitated with different precipitating agents, (Figure 3.28D), the use of ammonium carbamate leads to the appearance of the peaks above mentioned, which are associated to Mn_2O_3 phase. In the same way than in the analysis of the other variables, some differences are observed between the spectrum of sample co-precipitated with ammonium carbamate and pure manganese oxide spectrum. This reveals the interaction between Mn and Ce.

On the other hand, similar spectra are observed for the catalysts co-precipitated with NH_3, NaOH and Na_2CO_3. They show peaks located at 611, 579, 524, 450 and 535 cm^{-1} with shoulders at 730 and 656 cm^{-1}. It should be noted that the peaks in the range of 800-500 cm^{-1} are located in similar position than those observed in the catalyst co-precipitated with ammonium carbamate, whose main crystal phase is Mn_2O_3. However, the differences in the relative intensities of the peaks and the appearance of two peaks at wavenumber below 500 cm^{-1} suggest some differences in the Mn-O vibrational modes that could be associated to the fact that Mn_2O_3 is not the only manganese oxide crystal phase. In this sense, XRD technique corroborated the presence of Mn_5O_8 in the catalysts co-precipitated with NH_3, NaOH and Na_2CO_3, so the differences with respect to pure Mn_2O_3 spectrum could be probably associated to contributions of Mn-O vibrational modes of Mn_5O_8. Regarding literature, there is not much information about Mn_5O_8 FTIR spectrum,

although the peaks assigned to Mn_5O_8 are in accordance with those observed by Aghazadeh and co-workers [170].

Therefore, the results above exposed reveal that the precipitating agent not only affects the crystallinity degree of catalyst structure, but also may lead to the formation of different manganese oxide crystal structures.

In order to provide further information about the chemical environment of the active metals, that supports the conclusion obtained by structural analysis, UV-Vis technique was performed (DICCA, University of Genova). Figure 3.29 shows the UV-Vis spectra of the samples, structured on the basis of the different variables.

Figure 3.29A shows the UV-Vis spectra of the catalysts calcined at different temperatures. The one calcined at 500 ^oC exhibits two main bands in the UV region at 240 and 360 nm. The band at 360 nm is related to α-Mn_2O_3 [171], whereas there are some discrepancies in the literature about the assignment of the band located at 240 nm: some authors associate the band to $O^{2-} \rightarrow Mn^{2+}$ [172, 173], whereas others associate it to $O^{2-} \rightarrow Mn^{3+}$ [174]. XRD and Skeletal FTIR results showed no evidence of Mn^{2+} species in the catalysts, so the most plausible assignment is to $O^{2-} \rightarrow Mn^{3+}$. In the visible region, a broad band appears at 550 nm corresponding to the dark colour of these samples.

The increase of calcination temperature does not modify the bands located in the UV region, although it promotes a shift of the band located at 550 nm to lower wavelength (493 nm in the catalyst calcined at 800 ^oC). In the same way, the increase of calcination temperature also promotes the appearance of a new band at 746 nm, which is associated to Mn_2O_3. This fact would be in accordance with FTIR results, where an increase of crystallinity of Mn_2O_3 phase was evidenced by the good definition of the peaks associated to Mn-O vibrational modes at higher calcination temperatures.

Similar UV-Vis spectra are observed for the remaining catalysts. The UV region of the spectra obtained from the analysis of ageing time and precipitating agent (Figure 3.29B and 3.29D) is characterized by a high level of noise, although the same bands at 240, 310 and 350 nm are identified. In the visible region, all samples show the band associated to dark colour of the catalysts, but shifted depending on the selected value of the variable.

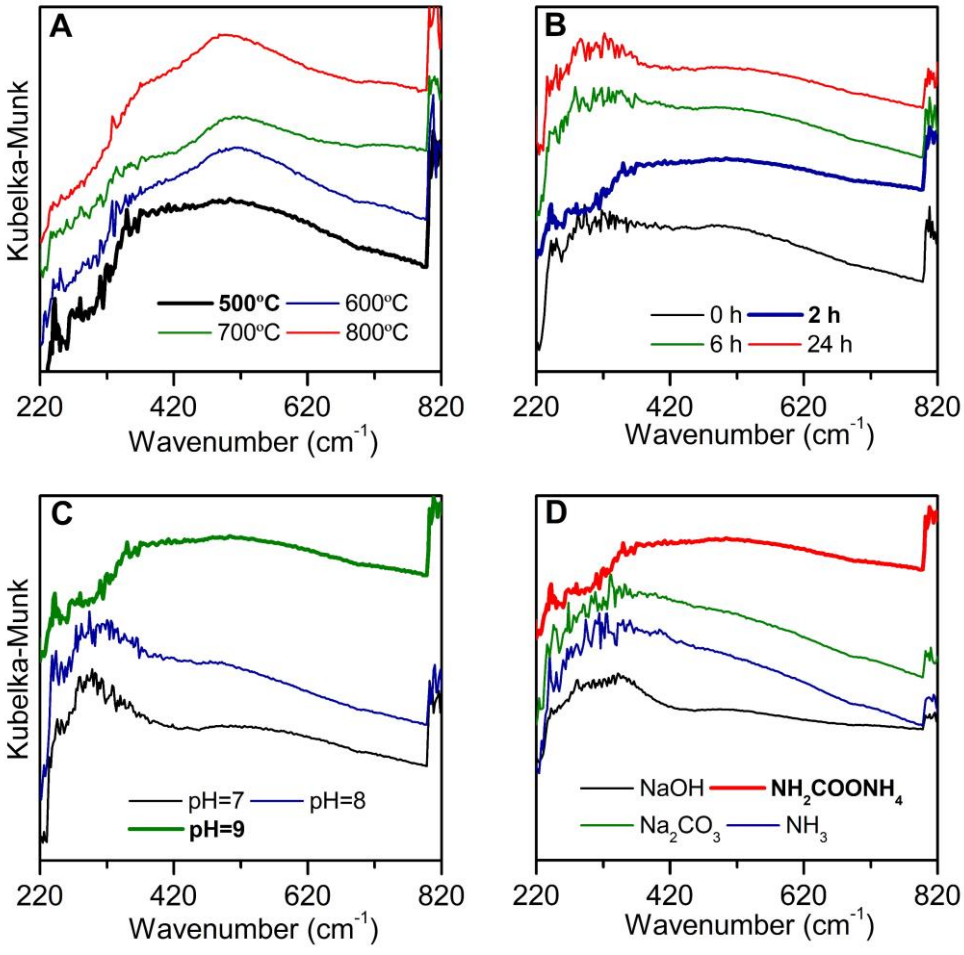

Figure 3.29. UV-Vis spectra of co-precipitated 85Mn15Ce catalyst. Variable analysed: A) calcination temperature, B) ageing time, C) pH and D) precipitating agent. Thick line: base sample.

Therefore, UV-Vis analysis has revealed that the variables involved in co-precipitation cause no changes in the spectra of the samples, which means that chemical environment of active metal is not clearly modified, in spite of the evidences provided by XRD and FTIR of the several changes produced at structural level.

The influence of the variables involved in co-precipitation was evaluated by N_2-physisorption. All samples exhibited type IV isotherm with H3 hysteresis loop corresponding to mesoporous materials, although the N_2 adsorption desorption isotherms are not shown. Table 3.11 lists the BET surface area, pore volume and mean pore diameter.

Table 3.11. Textural properties of co-precipitated 85Mn15Ce prepared modifying calcination temperature, ageing time, pH and precipitating agent.

Sample	**S_{BET} (m^2/g)**	**V_p (cm^3/g)**	**D_p (nm)**
Calcination temperature			
500 ^oC	87	0.25	9.0
600 ^oC	55	0.23	13.8
700 ^oC	30	0.21	24.7
800 ^oC	20	0.10	26.8
Ageing time			
0 h	87	0.27	9.8
2 h	87	0.25	9.0
6 h	97	0.25	8.7
24 h	97	0.27	8.7
pH			
pH=7	86	0.26	9.0
pH=8	91	0.27	9.2
pH=9	87	0.25	9.0
Precipitating agent			
NaOH	57	0.18	10.5
NH_3	57	0.18	10.1
Na_2CO_3	59	0.25	15.1
NH_2COONH_4	87	0.25	9.0

The higher the calcination temperature, the lower the specific surface area and pore volume. Since a promotion of crystallinity was evidenced with calcination temperature, an inverse relationship is obtained between specific surface area and crystal size of the two phases: fluorite and Mn_2O_3. The negative effect of crystallinity on morphological properties is a consequence of active metals segregation in their own oxides. This fact would lead to fewer defects in the catalytic structure, and lower pore volume. Obviously, the larger crystal size due to the increase of calcination temperature, favours larger pore diameter (Table 3.11) as a result of the larger intercrystallite space.

Ageing time and pH do not greatly affect morphological characteristics of the samples. All samples exhibit similar specific surface area, pore volume and pore diameter, although it should be noted that longer ageing times promote a better definition of pore distribution (not shown), that is, a homogeneous pore size.

Regarding precipitating agent, the samples co-precipitated with NaOH, NH_3 and Na_2CO_3 show similar specific surface areas, around 60 m^2/g, whereas a notable increase up to 87 m^2/g is promoted by the use of ammonium carbamate. It is well known that larger specific area allows for more active sites per gram of catalyst, so the use of this precipitating agent can be an important factor for the improvement of the catalytic properties. Moreover, the catalyst co-precipitated with ammonium carbamate has present the largest pore volume (same as that obtained with sodium carbonate), but with the smallest pore size.

3.3.1.2. Redox and acid properties.

The influence of variables involved in co-precipitation on the reducibility of the catalysts was studied by H_2-TPR. Figure 3.30 shows the TPR profiles of all the samples. All catalysts show a reduction profile with a relevant H_2 consumption in the temperature range of 200-500 ^oC and a small consumption at higher temperature (around 800 ^oC), as described in the previous sections for bimetallic catalysts with high Mn content.

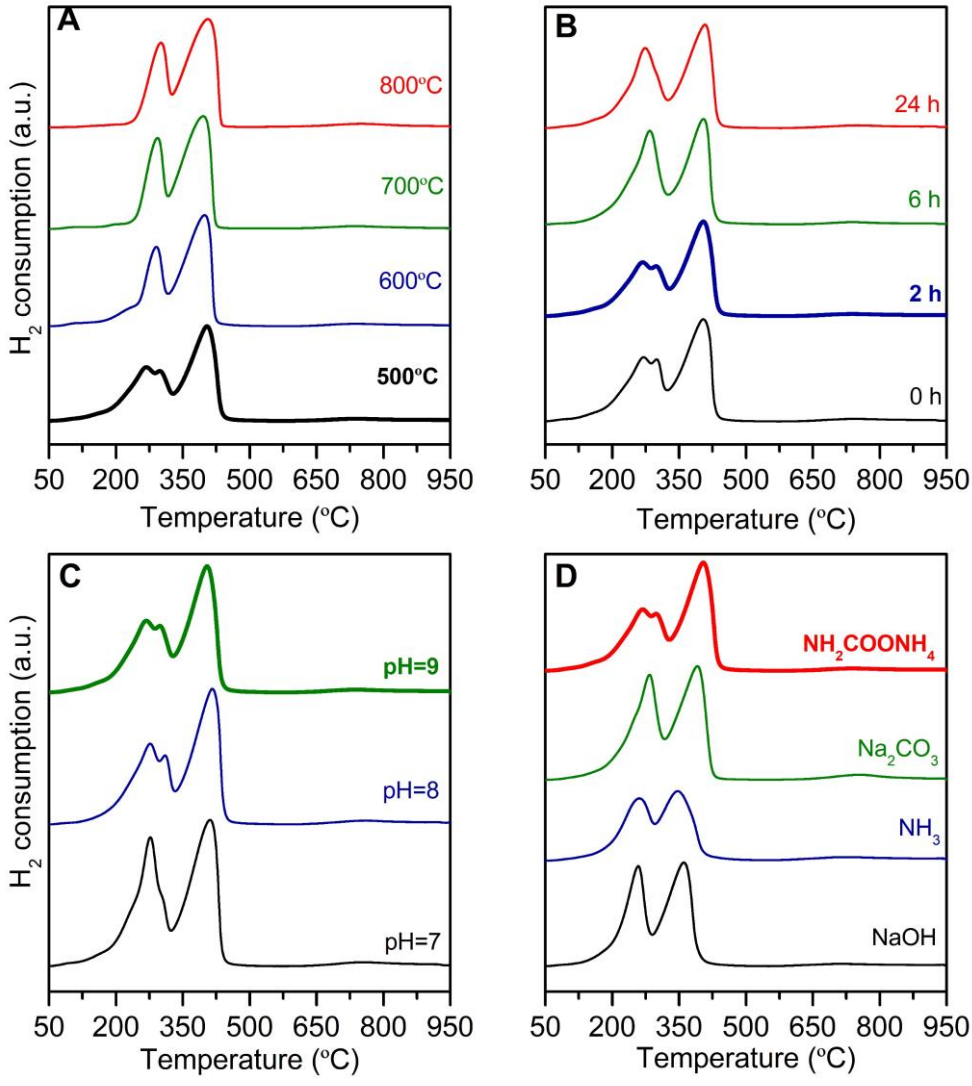

Figure 3.30. H_2-TPR profiles of co-precipitated 85Mn15Ce catalyst. Variable analysed: A) calcination temperature, B) ageing time, C) pH and D) precipitating agent. Thick line: base sample.

H_2 consumption between 200-500 ºC in Figure 3.30, consists of two peaks and it is mainly related to Mn reduction, and surface Ce reduction to a lesser extent. The first reduction peak at low temperature corresponds to the reduction of Mn in high oxidation state (MnO_2/Mn_2O_3) to Mn_3O_4, and the one located at high temperature

is associated to Mn_3O_4 reduction to MnO. As in previous sections, it should be noted that the low temperature reduction peak may be made up of two contributions depending on the analysed variable and its value. The contribution at lower temperature is associated to Mn reduction with high interaction with Ce (solid solution phase) and the contribution at higher temperature to the reduction of crystal aggregates of manganese oxide, mainly as Mn_2O_3.

Regarding calcination temperature (Figure 3.30A), its increase shifts the reduction peaks towards higher temperatures, from 260 and 393 ^oC in the catalyst calcined at 500 ^oC, to 300 and 400 ^oC in the catalyst calcined at 800 ^oC. The increase of calcination temperature also causes the disappearance of the two contributions that constitute the first Mn reduction peak, which becomes only one for catalysts calcinated above 600 ^oC. These changes are associated to the lower interaction between Mn and Ce, as a consequence of their segregation. Hence, TPR profiles of catalysts calcinated above 700 ^oC, are quite similar to those obtained for pure manganese oxide (showed in Figure 3.20).

Similar results are obtained in the analysis of the effect of pH. In this case, TPR profiles showed two H_2 uptakes in the first reduction peak, although they are more noticeable in the catalysts co-precipitated at pH above 7. In agreement with the above, this result suggests that the increase of pH favours the crystallinity of the manganese oxide phase, which was also reported by XRD.

Regarding the catalysts co-precipitated with different agents, those precipitated with NH_3, NaOH and Na_2CO_3 exhibit similar reduction profiles in which the first reduction peak does not present a clear split into two contributions. Splitting only occurs in the catalyst co-precipitated with NH_2COONH_4. This different reduction behaviour as a function of precipitating agent could be related with the different manganese oxide phases reported. Thus, Mn_2O_3 was the main crystal phase in the sample co-precipitated with NH_2COONH_4, whereas Mn_5O_8 was the main crystal phase in the remaining catalysts.

Table 3.12 lists the H_2 consumption from TPR analysis. A remarkable difference is observed in the catalysts calcined at different temperatures, specifically between the one calcined at 500 ^oC, which presents a larger H_2 consumption than those calcined at higher temperatures. Taking into account that: (1) the majority of H_2 consumption can be associated to Mn reduction, (2) all catalysts have the same metal content and (3) Mn tends to be in Mn^{4+} oxidation state when it is strongly

interacting with Ce (conclusion obtained from the previous sections); the higher H_2 consumption of the catalyst calcinated at the lowest temperature may be associated to a higher oxidation state of Mn as a consequence of its higher interaction with Ce.

Table 3.12. Results of H_2-TPR for co-precipitated 85Mn15Ce prepared modifying calcination temperature, ageing time, pH and precipitating agent.

Sample	Mn reduction peak (°C)		H_2 consumption (mmol H_2/g)
	Peak I	Peak II	
Calcination temperature			
500 °C	268-300	405	6.1
600 °C	289	398	5.5
700 °C	292	395	5.5
800 °C	301	406	5.5
Ageing time			
0 h	296-300	405	6.1
2 h	268-300	405	6.1
6 h	283	404	6.2
24 h	274	407	6.3
pH			
pH=7	277	393	6.9
pH=8	274-310	416	5.9
pH=9	268-300	405	6.1
Precipitating agent			
NaOH	257	367	4.9
NH_3	259	350	4.4
Na_2CO_3	283	392	6.0
NH_2COONH_4	268-300	405	6.1

Similar H_2 consumption is observed in the catalysts prepared with different ageing time, whereas larger consumption was measured in the catalyst prepared with the lowest pH (pH 7). This difference could be also caused by the higher interaction between Mn and Ce. However, this effect of pH has not been clearly evidenced in TPR profiles and XRD, so further analysis would be necessary to corroborate this hypothesis. On the other hand, regarding the effect of precipitating agent, the catalysts co-precipitated with carbon-containing precipitating agents, Na_2CO_3 and NH_2COONH_4, exhibit larger H_2 consumption.

Acid properties were also characterized by NH_3-TPD in order to study the influence of variables involved in co-precipitation method. All catalysts present similar NH_3 desorption profiles (not shown) than those reported in Sections 3.1.1 and 3.2.1. Table 3.13 shows total acidity of all samples, as well as the ratio between strong and weak acidity, the latter calculated considering 170 ^oC as the temperature above which NH_3 desorption occurs from strong acid sites.

Total acidity clearly decreases with the increase of calcination temperature. This decrease is firstly related to the loss of weak acidity, until 700 ^oC, and above this temperature, to the loss of both weak and strong acidity. These results are supported by the calculated strong/weak ratio, which firstly increases until the calcination temperature of 700 ^oC, and then decreases at 800 ^oC reaching a similar value than at 500 ^oC. It should be noted that the negative effect of calcination temperature on total acidity is associated to the detrimental effect that this variable has on specific surface (previously corroborated by N_2-physisorption), since total acidity per surface unit increases with calcination temperature.

On the other hand, ageing time and pH produce no relevant effect in total acidity. However, a clear trend in strong/weak ratio is observed in both families of catalysts. Longer ageing times promote strong versus weak acidity, whereas the increase of pH causes the opposite behaviour. The trends observed between both types of acidity are probably linked to manganese oxide crystal phase and its crystallinity degree, since this has been the only feature affected at structural level by the modification of both ageing time and pH. Thus, the contribution of strong acidity is promoted when the variation of these two variables promotes a decrease in the crystallinity of manganese oxide phase. These results suggest that in catalysts with similar interaction between Mn and Ce, such as those prepared changing ageing

time and pH, the crystallinity degree of segregated manganese oxide phase plays a key role in the contributions of the different types of acidity.

Table 3.13. Results of NH_3-TPD for co-precipitated 85Mn15Ce prepared modifying calcination temperature, ageing time, pH and precipitating agent.

Sample	Acidity (μmol NH_3/g)	Acidity (μmol NH_3/m^2)	Strong/weak
Calcination temperature			
500 °C	375.3	4.0	1.4
600 °C	168.6	3.1	1.8
700 °C	152.8	5.2	1.7
800 °C	94.4	4.8	1.4
Ageing time			
0 h	332.6	3.8	1.3
2 h	375.3	4.0	1.4
6 h	436.0	4.6	1.5
24 h	345.4	3.6	2.0
pH			
pH=7	301.1	3.5	2.4
pH=8	390.6	4.3	1.5
pH=9	375.3	4.0	1.4
Precipitating agent			
NaOH	150.4	3.4	2.2
NH_3	209.9	3.7	1.4
Na_2CO_3	231.3	3.9	1.0
NH_2COONH_4	375.3	4.0	1.4

Regarding the catalysts precipitated by different agents, the one precipitated with ammonium carbamate exhibits the highest acidity, which can be related to its higher specific surface area. Moreover, Mn_2O_3 is the main crystalline phase

together with fluorite in this catalyst, whereas it is Mn_5O_8 is in the others, so the phase of manganese oxide probably plays an important role in the acidity of the catalysts. On the other hand, the strong/weak ratio evidences the greater amount of strong acid sites in the sample co-precipitated with NaOH.

3.3.2. Catalytic performance of MnO_X-CeO_2 catalysts prepared modifying the variables involved in co-precipitation.

3.3.2.1. Analysis of NO and o-DCB conversions.

Among the four variables analysed in co-precipitation, only calcination temperature and precipitating agent have significant effects on catalytic activity in both reactions. For this reason, only NO and o-DCB conversion obtained with the catalysts prepared with different calcination temperature and precipitating agent are shown in Figure 3.31.

Regarding NO reduction, increasing the calcination temperature has a negative effect on NO conversion. Thus, catalysts calcinated at temperatures higher than 600 ^oC, unlike those calcinated below this temperature, do not reach total NO conversion in the whole range of low temperatures (below 250 ^oC). Similarly, in the high reaction temperature range, calcination temperatures above 600 ^oC lead to lower NO conversions between 300 and 400 ^oC.

The absence of total NO conversions at low temperatures was also observed in Section 3.2 after analysing the effect of metal composition. This behaviour was associated to low Mn content (which is the active metal for low temperature SCR) and/or low interaction between Mn and Ce. However, the fact that total NO conversion is reached with catalysts whose Mn content is the same, but calcined at lower temperatures, denotes that, in this case, the negative effect of calcination temperature on NO conversion is associated to the lower interaction degree between Mn and Ce, evidenced by the higher crystallinity degree of fluorite and Mn_2O_3 crystal phases measured by XRD.

The lower interaction between active metals at higher calcination temperature, also affects negatively to two key features for low temperature SCR. Firstly, the variability of Mn species with high oxidation state, as concluded by the disappearance of the contributions composing the first reduction peak of TPR

profile. Secondly, the amount of oxygen vacancies due to the lack of structural defects.

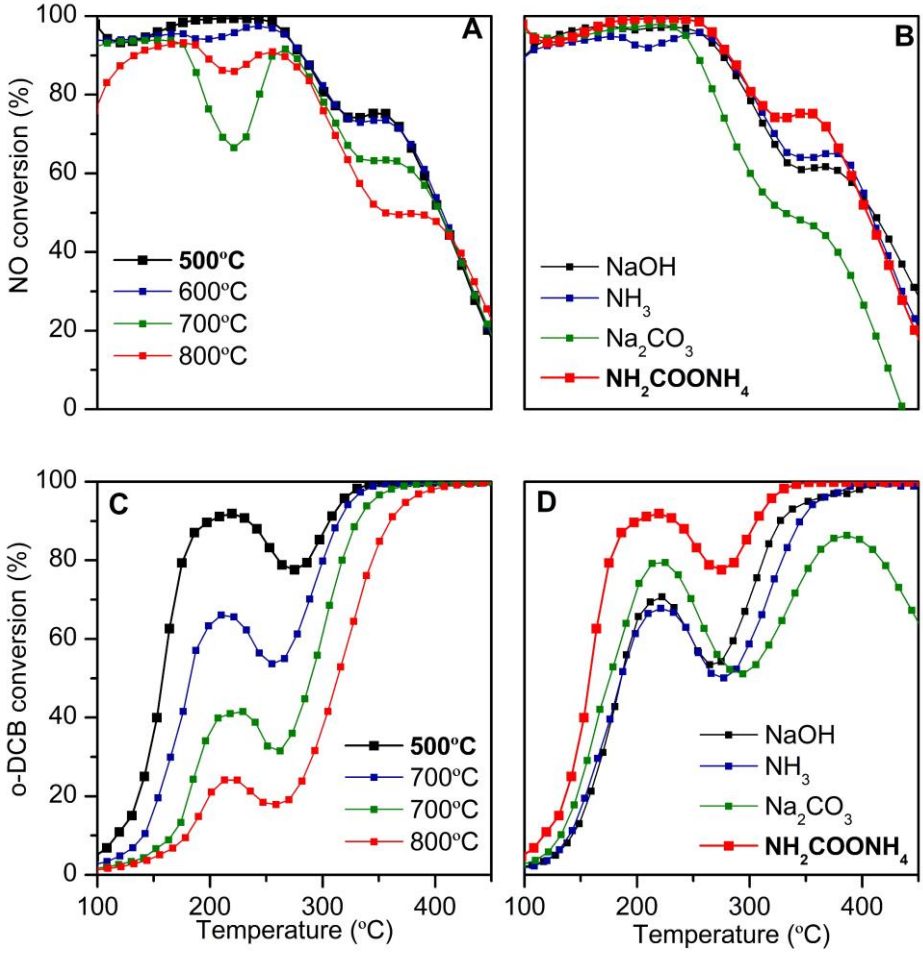

Figure 3.31. NO conversion at different A) calcination temperature and B) precipitating agent; and o-DCB conversion at different C) calcination temperature and D) precipitating agent; for 85Mn15Ce catalysts. Thick symbols: base sample.

Regarding the effect of precipitating agent, this variable does not affect NO conversion at low temperature. In this sense, total NO conversion is reached below 250 °C with all the samples. So, according to the previous discussion, all precipitating agents provide a good interaction between Mn and Ce. However, in

the high temperature range, NO conversion drops abruptly in the catalyst precipitated with sodium carbonate. In the remaining catalysts, the drop of NO conversion is lower and the catalyst co-precipitated with ammonium carbamate allows to obtain higher NO conversions. Thus, although NO conversion drop at high temperature is associated to SCR side-reactions, the catalyst co-precipitated with ammonium carbamate depresses SCR side reactions to a greater extent.

In the case of oxidation reaction, increasing calcination temperature affects negatively o-DCB conversion, shifting its profile to higher temperatures. Thus, T_{90} gradually increases from 307 ^{o}C in the catalyst calcinated at 500 ^{o}C, to 361 ^{o}C in that calcinated at 500 ^{o}C. Similarly, the increase of calcination temperature favours the decrease of o-DCB conversion at low temperature, from 91 to 23% in the catalysts calcined at 500 and 800 ^{o}C, respectively.

The analysis of the effect of preparation method and Mn content in catalytic activity (Sections 3.1 and 3.2) evidenced that the excellent catalytic performance of 85Mn15Ce (in comparison to other catalysts with different metal content) is associated with the high Mn content and the synergy between solid solution and manganese oxide phases. Moreover, it was proposed that the o-DCB conversion at low temperature was mostly related to the promotional effect provided by the solid solution phase.

Since Mn content is similar in all catalysts, the effect of calcination temperature on the solid solution phase becomes the key factor to understand the role of calcination temperature on oxidation reaction. As said above, characterization results corroborated the detrimental effect of calcination temperature on the interaction between Mn and Ce. Therefore, the detrimental effect on the oxidation reaction is caused by the lower amount of oxygen vacancies, which are involved in the replacement of surface-active oxygen consumed in the reaction and in the oxygen storage capacity of the catalysts. The worse oxidizing properties of the catalysts are also observed by the decrease in total acidity with the increase of calcination temperature, which also denotes a reduction in adsorption capacity.

On the other hand, it is important to note that the decrease of Mn and Ce interaction with calcination temperature additionally supports the fact that o-DCB conversion at low temperature is mostly promoted by the mixed oxide phase, because otherwise the same o-DCB conversion values should have been obtained

regardless of calcination temperature, as occurred in the analysis of the effect of Mn content on catalytic activity.

In the case of precipitating agent, the catalyst co-precipitated with ammonium carbamate favours o-DCB conversion in the whole range of temperatures, reaching total conversion at 340 ^{o}C. The catalysts co-precipitated with NaOH and NH_3 exhibit similar o-DCB conversion profiles, obtaining total conversion at 400 ^{o}C. On the other hand, the catalyst co-precipitated with sodium carbonate reaches a maximum o-DCB conversion around 85% at 450 ^{o}C, after which conversion decreases.

The better catalytic activity in the oxidation reaction of the catalyst co-precipitated with ammonium carbamate indicates a better synergy between mixed oxide and segregated manganese oxide phases. Regarding manganese oxide, both XRD and Skeletal FTIR showed Mn_2O_3 as the main crystal phase, whereas the remaining catalysts showed the Mn_5O_8 crystal phase. This could be an additional reason to justify the higher catalytic activity, although additional experiments should be performed to corroborate this hypothesis because there are no works in the literature comparing the catalytic activity of these two manganese oxide phases.

The catalysts co-precipitated with sodium carbonate and ammonium carbamate exhibit higher o-DCB conversion at low temperature than those co-precipitated with NaOH and NH_3. This result suggests that the interaction between the active metals is higher in the former two catalysts, which could be associated to the chemical compounds formed after precipitation. Thus, ammonium carbamate and sodium carbonate have a carbon-based precipitate, whereas NaOH and NH_3 promote the precipitation of Mn and Ce as hydroxide compounds. Carbon-based precipitate provides a more voluminous structure that makes migration of metal ions during the calcination stage more difficult, which avoids the segregation effects.

However, the high o-DCB conversion at low temperature of the catalyst precipitated with sodium carbonate in comparison to those co-precipitated with NaOH and NH_3 contrasts with its low catalytic activity at high temperature. This fact could be related to the retention of Na ions in the carbon-based precipitate structure, which would affect catalytic properties. In fact, the presence of Na ions has been reported to difficult the re-oxidation of Co_3O_4 and reduce oxygen mobility [175]

Therefore, based on the above results, the best catalytic performance in the simultaneous NO reduction and o-DCB oxidation are obtained with low calcination temperatures and with the use of ammonium carbamate as precipitating agent. The reasons are associated to the promotion of Mn and Ce interaction, and the use of carbon-based and Na-free precipitating agent, which favours the formation of Mn_2O_3 as main crystal phase.

3.3.2.2. Analysis of SCR and o-DCB oxidation by-products.

The analysis of the effect of variables involved in co-precipitation on by-products formation in SCR and o-DCB oxidation is shown below. As observed in NO and o-DCB conversion, pH and ageing time have no effect on by-product generation, so only the influence of calcination temperature and precipitating agent on by-products generation will be studied.

N_2O and NO_2 productions are shown in Figure 3.32. Regarding calcination temperature, there is no clear trend between this variable and N_2O production (Figure 3.32A). On the contrary, NO_2 production (Figure 3.32C) is higher and shifted to higher temperature as calcination temperature increases. Therefore, the latter result denotes a decrease in the oxidising capacity of the catalysts with the increase of calcination temperature. This is associated to the lower oxygen mobility due to the lower interaction of Mn and Ce as a consequence of their segregation.

In the case of precipitating agent, all catalysts exhibit N_2O production profile with two peaks around 200 and 300 ^{o}C (Figure 3.32B), except the catalysts co-precipitated with sodium carbonate, whose production profile is only composed by a peak at 250 ^{o}C. Similar N_2O production is observed at high temperature, whereas at low temperatures, the catalyst precipitated with ammonium carbamate presents the highest N_2O production. On the other hand, same production profiles of NO_2 are observed (Figure 3.32D), although in the catalyst co-precipitated with sodium carbonate, NO_2 production occurs at lower temperatures and to a greater extent than in the other catalysts. Interestingly, this result matches very well with the drop of NO conversion of catalyst co-precipitated with sodium carbonate at lower temperature (Figure 3.31B), which evidences the connection between NO conversion drop at high temperature and by-products generation.

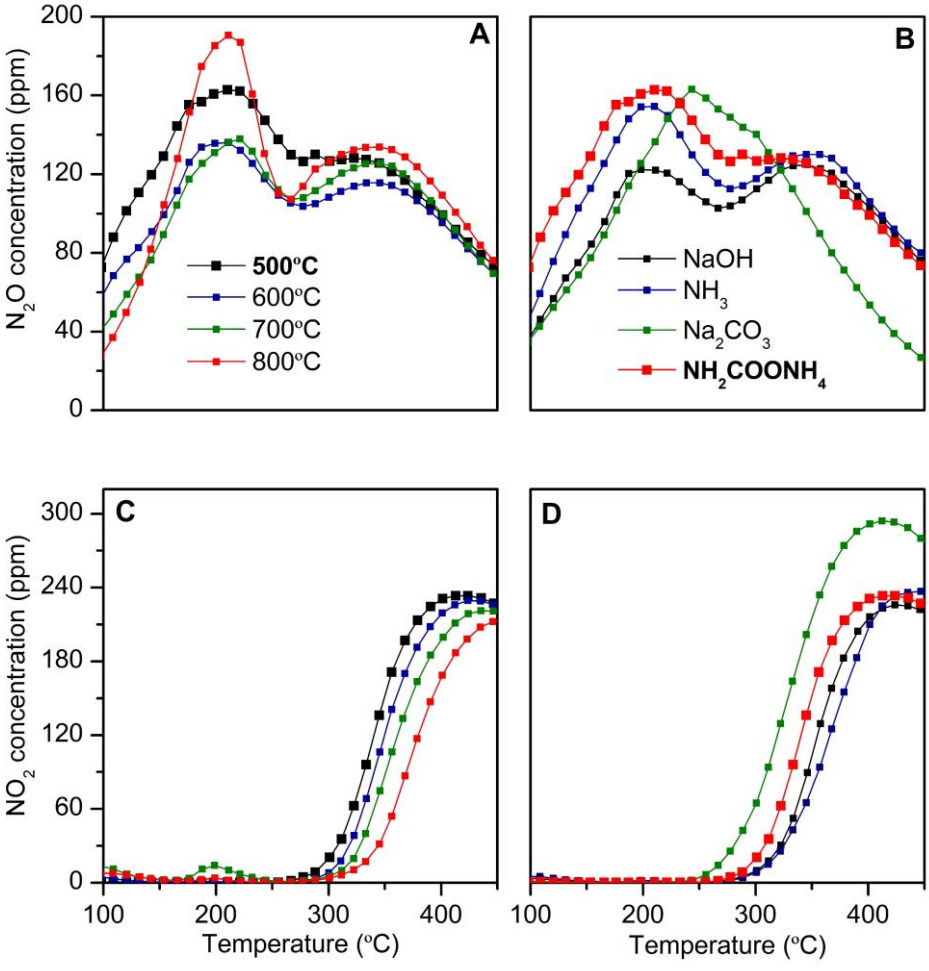

Figure 3.32. N_2O generation at different A) calcination temperature and B) precipitating agent; and NO_2 generation at different C) calcination temperature and D) precipitating agent; for 85Mn15Ce catalysts. Thick symbols: base sample.

Regarding oxidation reaction, the catalysts with different calcination temperature show typical CO selectivity profiles, with a plateau around 20% below 325 ºC (Figure 3.33A). At high temperature, CO selectivity strongly drops. It should be noted that the increase of calcination temperature slightly increases CO selectivity, which denotes its detrimental effect on oxidising capability also observed in NO_2 production. As for chlorinated organic compounds (Figure 3.33C), only the catalyst

calcinated at 800 °C has a notable production, reaching values of selectivity around 20% at 300 °C.

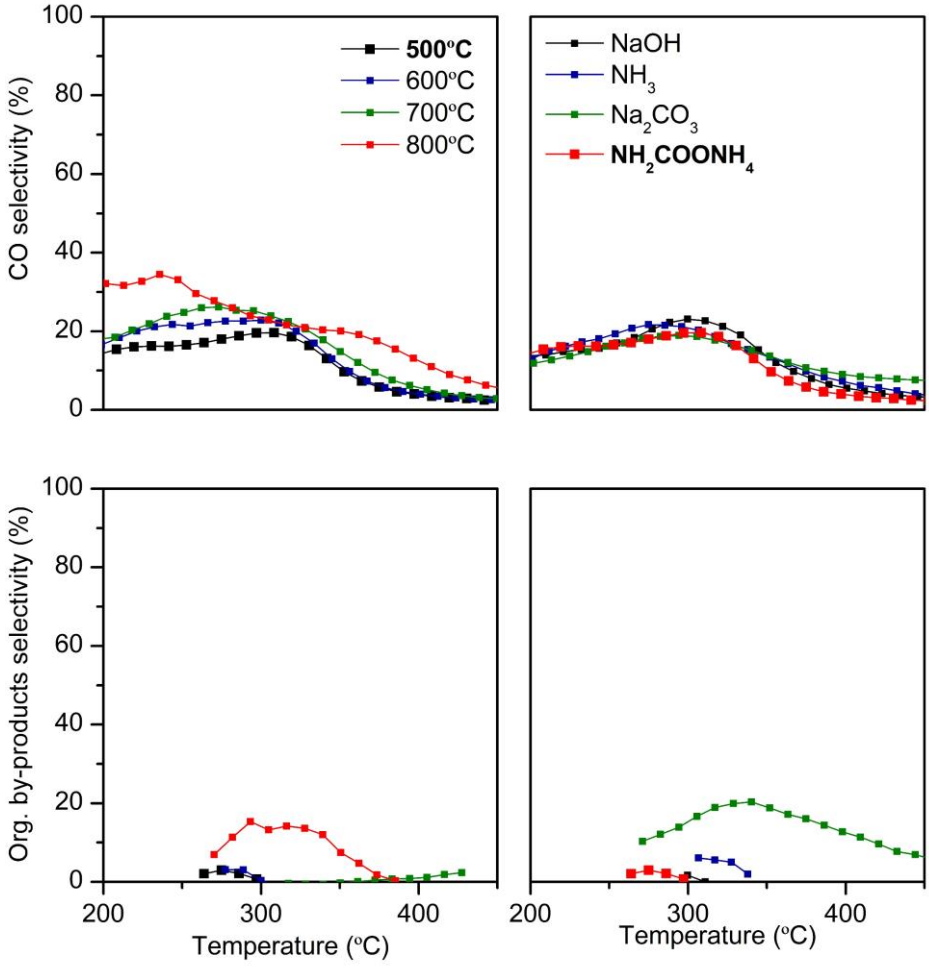

Figure 3.33. CO_2 selectivity at different A) calcination temperature and B) precipitating agent; and Chlorinated organic by-product selectivity at different C) calcination temperature and D) precipitating agent; for 85Mn15Ce catalysts. Thick symbols: base sample.

Regarding catalysts co-precipitated with different agents, similar CO selectivity profiles are obtained for all catalysts (Figure 3.33B). On the other hand, the catalyst co-precipitated with sodium carbonate exhibits the highest production of

chlorinated organic compounds above 300 ºC in comparison to the other precipitating agents (Figure 3.33D).

3.4. GLOBAL VIEW AND CONCLUSIONS.

MnO_X-CeO_2 catalytic formulation has been optimised in this chapter, in order to obtain the maximum catalytic performances for simultaneous NO reduction and o-DCB oxidation. For this purpose, several preparation methods, metal contents of Mn and Ce and, finally, the variables involved in the selected preparation method were evaluated. All the catalysts synthesized were characterized and tested in catalytic experiments in order to correlate their activities with their catalytic properties, and to select the optimum one.

The assessment of preparation method has corroborated that the catalysts prepared by sol-gel and co-precipitation methods are the most active ones, with NO and o-DCB conversion above 80% in the temperature ranges of 225-235 ^{o}C and 200-261 ^{o}C, respectively. This is associated to both methods leads to catalysts in which there is a high interaction between Mn and Ce in all the structure (surface and bulk), unlike physical mixing and impregnation methods, which promote hardly any interaction and only surface interaction between Mn and Ce, respectively.

The shift of the peaks associated to fluorite phase and the decrease of its crystal size, observed by XRD and Raman, have shown that the interaction between Mn and Ce promotes a common mixed oxide structure with a certain degree of structural defects, which favours a high oxygen mobility, that is, increases the activity of surface oxygen species and makes oxygen replacement easier. This fact is important for both reactions, hence the higher catalytic activity of catalysts prepared by co-precipitation and sol-gel at low temperature. Moreover, the high oxygen mobility improves redox properties and strong acidity in comparison to Mn and Ce pure oxides.

After selecting the most suitable methods to prepare the MnO_X-CeO_2 catalyst, the next step deals with the assessment of metal content (Mn and Ce) to obtain the best catalytic performance. The results showed that the catalysts with high Mn content, 85Mn15Ce, have higher catalytic activity in both reactions. Specifically, the catalyst prepared by co-precipitation led to higher o-DCB conversion at low

temperature than the one prepared by sol-gel, which ensures conversion above 80% of NO and o-DCB between 180-250 ^{o}C.

Therefore, the 85Mn15Ce catalyst prepared by co-precipitation has been selected as the optimal one. The excellent catalytic performance of this catalyst is associated, on the one hand, to the better morphological properties provided by co-precipitation method (higher surface area and pore volume); on the other hand, to the fact that high Mn content favours different crystalline structures, such as the solid solution phase with several degrees of interaction between Mn and Ce, and manganese oxide crystalline aggregates (clearly identified by STEM-HAADF, XRD, Raman and FTIR); whose synergy favours not only oxygen mobility, but also the coexistence of different Mn and Ce species (Mn^{4+}, Mn^{3+}, Ce^{4+} and Ce^{3+}). These species, that were corroborated at surface level by XPS and at bulk level by H_2-TPR, promote the presence of Mn^{4+}/Mn^{3+} and Ce^{3+}/Ce^{4+} redox pairs, which improve redox properties.

In the same way than redox properties, acidity also increases with Mn content due to the promotion of strong acidity, which could be associated to the solid solution phase due to its high oxidizing capacity. The analysis of adsorbed pyridine has corroborated the only presence of Lewis acid sites, whose strength increases with Mn content.

As for by-products, N_2O and NO_2 are the main by-products in SCR. N_2O is generated in all temperature range and its production is practically independent of Mn content, whereas NO_2 is only generated at high temperature and its production increases with Mn content, due to the improvement of oxidizing capacities of catalysts with Mn. In the case of the oxidation reaction, CO and chlorinated organic compounds are the main by-products. In the same way, the enhancement of oxidizing capacities provided by Mn leads to a lower production of chlorinated organic compounds, although it increases the production of CO.

According to the selection of co-precipitation as the best preparation method, some of the variables involved in this method were analysed (ageing time, pH and precipitating agent) together with calcination temperature. These four variables generate different changes at structural level that affect to a greater or lesser extent the rest of catalytic properties.

The increase of calcination temperature leads to the segregation of crystalline phases, decreasing the interaction between Mn and Ce. This fact reduces structural defects, which affects negatively to morphology (lower surface area and pore volume) and reduces redox and acid properties due to the lower oxygen mobility. As a consequence, the increase of calcination temperature has a negative impact on both NO conversion, especially at high temperature, and o-DCB conversion. On the other hand, the precipitating agent mainly affects manganese oxide crystal phase. The catalyst co-precipitated with ammonium carbamate exhibited the best catalytic performance. This catalyst was the only one to present Mn_2O_3 instead of Mn_5O_8 phase. The presence of Mn_2O_3 seems to be a key factor, because that catalyst exhibited the highest surface area, redox ability and acidity. Therefore, the selected values of calcination temperature and precipitating agent were 500 ^oC and ammonium carbamate, respectively.

Regarding ageing time and pH, these variables did not affect catalytic activity but affected structural properties. Thus, lower ageing time and higher pH promotes a higher crystallinity degree of manganese oxide phase, which leads to the presence of different manganese species in high oxidation state, as observed by H_2-TPR. Therefore, on this basis, the selected values for ageing time and pH are those promoting this effect, that is, 2 hours and 9, respectively.

Chapter 4

INSIGHTS ON SIMULTANEOUS NO REDUCTION AND o-DCB OXIDATION WITH 85Mn15Ce

Chapter 4

INSIGHTS ON SIMULTANEOUS NO REDUCTION AND o-DCB OXIDATION WITH 85Mn15Ce

ABSTRACT

This chapter aims the in-depth understanding of simultaneous NO reduction and o-DCB oxidation over 85Mn15Ce catalyst. Several experiments, with different feed streams and operating modes, were carried out to study the influence that these two reactions have on each other, the origin of by-products and the effect of each reactant. The effect of other gases, such as CO_2 and water, has also been evaluated.

The analysis of SCR by-products has revealed that N_2O originates from NSCR and NH_3 oxidation, whereas NO_2 comes from NO and NH_3 oxidation. o-DCB competes with NO and NH_3 for the active sites, decreasing NO conversion and the production of SCR by-products. In the case of o-DCB oxidation, the presence of NO and NH_3 has a positive effect due to NO_2 formation (at low temperature) and the removal of surface Cl, respectively. Moreover, TOS experiments have evidenced the presence of catalyst deactivation, which affects oxidation reaction at low temperature due to the deposition of chlorine and carbon-based compounds.

The effect of CO_2 is not important, while the increase of oxygen concentration promotes the increase of catalytic performance in the oxidation reaction. In the case of water, it has a negative effect in SCR and o-DCB oxidation because it competes for the active sites, although it has a positive effect in oxidation reaction, as it removes the deactivating carbon-based compounds.

4. INSIGHTS ON CATALYTIC PERFORMANCE OF 85Mn15Ce CATALYST IN SIMULTANEOUS NO REDUCTION AND o-DCB OXIDATION.

Chapter 3 has corroborated that MnO_X-CeO_2 catalytic formulation allows to reach high conversion of NO_X and o-DCB in the same temperature range, in the studied conditions. In fact, conversions above 80% and around 200 ^oC are achieved with 85Mn15Ce prepared by co-precipitation. These results improve those obtained by Gallastegi-Villa and co-workers [119] with the commercial catalytic formulation for SCR process in MSWI plants, i.e. V_2O_5/TiO_2, in the same operating conditions than those used in this work. The same authors also state the difficulty of reaching high NO and o-DCB conversion in the same temperature range.

The complexity of simultaneous catalytic removal of NO and o-DCB has been also shown in Chapter 3. On the one hand, because the nature of the reactions involved in this process is completely different: NO must be reduced and o-DCB oxidized, the reactions tend to occur at different conditions. As a result, the temperature range with the maximum conversion of both compounds does not match very well. On the other hand, because there are side reactions, which significantly affect selectivity, unwanted by-products such as N_2O, NO_2, CO and chlorinated organic compounds are generated. All these difficulties mean that there are few works addressing the study of NO_X reduction performed simultaneously with the catalytic oxidation of organic compounds, the majority of which focus on studying VOCs oxidation reaction with active catalysts for SCR [75, 101, 112].

Chapter 4 aims to analyse in detail the aspects related to the simultaneous removal of NO and o-DCB, beyond those addressed in Chapter 3 (used to discern the most active catalyst). These aspects are focused on widening the knowledge about the influence of o-DCB oxidation on NO reduction and vice versa, the side-reactions involved in the production of different by-products, the effect of reactant concentrations and the presence of other compounds involved in the process. For this purpose, several experiments have been carried out with different feed composition, both by increasing the reactor temperature, as in a light-off experiment, and under stationary conditions, measuring the reactor outlet composition over time-on-stream (TOS). The TOS experiments have also provided

information about stability of the catalyst with respect to each principal reaction and, also, with respect to secondary reactions.

4.1. DETAILED ANALYSIS OF NO REDUCTION AND o-DCB OXIDATION WITH 85Mn15Ce.

The detailed analysis of simultaneous removal of NO and o-DCB has been carried out with the optimal catalyst concluded in Chapter 3, i.e., the co-precipitated 85Mn15Ce. Figure 4.1 shows the conversion profiles for both compounds as a function of temperature.

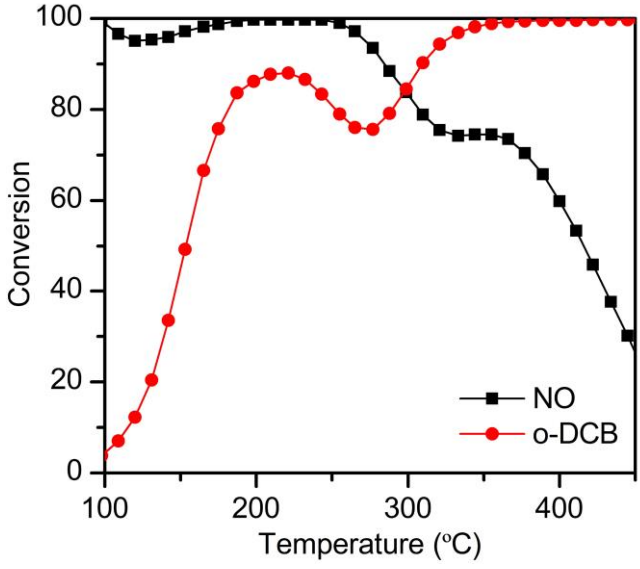

Figure 4.1. NO and o-DCB conversion over 85Mn15Ce catalyst.

NO conversion profile of 85Mn15Ce exhibits similar trend than others reported in the literature, for example: Cu and Fe supported on zeolite [176], V and W/TiO_2 [118, 177] and Mn oxide-based catalysts, either supported on Al_2O_3, TiO_2 and SAPO-34 [178, 179] or doped with other metals, such as Co, Ti and Fe [180-182]. In general terms, NO conversion is total below 250 °C, whereas the increase in temperature leads to a drop in NO conversion. However, the values of NO conversion reported in the literature are slightly lower than that obtained for 85Mn15Ce catalyst in this work. In the case of the 3% VO_X/TiO_2 catalyst reported by Gallastegi-Villa and co-

workers [119], that was tested in the same conditions as in this work, NO conversion was even below 70%. This reveals that the proposed 85Mn15Ce catalyst has an excellent activity for low temperature SCR.

Another notable difference between the NO conversion profile of this work and those reported in the literature is the NO conversion plateau between 320 and 370 ^{o}C, in which conversion remains constant around 75%. A possible explanation for this behaviour could be associated to the influence of o-DCB in NO reduction. In order to verify this hypothesis, NO reduction in the absence of o-DCB should be analysed and compared with the results obtained in the presence of o-DCB.

Regarding oxidation reaction, different T_{90} values, ranged from 210 to 440 ^{o}C, are reported in the literature for Mn and Ce-based catalysts [154, 183]. Such a big difference is due to the wide range of operating conditions reported in the literature [183]. The T_{90} value of the proposed 85Mn15Ce catalyst (325 ^{o}C) is enclosed within those reported in the literature and is considerably better than the one obtained with V-based catalysts in our previous experiments (375 ^{o}C), which were performed with the same operating conditions [119].

There is a notable difference between the light-off curves reported in the literature and the ones showed in this work. The light-off curves reported in the literature show a regular sigmoid of "S" shape. In the case of the catalysts tested in this work, the light-off curves exhibit a particular shape with two steps, as shown in Figure 4.1. In the first step, conversion increases with temperature, until a maximum of 87% at 200 ^{o}C. The second step occurs above 265 ^{o}C, where conversion also increases with temperature until total conversion is reached. Between these two steps, o-DCB conversion decays suggesting a decrease in reaction rate.

The particular profile of o-DCB conversion has already been observed in the light-off profiles of CO oxidation in automotive exhaust converters, in which multiple reactions occur simultaneously, such as oxidation of unburned hydrocarbons, oxidation and reduction of NO, etc. González-Velasco and co-workers [184] ascribed the two steps to two types of CO oxidation. At low temperature, CO is oxidized by oxygen, whereas at high temperature, CO is oxidized through NO reduction and water gas shift reactions. The conversion drop at intermediate temperature was attributed to strong CO adsorption on the catalysts, which inhibits the adsorption of gas oxygen. The same authors also identified an inhibition effect of olefins due to the competition with gas oxygen for the active site. Buzková-

Arvjová and co-workers [185] also attributed the drop in CO conversion at intermediate temperatures to the inhibition effect of C_3H_6 and Brunet and co-workers [186] also observed such inhibitory effect in the oxidation of VOC mixtures.

Then, a change in the reaction mechanism or an inhibition by other adsorbed species, such as those involved in SCR, can be the reason of the drop in o-DCB conversion at intermediate temperature. In order to verify this hypothesis, o-DCB oxidation in the absence of SCR should be analysed and compared with the results obtained in simultaneous operation.

Therefore, the above discussion highlights the need to compare the results of simultaneous operation of NO reduction and o-DCB oxidation with those obtained by operating each reaction independently. This issue will be discussed in Sections 4.1.1 and 4.1.2.

4.1.1. Independent and simultaneous NO reduction.

This section studies the effect of o-DCB oxidation on both SCR (Equation 1.1) and side reactions that promote the generation of N_2O and NO_2.

Firstly, it is important to identify which reactions can generate the SCR by-products. N_2O can be generated from the non-selective catalytic reduction of NO (NSCR) (Equation 4.1), NH_3 oxidation (Equation 4.2), and also from NO decomposition and/or disproportionation (Equations 4.3 and 4.4).

$$4NH_3+4NO+3O_2 \rightarrow 4N_2O+6H_2O \quad (4.1)$$

$$2NH_3+2O_2 \rightarrow N_2O+3H_2O \quad (4.2)$$

$$2NO \rightarrow N_2O+1/2O_2 \quad (4.3)$$

$$3NO \rightarrow N_2O+NO_2 \quad (4.4)$$

On the other hand, NO_2 could be generated by NH_3 oxidation (Equation 4.5) and from NO oxidation (Equation 4.6). In addition, it should be noted that the oxidation of NH_3 can also generate NO (Equation 4.7) or even N_2 (Equation 4.8). These reactions have the additional drawback of consuming one reactant to a greater extent than the other, resulting in a molar NO/NH_3 ratio different from 1 (usual value for SCR).

$$4NH_3+7O_2 \rightarrow 4NO_2+6H_2O \quad (4.5)$$

$$NO+1/2O_2 \rightarrow NO_2 \quad (4.6)$$

$$4NH_3+5O_2 \rightarrow 4NO+6H_2O \quad (4.7)$$

$$4NH_3+3O_2 \rightarrow 2N_2+6H_2O \quad (4.8)$$

According to that, in addition to NO reduction, two additional experiments have been selected in order to discuss the origin of the by-products generated in NO reduction, which are: NH_3 oxidation and NO oxidation. The composition of the feed stream for each of these experiments are as follows:

- NO reduction in the absence (300 ppm NO+300 ppm NH_3+10% O_2) and in the presence of o-DCB (300 ppm NO+300 ppm NH_3+10% O_2+100 ppm o-DCB).
- NH_3 oxidation in the absence (300 ppm NH_3+10% O_2) and in the presence of o-DCB (300 ppm NH_3+10% O_2+100 ppm o-DCB).
- NO oxidation in the absence (300 ppm NO+10% O_2) and in the presence of o-DCB (300 ppm NO+10% O_2+100 ppm o-DCB).

The results are shown in Figure 4.2, which is composed by several subplots. The subplots are arranged in a matrix form in order to facilitate a quantitative comparison between the different concentration profiles. There are three rows, A, B and C, where the profiles of NO, N_2O and NO_2 concentrations are shown, respectively. On the other hand, column 1 shows the results of NO reduction (black colour), whereas the subplots in column 2 show the results of the two additional reactions, NH_3 oxidation (green colour) and NO oxidation (blue colour). Filled symbols refer to the experiments in the absence of o-DCB, and open symbols refer to the experiments in the presence of o-DCB.

It should be noted that, in this section, catalytic activity in NO reduction is expressed as NO concentration Figure 4.2(A1), instead of NO conversion as shown in Figure 4.1, in order to facilitate comparison, since the results of NH_3 oxidation cannot be expressed as NO conversion, as NO is not a reactant but a product.

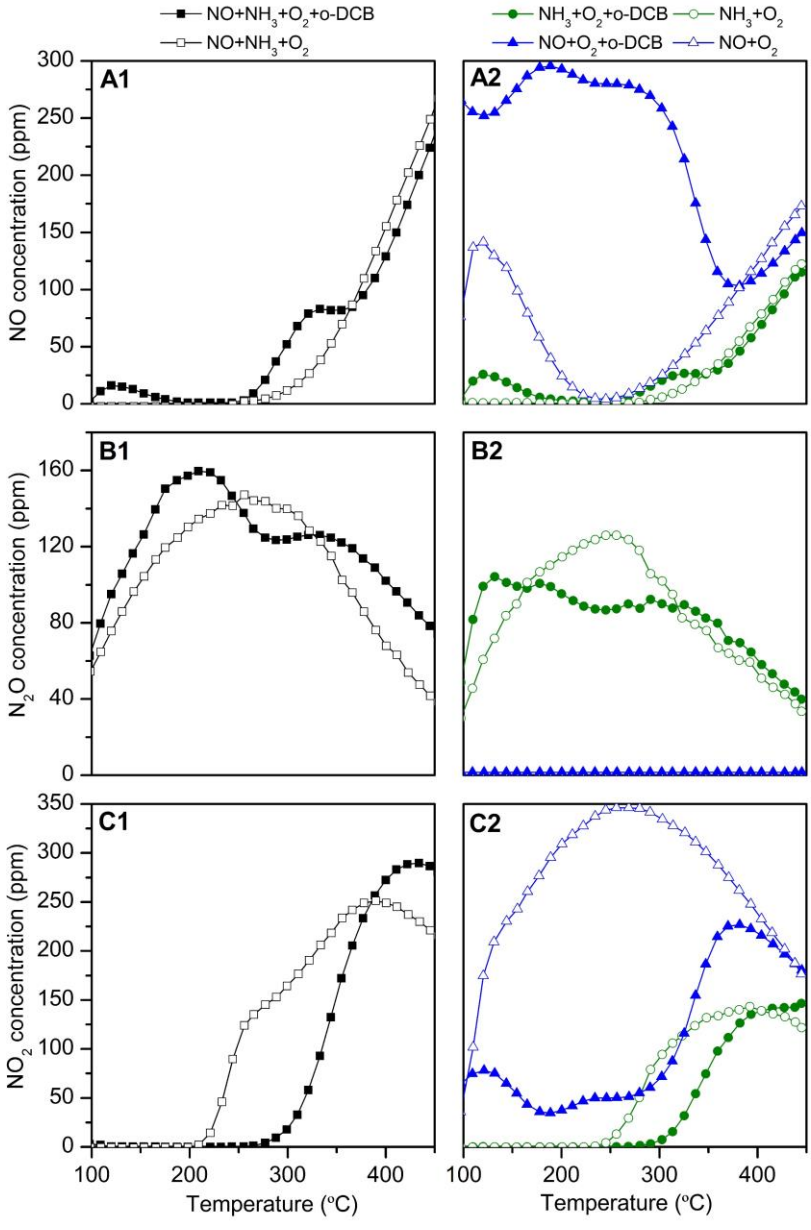

Figure 4.2. NO concentration (row A), N_2O concentration (row B) and NO_2 concentration (row C) in NO reduction (column 1) and NH_3 and NO oxidation (column 2). Reactions performed in the presence (filled symbols) and in the absence (open symbols) of o-DCB and over 85Mn15 catalyst.

In NO reduction (Figure 4.2(A1)), NO concentration is practically zero below 250 ^{o}C both in the presence and in the absence of o-DCB. However, at high temperature, where NO concentration increases (that is, when NO conversion drops), the characteristic plateau is only observed in the presence of o-DCB, in simultaneous operation. This result suggests that o-DCB is involved in this behaviour.

Figure 4.2(A2) shows the evolution of NO concentration during NO and NH_3 oxidation. In the case of NH_3 oxidation, two interesting features are observed. On the one hand, NO is generated at the same temperature that the concentration of NO starts to increase in SCR (Figure 4.2(A1)). This fact clearly corroborates that the typical drop in NO conversion in SCR at high temperature is mainly due to NH_3 oxidation. On the other hand, it should be noted that the NO profile from NH_3 oxidation has a plateau in the presence of o-DCB, not observed in the absence of o-DCB. This trend is similar to that observed in NO reduction and allows to propose a more accurate explanation for the plateau observed during the NO conversion drop at high temperature in SCR, which is associated to the influence of o-DCB on NH_3 oxidation.

Regarding the selectivity of NO reduction, N_2O is generated over the whole temperature range, although the production profile is different depending on the absence or the presence of o-DCB (Figure 4.2(B1)). In the absence of o-DCB, the N_2O profile has a single maximum, whereas in the presence of o-DCB the N_2O profile is clearly composed by two contributions. This different trend suggests that o-DCB affects the reactions involved in N_2O production.

In this sense, Figure 4.2(B2) exhibits the N_2O production profiles from NO and NH_3 oxidation. NO oxidation produces no N_2O, independently of the presence or the absence of o-DCB. This result also discards that decomposition and disproportation of NO contribute to the generation of N_2O. On the contrary, NH_3 oxidation promotes N_2O generation in all temperature range, although it is slightly lower in the presence of o-DCB, specifically between 175 and 225 ^{o}C, which suggests a competition between NH_3 and o-DCB for the active sites.

Moreover, it is important to note that the production of N_2O from NH_3 oxidation (Figure 4.2(B2), in the presence and in the absence of o-DCB) is lower than that obtained from NO reduction (Figure 4.2(B1)). This evidences an additional side-reaction contributing to N_2O generation besides NH_3 oxidation. This side-reaction is the non-selective catalytic reduction of NO (NSCR). Since the N_2O production

from NO reduction is higher than that from NH_3 oxidation in all temperature range, both side-reactions occur in all temperature range, although the contribution of NSCR becomes more important at low temperature and in the presence of o-DCB.

On the other hand, the production of NO_2 only occurs at high temperatures, although in the presence of o-DCB it is even shifted to higher temperatures (Figure 4.2(C1)). This result is probably associated to a competition between o-DCB and the compounds involved in NO_2 generation for the same active sites.

As for the reactions involved in NO_2 generation, both NO and NH_3 oxidations contribute to NO_2 production at high temperature (Figure 4.2(C2)). The presence of o-DCB inhibits the formation of NO_2 and shifts its production profile to higher temperature, especially in NO oxidation. These results corroborate that o-DCB oxidation probably occurs on the same active centres that generate NO_2 in both NO and NH_3 oxidations, as it was previously stated for N_2O generation from NH_3 oxidation.

Finally, Figure 4.2(C2) also evidences the production of a certain amount of NO_2 from NO oxidation below 250 ^{o}C in the presence of o-DCB. However, no NO_2 is detected at these temperatures in NO reduction in the presence of o-DCB (Figure 4.2(C1)). This result denotes the high tendency of NO to be reduced at low temperature in the presence of NH_3, which highlights the suitability of this catalytic formulation to perform low temperature SCR.

Therefore, this section has shown evidence that o-DCB competes with the reagents involved in SCR. As a result, NO conversion decreases at high temperature in the presence of o-DCB. This effect was not observed at low temperature, where the catalytic activity is very high and, thus, NO is completely removed. Later, in Section 5.2, the possible presence of this negative effect of o-DCB in the low-temperature range will be checked by increasing o-DCB concentration. Moreover, the characteristic plateau, not reported in the literature, appearing in NO conversion when it drops at high temperature has been corroborated to be also related to the influence of o-DCB, specifically to its effect on NH_3 oxidation side reaction.

Due to the competition between o-DCB and the reagents involved in SCR, by-product production in the presence of o-DCB decreases, especially NO_2 generation. Regarding the origin of SCR by-products, two important conclusions have been obtained: (1) N_2O is produced by NH_3 oxidation and NSCR in all temperature range;

(2) NO_2 production comes from NO and NH_3 oxidation, which mainly occur at high temperature.

4.1.2. Independent and simultaneous o-DCB oxidation.

In this section, the effect of SCR on o-DCB oxidation, in terms of catalytic activity and selectivity, will be discussed. The results are shown in Figure 4.3.

Figure 4.3A shows that o-DCB conversion exhibits the same shape in the presence and in the absence of SCR, although the conversion profile is shifted to lower temperatures when the reaction occurs simultaneously with SCR, which indicates that NO and/or NH_3 favours o-DCB oxidation. Thus, this result evidences that o-DCB oxidation and SCR are not independent, with one affecting the other, which was also observed by the influence of o-DCB in NO conversion at high temperature in the previous section (Figure 4.2(A1)). The positive effect of NO on VOCs oxidation is reported in the literature, specifically in chlorobenzene and pentachlorobenzene oxidation over $VO_X/WO_3/TiO_2$ catalysts [115, 187].

Moreover, o-DCB conversion profiles obtained in the presence and in the absence of SCR show the above described drop at intermediate temperatures (Section 4.1). These results corroborate that this behaviour is not related to an inhibitory effect of the compounds involved in SCR (NO and NH_3); so, the hypothesis of a change in the reaction pathway of o-DCB oxidation becomes more feasible.

According to experimental results (Figure 4.3A), the change in the reaction pathway depends on temperature. However, it may actually be related to the different metal oxide phases present in the catalyst, which exhibit different oxidative capabilities and become active at different temperatures. These phases were identified in Chapter 3: Mn and Ce oxide in high interaction (solid solution or mixed oxide phase) and Mn oxide aggregates. In fact, in Chapter 3, Mn in high interaction with Ce was evidenced to mostly contribute to o-DCB oxidation at low temperature.

Therefore, these results suggest that the change in the oxidation pathway is associated to the different metal oxide phases of the studied catalyst; hence, this behaviour has not been reported with other catalytic formulations. The oxide phase with high interaction between Mn and Ce would have a higher contribution in the oxidation reaction at low temperature (first step of o-DCB conversion profile), due

to its high oxidative capability, whereas the other oxide phases, such as segregated Mn oxide, would become active at higher temperatures (second step of o-DCB conversion profile).

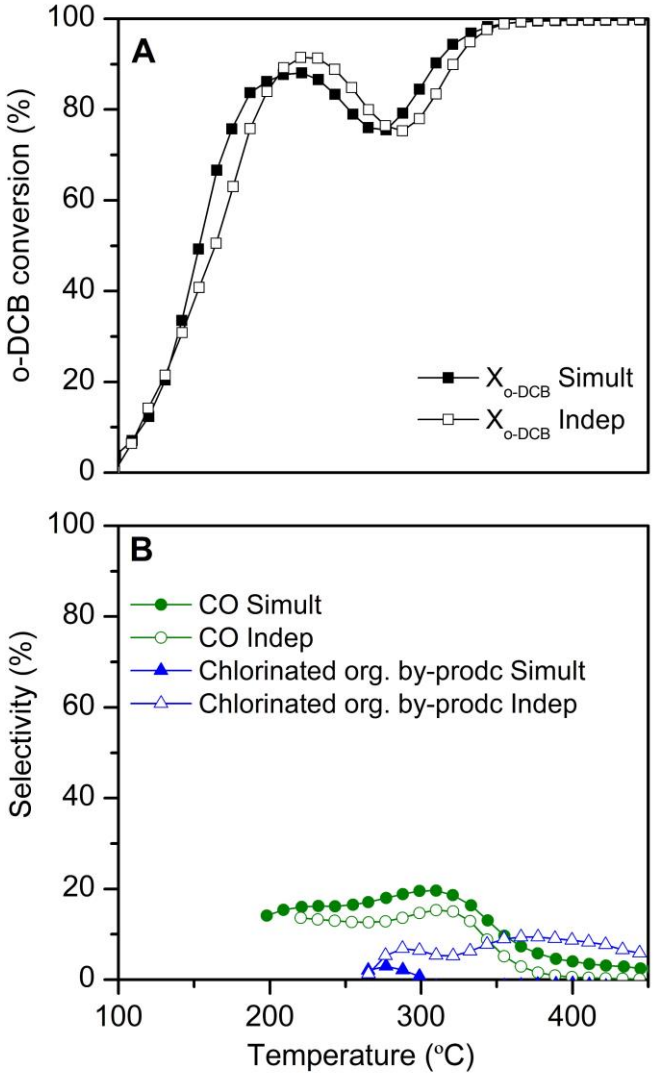

Figure 4.3. Comparison of A) o-DCB conversion and B) by-products from o-DCB oxidation performed independently and simultaneously with NO reduction over 85Mn15Ce catalyst.

Nonetheless, additional experiments would be necessary to corroborate this hypothesis, such as TOS experiments, which allow to test how the activity of each oxide phase is affected by time. The results of these experiments will be discussed in Section 4.2. Another interesting analysis would be the study of surface species by FTIR in order to check if there are differences in the intermediate species belonging to each reaction pathway. This issue will be addressed in Chapter 5.

On the other hand, by-products formation in o-DCB oxidation and the influence of SCR are analysed next. As reported in Chapter 3, o-DCB oxidation mainly generates CO_2 (desired product), although CO and chlorinated organic compounds are also produced to a lesser extent from partial oxidation of o-DCB. Moreover, it should be noted that, when o-DCB oxidation was performed simultaneously with SCR, there was no evidence of Cl_2 formation. The generation of Cl_2 through Deacon reaction is quite common in oxidation reactions of chlorinated hydrocarbons; so its absence is probably associated to the presence of SCR. In fact, ammonium chloride has been detected as a white precipitate at the reactor outlet. This fact explains that Cl_2 is not formed, due to the reaction between the hydrogen chloride generated in o-DCB oxidation and NH_3.

Figure 4.3B shows the selectivity towards CO and chlorinated organic compounds as a function of temperature. In o-DCB oxidation performed simultaneously with SCR, CO selectivity is around 20% below 325 ^{o}C, whereas in the absence of SCR the production of CO slightly decreases, with a selectivity around 17%. Above this temperature, CO selectivity strongly decreases due to the promotion of total oxidation of o-DCB. In the case of chlorinated organic by-products, when the oxidation reaction is performed in the absence of SCR, the production of these compounds occurs above 250 ^{o}C and is practically constant, with a selectivity close to 10%. However, in the presence of SCR, the selectivity towards chlorinated organic compounds does not exceed 5%, and these products are only observed between 250 and 300 ^{o}C.

Interestingly, the presence of SCR causes an opposite effect on the analysed by-products, decreasing the generation of chlorinated organic compounds, but increasing that of CO. This fact could be associated to SCR leading to the oxidation of chlorinated organic compounds to CO.

Finally, in order to increase the knowledge about the selectivity of o-DCB oxidation, an identification of the main chlorinated organic compounds has been carried out.

For this purpose, the same GC-MS protocol used for the quantification of o-DCB has been used. The identification of chlorinated organic compounds was based on their characteristic mass spectrum. The analysis was carried out at 300 ºC (Figure 4.3 confirms the formation of chlorinated organic compounds at this temperature) both in the presence and in the absence of SCR.

The resulting chromatograms are shown in Figure 4.4. Three compounds have been identified: tetrachloromethane, tetrachloroethylene and trichlorobenzene. In the presence of SCR, tetrachloromethane formation is favoured over the other compounds. This result evidences the increased oxidative capability of the catalyst in the presence of SCR, as tetrachloromethane is the chlorinated organic compound with the lowest number of carbon atoms.

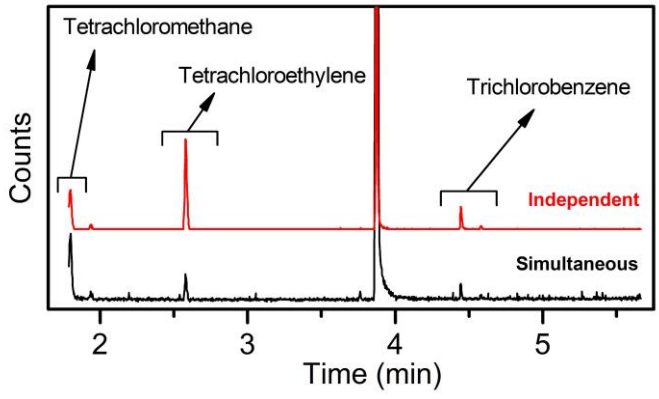

Figure 4.4. Chromatograms of o-DCB oxidation in the presence and in the absence of SCR with the 85Mn15Ce catalyst at 300 ºC.

4.2. CATALYST STABILITY ON SIMULTANEOUS NO REDUCTION AND o-DCB OXIDATION.

Previous sections have corroborated the excellent catalytic activity of 85Mn15Ce catalysts in the simultaneous removal of NO and o-DCB. However, the stability of the catalyst has not been evaluated yet, despite the fact that this is an important issue to consider in processes where the catalytic combustion of VOCs occurs, as they may promote the deactivation of the active species of the catalyst. Normally,

deactivation of the active species produces changes in the reaction rate or even changes in the reaction mechanism, resulting in loss of catalytic activity and/or loss of selectivity towards the desired products, which leads to by-products formation.

Stability tests are usually performed by monitoring the conversion and selectivity of the reactions along TOS, with constant feed stream, temperature and pressure conditions. In this case, stability has been evaluated at two different temperatures at which different behaviour of the analysed reactions has been observed. This will allow to obtain additional information about the reaction pathways.

The two selected temperatures are 200 and 300 ^{o}C. At 200 ^{o}C, NO conversion and the contribution of SCR (Equation 1.1) is very high in NO reduction, whereas o-DCB conversion is at the first step of its conversion profile. On the other hand, at 300 ^{o}C, NO conversion decreases due to the appearance of side reactions, whereas o-DCB conversion is in the second step of its conversion profile and chlorinated organic compounds are formed as by-products. The results are showed in Figure 4.5 (A: NO and o-DCB conversion; B: Concentration of SCR by-products; C: Concentration of CO_2 and oxidation by-products).

Regarding SCR, at 200 ^{o}C, NO conversion is constant after 24 hours of TOS. No significant NO_2 production was detected, whereas initial concentration of N_2O is similar to that obtained in the light-off experiment, it undergoes a certain decrease with time, and it stabilizes at the end of the experiment. Therefore, since NO conversion does not change and NO_2 is not produced, the decrease in N_2O production suggests a higher production of N_2. This result could be related to the deactivation of active sites promoting NSCR (Equation 4.1), although further experiments should be performed to explain this behaviour.

On the other hand, at 300 ^{o}C, NO conversion decreases in the first 2 hours of TOS and, then, it stabilizes at 81%, a value close to that obtained in the light-off experiment. This initial drop in NO conversion is likely associated to stabilisation of the catalyst, rather than deactivation. Evolution of NO_2 and N_2O concentration is parallel to that of NO conversion, with an initial drop and stabilization in the first 2 h. Moreover, it should be pointed out that the concentration in the steady state of both by-products is similar to that obtained in the light-off experiment.

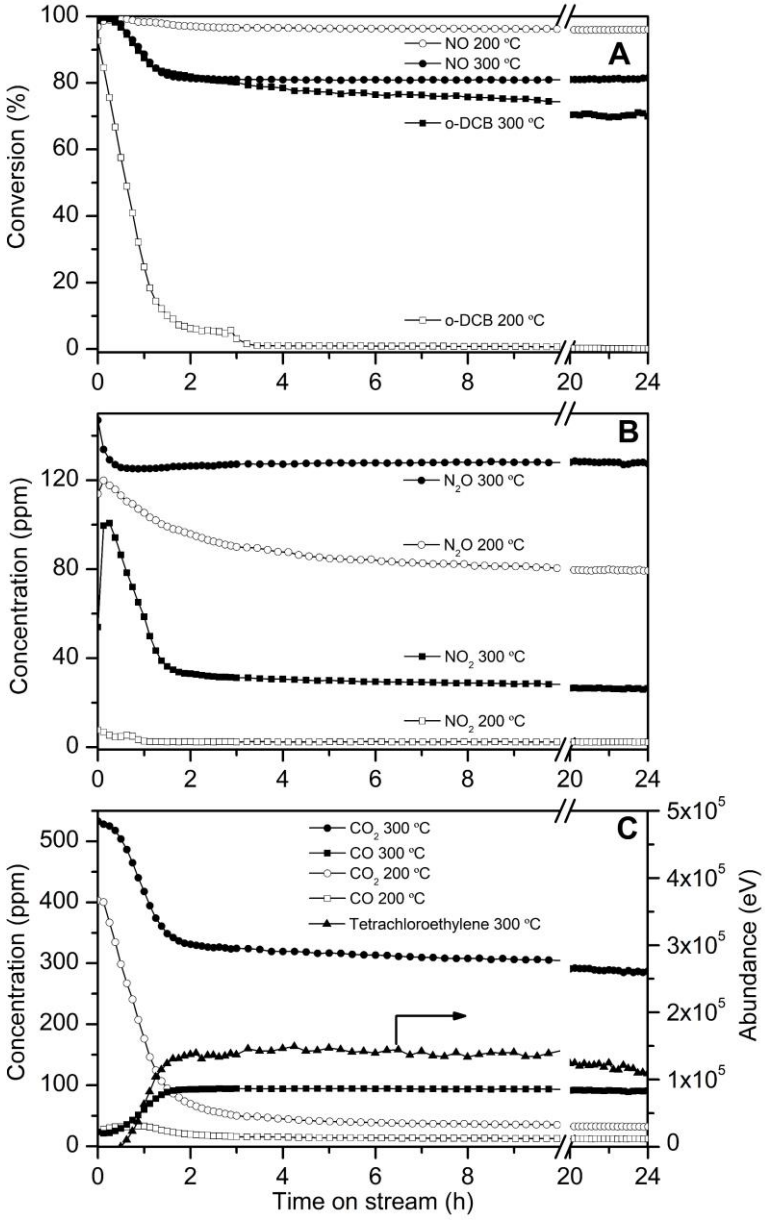

Figure 4.5. TOS experiments for simultaneous NO reduction and o-DCB oxidation. A) NO and o-DCB conversion, B) Formation of SCR by-products and C) Formation of CO_2 and oxidation by-products over 85Mn15Ce catalyst.

In the case of oxidation reaction, at 200 ºC, o-DCB conversion decreases until zero after 3 hours of TOS, which clearly denotes a time-deactivation of the catalyst that affects the active sites involved in oxidation reaction. Interestingly, CO_2 is the main product (CO is hardly generated and no chlorinated organic compounds were detected) and its concentration decreases over time, as a consequence of the decrease in o-DCB conversion. Therefore, this result suggests that the high o-DCB conversions obtained in light-off experiments at low temperature (Figure 4.1) are transient, because they are affected by deactivation.

On the other hand, at 300 ºC, o-DCB conversion decreases in the first one and a half hours but it stabilizes after 24 hours of TOS to a similar value than that obtained in the light-off experiment. Thus, at this temperature, o-DCB oxidation is not strongly affected by deactivation.

At 300 ºC, in addition to CO_2, typical by-products from o-DCB partial oxidation, such as CO and chlorinated organic compounds, are detected. CO_2 concentration follows the same trend than o-DCB conversion, strongly decreasing in the first hour and a half and then slowly until reaching the steady state at the end of the experiment. Interestingly, the generation of CO and chlorinated organic compounds strongly increases simultaneously with the drop of CO_2 concentration, which denotes a loss in the oxidative capability of the catalyst affecting to total oxidation of o-DCB. This result is particular noteworthy, since at 200 ºC, total oxidation of o-DCB was not affected (only CO_2 was produced) despite the decrease in o-DCB conversion due to catalyst deactivation.

The different trend in o-DCB oxidation as a function of temperature (200 and 300 ºC), in both conversion and product distribution, supports the change in the reaction pathway of o-DCB oxidation, which has been previously proposed in Section 4.1.2. Taking into account that the phase with high interaction between Mn and Ce is the one with the highest oxidative capability, due to the excellent oxygen mobility promoted by structural defects. This phase is responsible for o-DCB oxidation at low temperature, which yields only CO_2 and no products of partial oxidation. However, the remarkable drop in o-DCB conversion during the first hours of the TOS experiment at 200 ºC indicates that this phase is strongly deactivated.

On the other hand, at 300 ºC, surface oxygen species from Mn oxide aggregates (less active than the solid solution phase) become active for o-DCB oxidation. This phase is not as deactivated as solid solution phase, which is clearly concluded by

the stable trend of o-DCB conversion. However, the generation of CO and chlorinated organic compounds at this temperature suggests that o-DCB oxidation occurs through a reaction pathway that involves more partial oxidation reactions over the catalyst. Moreover, although it has been proposed that Mn oxide aggregates has a high contribution in o-DCB oxidation at high temperature (300 ºC), mixed oxide phase also contributes. This fact is deduced from the high o-DCB conversion and the only production of CO_2 at the beginning of the experiment.

Finally, a light-off experiment was carried out, keeping constant the reaction temperature until the steady state is reached in order to evaluate the effect of catalyst deactivation on the results provides by light-off type experiments. The results of this experiment are shown in Figure 4.6 together with those obtained with the same catalyst in a light-off experiment with temperature ramp (not designed to evaluated deactivation effect).

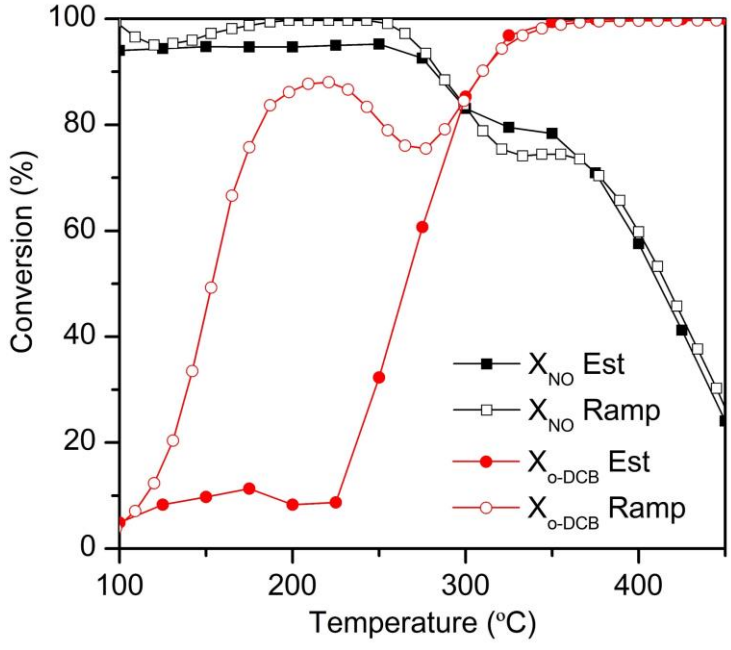

Figure 4.6. Comparison between light-off experiment performed with temperature ramp and steady state.

As can be seen in Figure 4.6, there are hardly differences in the NO conversion profiles obtained operating in light-off experiment with temperature ramp or with steady state. These results corroborate that NO reduction is hardly affected by catalytic deactivation, which is in agreement with the results obtained from TOS experiment.

On the other hand, a great difference is observed in the oxidation reaction at low temperature. Thus, the high o-DCB conversion obtained at low temperature (around 200 ^{o}C) in light-off experiment with temperature ramp is not observed in the light-off experiment with steady state, in which o-DCB conversion starts to increase above 225 ^{o}C, and below this temperature o-DCB conversion does not exceed 10%.

Therefore, this experiment confirms the negative effect of deactivation on o-DCB oxidation below 290 ^{o}C and shows how the light off curve of the dDiNOx process would look like if this effect is taken into account.

4.2.1. Characterization of 85Mn15Ce catalysts used in stability tests.

Stability tests have brought to light the deactivation of the 85Mn15Ce catalyst, which mainly affects o-DCB oxidation. In order to know in depth the nature of deactivating species and the effects they cause in catalytic properties, the 85Mn15Ce catalysts resulting from TOS experiments at 200 and 300 ^{o}C were characterized by TG, SEM-EDX, XRD, N_2-fisisorption, and H_2-TPR. In addition, the results of these techniques were compared with those obtained from characterization of fresh 85Mn15Ce catalyst.

TG experiments were performed with the aim of analysing the deactivating species adsorbed on the catalysts. For this purpose, the catalysts were subjected to a temperature increase in oxidising environment, monitoring the mass loss and the adsorbed compounds by mass spectroscopy. The derivative of TG profiles (dTG) (Figure 4.7A) exhibit two peaks around 225 and 485 ^{o}C. The area under the dTG peaks of the catalyst tested at 200 ^{o}C is clearly larger than that tested at 300 ^{o}C, which denotes the removal of a larger amount of deactivating species. In fact, the loss of mass associated to the removal of deactivating species in TG experiments resulted in a 4% in the former catalyst, whereas in the latter catalysts it was just a 2%. The larger deposition of deactivating species at 200 ^{o}C could be related to the

total loss of o-DCB conversion and suggests the inability of the surface oxygen species to remove the deactivating species at this temperature.

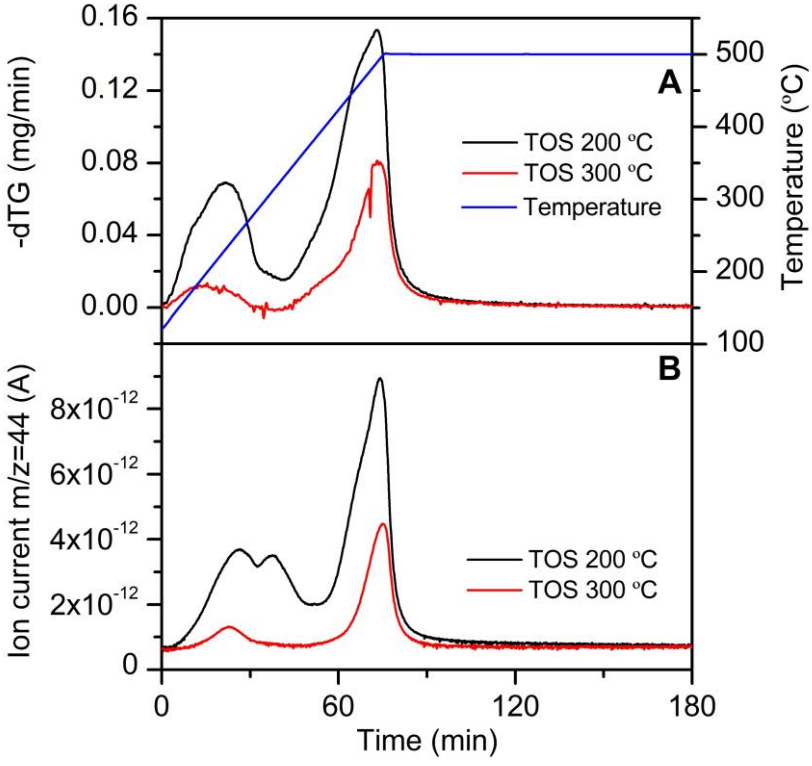

Figure 4.7. TG results of used 85Mn15Ce catalysts in TOS experiments. A) dTG profiles and B) m/z 44 profiles.

Figure 4.7B shows the obtained m/z=44 profiles, which match well with dTG profiles. m/z=44 is associated to CO_2, which evidences that deactivating matter is composed by carbon-based compounds. Moreover, m/z=17 and 30 have been detected around 300 ºC, which could be due to the desorption of SCR reagents. However, no m/z associated to chlorine has been detected.

Since chlorine is deeply referenced in the literature as a strong deactivating species in chlorinated organic compound oxidations and no evidence has been found of its presence in TG experiments, an additional EDX analysis was carried out. The results of this technique, listed in Table 4.1, reveal the presence of a remarkable amount of surface chlorine in both 85Mn15Ce catalysts used at 200 and 300 ºC in TOS

experiments, whereas the concentration of chlorine in fresh 85Mn15Ce sample was negligible. A similar result is observed for carbon-based deactivating species.

Table 4.1. Surface Cl and C composition from EDX analysis of fresh and used 85Mn15Ce catalysts in TOS experiments.

Catalyst	Cl content (%wt)	C content (%wt)
85Mn15Ce	0.1	--
85Mn15Ce (200 ^{o}C)	1.9	5.9
85Mn15Ce (300 ^{o}C)	1.7	4.9

Therefore, EDX analysis highlights the presence of chlorine species on the catalytic surface, and also confirms the presence of carbon-based compounds on catalyst surface. Moreover, the results of this technique agree with those obtained in TG, since the amount of deactivating species on the used sample at 200 ^{o}C is larger than that found on the used sample at 300 ^{o}C.

Table 4.2 shows the crystal size of the two main phases (fluorite and Mn_2O_3) obtained from XRD and the specific surface area, mean pore volume and mean pore diameter obtained from N_2-physisoprtion.

Table 4.2. Structural and textural properties of fresh and used 85Mn15Ce catalysts in TOS experiments.

Catalyst	Fluorite crystal size (nm)	Mn_2O_3 crystal size (nm)	S_{BET} (m^2/g)	V_P (cm^3/g)	d_P (nm)
85Mn15Ce	4	17	87	0.25	9.0
85Mn15Ce (200 ^{o}C)	6	25	58	0.23	13.3
85Mn15Ce (300 ^{o}C)	6	27	41	0.24	19.6

The crystal size of both fluorite and Mn_2O_3 phases increases in the used catalysts. This fact could be related to a sintering of crystal phases, promoted by oxygen consumption and the activation of redox pairs during the reaction. The sintering of

crystal phases probably causes a lower interaction degree between Mn and Ce, which would have a negative effect on the oxygen mobility of the catalyst.

The larger crystal size of the phases composing the used 85Mn15Ce catalysts contributes to the loss of structural defects, which decreases the specific surface area and makes higher the pore size in comparison to the fresh 85Mn15Ce catalyst. In addition, the deposition of deactivating matter also contributes to deteriorate the morphology of the catalyst through the blocking of pores, as it is denoted by the slight decrease in the pore volume in the used samples.

Figure 4.8 shows the TPR profiles of fresh and used catalysts in TOS experiments. The shift of reduction profile of used catalysts towards high temperature in comparison to fresh catalyst denotes a decrease in redox properties. The loss of reducibility is clearly associated to phase segregation evidenced by XRD, which reduces oxygen mobility. Moreover, there is a remarkable difference in the H_2 consumption associated to Mn in high oxidation state (H_2 uptake at low temperature), because it is composed by two well-differentiated subpeaks (at 270 and 300 ^oC) in the fresh sample, whereas it is composed by a tiny peak and a shoulder strongly overlapped with the H_2 uptake at high temperature in the used samples. On the other hand, Figure 4.8 also reports a higher H_2 consumption in the used 85Mn15Ce catalysts, which could be associated to an additional H_2 consumption of deactivating matter. This explanation is in accordance with the slight higher H_2 consumption of used catalyst in TOS experiment at 200 ^oC in comparison to that of used catalyst in TOS experiment at 300 ^oC, because of the higher amount of deactivating species observed by TG and EDX.

Therefore, the noticeable difference in the H_2 consumption at low temperature between fresh and used samples suggests that deactivating matter affects Mn in high oxidation state, either Mn^{4+} (in high interaction with Ce) or Mn^{3+} (in Mn_2O_3 oxide). As concluded in Chapter 3, the co-existence of these two Mn species is essential to provide an effective oxygen mobility, so their deficit affects the reducibility of the sample, which leads to a reduction of used catalysts at higher temperatures than the fresh catalyst.

Furthermore, H_2-TPR results agree with those obtained in TOS experiments, where the influence of catalytic deactivation on o-DCB oxidation at low temperature was evidenced. In this sense, at low temperature, oxygen mobility is a key factor for the activity of surface oxygen. Thus, the negative effects of deactivating matter on the

metal species that provide an effective oxygen mobility is the cause that leads to the decrease of o-DCB conversion at low temperature.

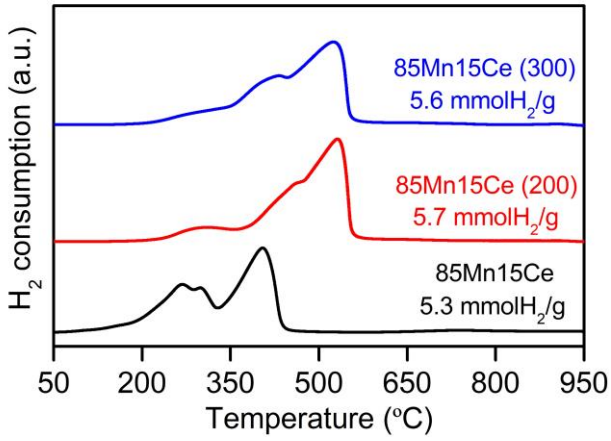

Figure 4.8. TPR profiles of fresh and used 85Mn15Ce catalysts in TOS experiments.

4.3. EFFECT OF FEEDING COMPOSITION.

All catalytic test reported up to now were performed with a composition similar to the average inlet composition of a SCR reactor in tail end configuration with the exceptions explained in Section 2.3.1. Nonetheless, the input composition to the SCR reactor depends on several variables, such as waste composition, incineration conditions and gas cleaning units before the catalytic unit. Hence, this section deals with the analysis of the effect of the concentration of some of compounds that may be present in the inlet stream of a SCR catalytic unit under real conditions.

For this purpose, two groups of compounds have been established, whose effects will be studied in different sections. Those compounds that are involved in $dDiNO_X$ process (NO, NH_3, O_2 and o-DCB) will be analysed in Section 4.3.1, whereas those that are not involved but may be present in the feed stream of a SCR catalytic unit (CO_2 and water) will be analysed in Section 4.3.2.

4.3.1. Effect of reagents involved in dDiNO$_X$ process: NO, NH$_3$, O$_2$ and o-DCB.

The gas feeding concentration of o-DCB, NO, NH_3 and O_2 has been changed in order to study: (1) the effect of o-DCB on NO reduction, (2) the effect of SCR reactants (NO and NH_3) on o-DCB oxidation and (3) the effect of O_2 on the simultaneous NO reduction and o-DCB oxidation.

4.3.1.1. Effect of o-DCB in NO reduction.

The catalytic test was performed in stationary conditions; so o-DCB concentration was changed after recording constant NO conversion and SCR by-products for one hour. The same way than in TOS experiments (Section 4.1.4), NO reduction was carried out at two temperatures, 200 and 300 ^oC, to compare the region of high NO conversion and that in which NO conversion drops due to SCR side reactions.

Figure 4.9 shows the effect of o-DCB concentration on NO conversion and on N_2O and NO_2 productions. The increase of o-DCB concentration has a clear negative effect on NO conversion, which decreases from total (with 0 ppm o-DCB) to 60% (with 300 ppm o-DCB) at both 200 and 300 ^oC. Therefore, these results corroborate the inhibitory effect of o-DCB on SCR at low and high temperatures, unlike those results obtained in the comparison of NO conversion performed simultaneously and independently with o-DCB oxidation (Figure 4.2), where the presence of o-DCB hardly caused effect on NO conversion profile below 250 ^oC. This fact is related to the high reaction rate of SCR at low temperature, which means that a high concentration of o-DCB is necessary to decrease NO conversion. In fact, this is clearly observed in Figure 4.9A, where the inhibitory effect of o-DCB over NO conversion is lower at 200 than 300 ^oC.

The presence of o-DCB also has a detrimental effect on SCR by-products (Figure 4.9B). In this sense, the larger the o-DCB concentration, the lower the concentration of NO_2 produced, and NO_2 generation is completely inhibited above 100 ppm o-DCB. In the case of N_2O, temperature plays a key role. Thus, at 200 ^oC, N_2O generation gradually decreases with o-DCB concentration, whereas, at 300 ^oC, it remains constant above 50 ppm o-DCB.

According to the origin of SCR by-products analysed in Section 4.1.1, one of the reactions involved in N_2O production is NH_3 oxidation. On the other hand, NO_2 production comes from NH_3 oxidation and NO oxidation. Each of these reactions necessarily involves NH_3 and NO adsorption. Therefore, the decrease in NO_2 and N_2O production with the increase of o-DCB concentration suggests that o-DCB competes with NO and NH_3, because both are the adsorbed compounds involved in the generation of SCR by-products.

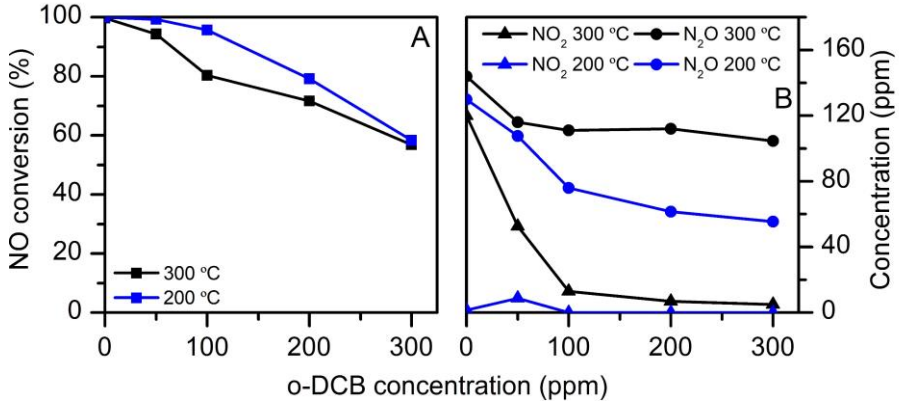

Figure 4.9. Effect of o-DCB concentration on NO reduction with 85Mn15Ce catalyst. A) NO conversion and B) N_2O and NO_2 concentration.

The competition of o-DCB with NO and NH_3 for the active sites avoids the oxidation of SCR reagents, which improves the N_2 selectivity, as reported in the literature [188, 189]. However, this competition is also the cause of the negative effect of o-DCB on NO conversion [190].

4.3.1.2. Effect of NO and NH_3 in o-DCB oxidation.

Previously, in Section 4.1.2, comparison between the conversion profiles of o-DCB oxidation performed simultaneously and independently with SCR revealed the promotional effect that SCR feeding causes in o-DCB conversion (Figure 4.3). Nonetheless, up to this point, that positive effect has not been ascribed to presence of NO, NH_3 or both. The following experiments will deal with this issue.

In this study, catalytic tests were also performed in stationary conditions; so, NO and NH_3 concentrations were changed after recording constant o-DCB conversion

for one hour. The experiments were performed at 300 °C, temperature at which deactivation does not affect the oxidation reaction and total o-DCB conversion is not reached. The results are shown in Figure 4.10.

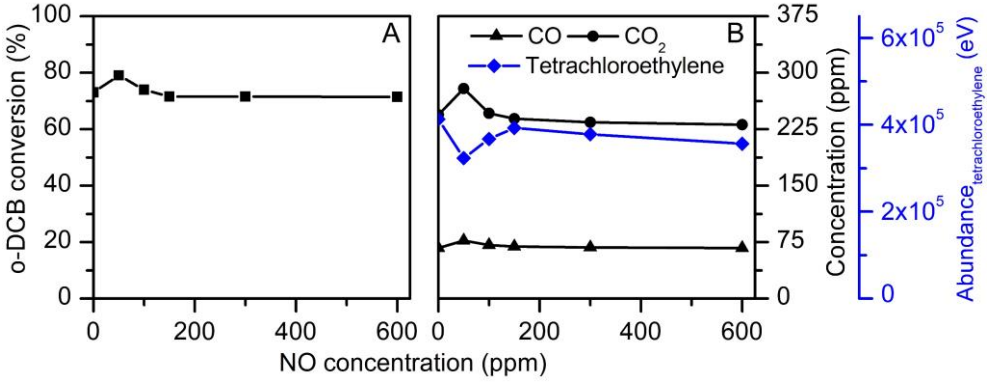

Figure 4.10. Effect of NO on o-DCB oxidation at 300 °C with 85Mn15Ce catalyst. A) o-DCB conversion and B) CO and CO_2 concentration, and tetrachloroethylene signal.

Figure 4.10A shows that low NO concentrations (50 ppm) slightly increase the o-DCB conversion (from 70 to 80%) and also promote total oxidation, which can be observed by the increase in CO_2 production and the decrease in the production of chlorinated organic compounds, such as tetrachloroethylene (Figure 4.10B). However, o-DCB conversion returns to the initial value with the further increase in NO concentration. Similar behaviour is observed for CO and CO_2 concentration and tetrachloroethylene signal.

The positive effect of low NO concentrations on o-DCB conversion is associated to the formation of NO_2 (from NO oxidation), which has higher oxidizing power than O_2. This promotes the reoxidation of surface oxygen speeding up the oxidation cycle [115, 187]. In fact, a similar promotional effect of NO on PCDD/Fs removal efficiency is reported by Wang and co-workers [191].

Nonetheless, as observed above in Sections 4.1.1 and 4.3.1.1, o-DCB also competes with NO. Consequently, further increase in NO concentration favours the negative contribution of competition versus the positive contribution associated to NO_2, decreasing o-DCB conversion.

On the other hand, Figure 4.11 shows the effect of NH_3 concentration on o-DCB oxidation. The increase in NH_3 concentration produces a gradual increase in o-DCB conversion from 69% (0 ppm NH_3) to 78% (600 ppm NH_3). A similar behaviour is observed for CO and CO_2 concentrations, which increase with NH_3 concentration, whereas the production of chlorinated organic compounds, such as tetrachloroethylene, drastically decreases. This fact denotes that NH_3 also favours o-DCB total oxidation.

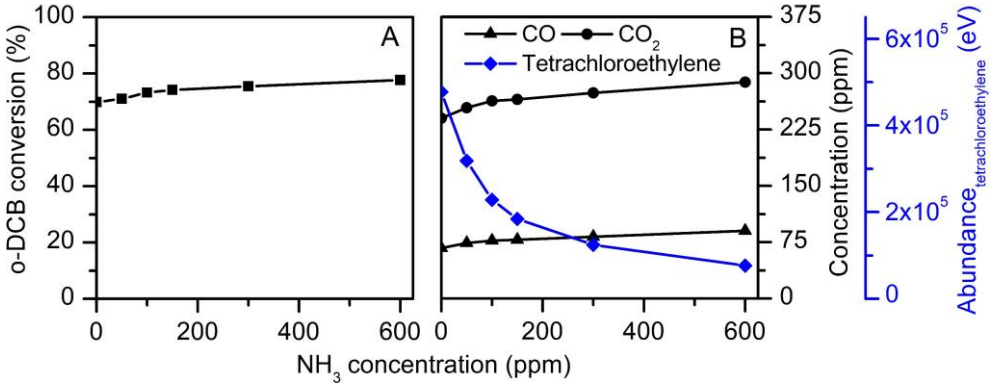

Figure 4.11. Effect of NH_3 on o-DCB oxidation at 300 °C with 85Mn15Ce catalyst. A) o-DCB conversion and B) CO and CO_2 concentration, and tetrachloroethylene signal.

The key to understand the positive effect of NH_3 on o-DCB oxidation is the behaviour followed by chlorinated organic compounds. As said above, these compounds are formed by chlorination reactions of the intermediate products of oxidation reaction. Thus, the lower production of chlorinated organic compounds reveals that NH_3 suppresses chlorination reactions, due to its reaction with chlorine adsorbed on the catalytic surface. This reaction produces ammonium chloride, which was detected as a white precipitate salt at the reactor outlet, as already mentioned (Section 4.1.2). Therefore, the removal of surface adsorbed chlorine (above identified in Section 4.2 as a deactivating species) would release the active centres allowing the observed increase in o-DCB conversion.

It is important to note that the positive effect of NH_3 on o-DCB oxidation found in this work contrasts with that reported in the literature, where several authors state a negative effect due to the competitive adsorption between both compounds [132, 190]. Competitive adsorption has also been identified in this work, but these

two effects are not incompatible. These results only mean that the contribution of chlorine removal is larger than that produced by competition.

Summing up, the above results obtained from the analysis of NO and NH_3 concentrations reveal that both compounds are involved in the effect that SCR feeding has on o-DCB oxidation.

4.3.1.3. Effect of O_2 on NO reduction and o-DCB oxidation.

This study was also carried out with catalytic tests in stationary conditions; so, O_2 concentration was changed after recording constant conversions of NO and o-DCB for 1 hour. The experiments were performed at 200 and 300 ^oC.

Figure 4.12A shows that the increase in O_2 concentration does not affect NO conversion at 200 ^oC, whereas NO conversion slightly increases at 300 ^oC. In the case of SCR by-products, there is no production of NO_2 at 200 ^oC, whereas the increase in O_2 concentration leads to higher NO_2 production at 300 ^oC. On the other hand, the N_2O generation is hardly affected by oxygen concentration independently of temperature.

The promotion of NO_2, that comes mainly from NO oxidation at 300 ^oC, suggests that the increase of O_2 concentration facilitates NO adsorption and further oxidation due to the improvement of oxygen adsorption rate. However, the promotion of NO oxidation does not seem to favour the over oxidation of adsorbed NH_3 (main species involved in N_2O formation), since N_2O production is hardly affected by the change in oxygen concentration. Therefore, the slight increase in NO conversion at 300 ^oC is probably associated to the NO consumed upon oxidation to NO_2.

On the other hand, Figure 4.12C and 4.12D shows the effect of oxygen in o-DCB oxidation at only 300 ^oC. The results obtained for oxidation reaction at 200 ^oC are not shown due to this reaction is affected by catalyst deactivation. The larger the O_2 concentration, the higher the o-DCB conversion. Similar trend is observed in CO_2 concentration, while the concentration of CO and the signal of tetrachloroethylene decrease when O_2 concentration increases above 10%. These results denote that the aforementioned enhancement in oxygen adsorption rate at higher O_2

concentration promotes not only the increase in o-DCB conversion, but also the total oxidation of this compound.

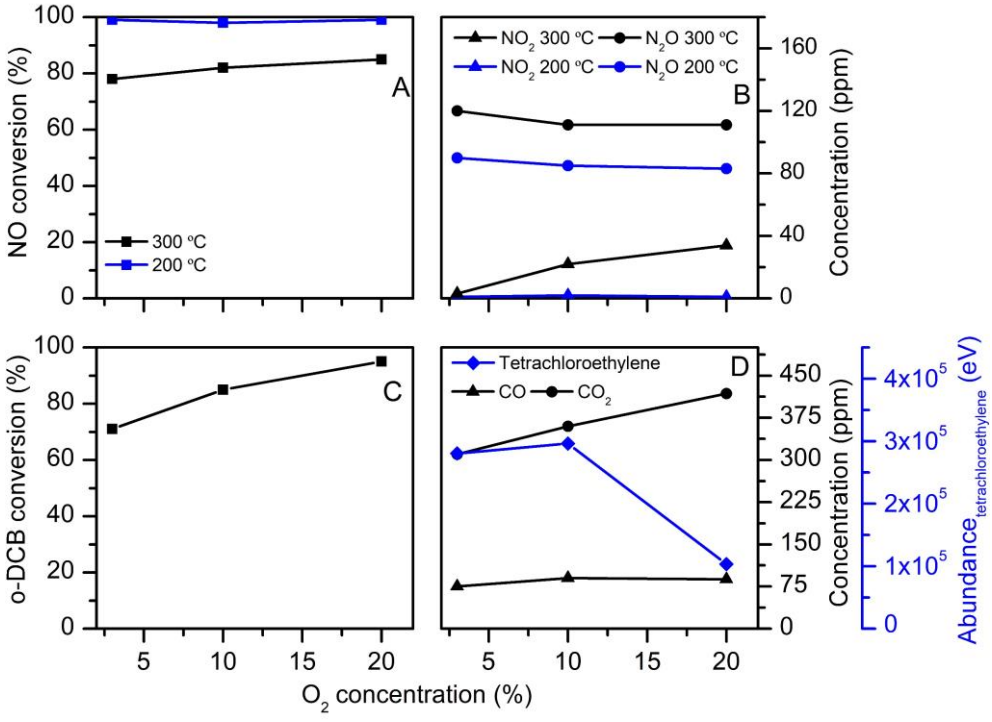

Figure 4.12. Effect of O_2 in simultaneous NO reduction and o-DCB oxidation with 85Mn15Ce catalyst. A) NO conversion, B) N_2O and NO_2 production, C) o-DCB conversion and D) CO and CO_2 concentration and tetrachloroethylene signal.

4.3.2. Effect of CO_2 and water in simultaneous NO reduction and o-DCB oxidation.

4.3.2.1. Effect of CO_2.

To study the effect of CO_2, the catalytic tests were performed in light-off mode with ramp temperature and the results are shown in Figure 4.13. The presence of CO_2 at different concentrations produces no changes in either NO or o-DCB conversion profiles. Moreover, similar production profiles (not shown) have been obtained for

SCR by-products, N_2O and NO_2, and for by-products from o-DCB oxidation, CO and chlorinated organic compounds.

Therefore, these results suggest that CO_2 does not compete for the active sites with the reagents involved in the $dDiNO_X$ process. This fact is important, since the concentration of this compound at the inlet of FGC line is quite large, around 5-10%.

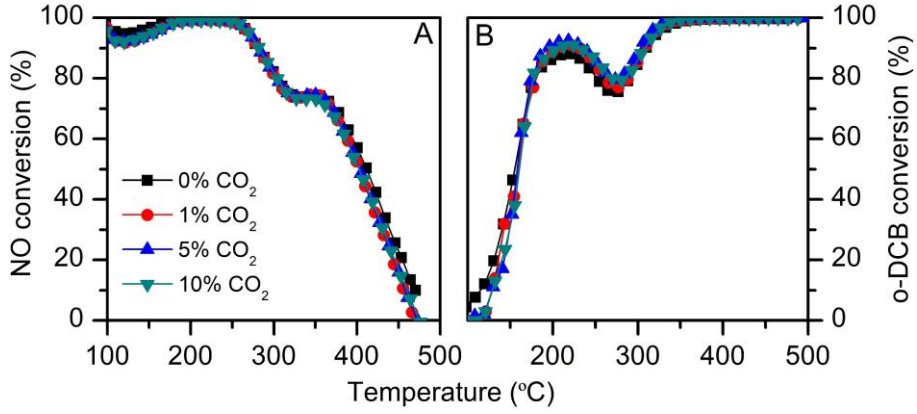

Figure 4.13. Effect of CO_2 on simultaneous NO reduction and o-DCB oxidation with 85Mn15Ce catalyst. A) NO conversion and B) o-DCB conversion.

4.3.2.2. Effect of water.

The effect of water was studied with a TOS experiment at the same two temperatures than in Section 4.2, 200 and 300 ºC. Firstly, a stream without water was fed to the catalytic reactor and, then, H_2O (0.5%) was added during a period of time. Finally, water was removed from the feed stream to observe whether its inhibiting or promoting effect was permanent or temporary. The results are shown in Figure 4.14.

Figure 4.14A shows that the addition of water slightly declines NO conversion from 96 to 94% at 200 ºC. The detrimental effect of water is also reported in the literature. Amiridis and co-workers [192] estimated that water decreases the SCR TOF around 40% and Huang and co-workers [193] observed stronger inhibiting effect with the increase in water concentration. This fact is associated to a competitive adsorption between SCR reagents and water [82, 194].

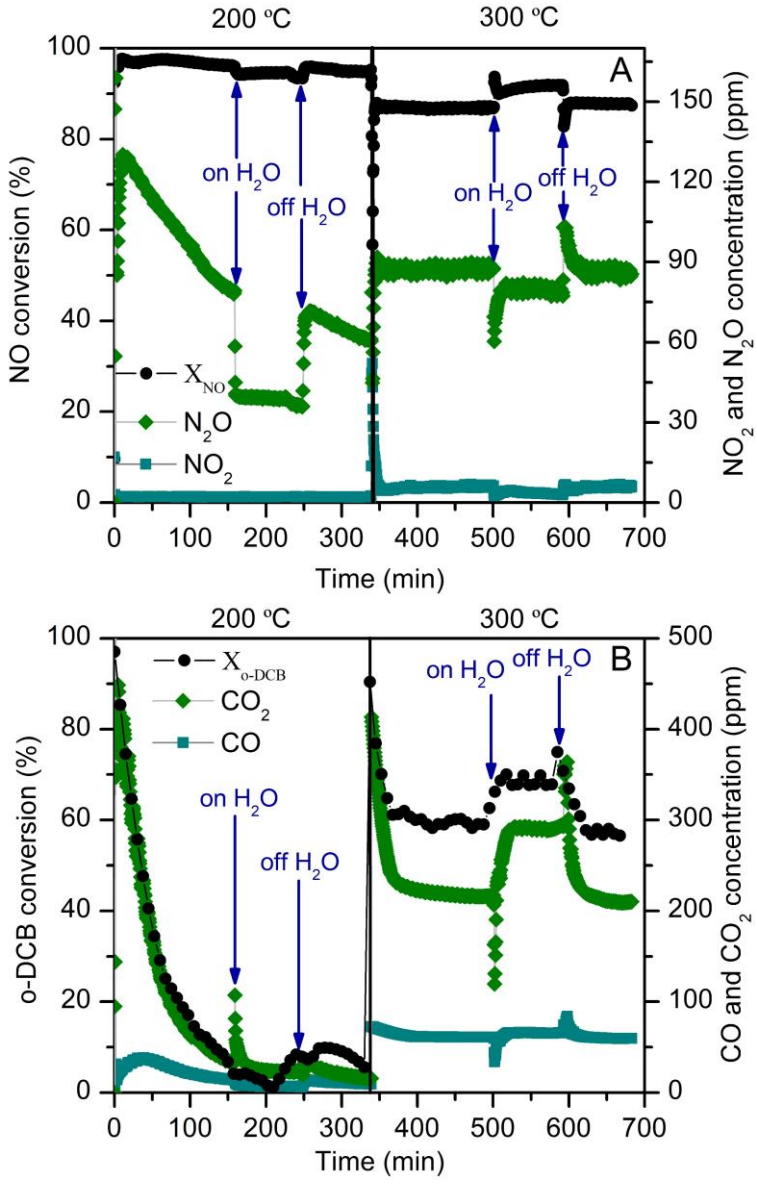

Figure 4.14. Effect of water on simultaneous NO reduction and o-DCB oxidation with 85Mn15Ce catalyst. A) NO conversion and N_2O and NO_2 concentrations; B) o-DCB conversion and CO and CO_2 concentrations.

However, at 300 ^{o}C, the presence of water promotes an increase on NO conversion from 86 to 92%, which contrasts with that mentioned in the previous paragraph. Since at this temperature SCR side reactions start to become important, an explanation for this behaviour could be associated to an influence of water in SCR side reactions, that would favour NO conversion.

Regarding the formation of SCR by-products, the presence of water clearly produces a decrease in N_2O generation, which is more notable at 200 ^{o}C. In the same way, NO_2 production is reduced in wet condition, although its production is already low at the both studied temperatures. Therefore, water inhibits SCR side reactions increasing the selectivity of NO reduction, which is in accordance with the results of Yao and co-workers [70].

Since at 300 ^{o}C NO_2 formation comes from NO oxidation, the negative effect of water on this reaction could be responsible for the increase in NO conversion at this temperature. Moreover, the notable effect of water on N_2O generation, in which adsorbed NH_3 plays an important role, evidences that water probably competes to a greater extent with NH_3 than with NO.

Regarding o-DCB oxidation (Figure 4.14B), the effect of water is not clear at 200 ^{o}C, because o-DCB conversion strongly decreases until zero as a consequence of catalytic deactivation, which was corroborated in Section 4.2. Nonetheless, at 300 ^{o}C, the addition of water produces an increase in o-DCB conversion from 60 to 70%, and CO_2 concentration from 220 to 290 ppm. CO hardly increases 4 ppm in wet condition. Moreover, water also promotes a strong decrease in the signal of chlorinated organic compounds (not shown). Therefore, water not only has a positive effect in the catalytic activity at high temperature, but also leads to total oxidation.

The positive effect of water could be associated to the removal of deactivating species, which were identified as adsorbed chlorine and carbon-based compounds. In fact, the presence of water has already been reported to lead to the easier removal of chlorine and coke during the oxidation of VOCs [195, 196]. For this reason, the concentrations of surface chlorine and carbon after operating in wet conditions were measured and have been listed in Table 4.3.

No carbon content was detected on the analysed catalysts, which denotes that water promotes the removal of carbon-based compounds. Interestingly,

Figure 4.14B shows a peak in CO_2 concentration at 200 ºC after the inlet of water. This peak could be associated to the removal of these carbon species adsorbed on the catalyst. However, the removal of carbon-based compounds does not improve o-DCB conversion at 200 ºC, as it would be expected. This is probably related to the competition between water and o-DCB for the active sites [98], which, added to the presence of non-removed chlorine (Table 4.3), would be responsible for the absence of improvement in o-DCB conversion.

Table 4.3. Surface Cl and C composition from EDX analysis of fresh and used 85Mn15Ce catalysts in TOS experiment after wet conditions.

Catalyst	Cl content (%wt)	C content (%wt)
85Mn15Ce	0.1	--
Wet 85Mn15Ce (200 ºC)	1.6	--
Wet 85Mn15Ce (300 ºC)	2.1	--

On the other hand, at 300 ºC, water promotes simultaneously the removal of carbon-based compounds, the increase in o-DCB conversion and the promotion of total oxidation; in spite of the presence of adsorbed chlorine and the competition effect. Therefore, these results suggest that the contribution of the different effects of water depend on the temperature. Thus, at high temperature (300 ºC), where surface oxygen replacement is faster and easier, the removal of carbon-based compounds is more important than the competition for the active sites.

Finally, it should be noted that the effect of water on both SCR and o-DCB oxidation is totally transient, since its effect disappears after removing water from the feed stream.

Influence of water on acid nature of 85Mn15Ce.

It is well known that water dissociation over metal oxide surface promotes the formation of hydroxy groups that may be active as Brønsted acid sites or H-bonds depending on their strength. In order to analyse the interactions and changes that water may provide in the catalytic surface, an experiment of pyridine adsorption was performed over a catalyst pre-treated under wet conditions and the results are

shown in Figure 4.15. This experiment was carried out at DICCA Department of the University of Genova.

In comparison to the spectrum of the catalyst after activation (before water adsorption), the adsorption of water (Figure 4.15A) promotes the appearance of a new band at 1630 cm^{-1} associated to H_2O scissoring mode [197]. At high wavenumbers, water also leads to the formation of a broad band in the OH stretching region, between 3600-2800 cm^{-1}, due to H-bonded species. After evacuation (outgassing condition), the intensity of bands due to adsorbed water decreases. Moreover, the scissoring mode of water and the bands in the OH stretching region shift down, suggesting stronger interactions, which evidence the changes produced by water over the catalytic surface. Over such hydroxylated surface, pyridine adsorption has been carried out and the results are displayed in Figure 4.15B.

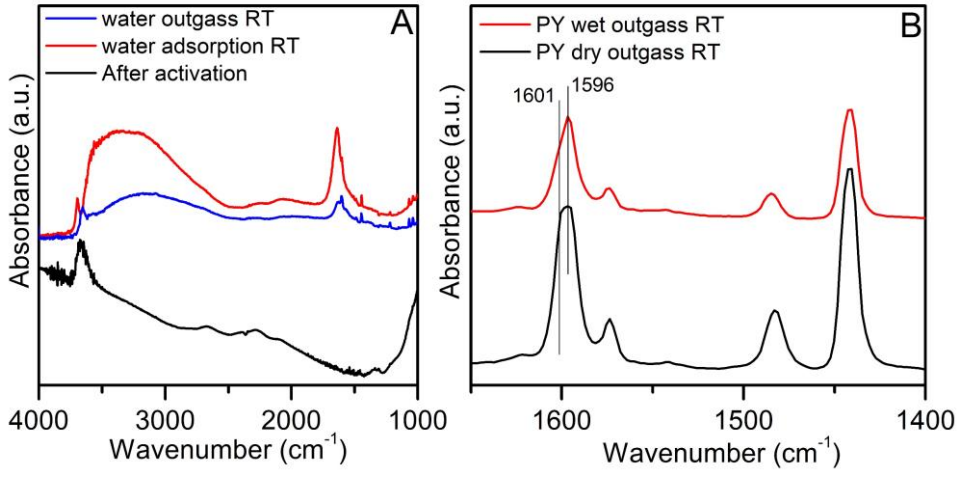

Figure 4.15. A) FTIR spectra at room temperature of 85Mn15Ce catalyst after activation (before water adsorption), in the presence of water, and after evacuation. B) Subtracted spectra of adsorbed pyridine over 85Mn15Ce with dry and wet surface (and subsequent evacuation at room temperature).

According to Figure 4.15B, the same bands are observed in pyridine adsorption over both dry and wet surfaces, associated to pyridine adsorbed over Lewis acid sites (ν_{8a}: 1632-1580 cm^{-1} and ν_{19b}: 1455-1438 cm^{-1}). Clearly, pyridine, a strong base, displaces water molecules likely coordinated over Lewis acid sites. In fact, the signal

of molecular water around 1630 cm^{-1} in non-subtracted spectra (not shown) disappears after pyridine adsorption. Moreover, there is no evidence of pyridine adsorbed over Brønsted acid sites in spite of the increased amount of hydroxyl groups in the catalyst previously treated with water. This fact suggests that the OH groups provided by coordinated water at the catalyst surface lack sufficient acidity to protonate the pyridine molecule, as also reported for alumina surface [197].

Nevertheless, a closer analysis of the spectra reveals that the contribution of strong Lewis acid sites, around 1601 cm^{-1}, is lower when pyridine was adsorbed over catalysts pre-treated with water. This result suggests that the increased presence of hydroxyl groups could slightly affect pyridine adsorption, favouring weak Lewis acid site contributions, which are usually located at lower wavenumber.

This slight change in the acidic nature of the catalytic surface could impact on the further reactions of adsorbed species. This fact could be the reason for the suppression of NSCR (Equation 4.1) in favour of SCR (Equation 1.1) in the presence of water. Additional experiments, such as the comparison between adsorbed NH_3 species in dry and wet conditions, would be necessary to corroborate this hypothesis.

4.4. GLOBAL VIEW AND CONCLUSIONS.

This chapter aims the study in detail of simultaneous NO reduction and o-DCB oxidation with the 85Mn15Ce catalyst. For this purpose, several experiments, with different feed streams and operating modes, were carried out to evaluate the influence that these two reactions have on each other, the origin of by-products and the effect of each reactant (NO NH_3, O_2 and o-DCB). The effect of other gases not involved in these reactions, but are in the real stream, such as CO_2 and water, has also been evaluated.

The different catalytic behaviour (conversion and by-product profiles) has been obtained after performing NO reduction and o-DCB oxidation simultaneously and independently. This fact has corroborated that both reactions affect each other.

Regarding NO reduction, the presence of o-DCB decreases NO conversion in the whole range of temperature due to the competition for the active sites, although its effect is less noticeable at low temperature (around 200 ^{o}C). The main by-

products of this reaction are N_2O, over the whole temperature range, and NO_2, at high temperature. The production of them is relatively high in comparison to other catalytic formulations, which is related to the high oxidative capability of MnO_X-CeO_2 catalysts.

N_2O is generated from NH_3 oxidation and NSCR. NO_2 comes from NH_3 and NO oxidation. The fact that these side reactions, especially NH_3 oxidation to NO and NO_2, take place at high temperature is the reason why NO conversion drops above 250 ^oC. The presence of o-DCB also reduces the production of SCR by-products, which is more noticeable in the case of NO_2, whose production profile shifts towards higher temperatures. This is a consequence of the competition between the reactants involved in NO reduction and o-DCB. In fact, the competition between NH_3 and o-DCB causes the plateau in NO conversion around 325-375 ^oC when it starts to drop at high temperature.

In the case of oxidation reaction, the presence of NO reduction shifts the o-DCB conversion profile towards lower temperatures. The individual analysis of each compound involved in SCR (NO and NH_3) has corroborated that this positive effect could be associated to both NO, which at low concentrations favours the oxidation reaction due to NO_2 generation; and NH_3, which promotes the removal of adsorbed Cl, releasing deactivated active sites. In fact, the latter also reduces the production of chlorinated organic compounds.

The main product in oxidation reaction is CO_2, although CO and chlorinated organic compounds (tetrachloromethane, tetrachloroethylene and trichlorobenzene) are also generated to a lesser extent. Cl_2 was not detected, even though it is widely reported in the literature related to VOC oxidation. This is probably due to the reaction between adsorbed chlorine and NH_3 to form NH_4Cl. Moreover, the presence of NO reduction decreases the production of chlorinated organics, although, conversely, it slightly increases the selectivity towards CO.

On the other hand, oxygen concentration hardly affects NO reduction, its increase only leads to a higher NO_2 production at high temperature. However, in oxidation reaction, the increase in oxygen concentration allows to improve o-DCB conversion and also decreases the production of chlorinated organic compounds.

The stability tests (TOS-type experiments) have corroborated NO conversion is stable over time. This does not occur with NO reduction selectivity towards N_2,

which increases at 200 ºC, due to the lower N_2O production with TOS. In the case of oxidation reaction, stability tests have elucidated two important features, which have supported several results from light-off curves. The first one is the influence of catalytic deactivation on o-DCB oxidation below 300 ºC. Deactivation is promoted by the adsorption of chlorine and carbon-based compounds. Characterization of used samples has revealed that these species lead to lower interaction between Mn and Ce. This fact reduces oxygen mobility, which negatively affects oxidative capability and redox properties of the catalysts.

The second one is the different way in which o-DCB is oxidized depending on temperature (change in the oxidation reaction pathway). This fact is associated to the different oxidative capability of the crystal phases that compose the catalyst. In this sense, at low temperature (around 200 ºC), o-DCB oxidation is mainly promoted by mixed oxide phase, whose oxygen species need lower temperature to be activated. On the other hand, at higher temperatures (around 300 ºC), o-DCB oxidation involves a higher contribution of partial oxidation because of the greater number of oxidation steps, which is evidenced by the appearance of chlorinated organic compounds. This change takes place because other surface oxygen species with lower oxidative capability, such as those coming from segregated manganese oxide, become more active with temperature to perform the oxidation reaction.

The role of CO_2 and water in simultaneous removal of NO and o-DCB has been also evaluated in this chapter. CO_2 has no effect on conversions and by-product formation. In the case of water, its presence has a negative effect on NO conversion because of the competition for the active sites, although it strongly decreases N_2O and NO_2 generation. In oxidation reaction, water has two different effects: to compete for the active sites and to remove the carbon-based deactivating species. The contribution of each one depends on temperature; thus, the presence of water leads to increase o-DCB conversion at high temperatures (around 300 ºC).

The adsorption of water, which competes with the reagents involved in SCR and o-DCB oxidation, on the catalyst has been also corroborated by FTIR. This adsorption does not change the acidic nature of the acid sites (Lewis), although it decreases its acidic strength.

Chapter 5

IDENTIFICATION OF ADSORBED SPECIES IN THE SIMULTANEOUS NO REDUCTION AND o-DCB OXIDATION OVER MnO_X-CeO_2 CATALYSTS

Chapter 5

IDENTIFICATION OF ADSORBED SPECIES IN THE SIMULTANEOUS NO REDUCTION AND o-DCB OXIDATION OVER MnO_X-CeO_2 CATALYSTS

ABSTRACT

This chapter aims to propose a reaction pathway for NO reduction and another for o-DCB oxidation on the basis of in situ FTIR analysis of adsorbed species in each reaction. For that purpose, experiments with several feeding streams have been proposed in order to assess the adsorption and co-adsorption of involved reactants.

NO reduction mostly follows, at low temperature, an Eley-Rideal pathway in which NH_3 adsorbs and reacts with NO in the gas phase. On the contrary, at high temperature, based on the ability of NO to adsorb and oxidise on the catalyst at these conditions, NO reduction is mostly proposed to follow a Langmuir-Hinshelwood type pathway, in which both NO and NH_3 are adsorbed.

Regarding o-DCB oxidation, a Mars-van Krevelen type pathway has been proposed, which has as initial steps two nucleophilic substitutions generating phenate and catecholate (or benzoquinone) species. Then, these species are further oxidized in different way depending on temperature. At low temperature, the oxidation is fast and complete towards CO_2, whereas the increase in temperature favours partial oxidation reaction, which involves the formation of additional intermediates, such as acetate, formate and enolic species.

5. IDENTIFICATION OF ADSORBED SPECIES IN THE SIMULTANEOUS NO REDUCTION AND o-DCB OXIDATION OVER MnO_X-CeO_2 CATALYSTS.

Simultaneous NO reduction and o-DCB oxidation is a heterogeneous catalytic process, as reactants are in the gas phase while the catalyst is a solid. This implies the requirement that all or some of the reagents must diffuse and adsorb on the catalytic surface. The adsorbed species generated react with one another or with other reactants in the gas phase to form reaction intermediates, which will eventually desorb as reaction products. The knowledge of the adsorbed species on the catalyst is very useful, since it provides information about intermediate species, which is important to propose a reaction pathway.

FTIR is one of the most used characterization techniques in heterogeneous catalysis. In this work, it has been used to obtain information about the bulk structure (Chapter 3), and also to analyse the presence of hydroxyl groups in the surface of the catalyst (Chapter 4). The analysis of adsorbed species formed during the reactions can be performed by means of FTIR, in a similar way than acidity analysis was performed using the adsorption of a probe molecule, such as pyridine (Chapter 3).

The aim of this chapter is the identification of the adsorbed species in the reduction of NO and o-DCB oxidation by using in situ FTIR technique. These results will allow to propose a reaction pathway for each reaction. The present chapter has been structured in three sections: (1) identification of adsorbed species in independent NO reduction, (2) identification of adsorbed species in independent o-DCB oxidation and (3) analysis of the influence of the species formed in SCR on o-DCB oxidation. The reason for not studying the effect of o-DCB adsorbed species on SCR is based on the results obtained after analysing the effect of o-DCB on NO reduction and vice versa (Chapter 4). Thus, while o-DCB only had a negative effect on NO reduction due to the competition with NO and NH_3 for the active centres, the presence of NO and NH_3 had a positive effect on o-DCB oxidation (besides the negative effect associated to competition). The experiments were performed with the optimum catalyst obtained in Chapter 3. In addition, the influence of Mn and Ce content on reactant adsorption has been briefly included in the first two sections.

5.1. IDENTIFICATION OF ADSORBED SPECIES IN NO REDUCTION OVER MnO_X-CeO_2 CATALYSTS.

In order to identify the adsorbed species in NO reduction, several experiments with different feeding streams have been carried out in this section:

- NO adsorption in the presence and in the absence of oxygen.
- NH_3 adsorption in the presence and in the absence of oxygen.
- Transient experiments with changes in the feeding stream
  - NH_3 adsorption on a catalyst previously exposed to a NO-containing stream.
  - NO adsorption on a catalyst previously exposed to a NH_3-containing stream.
- NO and NH_3 co-adsorption in the presence of oxygen (feeding stream containing the three reactants involved in SCR).

These experiments were performed at two different temperatures, 100 and 250 ^oC. The experimental procedure has been detailed in Chapter 2.

5.1.1. Adsorbed species in NO adsorption.

Figure 5.1 shows the FTIR spectra obtained after exposing the 85Mn15Ce catalyst to a gas stream with NO and balanced with Ar at different temperatures. Table 5.1 summarizes the assignment of the IR bands resulting from NO adsorption.

At 100 ^oC (Figure 5.1A), two broad bands appear at 1170 and 1105 cm^{-1} after introducing the feed stream, which have been assigned to nitrosyl (NO^-) [198-201] and hyponitrite ($N_2O_2^{2-}$) [72, 201] species. Several less intense bands are also detected at 1590, 1560 and 1535 cm^{-1}, which are associated to nitrate species [198, 200, 202-204]. Normally, nitrate species have more observable IR bands related to their ν_3 (split in two components) and ν_1 modes. In this case, due to the low intensity, these modes are not noticeable because they are overlapped with other bands, more intense. Moreover, in the 1400-1300 cm^{-1} range, there is a poorly defined absorbance, which can be assigned to the presence of nitrite species [203].

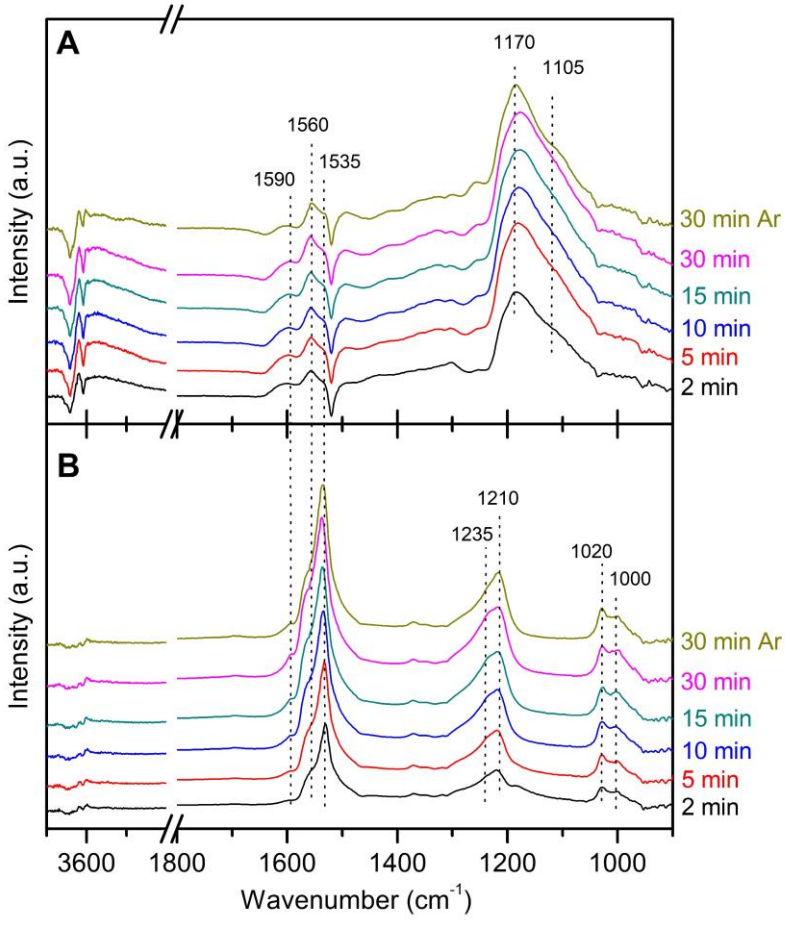

Figure 5.1. FTIR spectra after exposure of 85Mn15Ce catalyst to 1000 ppm NO in Ar followed by an Ar purging at (A) 100 ^{o}C and (B) 250 ^{o}C.

In the high wavenumber region, NO adsorption also promotes the alteration of surface hydroxyl groups. This is related to the negative bands located at 3680 and 3615 cm^{-1} [201, 205]. Note that the presence of these surface hydroxyl groups was corroborated in Chapter 4 (Figure 4.15A). The increase in the intensity between 3600-3000 cm^{-1} is related to H-bonded NO, which further supports the interaction between NO and hydroxyl groups. This interaction can also lead to the formation of nitrosyl species (NOH), which has been reported by Kantcheva and co-workers [201].

Table 5.1. Assignment of the IR bands detected in NO adsorption over 85Mn15Ce catalyst.

Band (cm^{-1})	Assignment	Reference
1120, 1105	Hyponitrite ($N_2O_2^-$)	[72, 201]
1180, 1170	Nitrosyl (NO^-)	[198-201]
1020, 1000	Nitrate	[74, 206, 207]
1275, 1240, 1235, 1210	Nitrate	[178, 199, 201]
1470	Nitro	[181, 202]
1590, 1560, 1535	Nitrate	[198, 200, 202-204]
3600-3000	NO H-bonded	[201]
3680, 3615	Hydroxyl	[201, 205]
1620	NO_2 weakly adsorbed or in the gas phase	[201, 205, 207, 208]

Increasing exposure time does not promote the appearance of new bands; in fact, it only makes the bands already detected more intense. After purging with Ar, the intensity of all bands decreases slightly, which evidences the high stability of nitrosyl and hyponitrite at low temperature.

On the other hand, the adsorption of NO at 250 ^oC (Figure 5.1B) promotes the appearance of some bands at 1560, 1535, 1235, 1210, 1020 and 1000 cm^{-1}, which are associated to nitrate species [74, 178, 201, 206]. All these bands become more intense with increasing exposure time. In addition, a new band at 1590 cm^{-1}, associated to nitrate species, appears after 5 minutes. No bands related to nitrosyl species have been detected. These results denote a change in the species resulting from NO adsorption as temperature increases, in which nitrates become the dominant adsorbed species.

Moreover, the different modes of nitrate species are better defined at high temperature. ν_3 is observable in the regions between 1600-1500 and 1250-1200 cm^{-1} and ν_1 between 1050-1000 cm^{-1}. There are many discrepancies in the literature concerning the location of the bands of each type of nitrate species, depending on their anchorage to the active centre [74, 200, 206]. In this work, the fact that the different modes (ν_3 and ν_1) seem to be composed by two or more

contributions suggests a wide variety of nitrate species adsorbed over different environment and with different anchoring (monodentate and bidentate).

The promotion of nitrate species in NO adsorption at high temperature is favoured by the fact that surface oxygen species become more active. The presence of oxygen in the feeding stream could also affect the activity of surface oxygen species. For this reason, co-adsorption of NO and O_2 was performed at different temperatures. The spectra are shown in Figure 5.2 and the assignment of IR bands detected is summarizes in Table 5.1.

NO and O_2 co-adsorption at 100 ^oC (Figure 5.2A) leads to the appearance of similar bands than those observed in the absence of oxygen: the bands located at 1180 and 1120 cm^{-1}, related to nitrosyl and hyponitrite species, and also those associated to nitrate and nitrite species in the range of 1600-1550 cm^{-1} and 1400-1300 cm^{-1}, respectively. Nonetheless, it should be pointed out that several of these bands are shifted to higher wavenumber in comparison to those obtained in the absence of oxygen.

Increasing exposure time, above 5 minutes, reduces the intensity of the bands associated to nitrosyl species in favour of the bands associated to nitrate. In addition, longer exposure time promotes the appearance of a new band around 1470 cm^{-1} associated to nitro species [181, 202].

After 10 minutes of experiment, additional vibrational modes of nitrate species, located between 1275-1240 cm^{-1} and between 1020-1000 cm^{-1}, become completely observable, although they are not well-defined. On the other hand, the bands of nitrosyl species disappear. These results indicate that NO is adsorbed as nitrosyl species and then oxidized to nitrate and nitrite, which may be faster or slower depending on adsorption conditions. Similar results have been reported in the literature for MnO_X-CeO_2 catalysts [199, 207, 209].

At 250 ^oC (Figure 5.2B), only bands associated to nitrate species are observed. No bands related to the presence of other species, such those observed at 100 ^oC (nitrosyl and nitro), were found. Comparison of the spectra obtained at low (Figure 5.2A) and high temperature (Figure 5.2B) reveals a better definition of nitrate bands at high temperature. This fact could be due to a higher definition of the anchoring of nitrate species to the active sites, which promotes the decrease in the variability of nitrates. Moreover, a small band located at 1620 cm^{-1} is observed

strongly overlapped with the ν_3 mode of nitrate species. This band is reported in the literature to be associated to NO_2 in the gas phase or weakly adsorbed [201, 205, 207, 208].

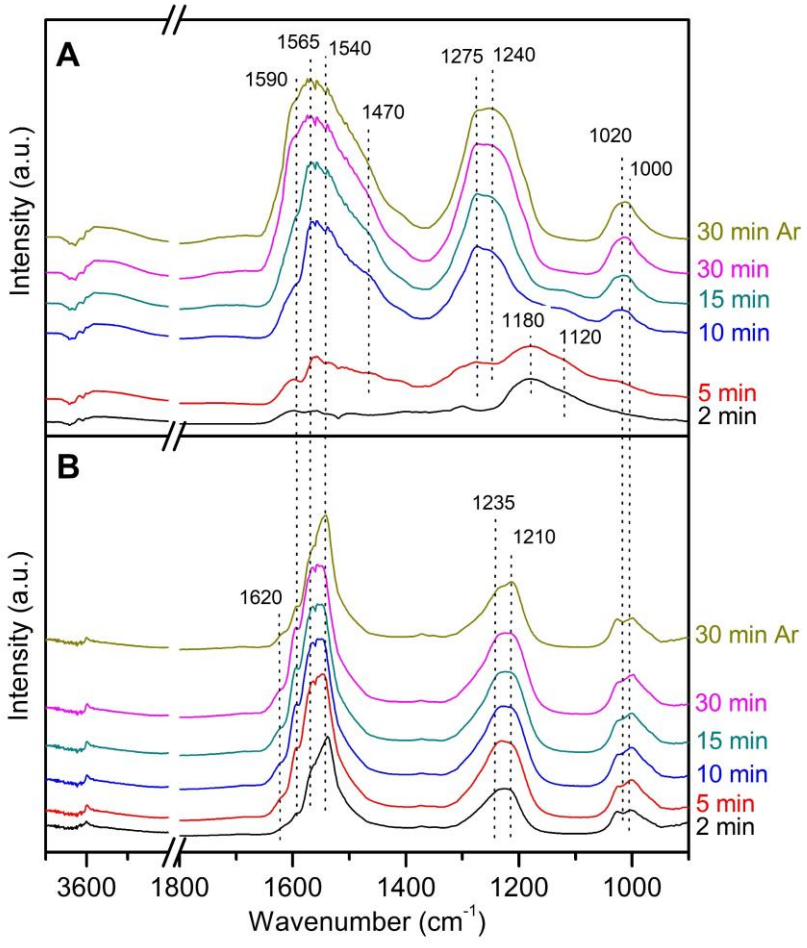

Figure 5.2. FTIR spectra after exposure of 85Mn15Ce catalyst to 1000 ppm NO and 5% O_2 in Ar followed by an Ar purging at (A) 100 ^{o}C and (B) 250 ^{o}C.

Therefore, according to the results described above the species resulting from NO adsorption on MnO_X-CeO_2 formulation have been corroborated to depend on temperature and the presence of oxygen in the gas phase.

Thus, at low temperature (100 ºC), NO adsorption occurs via nitrosyl and hyponitrite species, which are formed by NO interaction with a metal cation, or even with a surface OH group of the catalyst. However, although nitrosyl and hyponitrite species are stable (their bands remained in the spectrum after purging the catalyst with Ar), they are easily oxidised by surface oxygen of the catalyst, generating mostly nitrate species. This occurs when surface oxygen of the catalyst becomes active enough, which in turn occurs at high temperature (250 ºC).

The presence of oxygen in the gas phase also favours a high activity of catalytic surface oxygen, since it has been observed that, at 100 ºC, NO and O_2 co-adsorption promoted firstly the formation of nitrosyl species, which were subsequently oxidised to nitrate species after a short exposure time.

In addition to temperature and co-feeding oxygen in the gas phase, the influence of Mn content in NO and O_2 co-adsorption at 100 ºC has been briefly analysed because of the observed time dependence of NO adsorbed species in such conditions (nitrosyl species at low exposure time and nitrate species at high exposure time). The catalysts selected for this analysis were the pure oxides and two bimetallic catalysts, one with excess of Ce (15Mn85Ce) and the other with excess of Mn (85Mn15Ce). The results are shown in Figure 5.3.

The resulting spectra from NO and O_2 co-adsorption over bimetallic catalysts with different Mn content (85Mn15Ce and 15Mn85Ce) and pure manganese oxide shows NO adsorption through different species. After 5 minutes, the band at 1175 cm^{-1} indicates that NO is mainly adsorbed as nitrosyl species, whereas, after purging with Ar, the bands at 1555, 1250 and 1120 cm^{-1} denote that nitrosyl species were oxidized to nitrate species. Nonetheless, the same bands associated to nitrosyl and hyponitrite species, at 1270 and 1175 cm^{-1}, are observed after NO and O_2 co-adsorption on pure CeO_2 during all the experiment.

These results reveal that, on the one hand, Mn is the active metal that improves the oxidative capability of the catalysts, since nitrate species are only formed in Mn-containing catalysts. The easier oxidation of nitrosyl species to nitrate in pure MnO_X than in CeO_2 is also reported in the literature [72]. Moreover, the formation of nitrate species, even in the bimetallic catalysts with low Mn content, denotes that oxidative capability is greatly promoted even with a low Mn concentration.

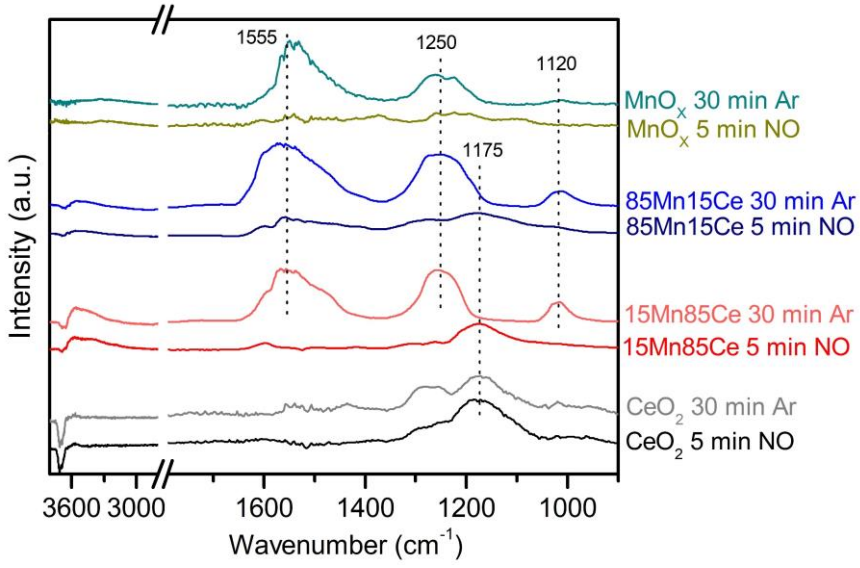

Figure 5.3. FTIR spectra after exposing catalysts with different Mn and Ce content to a stream composed by 1000 ppm NO and 5% O_2 in Ar followed by an Ar purging at 100 ^{o}C.

Interestingly, a similar result was obtained during the analysis of the effect of Mn content on SCR by-products (Chapter 3, Section 3.2). Specifically, the formation of N_2O and NO_2 strongly increased in Mn-containing catalysts with respect to pure cerium oxide, although differences were not remarkable between bimetallic catalysts with low and high Mn content. Therefore, the combination of both results suggests that by-product generation in SCR could be attributed to the oxidative capability provided by Mn.

5.1.2. Adsorbed species in NH_3 adsorption.

Figure 5.4 shows the FTIR spectra obtained after exposing the 85Mn15Ce catalyst to a gas stream containing NH_3 and Ar to balance at different temperatures. Table 5.2 summarizes the assignment of the IR bands resulting from NH_3 adsorption.

NH_3 adsorption at 100 ^{o}C (Figure 5.4A) leads to the appearance of notorious bands located at 1605, 1430, 1288, 1175 and 1095 cm^{-1}. The bands at 1605, 1288 and

1175 cm^{-1} are attributed to NH_3 coordinated over Lewis acid sites [179, 199, 207, 210]. The band at 1430 cm^{-1} is related to protonated ammonia (NH_4^+) [67, 181, 207, 211], and that located at 1095 cm^{-1} is associated to hydrogen-bonded ammonia [181, 212]. The adsorption of ammonia through its protonation and H-bonds involves the existence of surface hydroxyl groups, which were evidenced in Chapter 4 (Figure 4.15A).

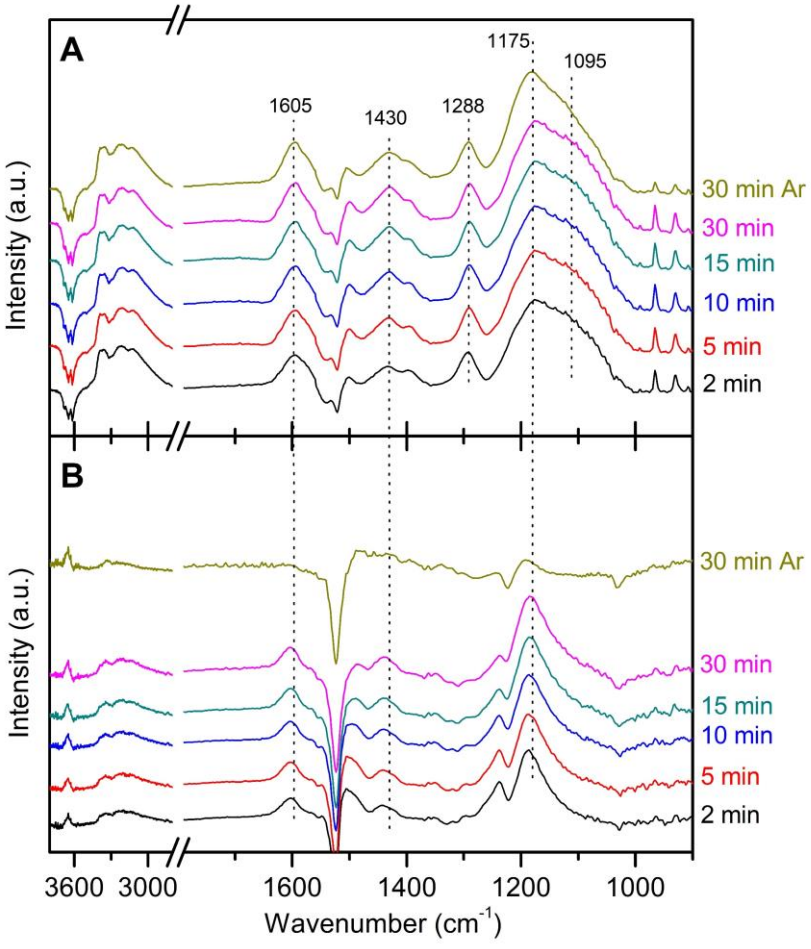

Figure 5.4. FTIR spectra after the exposure of 85Mn15Ce catalyst to 1000 ppm NH_3 in Ar followed by an Ar purging at (A) 100 °C and (B) 250 °C.

Table 5.2. Assignment of the IR bands detected in NH_3 adsorption over 85Mn15Ce catalyst.

Band (cm^{-1})	Assignment	Reference
965, 930	NH_3 weakly adsorbed or in gas phase	[205, 206, 215]
1605, 1600, 1295, 1288, 1190, 1175	Coordinated NH_3	[179, 199, 207, 210]
1095	NH_3 H-bonded	[181, 212]
1430	Protonated NH_3 (NH_4^+)	[67, 181, 207, 211]
1550, 1250, 1005	Nitrate	[203, 213]
1605	NO_2 weakly adsorbed or in gas phase	[201, 208]
3360, 3225, 3130	NH stretching	[202, 213, 214]
3630, 3650	Hydroxyl	[205, 212, 214]

The protonation of ammonia contrasts with the results obtained from acidity analysis (Chapter 3), where the protonation of pyridine was not observed (based on this, the presence of Brønsted acid sites was discarded). To understand the reason why surface hydroxyl groups donate the proton depending on the adsorbed molecule, it is necessary to compare the proton affinity (scale to measure the basic strength in the gas phase) of each compound. The proton affinity of pyridine is higher than that of ammonia, 3839.4 and 3553.2 kJ/mol, respectively [129]. This implies that pyridine is more acidic, so ammonia is more easily protonated.

In the high wavenumber region, the bands at 3360, 3225 and 3130 cm^{-1} are associated to NH stretching vibration of ammonia coordinated over Lewis acid sites [202, 213, 214]. The negative band around 3630 cm^{-1} is assigned to the consumption of surface hydroxyl groups, as a consequence of the protonation of ammonia and H-bonded ammonia. It should be noted that, in contrast to NO adsorption, H-bonded ammonia could not be evidenced in the high wavenumber in this case, since its characteristic bands are overlapped with those of NH stretching.

On the other hand, the bands located at 965 and 930 cm^{-1} are associated to NH_3 in the gas phase or weakly adsorbed, because their intensities strongly decrease after purging with Ar. In this regard, purging with Ar also affects, although to a lesser extent, the intensity of hydrogen-bonded ammonia, which suggests this species is less stable than coordinated ammonia and NH_4^+ (the intensity of their corresponding bands was not affected by Ar purge).

At high temperature, 250 ^oC (Figure 5.4B), NH_3 adsorption promotes the appearance of the bands located at 1605, 1288, and 1175 cm^{-1}, previously assigned to NH_3 coordinated over Lewis acid sites, and the band at 1430 cm^{-1}, related to the protonation of ammonia. However, after purging with Ar, only the band at 1175 cm^{-1} remained in the spectrum. This suggests that ammonia adsorption is weaker at high temperature, and also that coordinated ammonia species have the highest thermal stability.

In the high wavenumber region, the bands associated to NH stretching of coordinated ammonia, between 3600-3000 cm^{-1}, are not as well defined as at low temperature. This result evidences an important proton abstraction of adsorbed ammonia at high temperature. In addition, a band associated to surface hydroxyl groups appears at 3650 cm^{-1} (it had negative intensity at 100 ^oC). This change in the intensity of OH band could be associated to the protonation of catalytic surface oxygen, which would be favoured by the proton abstraction of adsorbed NH_3 as a consequence of its oxidation. In this sense, it is important to note that a similar band was observed in Chapter 4, after analysing the protonation of catalytic surface under wet conditions.

The presence of oxygen can also affect NH_3 adsorbed species, as has already been corroborated in NO adsorption. For this reason, co-adsorption of NH_3 and O_2 was performed. The spectra are shown in Figure 5.5 and Table 5.2 summarizes the assignment of the IR bands detected.

At 100 ^oC (Figure 5.5A), NH_3 and O_2 co-adsorption promotes similar adsorbed species than those obtained in the absence of O_2. Nonetheless, the bands located below 1400 cm^{-1}, associated to NH_3 coordinated over Lewis acid sites and hydrogen-bonded NH_3, are shifted to higher wavenumber in comparison to those observed in the absence of oxygen. This fact suggests stronger interaction between ammonia and surface active sites, as was also observed in Chapter 3 during pyridine adsorption.

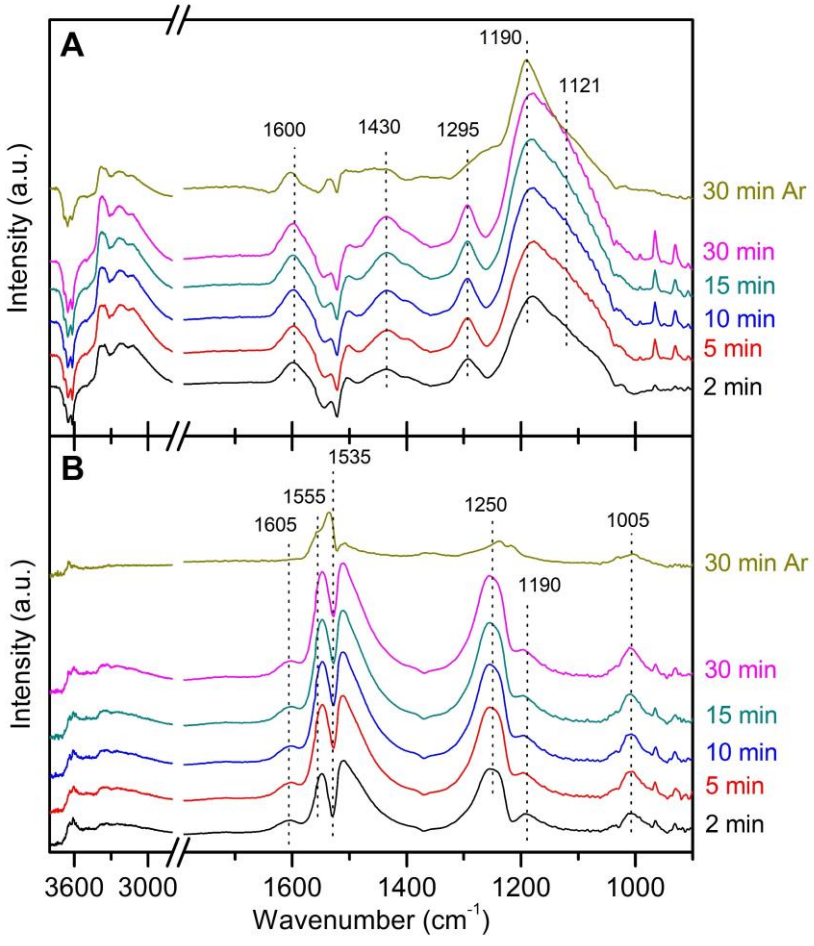

Figure 5.5. FTIR spectra after the exposure of 85Mn15Ce catalyst to 1000 ppm NH_3 and 5% O_2 in Ar followed by an Ar purging at (A) 100 ^oC and (B) 250 ^oC.

After purging with Ar, all the bands decrease their intensities except that assigned to protonated ammonia, which completely disappears. This result supports that adsorption of ammonia as NH_4^+ is weaker that ammonia coordination on Lewis acid sites, as explained above.

On the other hand, at 250 ^oC (Figure 5.5B), co-adsorption of NH_3 and O_2 leads to different bands located around 1550, 1250 and 1005 cm^{-1}. These bands have

already been assigned to the ν_3 and ν_1 vibrational modes of nitrate species [203, 213]. The appearance of nitrate bands suggests that, at high temperature and in the presence of oxygen, the catalyst becomes oxidizing enough as to rapidly oxidize adsorbed ammonia. Moreover, in the high wavenumber range, the band associated to hydroxyl groups at 3650 cm^{-1} evidences, as in the absence of oxygen, the protonation of surface oxygens as a consequence of the oxidation of adsorbed NH_3.

The easy oxidation of adsorbed ammonia at these conditions is not only evidenced by the presence of nitrate bands, but also by the appearance of the band located at 1605 cm^{-1}, associated to NO_2 in the gas phase or weakly adsorbed [201, 208] (this band which disappears after purging with Ar). Nonetheless, a small amount of ammonia keeps coordinated on Lewis acid sites, as indicates the presence of a small band at 1190 cm^{-1}.

Therefore, on the basis of the results obtained from NH_3 adsorption, it has been concluded that ammonia can coordinate on Lewis acid sites, protonate to form NH_4^+ and interact weakly with surface hydroxyl groups (H-bonds). The increase of temperature, by itself, does not produce significant changes in the adsorbed species, although the lower stability of ammonia adsorbed as NH_4^+ with respect to coordinated ammonia on Lewis acid sites has been evidenced. However, high temperature combined with the presence of oxygen mainly favours the formation of nitrate species due to the oxidation of adsorbed ammonia. The oxidation of surface ammonia has also been evidenced by the increase of the band associated to hydroxyl groups, as a consequence of the protonation of catalytic surface oxygen.

Moreover, it is important to note that purging with Ar produces a significant decrease in the intensity of the bands at 250 ^oC, in contrast to that observed in NO adsorption (Figure 5.1 and 5.2), where the intensities of the bands hardly changed after purging. These opposite results are very interesting, because they reveal that ammonia adsorbed species have lower thermal stability than those resulting from NO adsorption, despite the fact that, at 250 ^oC and in the presence of oxygen, nitrate is the species formed in both NO and NH_3 adsorption.

The influence of Mn content in NH_3 adsorption at 100 ^oC was also analysed and the results are shown in Figure 5.6. Except for pure manganese oxide, which only shows bands related to NH_3 adsorbed on Lewis acid sites, NH_3 adsorption occurs as coordinated NH_3 (1150 and 1585 cm^{-1}), NH_4^+ (1400 cm^{-1}) and H-bonded NH_3

(1140 cm^{-1}). These results reveal that Ce is the component that provides hydroxyl groups. In line with this, pure cerium has the best-defined contribution of ammonia adsorbed through hydrogen bonds.

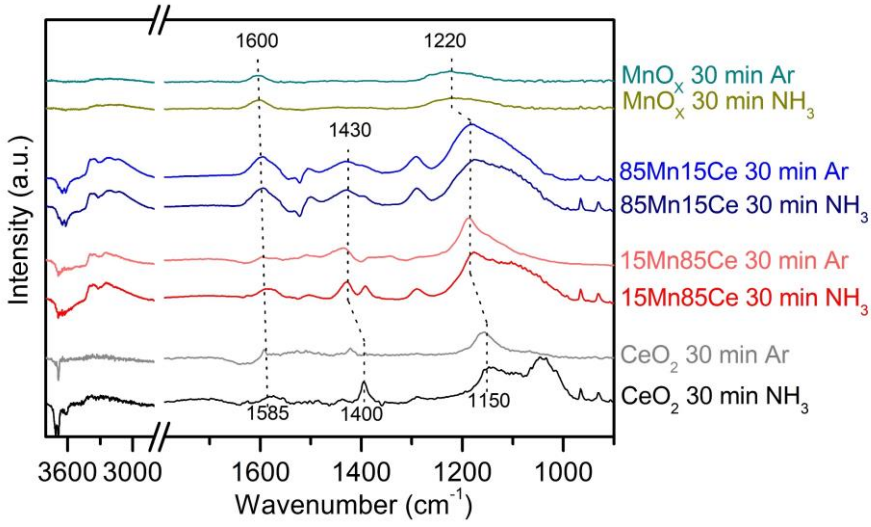

Figure 5.6. FTIR spectra after exposing catalysts with different Mn and Ce content to a stream composed by 1000 ppm NH_3 and 5% O_2 in Ar followed by an Ar purging at 100 ^oC.

All bands related to the different species are clearly shifted to higher wavenumber as the Mn content in the catalyst increases, which evidences different interaction degrees (strength) as a function of catalyst composition. In this sense, the bands associated to ammonia adsorbed on Lewis acid sites are more notorious in the bimetallic catalyst with the highest Mn concentration.

5.1.3. Adsorbed species in transient experiment with changes in the composition of the feeding stream.

Transient experiments have been performed in order to obtain information about the reactivity of the different species formed in NO and NH_3 adsorption over the 85Mn15Ce catalyst. For this purpose, the catalyst was first exposed to a certain feeding composition, which was switched to a different one after a certain time.

5.1.3.1. Reaction between ammonia and NO adsorbed species.

In this case, the catalyst was firstly exposed to a NO-containing feed stream until saturation. Then, the catalyst was purged with Ar to remove the weakly adsorbed NO species. After that, the catalyst was exposed to a NH_3 containing feed stream. Several experiments were carried out at different temperatures both in the presence and in the absence of oxygen. The results are shown in Figure 5.7.

Figure 5.7A shows the FTIR spectra after exposing the 85Mn15Ce catalyst to a first feed stream containing NO and Ar to balance, and then, changing the composition to NH_3 and Ar to balance at 100 ^oC. NO adsorption leads to nitrosyl species, band at 1185 cm^{-1}, and also a less intense band at approximately 1555 cm^{-1}, related to nitrate species. Moreover, in the high wavenumber region, the typical negative band, associated to the consumption of surface hydroxyl groups, appears at 3680 cm^{-1}.

The change to a NH_3 containing feed stream leads to an increase in the intensity of the existing band at 1185 cm^{-1} and the appearance of a new band at 1605 cm^{-1}, because of the contribution of coordinated ammonia over Lewis acid sites. In addition, other bands related to protonated ammonia and NH stretching vibration grow up at 1440 and 3300-3000 cm^{-1}, respectively, with time on stream.

The overlap of the bands associated to nitrosyl and ammonia on Lewis acid sites does not allow to elucidate the reactivity of nitrosyl species in the presence of NH_3. However, the fact that the band of surface hydroxyl groups is not affected by NH_3 addition suggests that, at 100 ^oC, nitrosyl species do not react with NH_3 neither in the gas phase nor adsorbed; otherwise, water generation would increase the intensity of surface hydroxyl groups.

On the other hand, the presence of ammonia leads to the disappearance of nitrate species (1555 cm^{-1}). Nonetheless, the absorbance of these species is very low, so it is not clear whether there has been a reaction between nitrate species and ammonia. To corroborate this, the adsorption of ammonia has been carried out after exposing the catalyst to a feed stream composed by NO and O_2 at 100 ^oC (Figure 5.7B) and to NO at 250 ^oC (Figure 5.7C). At these conditions, NO adsorbed species were nitrates (Figure 5.2 and Figure 5.1).

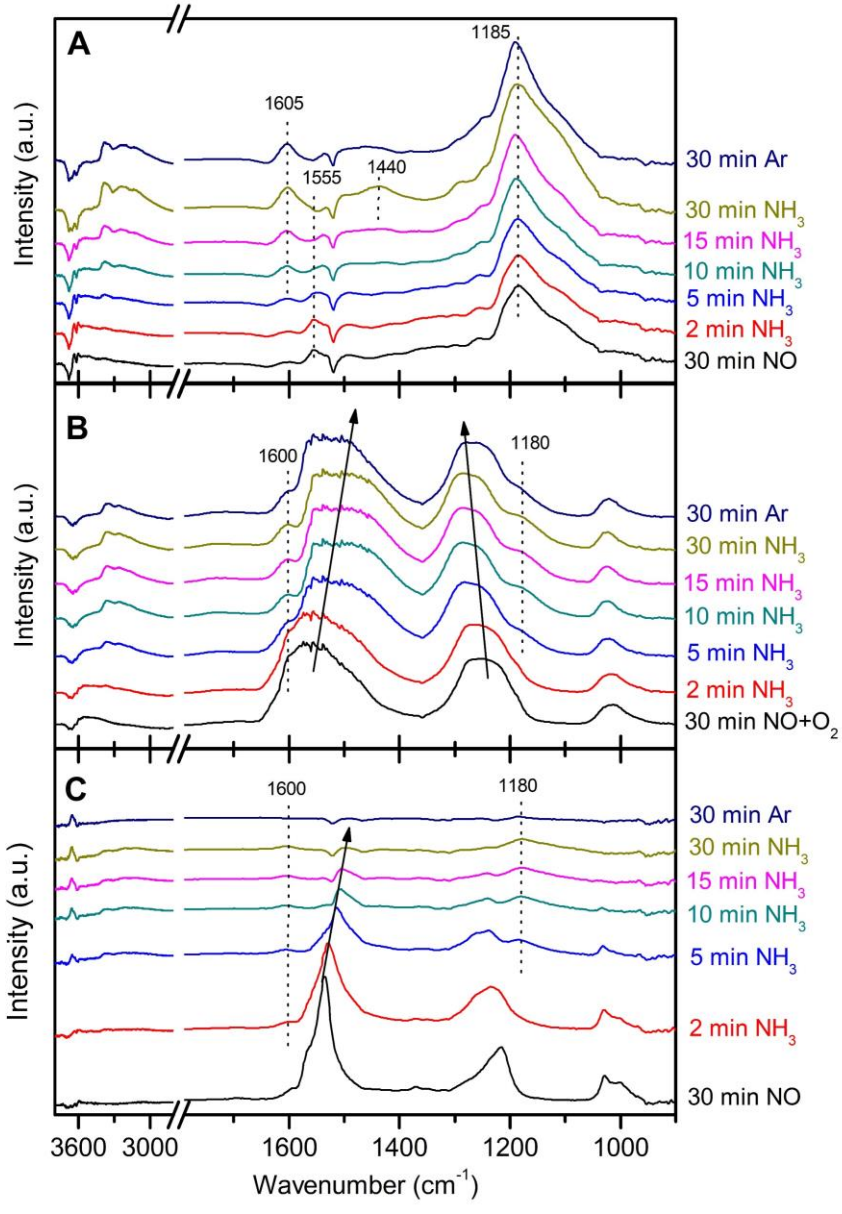

Figure 5.7. FTIR spectra of 85Mn15Ce catalyst pretreated with A) 1000 ppm of NO/Ar at 100 °C; B) 1000 ppm of NO and 5% O_2/Ar, at 100 °C; and C) 1000 ppm of NO/Ar at 250 °C. Then, exposed to 1000 ppm of NH_3/Ar at different time on stream.

Both NO and O_2 co-adsorption at 100 ^oC and NO adsorption at 250 ^oC promote the appearance of bands related to nitrate species around 1550, 1230 and 1010 cm^{-1}. These bands are formed by different contributions (different shape) depending on temperature, so there may be different nitrate species. The change in the feed stream leads to a clear shift of the nitrate bands located around 1550 and 1230 cm^{-1}, to lower and higher wavenumber, respectively. This fact indicates different degree of interaction between nitrates and surface active sites, as a consequence of ammonia adsorption. Ammonia adsorption is clearly evidenced after 5 minutes of time on stream, due to the appearance of the bands at 1180 and 3400-3000 cm^{-1}.

In addition, comparison between the results obtained at different temperatures reveals different reactivity of nitrates. Thus, at 250 ^oC (Figure 5.7C), the reactivity of nitrates and ammonia is very high, as can be concluded from the disappearance of nitrate bands with time on stream. This fact does not occur at 100 ^oC (Figure 5.7B), where the low reactivity of nitrate species is evidenced by the similar intensity of their bands. Nonetheless, the reactivity of nitrate species at 100 ^oC may not be entirely null, since in addition to the shift of the band at 1550 cm^{-1}, the presence of NH_3 produces its broadening to lower wavenumber, which could be associated to a partial reduction of nitrate to nitrites, which have their characteristic bands in this range.

5.1.3.2. Reaction between NO and O_2 and NH_3 adsorbed species.

In the same way to the previous experiments, the catalyst was firstly exposed to a NH_3 containing feed stream until reaching saturation. Then, the catalyst was purged with Ar to remove the weakly adsorbed NH_3 species. After that, the catalyst was exposed to a NO-containing feed stream (firstly composed by NO, and then, by NO and O_2). Two experiments were carried out at different temperatures. The results are shown in Figure 5.8.

Figure 5.8A shows the FTIR spectra after exposing the 85Mn15Ce catalyst to a first feed stream containing NH_3 and Ar to balance at 100 ^oC, and then, changing the feed stream to NO and Ar to balance both in the absence and in the presence of oxygen. The adsorption of NH_3 promotes its coordination on Lewis acid sites (bands at 1600, 1290, and 1180 cm^{-1}), its protonation (band at 1430 cm^{-1}) and the

appearance of the bands at 3400-3000 and 3650 cm^{-1}, associated to NH stretching vibration and surface hydroxyl, respectively.

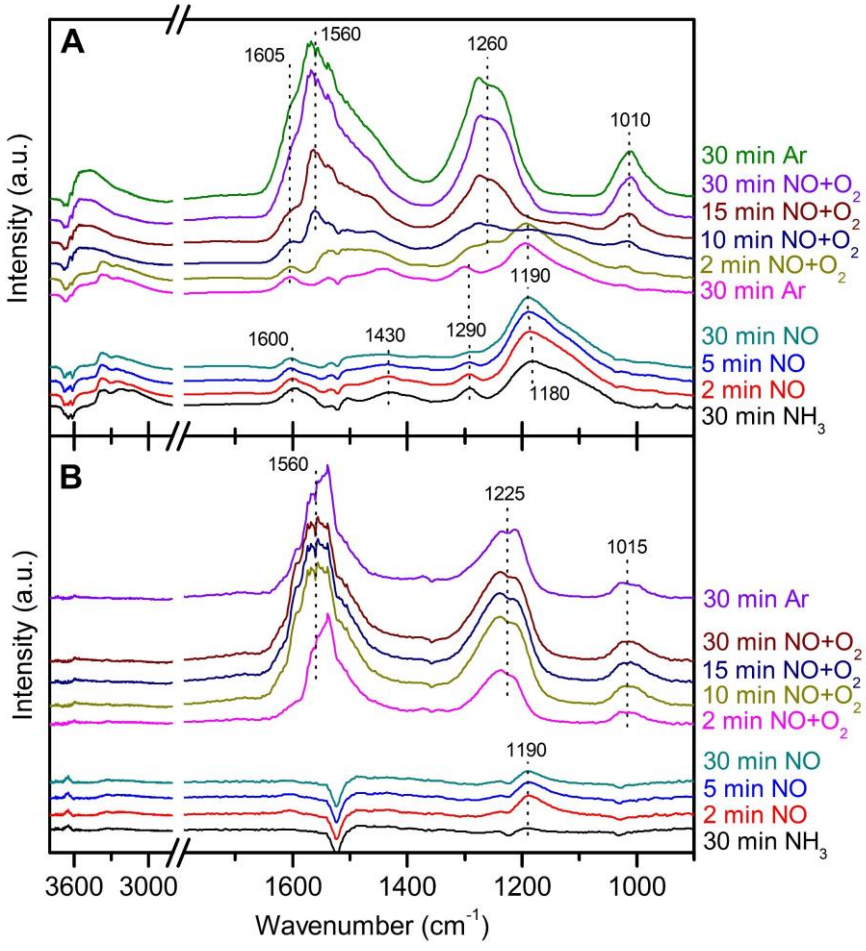

Figure 5.8. FTIR spectra of 85Mn15Ce catalyst pretreated with 1000 ppm of NH_3. Then, exposed to 1000 ppm of NO/Ar at different times on stream, followed by a second exposition to 1000 ppm NO and 5% O_2/Ar at A) 100 ^oC and B) 250 ^oC.

Once the catalyst was saturated with NH_3, the adsorption of NO leads to the formation of nitrosyl species, which produces an increase in the intensity and a shift to higher wavenumber of the bands located at 1180 cm^{-1}. This fact, that was also observed in the inverse experiment (NH_3 adsorption over NO adsorbed species,

Figure 5.7A), makes it difficult to follow the reactivity of ammonia adsorbed through its most intense band.

Nonetheless, a decrease in the intensity of the bands belonging to ammonia adsorbed over Lewis acid sites (1600 cm^{-1}) and NH stretching vibration is observed with time on stream. In this sense, a similar tendency seems to be followed by the bands at 1430 and 1290 cm^{-1}, although the increase of absorbance in this region, probably associated to the formation of a small amount of nitrate and nitrite species, makes it difficult to appreciate.

The progressive reduction of the bands associated to adsorbed ammonia reveals its high reactivity with NO. Another evidence of the reaction is the growth of the surface hydroxyl band (becomes less negative), due to protonation of the catalytic surface, either by the proton abstraction of ammonia or the adsorption of water produced in the reaction. However, it is important to elucidate whether adsorbed ammonia reacts with NO in the gas phase and/or adsorbed as nitrosyl species. In this sense, as stated above, the inverse analysis (ammonia adsorption over adsorbed NO) showed that the reaction between nitrosyl species and ammonia (in the gas phase or adsorbed) hardly took place because of hydroxyl bands remained unchanged. Therefore, these results suggest that the consumption of adsorbed ammonia species comes mostly from its reaction with NO in the gas phase.

It is important to note that, after 30 minutes of time on stream, the bands of ammonia adsorbed species still remain in the spectrum, which evidences that a certain amount of adsorbed ammonia has not been consumed in the reaction, even though NO is in excess. This fact could be associated to the absence of oxygen in the gas phase. For this reason, the catalyst was subsequently exposed to NO and O_2 and the recorded spectra are shown in Figure 5.8A. After 15 minutes of time on stream, adsorbed ammonia completely reacted, as can be concluded by the disappearance of its most intense band at 1190 cm^{-1} and also the NH stretching vibrations. Additionally, the reaction is supported by the progressive increase of surface hydroxyl band.

Simultaneously to the disappearance of adsorbed ammonia species, additional bands assigned to nitrate species appear around 1605, 1560, 1260 and 1010 cm^{-1}. From this result, a possible reaction between adsorbed ammonia and nitrate species could be inferred. However, it must be kept in mind that the inverse

experiment (Figure 5.7B) already confirmed the absence of reaction between adsorbed nitrates and ammonia at 100 ºC, neither in the gas phase nor adsorbed.

NO adsorption over pre-adsorbed NH_3 was also performed at 250 ºC and the resulting spectra are shown in Figure 5.8B. The adsorption of NH_3 only promotes a band associated to ammonia coordinated over Lewis acid sites (1190 cm^{-1}). The low intensity and the absence of other bands is in accordance with the results exposed during the analysis of ammonia adsorption at high temperature (Figure 5.1B). Subsequent adsorption of NO leads to the increase of the band at 1190 cm^{-1} due to the formation of nitrosyl species. After 5 minutes of time on stream, the band at 1190 cm^{-1} decreases its intensity, which evidences a possible reaction between both adsorbed species, ammonia and nitrosyl.

It is important to note that the inverse experiment (NH_3 adsorption over pre-adsorbed NO, Figure 5.7C) concluded there was a reaction between adsorbed nitrates and ammonia, although it could not be clarified whether ammonia was in the gas phase or adsorbed. Since this experiment has evidenced the reaction between adsorbed ammonia and nitrosyl species, nitrate species are also probable to react with adsorbed ammonia at high temperature. In fact, ammonia adsorption is considered in the literature as a key stage in SCR reaction path at both low and high temperature [212, 216, 217].

On the other hand, the adsorption of NO as only nitrosyl species is very surprising, since the analysis of NO adsorption at 250 ºC (Figure 5.1B) concluded that nitrate was the only species formed at these conditions. This fact could be related to the prior step of ammonia adsorption, which consumed surface active oxygen (this stage was carried out in the absence of oxygen) and reduced the oxidizing ability of the catalyst, making nitrosyl oxidation to nitrate impossible. To corroborate this idea, the catalyst was further exposed to NO and O_2. The results are also included in Figure 5.8B. As can be seen, immediately after introducing the stream, bands associated to nitrate species appear at 1560, 1225 and 1015 cm^{-1}, which corroborates the fast oxidation of nitrosyl species to nitrates.

5.1.4. Adsorbed species in NO, NH_3 and O_2 co-adsorption.

Figure 5.9 shows the FTIR spectra obtained after exposing the 85Mn15Ce catalyst to a gas stream composed by NH_3, NO, O_2 and balanced with Ar at different temperatures.

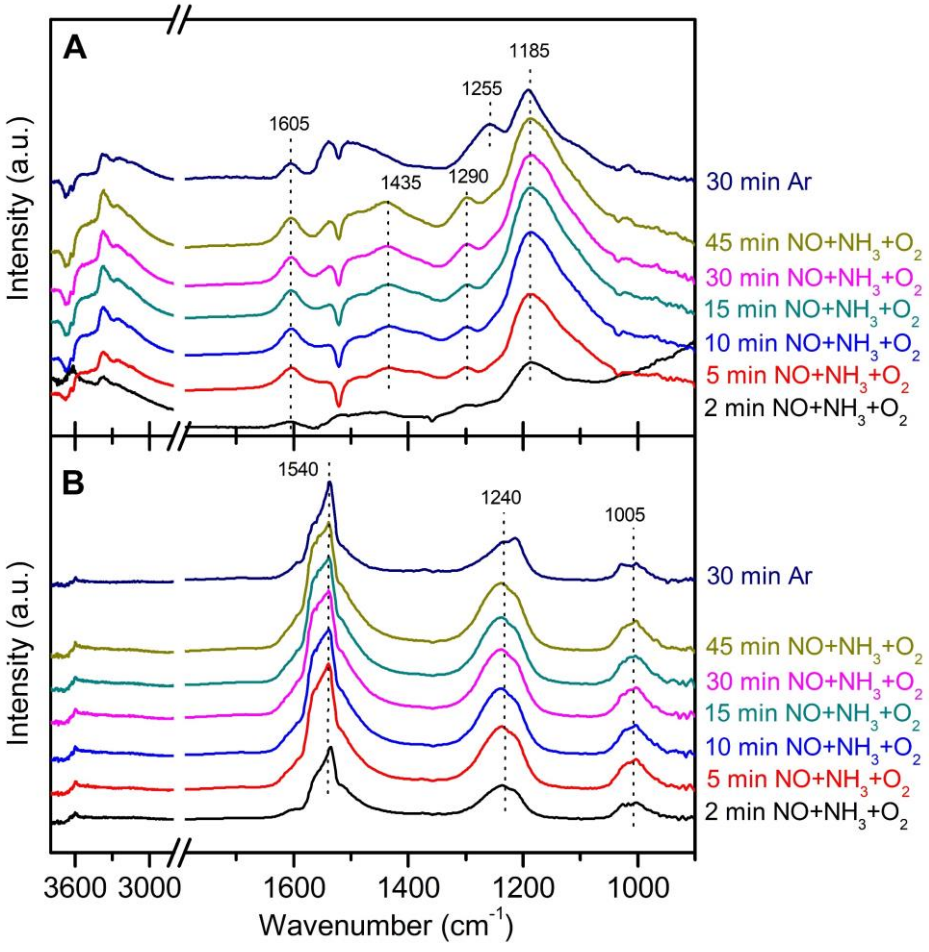

Figure 5.9. FTIR spectra after exposure of 85Mn15Ce catalyst to 1000 ppm NO, 1000 ppm NH_3 and 5% O_2 in Ar followed by an Ar purging at (A) 100 ^oC and (B) 250 ^oC.

At 100 ^{o}C (Figure 5.9A), the exposition of the catalyst to the feeding stream leads to the appearance of the bands associated to ammonia adsorbed species: coordinated ammonia over Lewis acid sites (1605, 1290 and 1185 cm^{-1}), protonated ammonia (1435 cm^{-1}) and NH stretching vibrations (3400-3000 cm^{-1}). The band associated to the consumption of surface OH groups also appears at 3650 cm^{-1}. It should be noted that the broad bands at 1185 cm^{-1} is also contributed by NO adsorption through nitrosyl species, as evidenced by transient experiments.

Generally, increasing exposure time up to 15 minutes causes an increase in the intensity of all bands. Longer exposure time only increases absorption in the region 1550-1250 cm^{-1}, which evidences larger contributions of protonated ammonia, and coordinated ammonia on Lewis acid sites (but only in the band at 1290 cm^{-1}). The oxidation of nitrosyl species towards nitrates during the experiment also contributes to the higher absorbance between 1550-1435 cm^{-1}.

After purging with Ar, all bands related to adsorbed ammonia and nitrosyl species decrease greatly their intensities. In fact, the band associated to protonated ammonia disappears completely, which supports the low stability of this species in comparison to coordinated ammonia. On the other hand, the purge causes no effect on the absorbance between 1550-1435 cm^{-1} and makes a new band visible at 1255 cm^{-1}, which was probably overlapped with those associated to ammonia on Lewis acid sites. This band is assigned to nitrate species. In this sense, the co-adsorption of NO and O_2 at 100 ^{o}C also reported the formation of stable nitrate species (Figure 5.2B).

Regarding nitrate species, it should be noted that, in the above mentioned NO and O_2 co-adsorption at 100 ^{o}C (Figure 5.2B), formation of these species took place after 5 minutes of exposure time. In this case, co-feeding NO, NH_3 and O_2, the absorbance of nitrate species is not as notorious (much less intense bands), appearing at even longer exposure time (15 minutes). These results denote a negative effect of adsorbed ammonia species on the formation of nitrates, which could be associated to the preferential reaction of surface active oxygen of the catalyst with SCR intermediate species rather than with nitrosyl species. These SCR intermediate species would come from the reaction of adsorbed ammonia and NO in the gas phase, since transient experiments provided several evidences against the reaction between adsorbed ammonia and adsorbed NO, either nitrosyl or nitrates.

On the other hand, at 250 ºC (Figure 5.9B), the spectra show the formation of only nitrate species, as denote the three bands at 1540, 1240 and 1005 cm^{-1}. These bands are broad, which evidences the presence of different species of nitrates. Similar spectra, with respect to the position and shape of the bands, were obtained in both NO and NH_3 adsorption in the presence of oxygen at 250 ºC (Figure 5.2B and Figure 5.5B). Therefore, the results obtained make it difficult to discern whether nitrate species come from NO adsorption, NH_3 adsorption or both.

5.1.5. Proposal of a reaction pathway for NO reduction over MnO_x-CeO_2.

The analysis of adsorbed species has evidenced that both NO and NH_3 are adsorbed over the catalyst. Nonetheless, the reactivity of these species in SCR depends on reaction conditions.

Independently of temperature, ammonia adsorption plays a key role as initial stage in NO reduction. However, at low temperature, FTIR experiments have evidenced that NO adsorbed species, either nitrosyl or nitrate, have a low reactivity. This suggests that NO adsorbed species are not greatly involved in the high NO conversion levels (close to 100%) observed at low temperatures in the catalytic activity tests. Therefore, it is proposed that, at low temperature, NO reduction takes place through an Eley-Rideal (ER) mechanism (Equations 5.1-5.5), in which NO reacts from the gas phase with adsorbed ammonia species.

$$NH_3(g) + Mn^{4+}{=}O \rightarrow NH_3 \cdots Mn^{4+}{=}O \quad (5.1)$$

$$NH_3 \cdots Mn^{4+}{=}O \rightarrow NH_2 \cdots Mn^{3+}\text{-}OH \quad (5.2)$$

$$NH_2 \cdots Mn^{3+}\text{-}OH + NO(g) \rightarrow NH_2NO \cdots Mn^{3+}\text{-}OH \quad (5.3)$$

$$NH_2NO \cdots Mn^{3+}\text{-}OH \rightarrow N_2 + H_2O + Mn^{3+}\text{-}OH \quad (5.4)$$

$$Mn^{3+}\text{-}OH + 1/4O_2 \rightarrow Mn^{4+}{=}O + 1/2H_2O \quad (5.5)$$

Ammonia adsorption mostly occurs over Lewis acid sites. In this stage, ammonia interacts via its lone electron pair with the active site, mainly a Mn atom (Equation 5.1). Then, coordinated ammonia could be submitted to a proton abstraction by surface oxygen. Proton abstraction favours the formation of surface hydroxyl groups, which has been clearly evidenced by the increasing intensity of its

band around 3650 cm^{-1}. The different degrees of proton abstraction of coordinated ammonia have a great influence on the selectivity of NO reduction.

The abstraction of a hydrogen leads to the activation of ammonia and the formation of NH_2 species (Equation 5.2), by reducing the active site. The reaction between NH_2 and NO in the gas phase promotes the formation of the NH_2NO intermediate (Equation 5.3), which is decomposed into N_2 and H_2O (Equation 5.4). Finally, the reduced active sites involved in NH_3 activation are oxidized (Equation 5.5). Unfortunately, NH_2 and NH_2NO were not directly observed by FTIR spectra, probably because of their short lifetime and/or low concentration, which suggests ammonia activation as the rate determining step [218, 219].

On the contrary, further proton abstraction of NH_2 (performed similarly by labile and lattice oxygen) leads to the formation of N- species (Equation 5.6), whose reaction with NO in the gas phase is proposed to produce N_2O (NSCR, Equation 5.7). It is important to note that, in Chapter 4, it was corroborated that NSCR is not the only source of N_2O, but NH_3 oxidation reaction also contributes. In this sense, the formation of N_2O from NH_3 oxidation would also involve the reaction between N-species and NO, although, unlike NSCR, NO would come from the subsequent oxidation of N- species.

$$2Mn^{4+}{=}O{+}NH_2{\cdots}Mn^{3+}\text{-}OH \rightarrow 2Mn^{3+}\text{-}OH{+}\ N{\cdots}Mn^{3+}\text{-}OH \quad (5.6)$$

$$N{\cdots}Mn^{3+}\text{-}OH{+}\ NO(g) \rightarrow NNO{\cdots}Mn^{3+}\text{-}OH \rightarrow\ N_2O{+}Mn^{3+}\text{-}OH \quad (5.7)$$

The reaction pathway proposed for N_2O production shows that excessive hydrogen abstraction of adsorbed ammonia has a negative effect on the selectivity of NO reduction towards nitrogen. Since proton abstraction is promoted by surface oxygen, the selectivity of NO reduction will be negatively affected by an excessive enhancement in the oxidative capability of surface oxygen species. This is in agreement with the results obtained in the activity tests for Mn-containing catalysts (Figure 3.23B), where a considerable increase in N_2O production was observed, in comparison to pure CeO_2 sample, as a result of the enhancement of oxidative capability provided by Mn.

Regarding this issue, interestingly, in Chapter 4, it was evidenced an increase of N_2 selectivity in NO reduction under wet conditions (N_2O production decreased while NO conversion was kept constant in Figure 4.14A). The positive effect of water on

selectivity towards N_2 is related to water adsorption over surface oxygen species (Figure 4.15A). This adsorption increases the amount of surface OH groups, which reduces the number of surface oxygen capable of performing the proton abstraction of adsorbed ammonia.

On the other hand, in addition to coordinated ammonia over Lewis acid sites, the FTIR spectra obtained from NH_3, NO and O_2 co-adsorption evidenced an increase in the absorbance of protonated ammonia over time. This fact could be favoured by the increase in the amount of surface hydroxyl groups due to the aforementioned proton abstraction of adsorbed ammonia and/or the adsorption of water produced during the reaction. The increase in the amount of protonated ammonia suggests that NO reduction could also take place through protonated ammonia.

A possible ER mechanism starting from protonated ammonia would be based on the mechanism proposed by Topsøe and co-workers for V-based catalysts [220, 221]. This mechanism involves the ammonia adsorption on an active site with a hydroxyl group (Equation 5.8). Then, the adsorbed ammonia is activated by the reduction of an adjacent active centre (Equation 5.9), which finally reacts with the NO in gas phase (Equation 5.10-12). The reduced active centre is oxidized by the adsorption of gas phase oxygen (Equation 5.13).

The hydroxyl groups are mainly associated to CeO_2, therefore, this mechanism would be promoted by Ce being close to Mn. Nonetheless, it is important to note that the low intensity of the bands related to protonated ammonia suggests that the contribution of this reaction pathway is very small, and also decreases with temperature due to the low stability of protonated ammonia in comparison to ammonia coordinated on Lewis acid sites.

$$NH_3(g) + Ce^{4+}\text{-}OH \rightarrow Ce^{4+}\text{-}O\cdots HNH_3 \quad (5.8)$$

$$Ce^{4+}\text{-}O\cdots HNH_3 + Mn^{4+}{=}O \rightarrow Ce^{4+}\text{-}O\cdots NH_3\cdots Mn^{3+}\text{-}OH \quad (5.9)$$

$$Ce^{4+}\text{-}O\cdots NH_3\cdots Mn^{3+}\text{-}OH + NO(g) \rightarrow Ce^{4+}\text{-}O\cdots NONH_3\cdots Mn^{3+}\text{-}OH \quad (5.10)$$

$$Ce^{4+}\text{-}O\cdots NONH_3\cdots Mn^{3+}\text{-}OH \rightarrow Ce^{4+}\text{-}O\cdots NONH_3 + Mn^{3+}\text{-}OH \quad (5.11)$$

$$Ce^{4+}\text{-}O\cdots NONH_3 \rightarrow Ce^{4+}\text{-}OH + N_2 + H_2O \quad (5.12)$$

$$Mn^{3+}\text{-}OH + 1/4O_2 \rightarrow Mn^{4+}{=}O + 1/2H_2O \quad (5.13)$$

At high temperature, around 250 ^{o}C, the spectra obtained in transient experiments showed a high reactivity of nitrate species formed from NO adsorption. As stated above, NH_3 adsorption is a key stage for SCR. Therefore, SCR can occur via a Langmuir-Hinshelwood (LH) pathway. Nonetheless, the fact that SCR can occur through a LH pathway does not reject the ER pathway. In fact, both ER and LH reaction pathways are proposed to take place at high temperature, although the contribution of the latter is probably higher due to the fast oxidation of NO on the catalytic surface.

The proposed LH mechanism is based on the reaction between a nitrate specie, two adsorbed ammonia and a NO in the gas phase. The formation of nitrate occurs by means of the reaction between surface oxygen and adsorbed NO (Equation 5.15). This step becomes easier at high temperature, as a consequence of the higher reactivity of surface oxygen and easier oxygen replacement from the gas phase (oxidation of the active sites). Nitrate species reacts with two adjacent adsorbed ammonia (Equation 5.17), which leads to the formation of a reaction intermediate whose reaction with an NO in gas phase allows to the formation of nitrogen and water (Equation 5.18).

$$1/2O_2 \rightarrow O(ads) \tag{5.14}$$

$$NO(g)+O(ads)+Mn^{4+}{=}O \rightarrow Mn^{3+}\text{-}O\text{-}NO_2 \tag{5.15}$$

$$2NH_3(g)+2Mn^{4+}{=}O \rightarrow 2\left(NH_3\cdots Mn^{4+}{=}O\right) \tag{5.16}$$

$$Mn^{3+}\text{-}O\text{-}NO_2+2\left(NH_3\cdots Mn^{4+}{=}O\right) \rightarrow Mn^{3+}\text{-}O\text{-}NO_2 \begin{matrix} \therefore NH_3\cdots Mn^{4+}{=}O \\ \because NH_3\cdots Mn^{4+}{=}O \end{matrix} \tag{5.17}$$

$$Mn^{3+}\text{-}O\text{-}NO_2 \begin{matrix} \therefore NH_3\cdots Mn^{4+}{=}O \\ \because NH_3\cdots Mn^{4+}{=}O \end{matrix} +NO(g) \rightarrow 2N_2+3H_2O+3Mn^{4+}{=}O \tag{5.18}$$

Regarding N_2O formation at high temperature, NSCR is suggested to occur through both ER and LH pathways, in a similar way to SCR. The ER mechanism for N_2O production would be similar to the one proposed for low temperature. On the other hand, the proposed LH mechanism for N_2O formation is based on the reaction between a nitrate species and an adsorbed ammonia by reducing the active site (Equation 5.19).

$$Mn^{3+}\text{-}O\text{-}NO_2+NH_3\cdots Mn^{4+}{=}O \rightarrow N_2O+H_2O+Mn^{4+}{=}O+Mn^{3+}\text{-}OH \tag{5.19}$$

The proposed LH pathway for N_2O production is simple, since it only requires one ammonia molecule, unlike the LH pathway for SCR, which requires the adsorption of two ammonia molecules (Equation 5.17). According to the proposed high temperature SCR pathway, the fact that the production of N_2O is easier than N_2 production is in agreement with the high N_2O production observed in the catalytic tests at high temperature.

In addition to N_2O, NO reduction also produced NO_2 at high temperature. The results obtained in Chapter 4 showed that NO_2 mostly comes from NO oxidation, although total oxidation of NH_3 also contributes. FTIR analysis of the adsorption of both compounds at high temperature and in the presence of oxygen (Figures 5.2B and 5.5B) evidenced the only formation of nitrate species. Based on these results, the generation of NO_2 is inevitably related to surface nitrates, specially to the decomposition of this species at high temperature.

5.2. IDENTIFICATION OF ADSORBED SPECIES IN o-DCB OXIDATION OVER MnO_X-CeO_2 CATALYSTS.

In the same way than in Section 5.1, two experiments with different feeding stream were carried out at two different temperatures, 100 and 250 ^oC. The experimental procedure has been detailed in Chapter 2. Firstly, o-DCB adsorption in the absence of oxygen was performed. Then, the influence of oxygen in the gas feeding stream was evaluated by means of o-DCB and O_2 co-adsorption. The latter experiment ensures a feeding stream containing the two reactants involved in o-DCB oxidation.

5.2.1. Adsorbed species in o-DCB adsorption.

FTIR spectra obtained after exposing the 85Mn15Ce catalyst to a gas stream with o-DCB and balanced with Ar is shown in Figure 5.10. The assignment of IR bands resulting from o-DCB adsorption are listed in Table 5.3.

At 100 ^oC (Figure 5.10A), o-DCB adsorption leads to the appearance of several bands at 1570, 1455 and 1435 cm^{-1} associated to the aromatic ring stretching modes (8a, 19a and 19b, respectively) [104, 222-224]. C-H bonds of the aromatic ring are also evidenced by the band located at 1255 cm^{-1} [75, 225]. The bands at 1170, 1125 and 1030 cm^{-1} are due to C-Cl stretching [104, 222]. In the high

wavenumber range, the negative band at 3670 cm^{-1} indicates the consumption of surface hydroxyl groups as a consequence of their interaction with o-DCB. Additionally, the band at 3070 cm^{-1} is due to stretching of aromatic C-H [104].

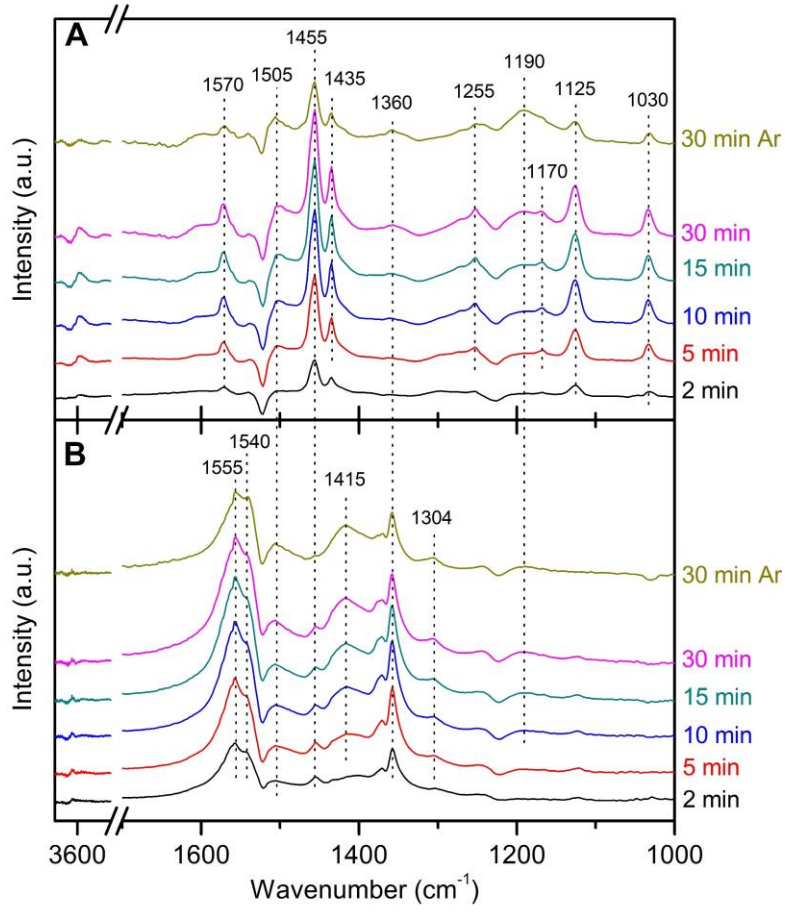

Figure 5.10. FTIR spectra after exposure of 85Mn15Ce catalyst to 1000 ppm o-DCB in Ar followed by an Ar purging at (A) 100 ^{o}C and (B) 250 ^{o}C.

The longer the exposure time the higher the intensity of above-mentioned bands and also the appearance of other bands at 1505, 1360 and 1190 cm^{-1}, related to intermediate species resulting from the reaction between adsorbed o-DCB and surface oxygen of the catalyst. According to that proposed by Larrubia and co-

workers [104], the band located at 1190 cm^{-1} is assigned to phenate species. This species is usually considered the first intermediate in o-DCB oxidation after chlorine abstraction. On the other hand, the bands at 1505 and 1360 cm^{-1} are assigned to maleate [75, 223] and formate species [226, 227], respectively.

The presence of characteristic bands of o-DCB, as described above, suggests that, at 100 ^{o}C, adsorption of o-DCB is stable. That is, it is hardly oxidized on the catalytic surface, because oxygen species are not active enough. o-DCB adsorption could occur by the interaction with a metal atom, which acts as a Lewis acid centre, or even on a surface hydroxyl group by means of the formation of weak H-bonds with chlorine atoms of o-DCB. However, after 30 minutes of exposure time (Figure 5.10A), the appearance of two overlapped bands at 2360 and 2340 cm^{-1}, related to CO_2 in the gas phase, indicates the complete oxidation of a part of adsorbed o-DCB.

Table 5.3. Assignment of the IR bands detected in the o-DCB adsorption over 85Mn15Ce catalyst.

Band (cm^{-1})	**Assignment**	**Reference**
1570, 1455, 1435	Aromatic stretching	[75, 225]
1255	C-H in plane bending	[75, 225]
1170, 1125, 1030	C-Cl stretching	[75, 225]
1190	Phenate (C-O stretching)	[75, 225]
1505	Maleate (C-O stretching)	[75, 225]
1540, 1360	Formate (C-O stretching)	[75, 225, 227]
1555, 1415	Acetate (C-O stretching)	[223, 228, 229]
1370	CH_2 stretching	[229]
1304	Enolic species	[226, 230]
1610	Hydroxyl	[227]
2360, 2340	CO_2 gas	[227, 232]
2930, 2860	C-H stretching	[228, 231]
3070	Aromatic C-H stretching	[104]

After purging with Ar, all bands related to o-DCB decrease in intensity, so the interaction between o-DCB and the catalytic surface is not as strong as, for example, those observed in the previous section for NO and NH_3 at low temperature (Figure 5.1A and Figure 5.3A). Nonetheless, the increase in the intensity of the bands related to phenate and CO_2 also evidences that part of the adsorbed o-DCB reacts with catalytic surface oxygen during the purge stage.

On the other hand, at 250 ^{o}C (Figure 5.10B), obtained spectra are completely different to those observed at low temperature. The bands at 1555 and 1415 cm^{-1} are related to acetate intermediate [223, 228, 229], whereas those at 1540 and 1360 cm^{-1} are associated to formate species [75, 225, 227]. The bands ascribed to the main intermediates identified at 100 ^{o}C, phenate (1505 cm^{-1}) and maleate (1190 cm^{-1}), are also present at 250 ^{o}C, although less intense compared to the bands of acetate and formate species. Moreover, the band at 1304 cm^{-1} has been attributed to the presence of enolic species [226, 230]. The presence of enolic intermediates is supported by the appearance of the bands at 2930 and 2860 cm^{-1}, which are associated in the literature to different types of C-H stretching [228, 231].

In the high wavenumber range, there are no bands supporting the interaction of o-DCB with surface hydroxyl groups through H-bonds. The band associated to stretching of aromatic C-H (3070 cm^{-1}) has not been observed either. The latter, together with the absence of other bands related to molecular adsorbed o-DCB (bands of aromatic ring and C-Cl bond) suggests that, at 250 ^{o}C, o-DCB is adsorbed and, then, rapidly oxidized by surface oxygen of the catalyst leading to formation of the above-mentioned intermediates. However, total oxidation of the intermediates is not fast, since the bands of CO_2, at 2360 and 2340 cm^{-1}, do not appear until 30 minutes of exposure time. One reason for this behaviour could be the absence of oxygen in the gas phase.

The oxidative capability of the catalyst is improved not only by increasing temperature, but also by the presence of oxygen in the gas phase, as corroborated in the analysis of NO and NH_3 adsorbed species in the previous section. For this reason, co-adsorption of o-DCB and O_2 was performed at different temperatures. The spectra are shown in Figure 5.11 and Table 5.3 summarizes the assignment of the IR bands detected.

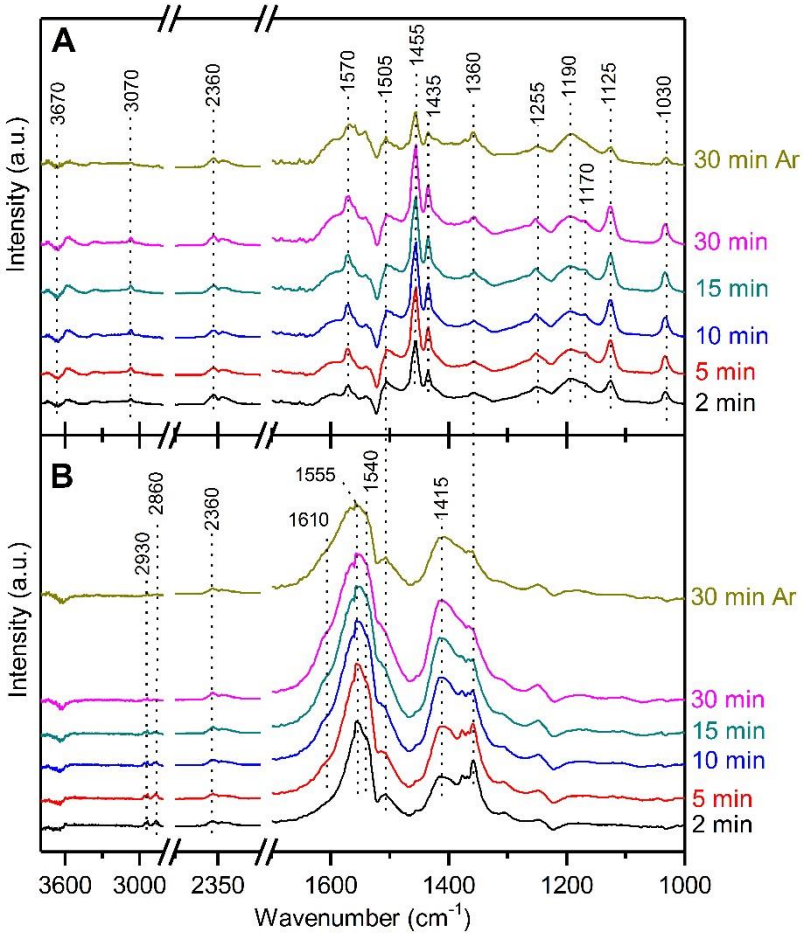

Figure 5.11. FTIR spectra after exposure of 85Mn15Ce catalyst to 1000 ppm o-DCB and 5%O_2 in Ar followed by an Ar purging at (A) 100 ^{o}C and (B) 250 ^{o}C.

o-DCB and O_2 co-adsorption promotes similar spectra than those observed in the absence of oxygen. At 100 ^{o}C (Figure 5.11A), there are bands associated to aromatic ring (1570, 1455 and 1435 cm^{-1}), C-Cl bonds (1170, 1125 and 1030 cm^{-1}) and C-H bonds (1255 and 3070 cm^{-1}) of adsorbed o-DCB. Moreover, bands related to maleate, phenate and formate intermediates also appear at 1505, 1360 and 1190 cm^{-1}, respectively. Interestingly, these bands appear just after exposing the catalyst to the feeding stream, whereas in the absence of oxygen (Figure 5.10A),

their presence was not noticeable until 30 minutes of exposition. This evidences that reaction between surface oxygen species and adsorbed o-DCB is faster, as a consequence of the enhancement of the oxidative capability of the catalyst in the presence of oxygen.

On the other hand, at 250 ^{o}C (Figure 5.11B), the main observed bands were related to acetate (1555 and 1415 cm^{-1}) and formate (1540 and 1360 cm^{-1}) species. Additionally, two broad shoulders appear between 1600-1500 cm^{-1}. The first one, around 1505 cm^{-1}, is due to maleate intermediate species. The second one, around 1610 cm^{-1}, has been assigned to the bending vibration of the OH groups of water [227]. The presence of enolic species is also evidenced by the small band at 1304 cm^{-1}. Furthermore, as a consequence of the wide variety of intermediate species, different types of C-H bonds are promoted, which are evidenced by the bands at 2930, 2860 and 1255 cm^{-1}.

Comparison between the obtained results evidences a different distribution of intermediates depending on temperature. Thus, at 100 ^{o}C, the main intermediates were phenates and maleates, whereas enolic, acetate and formate species were the ones at 250 ^{o}C. The reason for this difference could be related to the little activity of the catalyst at low temperature, not enough to promote the rupture of the aromatic ring, since the bands ascribed to different types of C-H bonds of intermediates (2930 and 2860 cm^{-1}) do not appear in the spectra at 100 ^{o}C. However, the presence of CO_2 bands at 2360 and 2340 cm^{-1} just after exposition of the catalyst to the feeding stream at both low and high temperature denotes that a small part of adsorbed o-DCB is indeed completely oxidized independently of temperature.

Therefore, these results suggest that o-DCB oxidation takes place through different pathways depending on temperature. Thus, at low temperature, o-DCB tends to be completely oxidized after its adsorption as phenate and maleate species, whereas the increase of temperature leads to a higher number of partial oxidations, which involve the formation of other intermediates. In line with this observation, the results of catalytic tests also provided evidence to support o-DCB oxidation follows different reaction pathways as a function of temperature. In these experiments, the decrease in the selectivity towards CO_2 in the medium range of temperature was corroborated, while the selectivity towards CO and chlorinated organic products increased (Figures 3.26 and 4.4). Additionally, it is important to note that

tetrachloromethane and tetrachloroethylene, two of the three chlorinated organic by-products identified in the catalytic tests, present a number of carbon atoms that matches with those of the main intermediates identified at 250 ºC (acetate and formate species), which evidences that these chlorinated organic compounds were formed by a different reaction pathway than that at low temperature, where no chlorinated organic compounds were detected.

The influence of Mn content on o-DCB adsorption was briefly analysed. This analysis was performed at 250 ºC because previous results have evidenced that o-DCB oxidation promotes a higher number of intermediates at high temperature. The results are shown in Figure 5.12.

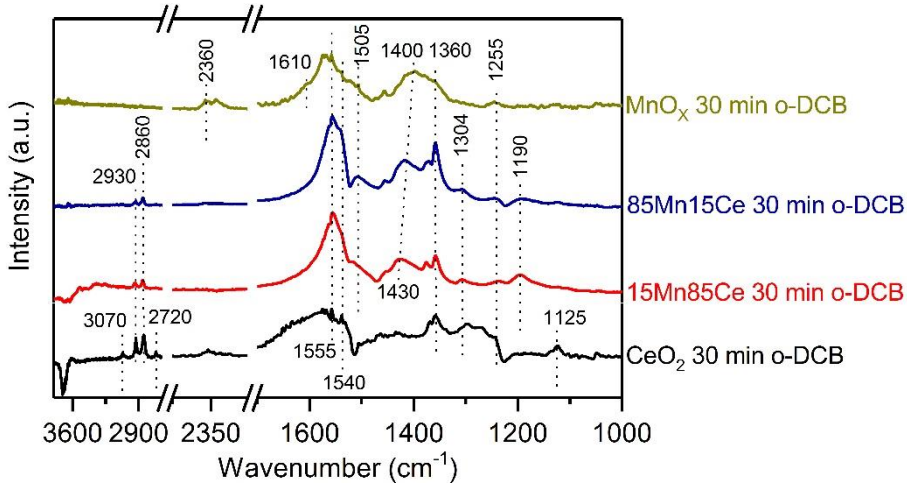

Figure 5.12. FTIR spectra after exposing catalysts with different Mn and Ce content to a stream composed by 1000 ppm o-DCB and 5% O_2 in Ar followed by an Ar purging at 250 ºC.

Bimetallic samples (85Mn15Ce and 15Mn85Ce) exhibit similar spectra than the one described for o-DCB adsorption at 250 ºC in the absence of oxygen (Figure 5.10B). That is, there are only bands associated to intermediate species (acetates, formates and enolics); so, o-DCB is adsorbed and, then, rapidly oxidized at both low and high Mn contents. However, in the bimetallic catalyst with the lowest Mn content (15Mn85Ce), in the high wavenumber range, there is a negative band related to the consumption of surface hydroxyl groups (3700-3650 cm^{-1}), and also a broad band in the H-bond region (3630-3570 cm^{-1}). This evidences the interaction between

surface OH groups and intermediate species through H-bonds, although this interaction does not seem to affect the reaction pathway, since the remaining bands are similar to those of the bimetallic catalyst with the highest Mn content.

On the other hand, several differences are observed in the spectra of o-DCB adsorption on pure oxides. In the case of MnO_X, the band associated to enolic species (1304 cm^{-1}) is not detected. The bands related to the different types of C-H bonds (2930 and 2860 cm^{-1}) do not appears either. This result reveals that the presence of different types of C-H bonds is strongly related to enolic species. The only intermediates identified were acetate and formate species. In this regard, the two bands related to acetates are shifted in comparison to bimetallic catalysts (the band at 1555 cm^{-1} to higher and the band at 1414 cm^{-1} to lower wavenumber), which evidences that the strength of the interaction between the intermediate species and the catalyst is different depending on Mn content. In addition, the formation of CO_2 is also identified (2360 cm^{-1}), which indicates the complete oxidation of a part of adsorbed o-DCB being in agreement with the appearance of the band at 1610 cm^{-1}, related to water.

In the case of o-DCB adsorption over pure CeO_2, the resulting spectrum denotes a lower oxidizing capability for this metal oxide, since the bands related to molecular adsorbed o-DCB are observed (3070, 1570, 1435 and 1125 cm^{-1}). In addition, the negative band in the hydroxyl region is more noticeable than in the other catalysts (Figure 5.12). The fact that the interaction between o-DCB and surface hydroxyl groups is more relevant in the catalysts with high Ce content (CeO_2 and 15Mn85Ce) is associated to cerium oxide is responsible for providing these surface groups, as was stated in previous sections.

Regarding the intermediate species formed on Ce, it should be noted that the bands are broader than in Mn-containing catalysts, which makes a good assignment difficult. Nonetheless, the peaks at 1555, 1360 and 1304 cm^{-1} evidence the presence of acetate, formate and enolic species. In fact, the presence of the latter is in agreement with the appearance of the bands related to different types of C-H bonds (2930 and 2860 cm^{-1}). Moreover, the formation of a broad absorption between 1700-1600 cm^{-1} suggests the additional formation of benzoquinone-type species [75, 229].

5.2.2. Proposal of a reaction pathway for o-DCB oxidation over MnO_X-CeO_2.

FTIR analysis of o-DCB adsorption has evidenced o-DCB is molecularly adsorbed and, then, it reacts with surface oxygen of the catalyst to form intermediate species, which are mostly oxidized towards CO, CO_2 and HCl. Therefore, these results corroborate that o-DCB oxidation follows a Mars-van Krevelen reaction pathway.

On the basis of intermediate species identified by FTIR, a reaction pathway for o-DCB oxidation has been proposed, which is shown in Figure 5.13. After o-DCB adsorption, a chlorine abstraction of one of the chlorine atoms of o-DCB takes place by nucleophilic substitution (step 1), whereby the leaving chlorine is replaced by an oxygen bonded to the active site, leading to the formation of phenate species (step 1→2). Nucleophilic substitution occurs in a carbon bonded to chlorine atom, because this bond is weaker than the bonds between carbon and hydrogen. This fact is in accordance with the reported lower activation energy of benzene oxidation as its chlorination degree increases [75].

Nucleophilic substitution is promoted by the interaction of non-bonding electron pair of oxygen (nucleophile) bonded to Mn and the interaction of the non-bonding electron pair of chlorine (leaving group) with Mn, that acts as a Lewis acid site (step 1.1). A similar adsorption is proposed by Finocchio and co-workers [222]. Nonetheless, FTIR results have shown o-DCB can interact with surface hydroxyl groups (step 1.2), which would also produce phenate species and HCl. The adsorption of o-DCB by means of surface hydroxyl groups has also been proposed for o-DCB oxidation on V-based catalysts [131]. o-DCB adsorption on surface hydroxyl groups only takes place at low temperature, since the corresponding FTIR bands disappeared at 250 ^{o}C.

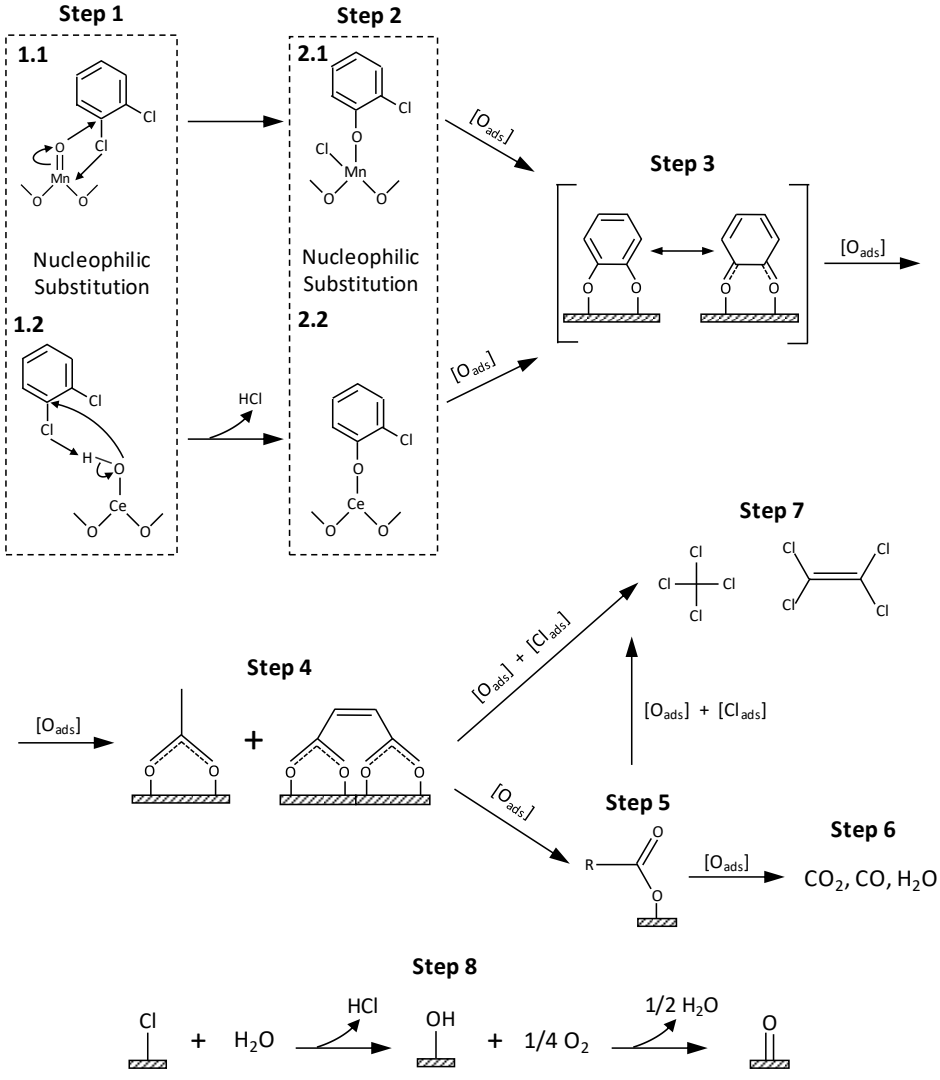

Figure 5.13. Reaction pathway proposed for o-DCB oxidation over MnO_X-CeO_2 catalysts.

FTIR results suggest that phenate intermediate reacts with surface oxygen leading to aromatic ring cleavage and, in turn, promoting the formation of maleate species. However, according to literature, prior to maleate species, the reaction between surface oxygen and phenate leads to benzoquinone-type intermediates.

Lichtenberger and co-workers [75] proposed that phenate species are oxidized to ortho and/or para-benzoquinone (formed through surface catecholates) by means of an electrophilic substitution, which was based on their FTIR evidence. A similar proposal was made by Wang and co-workers [229] for 1,3,5-trichlorobenzene oxidation. However, the proposed mechanisms for the formation of benzoquinone-type intermediates via electrophilic substitution are not consistent enough. As an alternative, the formation of benzoquinone is also proposed through partial oxidation in benzene oxidation [224], although this mechanism seems not consistent enough either.

According to FTIR results of this work, catecholate and benzoquinone-type species are not observed in the spectra for Mn-containing catalysts. They were only identified on pure cerium oxide (Figure 5.12), which evidences that the enhancement of the oxidative capability, promoted by the presence of Mn, favours a faster oxidation of these intermediates towards maleate species. However, although catecholate and benzoquinone species are rapidly oxidized to maleates, they have been included in the reaction pathway proposal and their formation is related to a second nucleophilic substitution (step 2.1 and/or 2.2), which is similar to that proposed in step 1. In this step 2, the second chlorine of o-DCB is replaced by an oxygen from the active site.

Subsequently, catecholate and/or benzoquinone-type intermediates react with surface oxygen leading to aromatic ring cleavage and forming maleate intermediates (step 3→4). In turn, maleate species are oxidized towards other intermediates, such as acetate, formate and enolic species (step 4→5), which are eventually oxidized towards CO, CO_2 and H_2O (main pathway) (step 5→6). However, these intermediates can react with adsorbed chlorine to form chlorinated organic compounds, which desorb as by-products (minority pathway) (step 4→7 and 5→7). Finally, the active sites involved in adsorption and reaction with o-DCB and intermediates are re-oxidised with oxygen from the gas phase. In addition, chlorine adsorbed on active sites is removed by reaction with water (produced during oxidation, step 8) or even with a hydroxyl group.

Regarding intermediate species, FTIR results have corroborated that the main intermediates obtained at 100 ^{o}C (phenate and maleate species) are different to those obtained at 250 ^{o}C (acetate, formate and enolic species), although FTIR results at both temperatures evidenced (by means of the presence of bands related

to CO_2) the complete oxidation of a part of adsorbed o-DCB. On the basis of this, o-DCB oxidation is proposed to occur in different way depending on temperature.

At low temperature, after o-DCB adsorption as phenate and the opening of the aromatic ring to form maleate species, no other reaction intermediate is observed, as they are completely oxidised to CO_2. That means oxidation reaction goes from step 4 to step 6 very quickly. On the other hand, at high temperature, o-DCB adsorption and cleavage of the aromatic ring is faster than at low temperature, since FTIR spectra did not show notable bands related to phenate and maleate intermediates. However, the subsequent oxidation of maleate species is slower, because of the formation of intermediates not observed at low temperature, such as formate, enolic and acetate species. This means that step 5 and step 7 have a notable contribution in the oxidation pathway.

In order to establish a connection between this innovative reaction pathway (change with temperature) proposed for o-DCB oxidation and the results of previous chapters in this work, a global discussion follows. Some of the catalytic tests performed in Chapters 4 and 3 also allowed to evidence a dependence between temperature and oxidation mechanism. In this sense, this dependence was proposed to be associated to the oxidative capability of Mn in different environment, i.e., Mn in high interaction with Ce or Mn segregated as manganese oxide (both phases were identified in Chapter 3). Moreover, it was concluded that Mn in high interaction with Ce becomes active at lower temperature than Mn segregated as oxide, as a consequence of the higher oxygen mobility provided by the interaction between Mn and Ce.

This previous proposal is in accordance with the results obtained in FTIR and the proposed reaction mechanism for o-DCB oxidation. Thus, at low temperature, the absence of reaction intermediates such as acetate, enol and formate is explained by the fact that, after cleavage of the aromatic ring, all formed species are rapidly oxidized to CO_2 due to the high oxidative capability of Mn phase where the reaction mostly takes place (Mn in high interaction with Ce). In fact, formation of only CO_2 is further supported by TOS results (Figure 4.5), in which o-DCB oxidation performed simultaneously with NO reduction only produced CO_2 at 200 ^{o}C.

On the other hand, catalyst deactivation affected negatively o-DCB conversion at low temperature (Figure 4.5). Deactivation was associated to the adsorption of chlorine and carbonaceous compounds. This also agrees with the reaction pathway

proposal, since chlorine adsorption has been explained by the bonding of chlorine atoms to the active site, as a result of the two nucleophilic substitutions. Obviously, the removal of adsorbed chlorine is promoted by the reaction with water [75] as can be seen in Figure 5.13. However, removal of surface chlorine seems not to be fast at low temperature, which causes catalyst deactivation.

According to the above-explanation, the formation of different intermediates with increasing temperature evidences that other Mn species (Mn segregated as oxide), with less oxidative capability, become active under these conditions. The formation of these intermediate species has been evidenced in the catalytic tests, where, interestingly, the presence of tetrachloromethane and tetrachloroethylene was detected around 250-300 ^{o}C. These compounds could be formed by chlorination reactions between adsorbed chlorine and acetate and formate species detected by FTIR.

Interestingly, catalytic tests have shown that increasing temperature above 250-350 ^{o}C leads to the disappearance of the intermediates detected in this temperature range. Unfortunately, FTIR analysis above 350 ^{o}C has not been carried out. However, the disappearance of intermediates can be ascribed to the improvement of the oxidative capabilities of Mn species, so they are able to rapidly and completely oxidise the compounds formed after the cleavage of the aromatic ring.

5.3. INFLUENCE OF NO AND NH_3 ADSORBED SPECIES ON o-DCB OXIDATION OVER MnO_X-CeO_2 CATALYSTS.

This section will address the analysis of the effect of NO and NH_3 adsorbed species on o-DCB oxidation. Before starting, it is important to note that the reason for studying the effect of NO and NH_3 adsorbed species on o-DCB oxidation but not the effect of o-DCB adsorbed species on NO reduction lies in the results obtained in Chapter 4. Thus, while o-DCB only had the expected negative effect on NO reduction due to the competition with NO and NH_3 for the active sites (Figure 4.9); the presence both of NO and NH_3 caused a positive effect on o-DCB conversion (Figure 4.10 and 4.11), which hides the negative effect from competition for the active sites.

Figure 5.14 shows the spectra obtained from o-DCB adsorption over a catalyst previously exposed to a NO-containing stream at different temperatures. At 100 ^{o}C (Figure 5.14A), only nitrosyl NO adsorbed species are identified (band at 1190 cm^{-1}), whereas at 250 ^{o}C (Figure 5.14B), NO is adsorbed as nitrate species (bands at 1530, 1215 and 1020 cm^{-1}). After o-DCB adsorption at low temperature, additional bands associated to molecular adsorbed o-DCB are identified, that is, related to the aromatic ring (1570, 1455 and 1435 cm^{-1}), C-H stretching (1255 cm^{-1}) and C-Cl bonds (1125 and 1030 cm^{-1}).

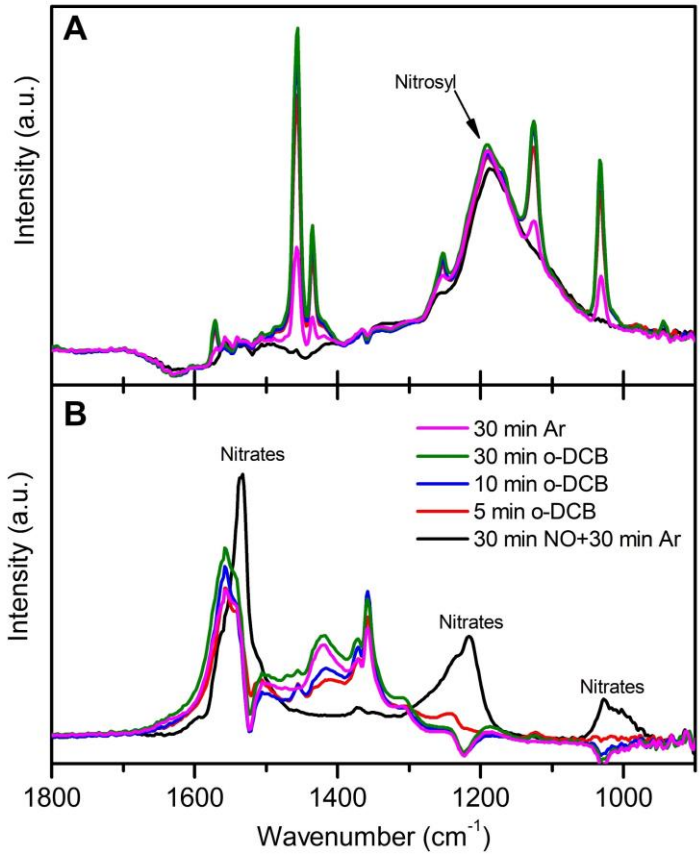

Figure 5.14. FTIR spectra of 85Mn15Ce catalyst pretreated with 1000 ppm NO/Ar and, then, exposed to 1000 ppm o-DCB/Ar at different exposition times followed by an Ar purging, at A) 100 ^{o}C and B) 250 ^{o}C.

However, the intensity of the bands associated to previous adsorbed NO species does not decrease. This trend can be clearly observed in the band at 1190 cm^{-1}, whose intensity becomes higher due to overlapping with the band related to phenate species, which also appears around 1190 cm^{-1}. The fact that the band related to nitrosyl species is not affected by o-DCB adsorption means that these species are not involved in o-DCB adsorption.

However, at high temperature, a different behaviour has been found, since the bands related to nitrate species disappear progressively with exposure to o-DCB feeding stream (no nitrate bands remain after 10 minutes). Simultaneously to the disappearance of nitrate bands, o-DCB adsorption also promotes the appearance of the bands related to intermediate species from o-DCB oxidation (acetate, formate and enolic species). Therefore, the disappearance of nitrate bands could be associated to nitrates participating in o-DCB oxidation. This would be in accordance with the results obtained in Chapter 4, where a slight improvement in o-DCB conversion was observed in the presence of a small concentration of NO (Figure 4.10). The improvement in o-DCB conversion, as reported in the literature, is due to nitrate species or NO_2 lead to a faster re-oxidation of the active sites involved in o-DCB oxidation [115, 187].

On the other hand, Figure 5.15 shows the spectra obtained from o-DCB adsorption over a catalyst previously exposed to a NH_3-containing stream at different temperatures. At 100 ^oC, NH_3 is mainly coordinated over Lewis acid sites (bands at 1605 and 1190 cm^{-1}), and also protonated (NH_4^+) (band at 1430 cm^{-1}) but to a lesser extent. At 250 ^oC, NH_3 only adsorbs on Lewis acid sites, although its stability is low, since only the band at 1190 cm^{-1} is observed.

At low temperature, subsequent o-DCB adsorption does not alter the NH_3 bands already formed. Moreover, the typical bands associated to molecular o-DCB adsorption appear. At high temperature, the adsorption of o-DCB leads to the appearance of bands related to intermediate species of o-DCB oxidation (1415, 1360, 1304 and 1190 cm^{-1}). However, the most characteristic bands of formate and acetate species around 1555 and 1140 cm^{-1} are not observed due to a negative band that seems to be associated to NH_3 adsorption at high temperature (Figure 5.4B). The appearance of bands related to oxidizing intermediates of o-DCB leads to an increase in the intensity of the only band of NH_3 (1190 cm^{-1}), identified previously to o-DCB adsorption, due to its overlapping with phenate band.

Nonetheless, the contribution of phenate species decreases after purging with Ar, the intensity of this band returning to the values previous to o-DCB adsorption, which evidences that NH_3 keeps adsorbed on the catalyst after o-DCB adsorption.

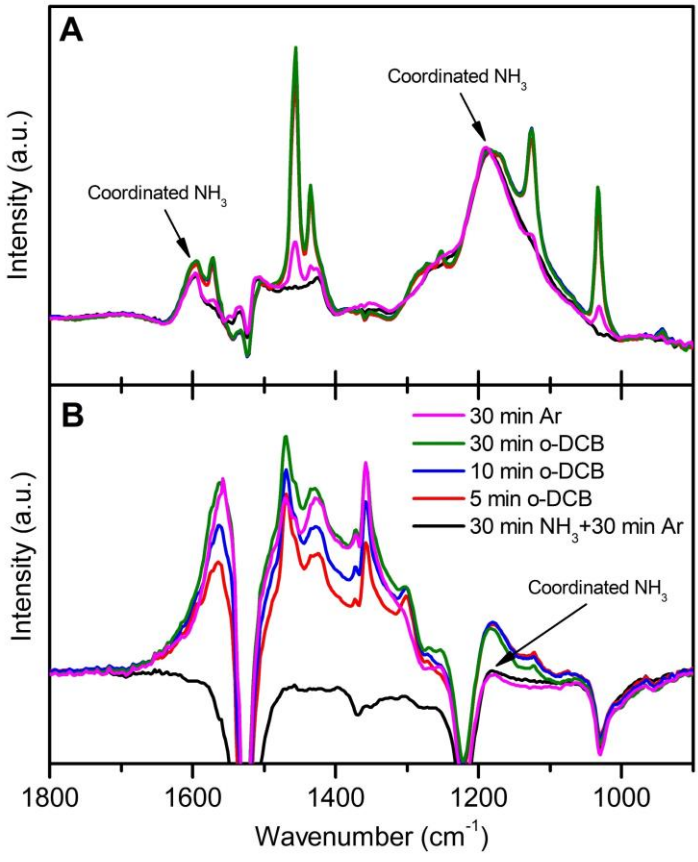

Figure 5.15. FTIR spectra of 85Mn15Ce catalyst pretreated with 1000 ppm NH_3/Ar and, then, exposed to 1000 ppm o-DCB/Ar at different exposition times followed by an Ar purging, at A) 100 ^oC and B) 250 ^oC.

Therefore, the fact that the bands associated to NH_3 remain in the spectra after o-DCB adsorption at both high and low temperature suggests that NH_3 does not participate in o-DCB adsorption. Therefore, these results do not allow to explain the small positive effect of NH_3 on o-DCB conversion. This is probably due to the positive effect of NH_3 is not related to o-DCB oxidation, but to the removal of Cl

adsorbed on the active sites as was proposed in Chapter 4. So, the use of other characterization techniques, such as EDX and XPS, that allow to quantify the amount of surface chlorine adsorbed would be interesting to verify this hypothesis.

5.4. GLOBAL VIEW AND CONCLUSIONS.

This chapter has addressed the identification of adsorbed species in NO reduction and o-DCB oxidation over MnO_X-CeO_2 catalysts in order to propose a reaction pathway for both reactions. The identification of adsorbed species has been performed using in situ FTIR.

Regarding NO reduction, the oxidative capability of the catalyst plays a key role in the species formed from both NO and NH_3 adsorption. In NO adsorption, NO adsorbs as nitrosyl species at low temperature, although increasing temperature leads to oxidize rapidly these nitrosyl species to nitrate. The presence of oxygen also favours the oxidative capability of the catalyst, as it decreases the stability of nitrosyl species, promoting their oxidation to nitrate.

As for NH_3 adsorption, it is adsorbed over Lewis acid sites (coordinated through its non-bonding electron pair), over hydroxyl groups (as NH_4^+) or interacting with H-bonds. Similar adsorbed species are promoted when increasing temperature, although coordinated ammonia has been identified as the most stable one. However, if the increase in temperature is combined with the presence of oxygen in the gas phase, surface oxygen species become active enough to oxidize NH_3 and, thus, nitrate species are generated. Interestingly, these nitrate species are less stable than those formed in NO adsorption at high temperature.

Transient experiments with different feeding stream (Section 5.1.3) and co-feeding of all reagents involved in SCR (Section 5.1.4) have evidenced that, at low temperature, adsorbed NH_3 mostly reacts with NO from the gas phase. Moreover, these experiments have allowed to elucidate re-oxidation of the catalyst as a key step in NO reduction, since NH_3 adsorbed species were not completely consumed in the presence of NO until NO and O_2 were co-fed. On the contrary, at high temperature, adsorbed NH_3 reacts with NO adsorbed as nitrate.

On the basis of the results described above, the reduction of NO at low temperature has been proposed to mostly follow an ER type pathway, through the reaction

between NO from the gas phase and adsorbed NH_3. NH_3 can be adsorbed in two different ways. On the one hand, it is adsorbed over a Lewis acid site, where it undergoes a proton abstraction by surface oxygen. On the other hand, NH_3 is also adsorbed on surface hydroxyl groups and, then, it is deprotonated by an adjacent active site. Then, adsorbed ammonia reacts with NO from the gas phase generating N_2. In this reaction pathway, the formation of N_2O through NSCR has been also considered. This reaction is proposed to occur when NO from the gas phase reacts with excessively deprotonated adsorbed ammonia.

At high temperature, NO reduction has been proposed to mostly follow a LH type pathway because, at this condition, NO is easily adsorbed and oxidised to nitrate. Nonetheless, some small contribution of ER pathway cannot be discarded. The proposed LH pathway involves three active sites for the adsorption of two NH_3 and one NO (as nitrate) molecules. The subsequent reaction of these three species with a NO from the gas phase leads to the generation of N_2. In contrast, if the reaction occurs between a nitrate and an adsorbed NH_3, it will promote the formation of N_2O. The fact that N_2O formation at high temperature follows a simpler route than SCR is in accordance with the decrease in N_2 selectivity evidenced from catalytic tests at high temperature.

Regarding oxidation reaction, at low temperature, o-DCB is hardly oxidized by surface oxygen, so it is adsorbed through its molecular structure. Nonetheless, a small amount of adsorbed o-DCB is subsequently oxidized, leading to phenate and maleate intermediates. This oxidation of adsorbed o-DCB is favoured by the presence of O_2 in the gas phase. The increase of temperature favours conversion of o-DCB into acetate, formate and enolic adsorbed intermediates, both in the presence and in the absence of oxygen.

Based on the species identified in o-DCB adsorption, o-DCB has been proposed to follow a Mars-van Krevelen-type pathway. The first step is a nucleophilic substitution in which one chlorine of o-DCB is substituted by one oxygen from the catalyst generating a phenate species. This mainly occurs on Lewis acid sites, although evidence of o-DCB adsorption on hydroxyl groups has been found. Then, phenate species are submitted to a second nucleophilic substitution leading to catecholate and/or benzoquinone-type species. Both species are easily oxidised by the catalyst, promoting the cleavage of aromatic rings and generating maleate species, which are subsequently oxidised to enolic, acetate and formate

intermediates. Finally, these compounds are mostly oxidised to CO and CO_2, although they can also react to a lesser extent with adsorbed chlorine on active sites (from nucleophilic substitution), which produces chlorinated organic compounds that desorb as by-products.

Moreover, FTIR results evidenced a different distribution of intermediate species as a function of temperature in o-DCB adsorption. This fact has been associated to the aforementioned pathway for o-DCB oxidation, which occurs in different way depending on temperature. In this sense, at low temperature, once the aromatic ring is opened to form maleate species, the oxidation of these intermediates is fast and complete towards CO_2. On the other hand, at higher temperatures, the opening of the aromatic ring is faster, although the oxidation of the generated intermediates is slower. Hence, other reaction intermediates not observed at low temperature, such as acetate, formate and enolic species, appear.

This change in the pathway of o-DCB oxidation with temperature is in agreement whit the characteristic o-DCB conversion profile with two steps observed in the light-off experiments, and also with the results obtained in the catalytic tests, where, at low temperature, o-DCB oxidation only produced CO_2, although o-DCB conversion was not total; whereas the increase in temperature between 250-300 ^{o}C promoted the formation of chlorinated organic by-products, such as tetrachloromethane and tetrachloroethylene.

In addition, the results of this chapter support the positive effect of NO on o-DCB oxidation that was previously observed in Chapter 4, since at high temperature, nitrate species formed in NO adsorption disappeared after o-DCB adsorption. This result indicates a clear participation of NO in o-DCB oxidation, probably associated to the re-oxidation of the active sites involved in the oxidation of o-DCB. However, the positive effect of NH_3 on o-DCB oxidation, also observed in Chapter 4, could not be corroborated, because this effect is probably not associated to an involvement of ammonia in the oxidation reaction, but in the removal of deactivating species such as adsorbed chlorine.

Chapter 6

IMPROVEMENT OF CATALYTIC PERFORMANCE OF MnO_X-CeO_2 BY DIFFERENT STRATEGIES

Chapter 6

IMPROVEMENT OF CATALYTIC PERFORMANCE OF MnO_X-CeO_2 BY DIFFERENT STRATEGIES

ABSTRACT

This chapter aims to improve the catalytic performance of MnO_X-CeO_2 catalytic formulation by: (1) supporting over Al_2O_3, TiO_2, H-ZSM5 and H-BETA; (2) doping with Fe, Zr, Co, Sr and W. For this purpose, all catalysts were characterized and tested in the simultaneous NO reduction and o-DCB oxidation.

Catalysts were successfully prepared and catalytic performance was significantly improved. The high surface area provided by H-ZSM5 and H-BETA promotes high dispersion of MnO_X-CeO_2 phase, which leads to a lower interaction between active metals and, thus, reduces the oxidative capability of the samples. W-doped sample has also improved catalytic performance due to the chemical characteristic of W, which reduces the activity of surface oxygen species.

The enhancement of catalytic performance has allowed to obtain high NO conversions at higher temperatures by suppressing SCR side reactions, which has decreased the production of N_2O and NO_2, and with little impact on o-DCB oxidation. This fact has allowed to shift the temperature range with high NO and o-DCB conversions to higher temperatures, where catalyst deactivation (which affects o-DCB oxidation) is significantly lower.

6. IMPROVEMENT OF CATALYTIC PERFORMANCE OF MnO_X-CeO_2 FORMULATION BY DIFFERENT STRATEGIES.

Results in the previous chapters have proved the feasibility of simultaneous removal of NO and o-DCB, with conversions of both pollutants higher than 80% between 180-250 ^oC with the catalyst prepared by co-precipitation and with concentration of 85%Mn and 15%Ce. This has allowed to improve the catalytic performance obtained with V-based catalysts in our previous researches [119, 233].

However, this work has also evidenced that the MnO_X-CeO_2 catalytic formulation has some negative points. Thus, although NO conversion is stable in the above-mentioned temperature range, conversion of o-DCB decreases over time due to catalytic deactivation. The effect of deactivation over o-DCB oxidation decreases greatly with temperature increase, i.e., above 300 ^oC. Nonetheless, at such temperature NO conversion decreases due to the appearance of side reactions.

This chapter addresses the modification of MnO_X-CeO_2 formulation in order to obtain stable and high NO and o-DCB conversions in the same temperature range. This could be achieved by avoiding catalytic deactivation at low temperatures. However, this seems rather difficult, as deactivation of Mn and Ce based catalysts on VOCs oxidation is widely reported in the literature [98, 145, 234]. Another strategy is the promotion of SCR at higher temperatures by suppressing SCR side reactions or shifting NO conversion towards higher temperatures. In addition, the improvement of catalytic performances will also aim an improvement of N_2 selectivity in NO reduction by means of the decrease in N_2O and NO_2 production.

It is important to note that characterization and catalytic activity tests showed high NO conversion at very low temperatures associated to the high oxygen mobility resulting from the high interaction between Mn and Ce. This high oxygen mobility also promotes the increase in oxidative capability of the catalyst, which favours that SCR side reactions tend to occur at lower temperatures. Therefore, a certain decrease of oxidative capability without greatly affecting NO and o-DCB conversions seems to be a key factor to reach high conversion of both compounds in the same temperature range.

In order that the decrease in the oxidative capacity does not affect catalytic activity, the loss of oxidative properties should be compensated by other catalytic

properties such as specific surface area and acidity. On the basis of this, two strategies have been proposed: (1) supporting the MnO_X-CeO_2 phase over supports with particular catalytic properties and (2) doping MnO_X-CeO_2 with a third metal.

6.1. EFFECT OF SUPPORTING MnO_X-CeO_2 PHASE.

The use of supports on catalysis is based on several reasons. They provide a high surface area that allows for a greater dispersion of the active phase and, thus, it favours the accessibility of reactants to the active centres. In some cases, they can interact with the active metals generating additional phases and particular properties.

In this section, the effect of four different supports will be studied. Al_2O_3 is a common support for metals, particularly noble metals, due to its excellent mechanical properties and high surface area. On the other hand, TiO_2 has lower surface area and more tendency to sinter than other supports. Nonetheless, its use as commercial support for NO_X abatement is widely known because it favours a good dispersion of the active components and provides resistance to SO_2 [235].

Both supports are commonly used for low temperature SCR. In fact, supporting MnO_X-CeO_2 over Al_2O_3 [236, 237] and TiO_2 [238, 239] has already been studied. In addition, Jin and co-workers [240] compared the effect of both supports on catalysts with the same active components than those used in this work and they found that MnO_X-CeO_2/TiO_2 showed better catalytic activity. A similar result was reported by Pan and co-workers [241] when comparing an active phase composed by Mn and Cu oxides supported over Al_2O_3 and TiO_2. However, the catalytic activity in o-DCB oxidation must also be evaluated. In this sense, MnO_X-CeO_2 catalysts become really effective for o-DCB removal above 300 ^oC. Therefore, the results of the aforementioned references should be complemented, since they are focused on low temperature SCR (below 200 ^oC), and the synthesis methods are different from the optimum proposed by this work.

On the other hand, H-ZSM5 and H-BETA zeolites have been selected as supports for MnO_X-CeO_2 phase. Both are microporous materials, which promotes high surface area, although they present different morphology. ZSM5 zeolite contains two perpendicularly intersecting bi-directional channels with sinusoidal and elliptical shape. BETA zeolite exhibits a structure with tri-directional interconnected channel

systems promoted by the presence of polymorph A and polymorph B phases [242]. As a result, ZSM5 exhibits a similar contribution of micro and mesoporosity, whereas the contribution of mesoporosity in BETA is much higher. Furthermore, both zeolites have common properties with their characteristic Brønsted acid sites. This would imply a higher number of surface hydroxyl groups, which would reduce the proton abstraction of adsorbed ammonia and lead to a negative effect on SCR side reactions, having a positive effect on NO conversion at high temperature.

The use of zeolites as supports for metal active phase, especially with copper and iron, has been extensively studied in recent years for NO_X abatement in mobile sources [67, 176]. The good results have encouraged the research of this type of support for NO_X abatement in stationary sources, paying special attention on the use of Mn [243] and MnO_X-CeO_2 [244] as active components. Moreover, it is important to note that the excellent acid properties of zeolites make them suitable supports for the oxidation of VOCs [225, 245].

Hence, four catalysts composed by MnO_X-CeO_2 and supported over Al_2O_3, TiO_2, H-ZSM5 and H-BETA have been studied in order to improve the catalytic performance of bulk MnO_X-CeO_2 phase. In supported catalysts, the MnO_X-CeO_2 phase has the optimum active metal ratio concluded in Chapter 3, i.e., 85Mn15Ce. The preparation procedure has been described in Chapter 2. Moreover, the MnO_X-CeO_2 loading has been referred to Mn content, with a 20 wt.% Mn loading selected in all catalysts.

6.1.1. Characterization of MnO_X-CeO_2 phase supported over Al_2O_3, TiO_2, H-ZSM5 and H-BETA.

Table 6.1 lists the results obtained from XRF technique, which was used to corroborate that Mn/Ce ratio of the prepared catalysts is close to the optimum one concluded in Chapter 3, i.e., 85Mn15Ce (Mn/Ce=5.7). As can be seen, all catalysts exhibit similar Mn/Ce ratio than the optimum sample. This result indicates a homogeneous co-precipitation of Mn and Ce. Furthermore, Table 6.1 shows the SiO_2/Al_2O_3 ratio for zeolite catalysts. The values obtained for both H-ZSM5 and H-BETA agree with the values given by the supplier.

Table 6.1. XRF results of supported MnO_X-CeO_2 and the corresponding supports.

Catalysts	Mn/Ce[a] (mol % Mn)	SiO_2/Al_2O_3
MnO_X-CeO_2/Al_2O_3	6.5 (86.7)	--
MnO_X-CeO_2/TiO_2	6.0 (85.6)	--
MnO_X-CeO_2/H-ZSM5	7.1 (87.7)	54.7
MnO_X-CeO_2/H-BETA	6.3 (86.3)	25.1

[a] Manganese composition in the active phase.

Dispersion of co-precipitated metals and elemental composition over the catalytic surface have been analysed by STEM-HAADF with EDX elemental maps. The results are shown in Figure 6.1.

The elemental maps reveal a good dispersion of Mn (green colour) and Ce (red colour) over the different particles analysed. In the case of the sample supported on H-ZSM5, small agglomerations of Mn or Ce are also evidenced in some areas. However, no particles composed by only Mn and Ce have been observed in any sample. This is important, as it corroborates that the active metals have co-precipitated over the supports and not around them forming a bulk MnO_X-CeO_2 phase. Finally, it should be noted STEM-HAADF analysis with EDX maps has been carried out in several areas of each sample. All the results showed similar dispersion of Mn and Ce than those shown in Figure 6.1.

Therefore, on the basis of the results obtained from XRF and STEM-HAADF with EDX elemental maps, MnO_X-CeO_2 can be concluded to have been successfully supported on the different materials, leading to the expected Mn/Ce ratio and a good dispersion over the supports.

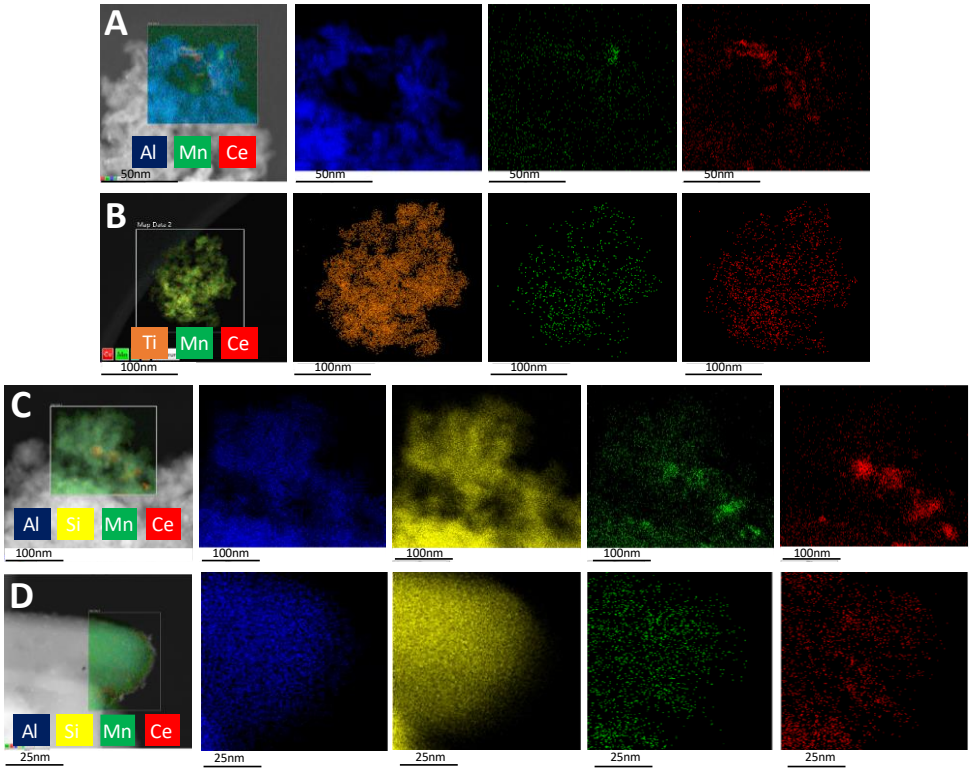

Figure 6.1. STEM-HAADF images and EDX elemental maps of MnO_X-CeO_2 over different supports: Al_2O_3, row A; TiO_2, row B; H-ZSM5, row C and H-BETA, row D.

Textural properties of the samples were evaluated by N_2-physisoprtion. N_2 adsorption/desorption isotherms are shown in Figure 6.2. According to IUPAC classification, the samples supported on Al_2O_3 and TiO_2 exhibit type IV isotherms, characteristic of mesoporous materials. In the case of zeolite supported samples, they show type I isotherms. Type I isotherms present large N_2 adsorption at very low relative pressure (below $P/P_0<0.03$) and are characteristic of microporous materials. Interestingly, the isotherms of samples supported on zeolites also exhibit a hysteresis loop, which evidences the presence of mesoporosity. In fact, the mesoporosity of H-BETA is even larger than that obtained for Al_2O_3 and TiO_2.

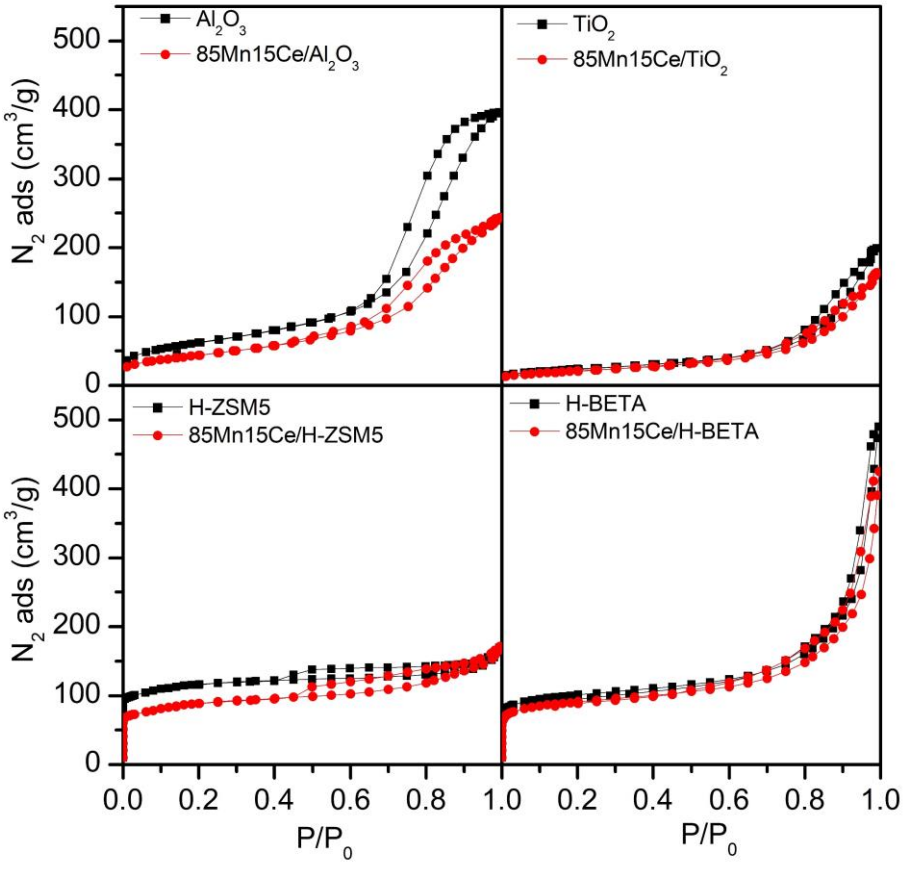

Figure 6.2. N_2 physisorption isotherms of MnO_X-CeO_2 supported over different supports and bare supports.

According to N_2-physisorption results, Table 6.2 lists the surface area and pore volume of supported samples and bare supports. There are remarkable differences in the surface area of bare supports. Zeolite catalysts exhibit the highest values due to the contribution of microporosity. TiO_2 is the support with the lowest surface area.

Loading of MnO_X-CeO_2 causes a considerable decrease in BET surface area of the supports (with the exception of H-ZSM5), which evidences the coverage of pores by the MnO_X-CeO_2 phase. This fact can be appreciated in Table 6.2, where the loading of MnO_X-CeO_2 phase also causes a decrease in total pore volume of all

supported samples in comparison to bare supports, except for the one supported over H-ZSM5, whose value hardly changes. Table 6.2 also lists the volume of micropores and mesopores. Interestingly, sample supported on H-ZSM5 is the only one whose volume of mesopores increases after loading MnO_X-CeO_2 phase. This fact suggests that the different behaviour of morphological properties of the sample supported over H-ZSM5 could be associated to a mesoporosity gain.

Table 6.2. Textural properties of MnO_X-CeO_2 supported over different supports.

Sample	BET surface area (m^2/g)	Pore volume (cm^3/g)		
		Total	Micropore volume	Mesopore volume
Al_2O_3	225	0.618		0.618
MnO_X-CeO_2/Al_2O_3	149	0.381		0.381
TiO_2	86	0.309		0.309
MnO_X-CeO_2/TiO_2	76	0.255		0.255
H-ZSM5	399	0.230	0.116	0.114
MnO_X-CeO_2/H-ZSM5	309	0.237	0.065	0.172
H-BETA	346	0.613	0.099	0.514
MnO_X-CeO_2/H-BETA	312	0.460	0.081	0.379

The structural properties of the catalysts have been investigated by XRD. Figure 6.3 shows the diffraction patterns of supported catalysts and their respective bare supports.

Al_2O_3 exhibits two well-defined diffraction peaks at 37.5 and 46.0°, and other less intense ones at 32.7 and 39.7°, which are associated to γ-Al_2O_3 (ICDD, 050-0741). The loading of MnO_X-CeO_2 phase promotes broadening of the diffraction peaks, which evidences the inhibition of crystalline domains of Al_2O_3. Moreover, additional diffraction peaks appear at 28.8 and 56.0°, associated to characteristic fluorite phase of CeO_2, and at 33.2°, related to α-Mn_2O_3. It should be noted that the location of the most intense peak of fluorite phase (28.8°) is shifted to a higher 2Θ position compared to the position of this peak in the diffractogram of pure CeO_2 (Figure 3.10). This indicates that the fluorite structure is modified due to, on the

one hand, the interaction between of Mn and Ce, as it was concluded in Chapter 3, and/or, on the other hand, the interaction of Ce with the support. The latter could be related to the shift of the most intense peak of Al_2O_3 from 46.0 to 46.2º after loading the MnO_X-CeO_2 phase.

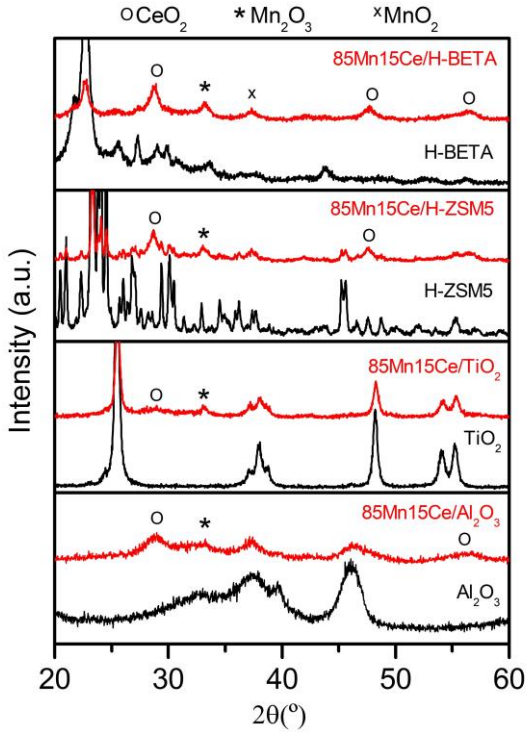

Figure 6.3. XRD patterns of MnO_X-CeO_2 supported over different supports and bare supports.

In the case of the catalyst supported over TiO_2, the peaks at 25.4, 38.0, 48.0, 54.1 and 55.1º are associated to anatase crystal phase (ICDD, 71-1169). The loading of MnO_X-CeO_2 promotes the appearance of a tiny diffraction peak at 33.2º associated to α-Mn_2O_3, whereas the peak at 28.8º associated to fluorite phase is hardly distinguishable. Interestingly, this catalyst is the only one in which the intensity of the peak of fluorite is lower than that associated to the peak of α-Mn_2O_3. This result is opposite to what would be expected from N_2-physisorption, as the lower surface area of TiO_2 would favour a higher agglomeration of the MnO_X-CeO_2 phase,

observable by XRD. One reason for this fact could be associated to TiO_2 support does not favour a CeO_2 structural ordering due to an excessive interaction between Ce and Ti, which would be in agreement with the shift of the most intense peak of anatase phase from 25.4 to 25.5º after loading the MnO_X-CeO_2 phase.

The diffractogram of H-ZSM5 is characterized by the presence of many peaks related to MFI structure [246]. On the other hand, the one corresponding to H-BETA exhibits the typical diffraction peaks of BEA structure [247]. As in the other catalysts, loading of MnO_X-CeO_2 has a detrimental effect on the crystallinity of zeolites, evidenced by the decrease and slight broadening of diffraction peaks. In addition, the peaks related to fluorite appear at 28.7, 47.7 and 56.5º, and also the one characteristic of α-Mn_2O_3 at 33.2º. The appearance of the peak at 37.3º also evidences the presence of MnO_2 in the catalyst with H-BETA support. MnO_2 phase is probably also present in the other supported catalysts, although it has not been observed due to overlapping of its most intense peak with those corresponding to supports.

Interestingly, the shift of the most intense peak of fluorite phase (with respect to pure CeO_2, Figure 3.10), observed in the samples supported over Al_2O_3 and TiO_2, does not take place in the samples supported over zeolites. Additionally, the most intense peaks of zeolites are not shifted either after loading the MnO_X-CeO_2 phase, as was the case for Al_2O_3 and TiO_2. This reveals that zeolites promote a high dispersion of the active phase, as was observed by STEM-HAADF (Figure 6.1), due to their high surface area. However, this dispersion does not generate as strong an interaction as on Al_2O_3 and TiO_2. This fact will probably affect the catalytic activity in the low temperature range.

Redox properties have been studied by H_2-TPR. The reduction profiles of supported samples as well as the supports are shown in Figure 6.4. Both Al_2O_3 and the two zeolites exhibit a negligible H_2 consumption compared to their respective supported samples. This reveals the lack of redox abilities of these supports. On the contrary, the reduction profile of bare TiO_2 shows a reduction peak located at 565 ºC with a tiny shoulder at 580 ºC, which is ascribed to the reduction of surface Ti^{4+} ions [248].

After supporting the MnO_X-CeO_2 phase, the reduction profiles obtained are very similar to those described in Chapter 3. The main H_2 consumption takes place between 100-500 ºC and is associated to the reduction of Mn, and also to the

reduction of surface Ce and Ce in high interaction with other species. In turn, the H_2 consumed in this temperature range is divided in two components: (1) that located between 175 and 330 °C, which is composed by several contributions depending on the supports; and (2) that located between 330 and 450 °C, which is quite similar in all supported samples. According to the assignments in Chapter 3, H_2 consumed in the low temperature range (1) is mainly related to the reduction of Mn in high oxidation state, either in high interaction with other species (Ce or surface species of the support) or segregated as an oxide, to Mn_3O_4; whereas H_2 consumed in the high temperature range (2) is mainly associated to the reduction of Mn_3O_4 to MnO.

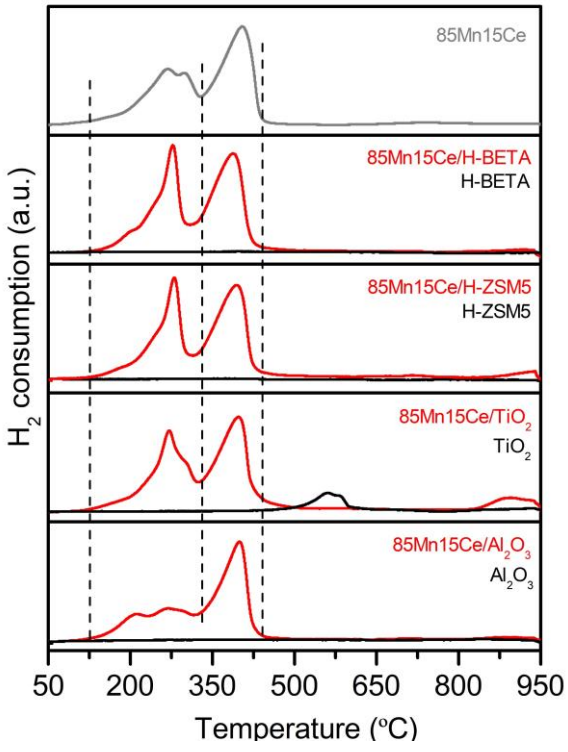

Figure 6.4. H_2-TPR profiles of MnO_X-CeO_2 supported over different supports, bare supports and bulk MnO_X-CeO_2.

On the other hand, the reduction profiles of supported samples also present another H_2 consumption at temperatures above 700 °C, which is associated to the

reduction of bulk cerium oxide (from CeO_2 to Ce_2O_3). Nonetheless, due to the low Ce content, this H_2 consumption is not appreciable in most of the samples, except for that supported on TiO_2. One reason for this exception could be related to the lower surface area of TiO_2 in comparison to other supports, as was evidenced by N_2-physisorption. This fact would cause a lower dispersion of Mn and Ce, leading to the possibility of generating bulk CeO_2. Obviously, this bulk CeO_2 would have amorphous structure, since the fluorite structure was hardly observed by XRD (Figure 6.3)

Comparing with the bulk 85Mn15Ce, the main differences among the reduction profiles of the samples are found in the H_2 consumption located at low temperature (175-330 ^oC), which is mostly related to the reduction of Mn in high oxidation state. Focusing on this temperature range, it was proposed in Chapter 3 that, for bulk 85Mn15Ce, the contribution located at low temperature (270 ^oC) was associated to the reduction of Mn in high interaction with Ce, whereas the remaining at 300 ^oC was ascribed to the reduction of Mn as oxide. Based on this, the results evidence that supporting the MnO_X-CeO_2 phase promotes a high contribution of Mn in high interaction with Ce or, in this case, also with the support. This fact improves the redox properties of the samples, as can be deduced from the shift of the H_2 consumption profile towards low temperatures and the promotion of the H_2 uptake related to Mn in high interaction with Ce or support, in comparison to the bulk MnO_X-CeO_2 reduction profile.

Finally, Table 6.3 lists the quantification of the H_2 consumed for each sample. It should be noted that similar H_2 consumption per unit mass is observed for supported samples. This corroborates the good preparation of the catalysts, since similar amount of active phase was loaded over each support. Nonetheless, the catalyst supported over TiO_2 exhibits a higher H_2 consumption. According to Figure 6.4, bare TiO_2 was the only support that exhibited a H_2 consumption on its reduction profile (0.4 mmol H_2/g); so, the higher H_2 consumption on the MnO_X-CeO_2/TiO_2 sample could be related to the reduction of surface Ti^{4+}.

Table 6.3. Results of H_2-TPR and NH_3-TPD of MnO_X-CeO_2 supported over different supports and bare supports.

Sample	H_2 consumption (mmol H_2/g)	Acidity (μmol NH_3/g)	Acidity (μmol NH_3/m^2)	Strong / Weak
Al_2O_3	--	236	1.1	1.7
MnO_X-CeO_2/Al_2O_3	2.4	233	1.5	1.9
TiO_2	0.4	242	2.8	1.6
MnO_X-CeO_2/TiO_2	2.9	170	2.2	1.7
H-ZSM5	--	419	1.1	0.8
MnO_X-CeO_2/H-ZSM5	2.6	497	1.6	1.8
H-BETA	--	483	1.4	0.9
MnO_X-CeO_2/H-BETA	2.5	539	1.7	1.6

Acid properties have been evaluated by NH_3-TPD. The NH_3 desorption profiles of supported samples as well as the bare supports are shown in Figure 6.5. In the same way, total acidity as well as the ratio between strong acidity (NH_3 desorption above 170 ^oC) and weak acidity (NH_3 desorption below 170 ^oC) are summarized in Table 6.3.

Regarding desorption profiles of bare supports (Figure 6.5), all of them show a notorious NH_3 desorption, which evidences their acid nature. Zeolite supports, and specifically H-BETA, have the highest total acidity, whereas Al_2O_3 and TiO_2 exhibit similar values. The excellent acidity of zeolites is related to their high surface area, since if acidity is referred to the surface area of the supports, as shown in Table 6.3, TiO_2 would be the most acidic one.

Moreover, all the supports are characterized by the presence of both weak acidity, whose desorption peak is located around 100 ^oC; and strong acidity, whose desorption peak appears at different temperature depending on the support. The contribution of each type of acidity to total acidity depends on the support, the contribution of strong acidity is larger in Al_2O_3 and TiO_2, as denotes the strong/weak ratio above one (Table 6.3); whereas the contribution of weak and strong acidity is practically similar on zeolites.

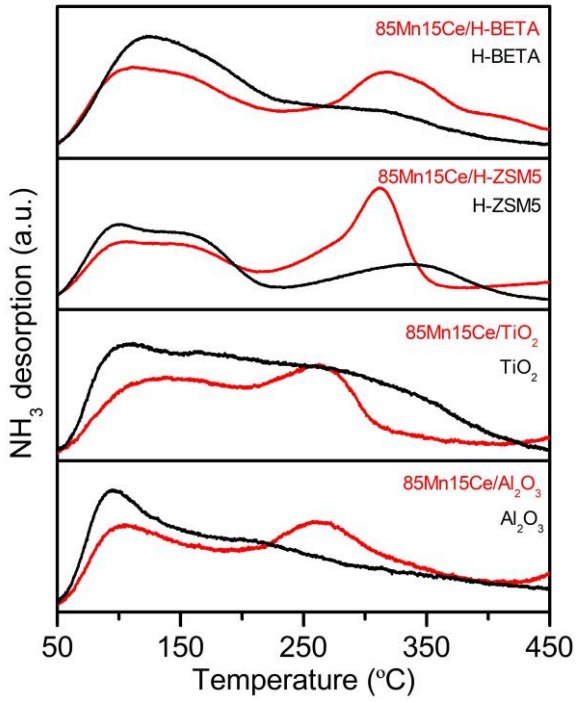

Figure 6.5. NH_3-TPD profiles of MnO_X-CeO_2 supported over different supports, bare supports and bulk MnO_X-CeO_2.

As Figure 6.5 shows, loading the MnO_X-CeO_2 phase clearly promotes strong acidity, although, at the same time, weak acidity also decreases. This fact is supported by the higher strong/weak ratio (Table 6.3) of all supported samples in comparison with their respective supports. Therefore, this means that the interaction between the well-dispersed MnO_X-CeO_2 phase and the supports promotes strong acid sites. This promotion of strong acidity versus weak acidity allows to increase the total acidity of zeolites (Table 5.3).

In addition, due to the promotion of strong acidity, the maximum desorption peak of NH_3 at high temperature becomes distinguishable. The samples supported on zeolites exhibit the location of this desorption peak around 300 ^oC, whereas in those samples supported over Al_2O_3 and TiO_2 the peaks are located around 260 ^oC. This suggests that the interaction between active phase and zeolites generates stronger acid sites.

6.1.2. Catalytic performance of MnO_X-CeO_2 phase supported over Al_2O_3, TiO_2, H-ZSM5 and H-BETA.

After analysing the effect that supporting the MnO_X-CeO_2 phase has on the catalytic properties, this section aims to evaluate the catalytic activity of these samples in the simultaneous NH_3-SCR and o-DCB oxidation. Figure 6.6 shows the NO and o-DCB conversion profiles of supported catalysts and the optimum bulk 85Mn15Ce, analysed previously in Chapter 3, as a function of temperature.

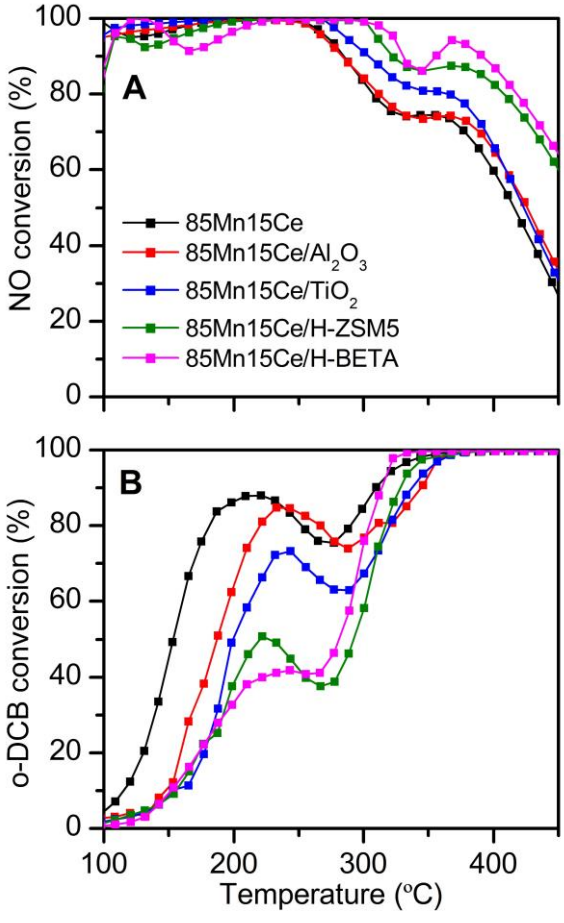

Figure 6.6. A) NO and B) o-DCB conversion with MnO_X-CeO_2 supported over different supports and bulk MnO_X-CeO_2.

Regarding NO reduction (Figure 6.6A), the samples supported on Al_2O_3 and TiO_2 exhibit similar NO conversion profiles similar than those obtained with the bulk 85Mn15Ce catalyst. In other words, total NO conversion is reached below 250 ^oC, whereas higher temperatures produce a drop in NO conversion. It should be noted that the catalyst supported on TiO_2 allows to reach slightly higher NO conversion in the high temperature range with respect to the bulk sample.

Similarly, the samples supported on zeolites also show NO conversions higher than 95% below 250 ^oC, although, unlike the other samples, full NO conversion is not reached below 120 ^oC. In addition, these samples promote a notable increase in NO conversion at high temperatures, and side reactions are not significant up to 300 ^oC. This is really important because, it allows high NO conversion to be shifted to temperatures where o-DCB oxidation is not affected the catalytic deactivation.

The differences found in NO conversion profiles reveal that the samples supported over zeolites have a lower oxidative capability, which could be associated, on the one hand, to the lower interaction between active metals as a consequence of the excellent dispersion of the MnO_X-CeO_2 phase; and, on the other hand, to the lower interaction between MnO_X-CeO_2 phase and zeolite supports, as evidenced by XRD. The lower the interaction degree, the less the surface defects improving oxygen mobility. However, this reduction in oxidative capability affects neither the reducibility of the samples (evidenced by H_2-TPR), which allows high NO conversions, nor the acidity (NH_3-TPD).

As for o-DCB oxidation, light-off curves of supported samples are very similar to those obtained with bulk catalysts, i.e., they exhibit a particular shape with two steps, as shown in Figure 4.1. In the first step, o-DCB conversion increases with temperature until reaching a maximum. In the second step, o-DCB conversion increases until total conversion. Between these two steps, o-DCB conversion decays.

The maximum o-DCB conversion in the first step takes place practically at the same temperature in all supported samples, which is around 30 ^oC above that of the bulk 85Mn15Ce catalyst. This fact is probably associated to the lower Mn content per mass unit of catalyst, since a similar shift in the o-DCB conversion profile towards lower temperatures was observed in Chapter 3 by increasing Mn content.

Moreover, the maximum conversion reached in the first step depends on the support. Thus, the samples supported over Al_2O_3 and TiO_2 exhibit the highest conversions of o-DCB, 85 and 70% respectively; whereas those samples supported over zeolites do not exceed 40%. In Chapter 3, maximum o-DCB conversion in the first step was concluded to be deeply related to Mn and Ce interaction (Mn, Ce and support, in the case of supported samples). Therefore, the higher o-DCB conversions of the samples supported on Al_2O_3 and TiO_2 respect to samples supported on zeolites is probably associated to a higher interaction between the active metals and the supports. This fact also affected NO reduction, as described above, by increasing conversion of NO at low temperatures.

However, although zeolite-supported samples exhibit lower o-DCB conversions at the first step, they reach full conversion of o-DCB at slightly lower temperatures (325 ^{o}C) than the bulk 85Mn15Ce catalyst (350 ^{o}C) in the second step. This improvement in the activity of oxidation reaction together with the increase in NO conversion at high temperatures of zeolite-supported samples, allows to reach higher conversions of both NO and o-DCB in the same temperature range with respect to the optimum bulk 85Mn15Ce catalyst.

Table 6.4 lists the temperature range at which both NO and o-DCB conversion is above 80 and 95%. The sample supported on Al_2O_3 exhibits the temperature range with NO and o-DCB conversion above 80% placed at lower temperature, although, according to o-DCB conversion profiles (Figure 6.6B), full conversion of this compound could not be achieved in the studied conditions and in this temperature window of Table 6.4. Besides this reaction is affected by deactivation in this temperature range, as shown in Chapter 4.

Table 6.4. Temperature range in which NO and o-DCB conversions are, simultaneously, above 80 and 95%.

Sample	**Temperature range (^{o}C) X > 80%**	**Temperature range (^{o}C) X ≥ 95%**
85Mn15Ce	180-250; 290-300	-
MnO_X-CeO_2/Al_2O_3	220-270	-
MnO_X-CeO_2/TiO_2	322-360	-
MnO_X-CeO_2/H-ZSM5	325-410	-
MnO_X-CeO_2/H-BETA	300-420	315

For the other supported samples, the range of high conversions of both pollutants is located at higher temperatures. This range is wider for samples supported on zeolites. In fact, the one supported on H-BETA allows to reach simultaneous NO and o-DCB conversions above 95% at 315 ^oC in the studied conditions, i.e., at a temperature where the oxidation reaction is not affected by deactivation of the catalyst. This means a significant enhancement in the catalytic performance with the use of zeolitic-type supports.

The main improvement provided by zeolites lies in the increase of NO conversion at high temperatures. This fact is related to the decrease of the oxidative capability of MnO_X-CeO_2 phase, which reduces SCR side reactions and, thus, the drop of NO conversion, without affecting o-DCB conversion at high temperature. Due to the above-mentioned decrease in oxidative capability, a decrease in SCR by-products formation is also expected, although this issue will be discussed later.

6.1.2.1. Analysis of SCR and o-DCB oxidation by-products.

In SCR, N_2O and NO_2 are the main by-products, and their production profiles are shown in Figure 6.7. All catalysts show similar N_2O production profiles (Figure 6.7), with two maxima at 200 and between 300-350 ^oC. Interestingly, the amount of N_2O produced by supported samples, especially in those supported on TiO_2 and zeolites, is lower than that produced by the bulk sample in all temperature range. Similarly, NO_2 production is significantly lower on supported catalysts. Among them, those supported on zeolites produce the least amount of NO_2, and its production is shifted towards higher temperatures. It is remarkable the good behaviour of catalyst supported on H-BETA, which, at 315 ^oC (temperature where both NO and o-DCB conversion is 95%), presents a production of N_2O and NO_2 of 60 ppm and zero, respectively, whereas the production of bulk 85Mn15Ce is 125 and 70 ppm, respectively. This comparison reveals the huge improvement in terms of selectivity.

Therefore, supporting the MnO_X-CeO_2 phase allows to reduce the production of N_2O and NO_2. This improvement SCR selectivity is one of the goals proposed at the beginning of Chapter 6. In this sense, samples supported over zeolites were those producing the least amount of both N_2O and NO_2 due to the reduction of the oxidative capability of MnO_X-CeO_2 phase.

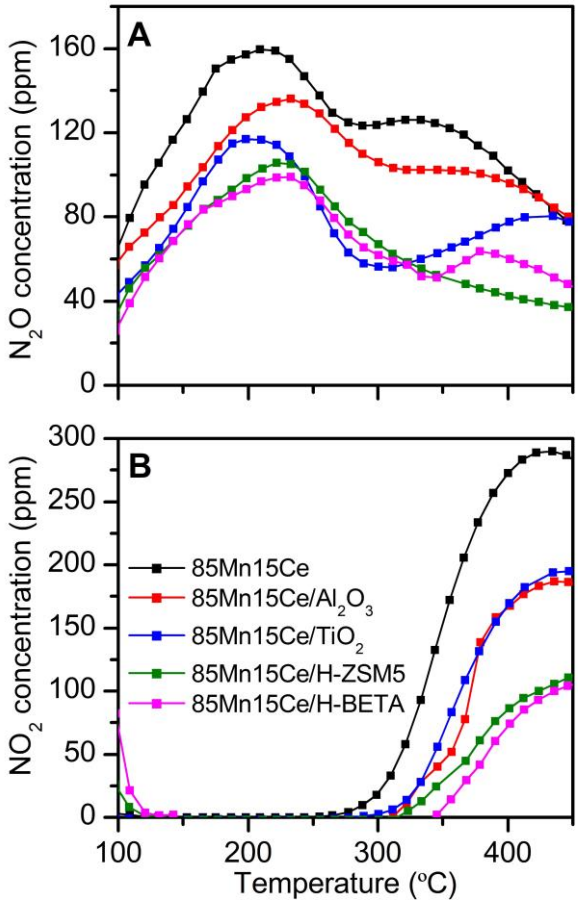

Figure 6.7. A) N_2O and B) NO_2 generation with MnO_X-CeO_2 supported over different supports and bulk MnO_X-CeO_2.

Figure 6.8 shows the selectivity towards CO, which is the main oxidation by-product in o-DCB oxidation. Due to the lower oxidative capability, the selectivity of supported samples is slightly higher than that obtained with the bulk 85Mn15Ce catalyst over the whole temperature range. Regarding chlorinated organic by-products (not shown in Figure 6.8), their formation has been only detected in the catalysts supported over zeolites. However, the disadvantage of lower oxidative capability leading to slightly higher selectivity to CO and chlorinated compounds, is compensated with higher NO conversion and less SCR side reactions.

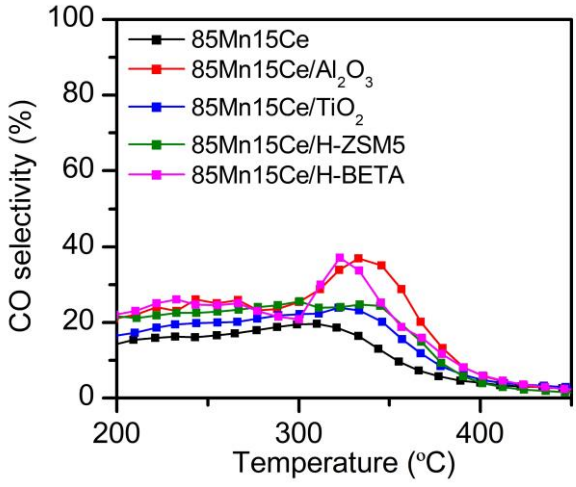

Figure 6.8. CO selectivity with MnO_X-CeO_2 supported over different supports and bulk MnO_X-CeO_2.

6.2. SURFACE DOPING OF MnO_X-CeO_2 WITH DIFFERENT METALS.

Mixing or doping one metal with another one can enhance the catalytic properties of the former. This effect has already been corroborated in this work, where the catalytic properties of the samples composed by Mn and Ce were better in SCR and in o-DCB oxidation than those of their own pure oxides.

This section will address the doping of MnO_X-CeO_2 formulation with a third metal in order to promote a reduction in the oxidative capability of the catalysts. This would allow the decrease of SCR side reactions, improving NO conversion in the high temperature range. The selected dopant metals are: Fe, Zr, Co, Sr and W. The selection of these metals has been made on the basis of reported results in the literature and a pre-selection based on catalytic tests, not included in this work.

Fe-doped manganese oxide catalysts are considered excellent catalysts for low temperature SCR [249-251]. Qi and co-workers [72] stated an improvement of NO conversion and N_2 selectivity with Fe doping of MnO_X-CeO_2 formulation. Similar results were reported by the same authors with Zr doping [72]. However, Zr is less reported in the literature because it is usually used as a component of supports [252, 253], rather than as a component of the active phase.

On the other hand, Co is not very common for SCR, although, recently, Zhu and co-workers [254] reported that the combination of Mn and Co leads to N_2 selectivity higher than 80% below 320 ^{o}C. Nonetheless, the oxide composed of Ce and Co leads to worse catalytic performance [255]. In the case of Sr doping, no references have been found about the use of this metal in SCR. However, strontium oxide is well known to have high concentration of surface hydroxyl groups, like cerium oxide. The results of Chapter 5 suggested surface hydroxyl groups reduce proton abstraction of adsorbed NH_3 and, consequently, the oxidation of this reactant in catalyst surface. So, a reduction of the formation of SCR by-products with Sr doping is expected.

Finally, W is probably one of the most reported metals used for SCR. It is characterised by a lower catalytic activity than other transition metals, such as Mn and Fe, at low temperatures, although its use as dopant leads to improving the selectivity towards N_2 [256-258]. At high temperatures, W-doping allows to broaden the working window with high NO conversion due to the suppression of SCR side reactions. For example, Ma and co-workers [259] reported NO conversion and N_2 selectivity above 90% at 300 ^{o}C.

Thus, five catalysts composed of a MnO_X-CeO_2 phase and surface-doped with Fe, Zr, Co, Sr and W will be studied in order to improve the catalytic performance of the best bulk MnO_X-CeO_2 according to Chapter 3, i.e., 85Mn15Ce. The catalysts have been prepared according to the procedure described in Chapter 2. Dopant loading has been referred to metal content and fixed to a 5 wt.% in all catalysts. The nomenclature used for these samples is as follows: 5Fe/85Mn15Ce, 5Zr/85Mn15Ce, 5Co/85Mn15Ce, 5Sr/85Mn15Ce, 5W/85Mn15Ce.

6.2.1. Characterization of surface-doped MnO_X-CeO_2 with metal oxides based on Fe, Zr, Co, Sr and W.

Table 6.5 lists the results obtained from XRF, which has been used to corroborate the metal dopant content, and the Mn/Ce ratio, which should be close to the optimum resulting from Chapter 3, i.e., 85Mn15Ce (Mn/Ce=5.7). As can be seen, dopant metal contents are close to the nominal value. Concerning the MnO_X-CeO_2 support, the Mn/Ce ratio is also very close to the desired value. Therefore, both parameters corroborate that the synthesis of these catalysts is successful.

Table 6.5. XRF results of metal-doped MnO_X-CeO_2 catalysts.

Catalysts	Metal concentration (wt. %)	Mn/Ce [a] (mol % Mn)
5Fe/85Mn15Ce	5.5	6.3 (86.3)
5Zr/85Mn15Ce	4.7	6.2 (86.2)
5Co/85Mn15Ce	5.8	6.1 (86.0)
5Sr/85Mn15Ce	5.0	6.0 (85.8)
5W/85Mn15Ce	6.1	6.0 (85.8)

[a] Manganese composition in the active phase.

On the other hand, the good dispersion of dopant metal was analysed by STEM-HAADF with EDX elemental maps. The results of this technique for W-doped sample are shown in Figure 6.9. The distribution of W (purple colour) is uniform throughout the analysed section of the catalyst. This good dispersion was observed in all the areas of the catalyst analysed, which evidences the good dispersion of dopant metal obtained by impregnation method. Thus, these results could be extended to the other doped catalysts.

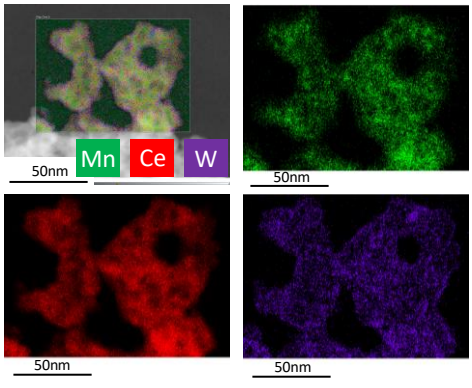

Figure 6.9. STEM-HAADF images and EDX elemental maps W-doped of MnO_X-CeO_2 catalyst.

N_2-physisorption was used to evaluate textural properties of the samples. Figure 6.10 shows the adsorption isotherms and pore size distribution of the prepared catalysts. Table 6.5 lists the values of surface area, total pore volume and mean pore size of the samples.

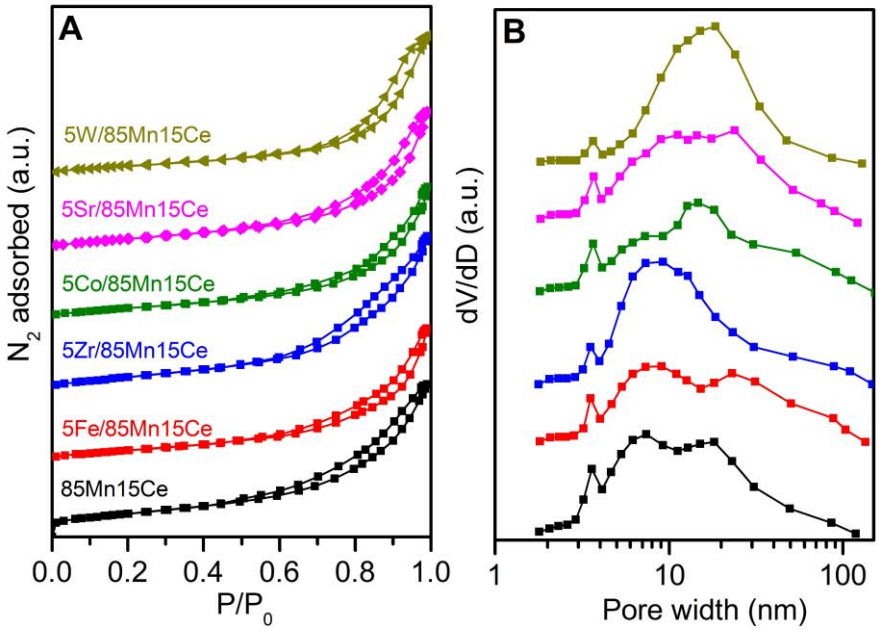

Figure 6.10. A) N_2 physisorption isotherms and B) pore size distributions of metal-doped MnO_X-CeO_2 catalysts.

Table 6.5. Textural properties of metal-doped MnO_X-CeO_2 catalysts.

Sample	BET surface area (m^2/g)	Pore volume (cm^3/g)	Pore diameter (nm)
85Mn15Ce	87	0.25	9.0
5Fe/85Mn15Ce	70	0.23	10.4
5Zr/85Mn15Ce	90	0.27	9.1
5Co/85Mn15Ce	68	0.23	10.6
5Sr/85Mn15Ce	76	0.24	10.4
5W/85Mn15Ce	65	0.24	12.5

As can be seen in Figure 6.10A, all doped samples exhibit type IV isotherms characteristic of mesoporous solids. This is consistent, taking into account the mesoporous nature of MnO_X-CeO_2 support. In addition, metal doping produces a decrease in surface area, as well as a slight decrease in total pore volume and a

slight increase in mean pore size. These results suggest that doping causes a loss of some pores with small size, which leads to a decrease in surface area. However, in the Zr-doped sample, the behaviour is opposite (surface area increases), because it simultaneously promotes the increase in the number of the smaller pores and the loss of part of the larger pores.

The effect of dopant metal on pore size distribution is observed in Figure 6.10B. Fe, Co and Sr-doped samples exhibit similar distribution than that of the support, composed by two main contributions (around 7 and 18 nm), although the presence of pores with larger size is also evidenced. On the contrary, Zr and W-doped samples have a pore distribution composed by a single contribution centred at 9 and 18 nm, respectively. Interestingly, Zr-doped catalyst hardly exhibits pores larger than 15 nm. This is in agreement with the loss of large pores of the support.

Structural properties of doped catalysts have been assessed by XRD. The results are shown in Figure 6.11.

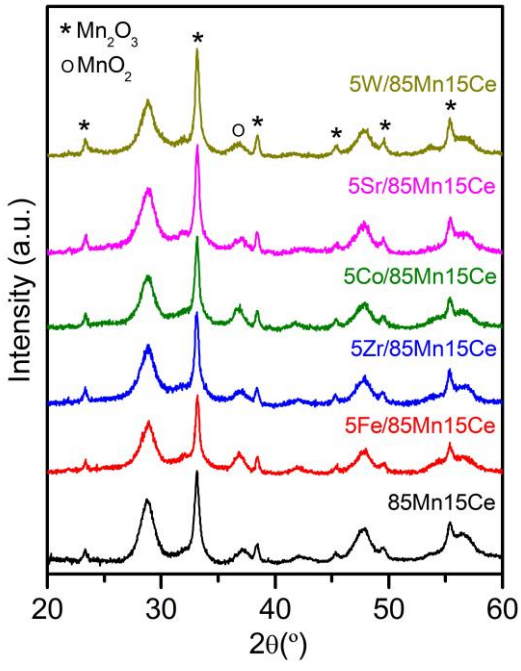

Figure 6.11. XRD results of metal-doped MnO_X-CeO_2 catalysts.

All samples exhibit similar peaks, which are mainly associated to fluorite phase and α-Mn_2O_3, although there is evidence of the presence of MnO_2 to a lesser extent. No peaks ascribed to any crystalline phase of the corresponding dopant metal oxides have been identified, which suggests that dopant content is not enough as to promote the formation crystal structure. This denotes that the dopant metals are highly dispersed over the support with amorphous structure, which ensures a coverage below the monolayer and, thus, a high interaction with the MnO_X-CeO_2 support.

Redox properties of the catalysts doped with different metals have been studied by H_2-TPR. Figure 6.12 shows the TPR profiles of all samples and Table 6.6 lists their corresponding H_2 consumption.

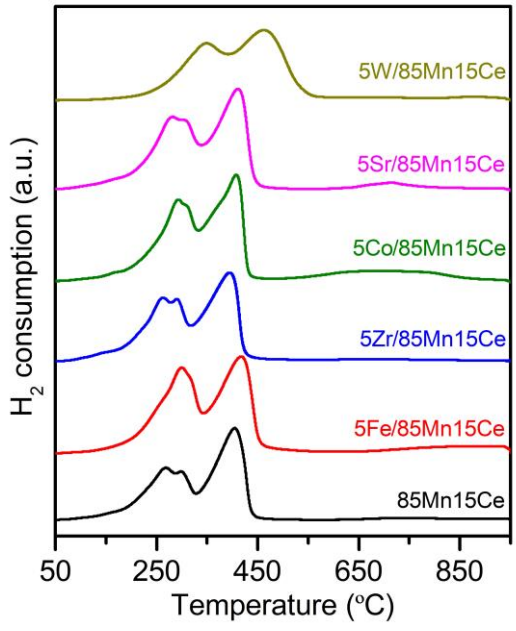

Figure 6.12. H_2-TPR profile of metal-doped MnO_X-CeO_2 catalysts.

Table 6.6. Results of H_2-TPR and NH_3-TPD of metal-doped MnO_X-CeO_2 catalysts.

Sample	H_2 consumption (mmol H_2/g)	Acidity (µmol NH_3/g)	Strong / Weak
85Mn15Ce	5.3	299.4	1.3
5Fe/85Mn15Ce	8.0	214.9	0.9
5Zr/85Mn15Ce	5.9	267.4	0.8
5Co/85Mn15Ce	7.4	233.3	0.8
5Sr/85Mn15Ce	6.8	228.9	0.7
5W/85Mn15Ce	6.3	217.5	0.8

H_2 consumption of doped samples is higher than that of MnO_X-CeO_2. This result evidences the promotion of a larger amount of species susceptible to be reduced after doping. These species can be related to the dopant metal itself or to surface defects generated by the interaction between dopant metal and MnO_X-CeO_2.

However, the increase in the amount of reducible species only causes an improvement in reducibility of the Zr-doped sample, as its reduction profile is the only one shifted toward lower temperatures compared to the bulk 85Mn15Ce catalyst (Figure 6.12). Reduction profiles of remaining samples occurs at the same temperatures as the bulk 85Mn15Ce catalyst, with the exception of the W-doped sample, whose reduction profile shifted towards higher temperatures indicates a loss of reducibility.

All the samples exhibit similar H_2 consumption profiles; composed of two H_2 uptakes between 150-550 ^oC, which are mainly related to Mn reduction. Thus, the H_2 consumption located at lower temperature is associated to the reduction of the different Mn species in high oxidation state (Mn interacting with other components and Mn segregated as an oxide). These species are evidenced by the different contributions that compose this reduction peak. On the other hand, the H_2 consumption at higher temperature is associated to the reduction of Mn_3O_4 to MnO.

Additionally, the reduction of the dopant metals and Ce in high interaction with other components can also contribute to some extent to H_2 consumption. This can

be deduced from the reduction profile of the Fe-doped catalyst, whose first reduction peak shows different contributions to those of the other catalysts, because iron oxide is also reduced in that temperature range from Fe_2O_3 to Fe_3O_4 [213]. Similarly, the shoulder around 370 °C in the high temperature reduction peak of the Co-doped catalyst, is associated to the reduction of Co^{2+} to metallic Co [260].

Acid properties have been assessed by NH_3-TPD. Table 6.6 lists total acidity of all doped samples and the ratio between strong acidity (NH_3 desorption above 170 ^oC) and weak acidity (NH_3 desorption below 170 ^oC). NH_3 desorption profiles are not shown because they are quite similar to that of the MnO_X-CeO_2 catalyst.

Surface loading of all dopant metals causes a clear decrease in total acidity and in the strong/weak ratio in comparison to MnO_X-CeO_2 catalyst (Table 6.6). These results indicate that the drop in acidity is mainly promoted by a decrease in the strong acidity of all samples, which suggests metal dopant loading probably occurs preferentially over strong acid sites.

Previously, it has been considered that strong acidity plays a key role in the oxidative capability of the catalysts. Nonetheless, an excess of oxidative capability has been shown to favour the excessive oxidation of the reagent involved in NO reduction, leading to by-products production. Thus, the decrease in strong acidity caused by MnO_X-CeO_2 doping is expected to have a positive effect on selectivity of NO reduction, although this can also have a negative effect on o-DCB conversion.

6.2.2. Catalytic performance of surface doped MnO_X-CeO_2 with metal oxides based on Fe, Zr, Co, Sr and W.

This section evaluates the catalytic performance of MnO_X-CeO_2 catalyst doped with different metals in the simultaneous NH_3-SCR and o-DCB oxidation. The NO and o-DCB conversion profiles of the different catalysts are shown in Figure 6.13.

In NO reduction (Figure 6.13A), all samples, except the W-doped one, show similar NO conversion profiles: total conversion below 250 ^oC, which drops with the further increase in temperature. In the case of W-doped catalyst, the NO conversion profile shifts towards higher temperatures. Thus, full conversion is reached above 150 ^oC and keeps constant up to 310 ^oC, above which it drops. Interestingly, this drop in

NO conversion does not present the characteristic plateau observed in the other catalysts, which has been associated to o-DCB and NH_3 competition.

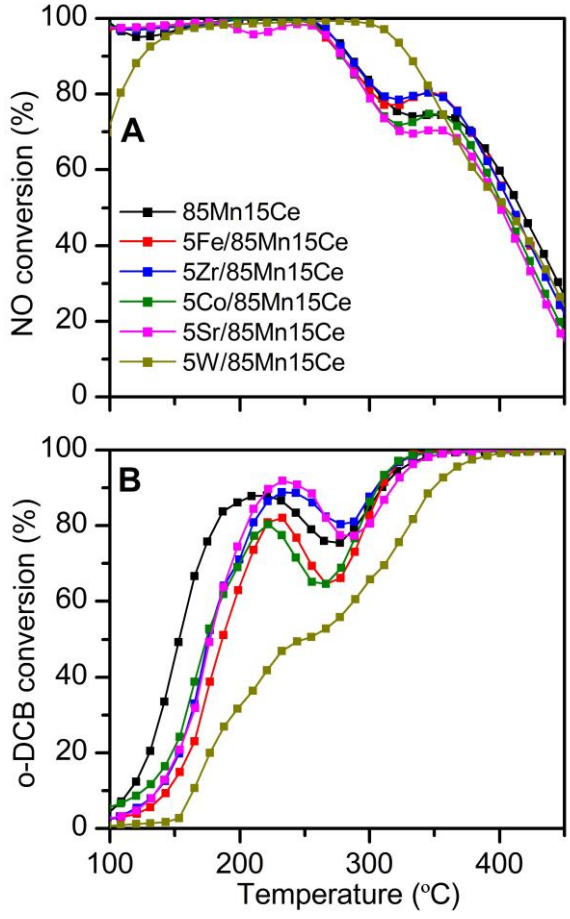

Figure 6.13. A) NO and B) o-DCB conversion with metal-doped MnO_X-CeO_2 catalysts.

Similarly, in o-DCB oxidation (Figure 6.13B), all catalysts, with the exception of the W-doped one, exhibit similar conversion profiles with two steps. In the first step, o-DCB conversion increases with temperature until a maximum is reached. In the second step, o-DCB conversion increases until total conversion. Between these two steps, o-DCB conversion decays. The MnO_X-CeO_2 catalyst shows higher conversions in the low temperature range, although full conversion is reached at same

temperature as with the doped catalysts (around 320 ºC). In contrast, the W-doped catalyst has an o-DCB conversion profile composed of a single rise with lower conversion values than the other doped catalysts over the whole temperature range.

These results evidence that doped catalysts exhibit similar catalytic behaviour than that observed with the MnO_X-CeO_2 catalyst. Table 6.7 lists the temperature range in which each of the evaluated samples obtains NO and o-DCB conversions above 80% at the same time (criterion followed throughout this thesis to select the most active catalysts). As can be seen, Zr and Sr-doped catalysts are the ones that allow high conversion of both compounds over a wider temperature range. However, it should be noted that, in these conditions (between 200 and 300 ºC), the oxidation reaction is affected by the deactivation of the catalyst, as was corroborated in Chapter 4.

Table 6.7. Temperature range in which NO and o-DCB conversions are, simultaneously, above 80%.

Sample	Temperature range (ºC) X > 80%
85Mn15Ce	180-250; 290-300
5Fe/85Mn15Ce	220-230
5Zr/85Mn15Ce	210-300
5Co/85Mn15Ce	--
5Sr/85Mn15Ce	200-270
5W/85Mn15Ce	330-350

W-doped catalyst is the only one that allows high conversions of NO and o-DCB in a temperature range in which the oxidation reaction is not affected by catalyst deactivation (above 300 ºC). This result involves a notable improvement in the catalytic performance with respect to MnO_X-CeO_2 catalyst.

The fact that the W-doped catalyst has been the only one able to improve the catalytic performance of bulk 85Mn15Ce catalyst is mainly associated to the chemical features of W and to the decrease in the reactivity of surface oxygen species due to the coverage of MnO_X-CeO_2 phase by the dopant metal oxide, in this case WO_X. These facts have promoted a decrease in the oxygen mobility, decreasing

in turn the oxidative capability, which is a key factor to avoid the drop in NO conversion by means of the suppression of SCR side reactions.

6.2.2.1. Analysis of SCR and o-DCB oxidation by-products.

N_2O and NO_2 are the main by-products of NO reduction, and their production profiles for metal-doped MnO_X-CeO_2 catalysts are shown in Figure 6.14. Doped catalysts significantly decrease the production of N_2O (Figure 6.14A) and NO_2 (Figure 6.14B). Among all samples evaluated, the W-doped catalyst is the one that most reduces the formation of both compounds; in fact, it even shifts the NO_2 production towards higher temperatures.

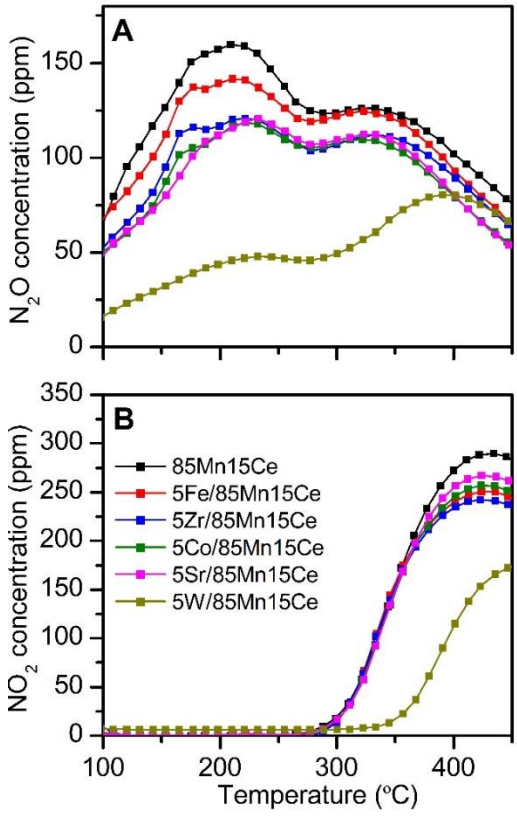

Figure 6.14. A) N_2O and B) NO_2 generation with metal-doped MnO_X-CeO_2 catalysts.

Therefore, doping the MnO_X-CeO_2 formulation reduces the oxidative capability, decreasing by-product generation in SCR. This issue was one of the goals proposed at the beginning of this chapter. Focusing on the W-doped catalyst and the temperature range in which NO and o-DCB conversion above 80% are obtained simultaneously (Table 6.7), this catalyst also allows to practically halve N_2O production compared to bulk 85Mn15Ce catalyst, while NO_2 production is totally eliminated. These results reveal the great improvement achieved with W-doped catalyst in terms of selectivity in SCR.

On the other hand, in o-DCB oxidation, CO is the main by-product. The selectivity towards this compound of metal-doped MnO_X-CeO_2 catalysts is shown in Figure 6.15. As in the analysis of conversion, all doped catalysts, with the exception of the one doped with W, exhibit similar profiles to that observed in MnO_X-CeO_2 catalyst. That is, CO selectivity remains constant up to 300 ºC, temperature from which it decreases. However, the values of selectivity obtained for doped catalysts are somewhat higher to that of MnO_X-CeO_2, which is associated to the lower oxidative capability promoted by the dopant metal.

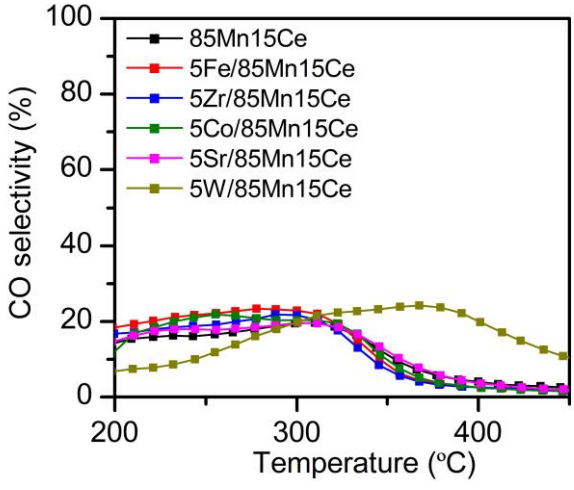

Figure 6.15. CO selectivity with metal-doped MnO_X-CeO_2 catalysts.

In the case of W-doped catalyst, the CO selectivity profile is completely different. Firstly, the selectivity increases with temperature until a maximum around 300 ºC is reached, where it remains constant until 400 ºC, temperature after which it

decreases. The promotion of partial oxidation of o-DCB at high temperature with W-doped catalyst is related to its lower oxidative capability, which was also the cause of the positive increase in SCR selectivity observed with this catalyst.

6.3. COMPARATIVE ANALYSIS OF THE TWO STRATEGIES FOLLOWED FOR THE IMPROVEMENT OF CATALYTIC PERFORMANCE OF MnO_X-CeO_2.

Once each of the proposed strategies for the improvement of catalytic performance of MnO_X-CeO_2 formulation has been analysed separately, the catalytic behaviour of the optimal catalyst resulting from each strategy, 85Mn15Ce/H-BETA and 5W/85Mn15Ce, are compared. This comparison is based on the results obtained in the catalytic tests. Figure 6.16 shows light-off curves of both catalysts. The light-off curves of bulk 85Mn15Ce catalyst, whose catalytic performance aims to be improved, are also included.

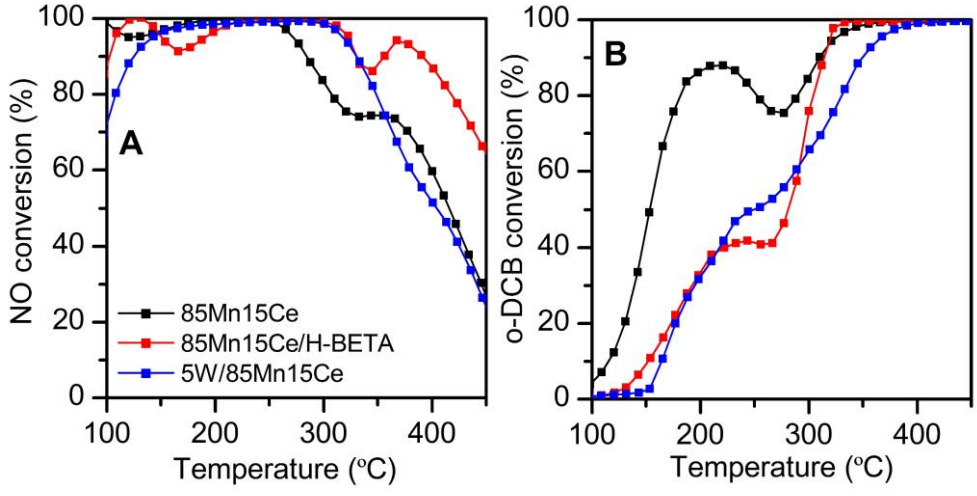

Figure 6.16. A) NO and B) o-DCB conversions of optimal catalysts resulting from each strategy.

In NO reduction (Figure 6.16A), both 85Mn15Ce/H-BETA and the 5W/85Mn15Ce shift NO conversion profiles to higher temperatures, compared to bulk 85Mn15Ce. This meets the first goal proposed to enhance the catalytic performance in the simultaneous removal of NO and o-DCB, which is to reach high NO conversion at higher temperatures than bulk 85Mn15Ce by suppressing SCR side reactions. The

suppression of SCR side reaction occurs by decreasing the oxidative capability of MnO_X-CeO_2 formulation.

However, the decrease in the oxidative should affect o-DCB oxidation reaction as little as possible. As can be seen in Figure 6.16B, either supporting 85Mn15Ce phase on H-BETA or surface doping 85Mn15Ce with W causes a loss in the catalytic activity in the low and medium temperature range (below 300 ^oC) in comparison to bulk 85Mn15Ce. In the high temperature range, where full o-DCB conversion is reached and the oxidation reaction is not affected by catalyst deactivation, the 85Mn15Ce/H-BETA catalyst shows similar results than bulk 85Mn15Ce, whereas the 5W/85Mn15Ce catalyst exhibits worse catalytic performance.

On the basis of NO and o-DCB conversion profiles, the temperature range in which conversions above 80% of both compounds are obtained has been established in Table 6.8. Obviously, the optimal catalyst should have the widest temperature range and place at the lowest temperature, but in a temperature range where deactivation of MnO_X-CeO_2 phase does not affect o-DCB oxidation. In this sense, although both 85Mn15Ce/H-BETA and 5W/85Mn15Ce allow to reach high conversion of NO and o-DCB simultaneously, according to the previous conditions, the 85Mn15Ce/H-BETA catalysts is the optimal one. In fact, it even allows conversions of 95% of both compounds at 315 ^oC in the studied conditions.

Table 6.8. Temperature range in which simultaneous NO and o-DCB conversions are above 80% with the optimal catalysts resulting from each strategy.

Sample	Temperature range (^oC) X > 80%
85Mn15Ce	180-250; 290-300
85Mn15Ce/H-BETA	300-420
5W/85Mn15Ce	330-350

The second objective proposed in this chapter is to improve the selectivity in SCR by reducing the amount of N_2O and NO_2 generated by MnO_X-CeO_2 phase. Figure 6.17 shows the production of these two by-products. The catalysts resulting from supporting the 85Mn15Ce phase on H-BETA or surface doping of 85Mn15Ce with W greatly reduce the generation of N_2O and NO_2 with respect to bulk

85Mn15Ce catalyst over the whole temperature range. The 5W/85Mn15Ce catalyst produces less N_2O than 85Mn15Ce/H-BETA catalyst at low temperature, although this behaviour is opposite at the conditions where high NO and o-DCB conversions occur (Table 6.8). Regarding NO_2 generation, the 85Mn15Ce/H-BETA catalyst produces the least.

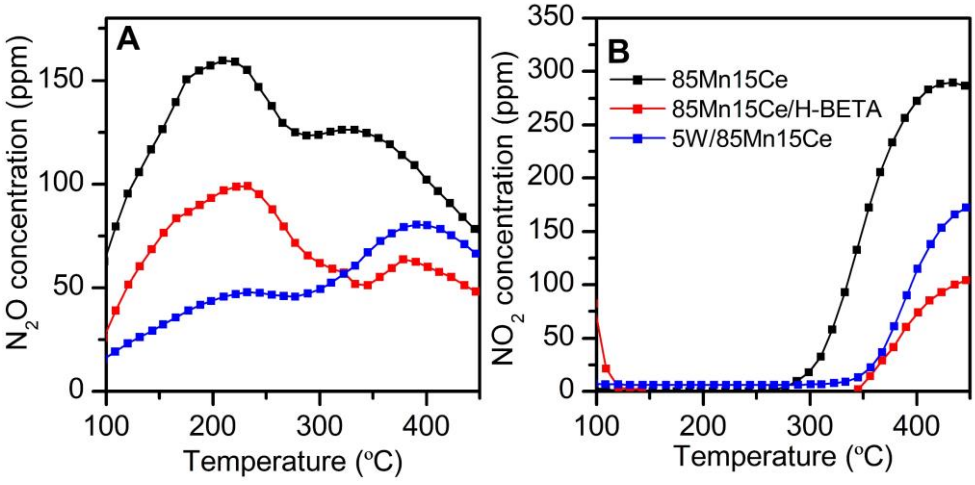

Figure 6.17. A) N_2O and B) NO_2 concentrations of optimal catalysts resulting from each strategy.

Therefore, on the basis of the results above discussed, the best strategy to enhance both the catalytic performance in the simultaneous removal of NO and o-DCB and the selectivity in SCR is the deposition of MnO_x-CeO_2 phase over a microporous support, such as H-BETA, that ensure high surface area, but at the same time with high contribution of mesoporosity, and also with excellent acid properties.

Finally, in order to evaluate the thermal stability of the optimal 85Mn15Ce/H-BETA, this catalyst was evaluated in a stability test for 24 h of TOS and 300 ºC with the same feed stream as the one used in the light-off experiments. The results are shown in Figure 6.18.

In SCR (Figure 6.18A), NO conversion slightly decreases in the first 4 hours of time on stream, after which it stabilises at a value of 87%. This result suggests that SCR is hardly affected by a possible deactivation of the catalyst. A similar trend occurs with N_2O and NO_2 by-products, whose production eventually stabilises at 75 and

0 ppm, respectively. The lower N_2O and NO_2 productions with respect to bulk 85Mn15Ce catalyst in the same experiment (Chapter 4, Figure 4.5B) corroborate the improvement in SCR selectivity, already evidenced the light-off experiment.

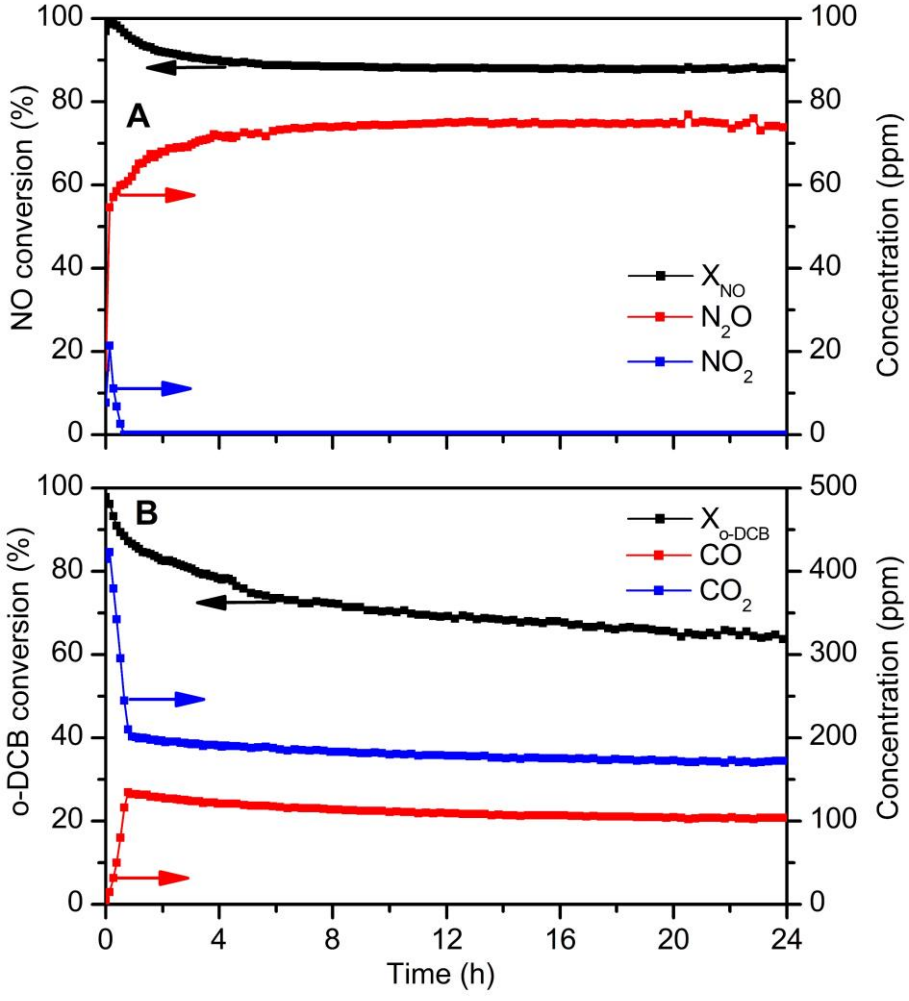

Figure 6.18. Simultaneous NO reduction and o-DCB oxidation time on stream experiment at 300 °C. A) NO conversion and N_2O and NO_2 concentrations; B) o-DCB conversion and CO and CO_2 concentrations.

In oxidation reaction (Figure 6.18B), o-DCB conversion progressively decreases with time on stream. The longer the time on stream, the slighter the drop in o-DCB

conversion; thus, o-DCB conversion is 65% at the end of the experiment. This result suggests that o-DCB oxidation is affected by catalyst deactivation, although in a different way that at lower temperatures, where o-DCB conversion drops to 0 (Chapter 4, Figure 4.5A). CO and CO_2 profiles reveal the negative effect of the first hour of time on stream on total oxidation of o-DCB (decrease in CO_2 concentration while CO concentration increases). Interestingly, a similar trend was also observed for the bulk 85Mn15Ce catalyst (Chapter 4, Figure 4.5C), although it occurred more slowly (first 2 hour of time on stream).

The fact that the partial oxidation of o-DCB appears earlier in the 85Mn15Ce/H-BETA could be associated to the lower amount of MnO_X-CeO_2 phase per gram of catalyst in comparison to the bulk 85Mn15Ce catalyst. However, it is important to note that reducing the amount of MnO_X-CeO_2 phase supporting over H-BETA is a positive aspect, since it allows similar or even better catalytic performance than that obtained with bulk 85Mn15Ce catalyst but saving and using more efficiently the MnO_X-CeO_2 active phase.

6.4. GLOBAL VIEW AND CONCLUSIONS.

This chapter aims to improve the catalytic performance of MnO_X-CeO_2 formulation in order to obtain high and stable NO and o-DCB conversions in the same temperature range and to reduce the production of N_2O and NO_2 from NO reduction.

For this purpose, the MnO_X-CeO_2 formulation has been modified in order to partially decrease its oxidative capability and compensate with other catalytic properties. Two strategies have been followed: (1) supporting of MnO_X-CeO_2 phase over different supports (Al_2O_3, TiO_2, H-ZSM5 y H-BETA) and (2) surface doping of MnO_X-CeO_2 phase with a third metal (Fe, Zr, Co, Sr y W). All the samples were characterized to correlate their catalytic activities with their catalytic properties and, then, to select the optimum one. In addition, some characterization techniques were used to check the success of the used preparation methods, such as XRF and STEM-HAADF with EDX.

Regarding MnO_X-CeO_2-supported catalyst, the samples supported over zeolite were the only ones that shift NO conversion profile towards higher temperature, decreasing at the same time the generation of SCR by-products, and not affecting

o-DCB conversion above 300 ºC. These results allow to shift the temperature range with high conversions of NO and o-DCB towards higher temperatures, thus, avoiding conditions where the oxidation reaction is affected by deactivation, as occurs in the case of the remaining samples supported over TiO_2 and Al_2O_3.

The enhancement in the catalytic performance is associated to the lower oxidative capability as a consequence of the lower interaction between Mn and Ce active metals. Lower interaction between Mn and Ce is promoted by high dispersion of MnO_X-CeO_2 phase on the supports; hence, the samples supported over zeolite show the highest catalytic performance, since they exhibit the highest surface area.

Reduction in the oxidative capability does not negatively affect reducibility of the sample, as the reduction profiles are shifted to lower temperatures with respect to the bulk 85Mn15Ce catalyst, neither acid properties. In fact, supporting the MnO_X-CeO_2 phase increases total acidity of bare zeolites. The latter, together with the high surface area of zeolite-supported samples, are probably the key factors to obtain similar o-DCB conversion than bulk 85Mn15Ce catalyst above 300 ºC.

Among the two samples supported over zeolites, the one supported over H-BETA has been selected as the optimal, since it has the widest range of temperature in which high NO and o-DCB conversion are obtained. This result is probably associated to the fact that this zeolite has a higher contribution of mesoporosity.

On the other hand, in the case of metal-doped catalysts, the W-doped sample was the only one reaching high NO and o-DCB conversions above the temperature at which catalyst deactivation does not affect the oxidation reaction. In addition, this catalyst showed the lowest production of SCR by-products compared to the other doped samples and bulk 85Mn15Ce catalyst.

The improvement in the catalytic performance of the W-doped catalyst with respect to the bulk 85Mn15Ce is associated to the chemical features provided by W and the decrease in the reactivity of surface oxygen species of the catalyst due to the partial coverage of MnO_X-CeO_2. These features decrease the oxidative capability of the catalyst by decreasing oxygen mobility. This fact is the key factor to increase NO conversion at high temperature by means of the suppression of SCR side reactions.

Based on the catalytic activity results of the best catalyst obtained from each strategy, a comparison has been made. 85Mn15Ce/H-BETA catalyst has been concluded to be the optimum one since it has a wider temperature range (300-420 ^{o}C) in which NO and o-DCB conversion above 80% is simultaneously reached.

Chapter 7

SUMMARY, CONCLUSIONS AND FUTURE WORKS

7. SUMMARY, CONCLUSIONS AND FUTURE WORKS.

7.1. SUMMARY.

Directive 2008/98/CE is the main regulatory instrument to deal with the increasing problems arising from MSW generation and management. This directive establishes a hierarchy that prioritizes an order in waste management, where any recovery process prevails over disposal. Energy recovery uses those fractions of waste that could not be reused to produce energy. Incineration is currently the most widely used process for energy recovery. However, this process usually faces public opposition because the complete suppression of pollutants during incineration stage is impossible. The typical pollutants that compose the raw flue gas are: particulate matter, acid gases (HCl, SO_2, etc.), nitrogen oxides, heavy metals (Hg, Cd, Ni, etc.) and other carbon-based compounds, such as CO, VOCs, PCDD/Fs, etc. This thesis has focused on providing an alternative process for the removal of two of those compounds, NO_X and PCDD/Fs from incineration exhaust gases.

NO_X has been commonly removed by SNCR, although the tightening of pollutant emission limits is currently encouraging the use of catalytic technology, namely SCR, which exhibits a higher removal efficiency. On the other hand, PCDD/Fs in the gas phase are usually removed by means of adsorption processes. However, adsorption processes have the disadvantage of only transferring the pollutant from the gas phase to the adsorbent, thus generating a new waste that needs to be treated or disposed of.

Catalytic oxidation of PCDD/Fs is starting to be considered as an alternative to adsorption processes, since it promotes total destruction of PCDD/Fs. In this context, research has reported that the typical catalysts of SCR systems, $V_2O_5/WO_3/TiO_2$, are also active for catalytic oxidation of PCDD/Fs. This evidence is the initial point of the single-stage process that this thesis proposes ($dDiNO_X$) for the simultaneous removal of NO_X and PCDD/Fs. In fact, research previous to this thesis has already corroborated the feasibility of this process by studying the simultaneous removal of NO and o-DCB (model compound of PCDD/Fs) with V-based catalysts.

However, the use of V-based formulations for SCR has some weaknesses, such as its relatively high temperature of operation. Currently, many research is focusing

on alternative catalysts to perform the SCR in a more efficient way, that is, at lower temperature. MnO_X-CeO_2 catalytic formulations are widely reported to be excellent catalysts for low temperature SCR. So, the feasibility of $dDiNO_X$ process lies on the activity of MnO_X-CeO_2 formulations in the simultaneous removal of NO_X and PCDD/Fs.

In this context, this thesis aims to assess MnO_X-CeO_2 catalytic formulations in the simultaneous removal of NO and o-DCB. For this purpose, firstly, this work dealt with the optimisation of the synthesis of MnO_X-CeO_2 formulations. Then, the optimal catalyst was used to analyse in depth its catalytic behaviour and to propose a reaction pathway for the two reactions under study. Finally, several strategies were evaluated to improve the catalytic performance of the optimal bulk MnO_X-CeO_2 formulation.

The optimisation of MnO_X-CeO_2 formulation was performed in three different sections throughout Chapter 3. In the first one, four preparation methods were evaluated: impregnation, sol-gel, co-precipitation and physical mixing; on the basis of the different interaction that each one promotes between Mn and Ce active metals. Sol-gel and co-precipitation methods lead to the best catalytic activity. This result is related to the fact that both favour a high interaction between Mn and Ce in the whole catalyst structure (surface and bulk), which is important for the reactions because it improves oxygen mobility. The interaction between Mn and Ce was confirmed with XRD and Raman techniques by means of the distortion of crystal phases.

The next step dealt with the assessment of Mn and Ce content. Three different Mn and Ce loadings (15Mn85Ce, 50Mn15Ce and 85Mn15Ce) were studied together with pure oxides (MnO_X and CeO_2). The catalysts with the highest Mn loadings (85Mn15Ce) were the most active, specifically the one prepared by co-precipitation, due to its high activity in the oxidation reaction at low temperature. These results showed that Mn is the most active metal and, thus, its presence plays a key role in catalytic activity.

Moreover, high Mn content in the catalyst led the presence of a mixture of crystalline phases: a solid solution (with several degrees of interaction between Mn and Ce) and a MnO_X phase. The co-existence of these two phases increased the amount of structural defects, which improved morphological properties (larger surface area and pore volume). On the other hand, XPS and H_2-TPR results

corroborated that the presence of Mn in different phases also promotes Mn and Ce species with different oxidation state (Mn^{4+}, Mn^{3+}, Ce^{4+} and Ce^{3+}). The synergy between these species was important for redox properties in these catalysts.

After selecting co-precipitation method and a molar composition of 85%Mn and 15%Ce as optimal, the effect of calcination temperature and some of the main variables involved in co-precipitation method (ageing time, pH and precipitating agent) were studied. Increasing calcination temperature led to a segregation of crystalline phases and, thus, a lower interaction between Mn and Ce. This fact had a negative impact on morphology (lower specific area and pore volume), oxygen mobility and redox and acid properties. As a consequence, the increase in calcination temperature reduced catalytic activity in both NO reduction and o-DCB oxidation.

On the other hand, ageing time and pH mainly affected the crystallinity degree of MnO_X phase, although this change at the structural level had no impact on catalytic performance. On the contrary, precipitating agent affected to the type of MnO_X phase obtained. The use of sodium hydroxide, ammonia and sodium carbonate promoted the Mn_5O_8 phase, whereas the use of ammonium carbamate favoured the Mn_2O_3 phase. The promotion of the Mn_2O_3 phase is a key factor, as the catalyst co-precipitated with ammonium carbamate showed the best catalytic results, due to its high surface area, reducibility and acidity.

On the basis of this, 500 ^{o}C was selected as the optimum calcination temperature (the lowest value analysed) and ammonium carbamate as the precipitating agent that favours the best catalytic performance. On the other hand, the lowest ageing time (2 h) and the highest pH value (9) were selected to promote a structural order of manganese oxide phase, which leads to different Mn species with high oxidation state.

The next stage of this thesis addressed, in Chapter 4, the analysis in detail of catalytic activity and the effect of concentration of reagents and other compounds involved at full-scale process. After operating NO reduction and o-DCB oxidation simultaneously and independently, the different evolution of conversion and by-products production corroborated that both reactions affect each other. Thus, the presence of o-DCB had a negative effect on NO conversion. On the contrary, o-DCB conversion improved in the presence of NO reduction. The individual analysis of each compound involved in SCR allowed to conclude that the presence of both NO

(at low concentrations) and NH_3 has a positive effect on the o-DCB abatement. In the case of NO, this behaviour has been related to NO_2 generation, whereas in the case of NH_3 it has been associated to removal of adsorbed chlorine.

Regarding selectivity, N_2O (in the whole range of temperature) and NO_2 (at high temperatures) were the main by-products generated in NO reduction. Their production is relatively high in comparison to other catalytic formulations and has been associated to the excellent oxidative capability of MnO_X-CeO_2 formulation. The side reactions involved in the origin of N_2O were NH_3 oxidation and NSCR, whereas oxidation of NH_3 and NO was involved in the origin of NO_2. The contribution of these side reactions became greater at high temperature, which causes the drop in NO conversion above 250 ^oC. The presence of o-DCB reduced the formation of SCR by-products, especially NO_2. This fact has been associated to the competition between SCR reactants and o-DCB for the active sites.

In the oxidation reaction, the main product was CO_2, although CO and chlorinated organic compounds (tetrachloromethane, tetrachloroethylene and trichlorobenzene) were also generated to a lesser extent. The formation of Cl_2 was not detected, even though it is widely reported in the literature related to VOC oxidation, due to the reaction between adsorbed chlorine and NH_3 to form NH_4Cl. Moreover, the presence of SCR favoured a decrease in the production of chlorinated organics, although the selectivity towards CO increases slightly.

TOS experiments evidenced the presence of catalyst deactivation, although it only affected o-DCB conversion below 300 ^oC. Characterization of used samples identified chlorine and carbon-based compounds as deactivating species. The adsorption of deactivating species reduces oxygen mobility, which negatively affects oxidative capability and redox properties. Moreover, TOS experiments provided important information about the reaction pathway of o-DCB oxidation, which is proposed to change with reaction temperature due to the different oxidative capability of Mn phases that compose the catalyst. Hence, at low temperature, o-DCB oxidation is mainly promoted by the mixed oxide phase, which exhibits a higher oxidative capability due to the higher interaction between Mn and Ce. However, at high temperature, o-DCB oxidation mainly occurs through partial oxidation reactions (evidenced by the detection of chlorinated organic compounds). This change takes place because, on the one hand, active sites involved in o-DCB oxidation at low temperature are deactivated; and, on the other

hand, other surface oxygen species with lower oxidizing capacity, such as those coming from segregated Mn_2O_3, become more active to perform the oxidation reaction with increasing temperature.

The effect of oxygen, CO_2 and water on simultaneous NO and o-DCB oxidation was also studied in Chapter 4. Oxygen concentration hardly affected NO conversion, although it favoured o-DCB oxidation. The presence of CO_2 did not affect the reactions. In the case of water, its presence decreased NO conversion, but also greatly decreased the production of N_2O and NO_2. In oxidation reaction, water had two different effects, competition for the active sites and removal of the deactivating species.

After carrying out the detailed assessment of catalytic activity, Chapter 5 dealt with the analysis of the active species formed during the adsorption of the reactants involved in NO reduction and o-DCB oxidation with the optimal catalyst by FTIR, in order to propose a reaction pathway for each of these reactions.

SCR has been proposed to follow an ER-type pathway at low temperature, and a LH-type pathway at high temperature. This change in the reaction pathway is based on the low reactivity of NO adsorbed species at low temperature. According to the ER pathway, NH_3 adsorbs on a Lewis-type acid site, subsequently it is submitted to a proton abstraction by surface oxygen and, finally, it reacts with NO in gas the phase generating N_2. This reaction pathway also explains the formation of N_2O through NSCR by the reaction of NO in the gas phase and an excessively-deprotonated adsorbed ammonia. On the other hand, the proposed LH pathway involves three active sites for the adsorption of two NH_3 and one NO (as nitrate) molecules. The subsequent reaction between these three adsorbed species and a NO molecule in the gas phase produces N_2. In contrast, if the reaction occurs between a nitrate and adsorbed ammonia, N_2O is generated.

As for oxidation reaction, a Mars-van Krevelen type reaction pathway has been proposed. The first step is a nucleophilic substitution in which one chlorine of o-DCB is replaced by an oxygen of the catalyst generating phenate species. Then, phenate species undergoes a second nucleophilic substitution, forming catecholate and/or benzoquinone-type species. At this point, a change in the reaction pathway as a function of temperature was evidenced due to the different distribution of intermediate species, which was in agreement with the findings in the detailed analysis of the catalytic activity in Chapter 4. Thus, at low temperature, the

aromatic ring is opened forming maleate species, which are then rapidly oxidised to CO_2. On the other hand, at high temperature, the opening of the aromatic ring is faster, although the subsequent oxidation of maleate species is slower. This promotes the appearance of additional intermediates, such as acetate, formate and enolic species, which are finally oxidised to CO and CO_2, although they can also react with adsorbed chlorine, forming the chlorinated organic compounds detected in catalytic activity tests.

Finally, Chapter 6 addressed an improvement in catalytic performance of the optimal catalyst in order to reach high NO and o-DCB conversions in a temperature range where these are not affected by catalyst deactivation. The second goal is to reduce the amount of N_2O and NO_2 produced in NO reduction. For this purpose, a slight decrease in the oxidative capability of bulk 85Mn15Ce catalyst was proposed, to be compensated with other catalytic properties by means of two strategies: either supporting the MnO_X-CeO_2 phase over different supports (Al_2O_3, TiO_2, H-ZSM5 and H-BETA) or surface doping of MnO_X-CeO_2 with a third metal (Fe, Zr, Co, Sr and W).

The catalytic performance was notably improved with, on the one hand, the catalysts supported over H-ZSM5 and H-BETA and, on the other hand, the catalyst exclusively doped with W. These catalysts allowed to increase NO conversion in the high temperature range by suppressing SCR side reactions and without affecting o-DCB conversion (in the high temperature range). Thus, NO and o-DCB conversions above 80% were simultaneously obtained above 300 ^{o}C, where o-DCB conversion is not affected by catalyst deactivation. In addition, as a result of the suppression of SCR side reactions, the production of N_2O and NO_2 was greatly reduced.

7.2. RESUMEN.

La Directiva 2008/98/CE es el principal instrumento regulador para abordar la problemática actual derivada de la generación y gestión de los residuos sólidos urbanos (RSU). Esta directiva establece una jerarquía que prioriza cualquier forma de valorización sobre la deposición del residuo en vertedero. La valorización energética usa aquellas fracciones de residuos que no pudieron ser reusados o reciclados para producir energía. La incineración es actualmente el proceso más ampliamente utilizado para llevar a cabo la valorización energética de los residuos. Sin embargo, este proceso tiene en contra a una parte de la opinión pública debido

a la imposibilidad de evitar la generación de contaminantes durante el proceso de combustión. Los contaminantes típicos que componen los gases de incineración son: material particulado, gases ácidos (HCl, SO_2, etc.), óxidos de nitrógeno, metales pesados (Hg, Cd, Ni, etc.) y otros compuestos basados en carbono, como por ejemplo CO, COV, dioxinas y furanos, etc. Esta tesis se centra en proponer un proceso alternativo para la eliminación de dos de estos contaminantes, los NO_X y las dioxinas y furanos procedentes de la incineración de RSU.

Los NO_X han sido comúnmente eliminados mediante reducción selectiva no catalítica, aunque los cada vez más ajustados límites de emisión están fomentando el uso de la tecnología catalítica denominada reducción catalítica selectiva, la cual presenta una mayor eficacia. Por otro lado, las dioxinas y furanos en fase gas se eliminan normalmente mediante procesos de adsorción. Sin embargo, los procesos de adsorción tienen la desventaja de únicamente transferir el contaminante de la fase gas al adsorbente, generando, por tanto, un nuevo residuo que necesita ser gestionado.

La oxidación catalítica de dioxinas y furanos está considerada actualmente como una alternativa a los procesos de adsorción, dado que promueve la destrucción total del contaminante. En este sentido, se ha reportado que el catalizador utilizado normalmente en los sistemas SCR, $V_2O_5/WO_3/TiO_2$, también es activo para la oxidación catalítica de dioxinas y furanos. Esta evidencia es el punto inicial de un proceso para la eliminación simultánea de NO_X y dioxinas y furanos en una única etapa (dDiNOx). De hecho, investigaciones previas a esta tesis ya han corroborado la viabilidad de este proceso mediante el estudio de la eliminación simultánea de NO y o-DCB (compuesto modelo de dioxinas y furanos) con catalizadores basados en vanadio.

Sin embargo, el uso de formulaciones basadas en vanadio para la reducción selectiva de NO_X presenta algunas desventajas, como por ejemplo una alta temperatura de operación. Actualmente, muchas investigaciones se centran en la búsqueda de catalizadores alternativos para llevar a cabo la SCR de una forma más eficiente, es decir, a menor temperatura. La formulación catalítica basada en MnO_X-CeO_2 es ampliamente reportada por su idoneidad para la reducción selectiva de NO_X a baja temperatura. Así pues, la viabilidad del proceso dDiNOx pasa por que esta formulación catalítica alternativa sea activa para la eliminación simultánea de NO_X y dioxinas y furanos.

En este contexto, esta tesis tiene por objetivo la evaluación de la formulación catalítica MnO_X-CeO_2 en la eliminación simultánea de NO y o-DCB. Para este propósito, primeramente, este trabajo abordó una optimización de la síntesis de la formulación MnO_X-CeO_2. Después, el catalizador óptimo fue usado para analizar en profundidad el comportamiento catalítico y proponer una ruta de reacción para cada una de las reacciones estudiadas. Finalmente, varias estrategias fueron evaluadas para mejorar la actividad catalítica del catalizador MnO_X-CeO_2 seleccionado como óptimo.

La optimización de la formulación MnO_X-CeO_2 fue realizada en tres secciones diferentes a lo largo del Capítulo 3. En la primera sección se analizaron cuatro métodos de preparación (impregnación, sol-gel, coprecipitación y mezcla física) en base a la diferente interacción que cada uno puede favorecer entre los metales activos. Los catalizadores más activos se corresponden con los preparados por sol-gel y coprecipitación. Este resultado está relacionado con el hecho de que ambos métodos favorecen una alta interacción entre Mn y Ce, lo cual es importante para las reacciones estudiadas, ya que mejora la movilidad del oxígeno. Esta interacción entre el Mn y el Ce fue confirmada por las técnicas de DRX y Raman.

La siguiente etapa de la optimización abordó el análisis del contenido de Mn y Ce. Se estudiaron tres composiciones diferentes (15Mn85Ce, 50Mn50Ce y 85Mn15Ce) junto con los óxidos puros (CeO_2 y MnO_X). Los catalizadores con alto contenido de Mn (85Mn15Ce) fueron los más activos, concretamente el preparado por coprecipitación, debido a su alta actividad a baja temperatura en la reacción de oxidación. Estos resultados mostraron que el Mn es el componente activo y, por tanto, su presencia juega un papel fundamental en la actividad catalítica.

Además, altos contenidos de Mn favorecen la presencia de diferentes fases cristalinas: disolución sólida (con varios grados de interacción entre Mn y Ce) y óxido de Mn segregado. La coexistencia de estas dos fases aumenta la cantidad de defectos estructurales, lo que mejora las propiedades morfológicas (mayor área superficial y volumen de poros). Por otro lado, los resultados de las técnicas de XPS y H_2-TPR corroboraron que esta presencia de Mn en diferentes fases favorece la presencia de especies de Mn y Ce con diferente estado de oxidación (Mn^{4+}, Mn^{3+}, Ce^{4+} y Ce^{3+}). La sinergia entre estas especies se ha demostrado que es importante para las propiedades redox en estos catalizadores.

Después de seleccionar el método de coprecipitación y la composición molar de 85%Mn y 15%Ce como óptima, se evaluaron el efecto de la temperatura de calcinación y algunas variables implicadas en el método de coprecipitación (tiempo de envejecimiento, pH y agente precipitante). El incremento de la temperatura de calcinación favorece la segregación de las fases cristalinas y, por tanto, una menor interacción entre Mn y Ce. Este hecho tuvo un efecto negativo en la morfología (bajada del área específica y volumen de poros), movilidad del oxígeno y propiedades redox y ácidas. Como consecuencia, el incremento de la temperatura de calcinación disminuyó la actividad catalítica en la reducción de NO y oxidación de o-DCB.

Por otro lado, el tiempo de envejecimiento y el pH afectaron principalmente al grado de cristalinidad de la fase de óxido de Mn, aunque este efecto a nivel estructural no tuvo repercusión a nivel de actividad catalítica. Por el contrario, el agente precipitante afectó a la fase cristalina del óxido de Mn segregado. Así pues, el uso de hidróxido sódico, amoniaco y carbonato sódico promueven la fase Mn_5O_8, mientras que el uso de carbamato amónico favorece la fase Mn_2O_3. La promoción de la fase Mn_2O_3 es fundamental ya que el catalizador coprecipitado con carbamato amónico mostró los mejores resultados en las pruebas de actividad catalítica, gracias a su mayor área superficial, reducibilidad y acidez.

Por tanto, en base a estos resultados, se seleccionó 500 ^{o}C como temperatura óptima de calcinación (la menor temperatura analizada) y carbamato amónico como agente precipitante. Por otro lado, también se seleccionaron el menor tiempo de envejecimiento (2 h) y el mayor valor de pH (9) para promover el ordenamiento estructural de la fase de óxido de Mn, lo que favorece la presencia de diferentes especies de Mn con alto estado de oxidación.

La siguiente etapa de esta tesis abordó, en el Capítulo 4, el análisis en detalle de la actividad catalítica y el efecto de la concentración de reactivos y otros compuestos implicados en el proceso a escala industrial. Tras comparar los resultados obtenidos de la reducción de NO y la oxidación de o-DCB llevadas a cabo de forma independiente y simultánea, se ha llegado a la conclusión de que ambas reacciones influyen la una sobre la otra. Así, la presencia de o-DCB tiene un efecto negativo en la conversión de NO. Por el contrario, la conversión de o-DCB mejora cuando la oxidación ocurre en presencia de la reducción de NO. El análisis individual de cada compuesto implicado en la reducción de NO permitió concluir que la presencia de

ambos, NO (a bajas concentraciones) y NH_3 tiene un efecto positivo en la eliminación de o-DCB. El efecto positivo del NO está relacionado con la generación de NO_2, mientras que el efecto positivo del NH_3 se ha asociado a la eliminación del cloro adsorbido en el catalizador.

Respecto a la selectividad, los principales subproductos de la reducción de NO son el N_2O (en todo el rango de temperaturas) y el NO_2 (a altas temperaturas). Las producciones de cada uno de estos subproductos son relativamente altas en comparación con otras formulaciones catalíticas, lo cual está relacionado con la alta capacidad oxidante de la formulación MnO_X-CeO_2. Las reacciones secundarias implicadas en la formación del N_2O son la oxidación del NH_3 y la reducción catalítica no selectiva; mientras que la oxidación de NH_3 y NO están implicadas en el origen del NO_2. La contribución de estas reacciones secundarias llega a ser importante a alta temperatura, lo que causa una caída en la conversión de NO por encima de 250 ^oC. La presencia de o-DCB reduce la formación estos subproductos, especialmente el NO_2. Este hecho está asociado a la competición entre los reactivos implicados en la reducción de NO y el o-DCB por los centros activos.

En la reacción de oxidación, el principal producto fue el CO_2, aunque también se producen en menor medida CO y compuestos orgánicos clorados (tetraclorometano, tetracloroetileno y triclorobenceno). No se han encontrado indicios de la formación de Cl_2 a pesar de que este compuesto es reportado en la bibliografía por formarse en la oxidación de COV. Este hecho puede estar relacionado con la formación de NH_4Cl debido a la reacción entre el Cl adsorbido y el NH_3. Además, la formación de subproductos orgánicos clorados disminuye en presencia de la reducción de NO, aunque la selectividad hacia CO aumenta ligeramente.

Los experimentos TOS evidenciaron la desactivación del catalizador, aunque ésta únicamente afectó a la conversión de o-DCB por debajo de 300 ^oC. La caracterización de las muestras usadas permitió identificar a compuestos basados en carbono y cloro como especies desactivantes. La adsorción de estas especies desactivantes reduce la movilidad del oxígeno, lo que afecta negativamente a la capacidad oxidante y a las propiedades redox. Además, los experimentos TOS aportaron información importante sobre la ruta de reacción de la oxidación de o-DCB, la cual se ha propuesto que cambia con la temperatura de reacción debido a las diferentes capacidades oxidantes de las fases de Mn que componen el

catalizador. De esta forma, a baja temperatura, la oxidación de o-DCB es promovida principalmente por la fase de óxido mixto, que tiene una mayor capacidad oxidante debido a la mayor interacción entre Mn y Ce. Sin embargo, a alta temperatura, la oxidación de o-DCB ocurre principalmente a través de un mayor número de oxidaciones parciales (evidenciadas por la detección de compuestos orgánicos clorados). Este cambio tiene lugar porque, por un lado, los centros activos en la oxidación del o-DCB a baja temperatura son desactivados; y, por otro lado, otras especies activas con menor capacidad oxidante, como son aquellas procedentes del Mn_2O_3 segregado, llegan a ser activas para llevar a cabo la reacción de oxidación con el incremento de temperatura.

El efecto del oxígeno, el CO_2 y el agua también se estudió en el Capítulo 4. La concentración de oxígeno apenas afecta a la conversión de NO, aunque favorece la oxidación de o-DCB. La presencia de CO_2 no afectó a las reacciones. Por otro lado, la presencia de agua decrece la conversión de NO, pero también disminuye enormemente la producción de N_2O y NO_2. En la reacción de oxidación, el agua compite por los centros activos y, al mismo tiempo, favorece la eliminación de especies desactivantes.

Tras el análisis detallado de la evaluación de la actividad catalítica, el Capítulo 5 abordó el análisis de las especies activas formadas durante la adsorción de los reactivos implicados en la reducción de NO y la oxidación de o-DCB con el catalizador óptimo por FTIR, todo ello con el objetivo de proponer una ruta de reacción para cada una de las reacciones analizadas.

De acuerdo con los resultados obtenidos, se ha propuesto que la reducción de NO sigue una ruta de tipo ER a baja temperatura, mientras que a alta sigue mayoritariamente una de tipo LH. Este cambio en la ruta de reacción se basa en la baja reactividad de las especies procedentes de la adsorción del NO a baja temperatura. En la ruta de tipo ER, el NH_3 se adsorbe sobre un centro ácido de tipo Lewis; a continuación, el oxígeno superficial del catalizador elimina un protón del NH_3 adsorbido, que finalmente reacciona con NO procedente de la fase gas generando N_2. En esta ruta de reacción, la formación de N_2O mediante la reducción no selectiva se produce por la reacción del NO procedente de la fase gas con un NH_3 adsorbido y excesivamente desprotonado. Por otro lado, la ruta LH propuesta implica la participación de tres centros activos para la adsorción de dos moléculas NH_3 y una molécula de NO (como nitrato). La posterior reacción entre estas tres

especies adsorbidas y una molécula de NO procedente de la fase gas produce N_2. Por el contrario, si la reacción ocurre entre un nitrado y un NH_3 adsorbido se produce la formación de N_2O.

En cuanto a la reacción de oxidación, se ha propuesto que ésta sigue una ruta de tipo Mars-van Krevelen. La primera etapa es una sustitución nucleofílica en la que uno de los cloros del o-DCB es reemplazado por un oxígeno del catalizador generando una especie fenato. Después, las especies fenato son sometidas a una segunda sustitución nucleofílica, formándose especies catecolato y/o benzoquinona. En este punto, las diferentes especies identificadas evidenciaron un cambio en la ruta de reacción con la temperatura, lo que está de acuerdo con los resultados obtenidos del análisis detallado de la actividad en el Capítulo 4. Así, a baja temperatura, se produce la ruptura del anillo formando especies maleato, que son rápidamente oxidadas a CO_2. Por otro lado, a alta temperatura, la apertura del anillo aromático es más rápida, aunque la posterior oxidación de las especies maleato es más lenta. Esto produce la aparición de intermedios de reacción diferentes, tal como especies acetato, formato y enol. Estas especies son finalmente oxidadas hacia CO y CO_2, aunque también pueden reaccionar con el cloro adsorbido, formando los compuestos orgánicos clorados detectados en las pruebas de actividad catalítica.

Finalmente, el Capítulo 6 abordó una mejora del comportamiento catalítico con el objetivo de alcanzar altas conversiones de NO y o-DCB en un rango de temperatura en el que ambas conversiones no se vean afectadas por la desactivación del catalizador. El segundo objetivo es reducir la cantidad de N_2O y NO_2 producido en la reducción de NO. Para cumplir ambos objetivos, se buscó una reducción de la capacidad oxidante del catalizador coprecipitado 85Mn15Ce, que fue compensada a su vez con otras propiedades catalíticas. Estas nuevas propiedades catalíticas fueron aportadas mediante dos estrategias: soporte de la fase MnO_X-CeO_2 sobre diferentes soportes (Al_2O_3, TiO_2, H-ZSM5 y H-BETA) y dopaje superficial de la fase MnO_X-CeO_2 con un tercer metal (Fe, Zr, Co, Sr y W).

El rendimiento catalítico fue notablemente mejorado (de acuerdo con los dos objetivos mencionados anteriormente) con los catalizadores soportados sobre H-ZSM5 y H-BETA; y también con el catalizador exclusivamente dopado con W. Estos catalizadores aumentaron la conversión de NO en el rango de alta temperatura mediante la supresión de las reacciones secundarias, sin afectar a la conversión de

o-DCB en el rango de alta temperatura. De esta forma, se obtuvieron conversiones de NO y o-DCB mayores del 80% de forma simultánea y por encima de 300 ^{o}C, rango de temperatura donde la conversión de o-DCB no se ve afectada por la desactivación del catalizador. Además, como resultado de la supresión de las reacciones secundarias en la reducción de NO, la producción de N_2O y NO_2 fue enormemente reducida.

7.3. CONCLUSIONS.

The conclusions are presented in accordance with the specific objectives proposed in Section 1.6.

Optimisation of the synthesis of MnO_X-CeO_2 formulation.

- The highest catalytic activity is obtained with the preparation methods that promote high interaction between Mn and Ce at both surface and bulk level: sol-gel and co-precipitation. The interaction between active metals generates structural defects that favour oxygen mobility, which improves catalytic properties.
- Among the preparation methods that favour high interaction between the active metals, co-precipitation is the best because it provides better morphological properties and promotes the ordering of segregated manganese oxide. These factors increase catalytic activity in the o-DCB oxidation reaction.
- High Mn contents improve catalytic performance as they promote the co-existence of Mn in different phases: mixed oxide phase (high interaction between Mn and Ce) and segregated MnO_X phase. The presence of both phases increases structural defects and promotes Mn and Ce species in different oxidation states. A molar composition of 85%Mn and 15%Ce has been found to be the optimum.
- The higher the calcination temperature, the lower the catalytic activity, due to the segregation of the phases that compose the catalyst. A calcination temperature of 500 ^{o}C has been chosen to be the most adequate for this process.

- The precipitating agent has been found to be the most significant variable affecting catalytic performance of co-precipitated catalysts. Ammonium carbamate leads to the best catalytic performance because it favours the formation of the Mn_2O_3 crystal phase.

- Simultaneous removal of NO and o-DCB has been found to be possible. According to the results from light-off experiments of the optimal catalyst, NO and o-DCB conversions above 80% are obtained in the temperature ranges between 180-250 ^oC and 290-300 ^oC, under the operational conditions studied.

Detailed analysis of catalytic performance of MnO_X-CeO_2 formulations.

- NO reduction and o-DCB oxidation have been found to affect each other in dDiNOx. o-DCB has a negative effect on NO reduction, as it competes with the reactants involved in this reaction for the active sites. On the contrary, NO reduction increases o-DCB conversion due to the positive effect of both NO (promotes NO_2 production) and NH_3 (favours the removal of surface adsorbed chlorine).

- The main by-products in NO reduction are N_2O and NO_2. o-DCB has been found to decrease their generation. The side reactions involved in the origin of N_2O have been identified to be NH_3 oxidation and NSCR, whereas NO and NH_3 oxidation are involved in the formation of NO_2. The promotion of these side reactions at high temperature, especially NH_3 oxidation towards NO and NO_2, are key for the drop in NO conversion above 250 ^oC.

- o-DCB oxidation exhibits a high selectivity towards CO_2, although CO and chlorinated organic compounds are also produced to a lesser extent. The presence of NO reduction reduces the production of chlorinated organic compounds, although it increases the selectivity towards CO.

- Catalyst deactivation becomes important below 300 ^oC, where it negatively affects o-DCB oxidation. Deactivation has been associated to adsorption of chlorine and carbon-based compounds over mixed oxide phase.

- Increasing temperature leads to a change in the reaction pathway of oxidation reaction due to the different reactivity (oxidative capability) of

the phases that compose the catalyst. Due to its higher oxidative capability, the mixed oxide phase becomes active at lower temperature than Mn_2O_3 segregated phase. However, this phase undergoes deactivation. Thus, the Mn_2O_3 phase is mainly responsible for catalytic activity above 300 ^oC.

- The higher the oxygen concentration, the higher the oxidative capability, which leads to a larger production of NO_2 in NO reduction and higher o-DCB conversions. High oxygen concentration also decreases the production of chlorinated organic compounds.

- CO_2 has no significant effect on conversion and selectivity of the reactions studied.

- Water has a negative effect of NO conversion due to the competition for the active sites, although it notably decreases the production of N_2O and NO_2. In oxidation reaction, water has a bimodal effect, since it competes for the active sites and simultaneously removes the carbon-based deactivating species. The contribution of each effect depends on temperature; thus, at high temperature, the presence of water increases o-DCB conversion.

- Water adsorption does not alter the Lewis nature of acid sites, but it does affect their strength.

<u>Reaction pathway for SCR and o-DCB oxidation over MnO_X-CeO_2 formulation.</u>

- NO adsorbs as nitrosyl species, although the increase in temperature and the presence of oxygen favours the formation of nitrate species. NH_3 adsorbs through the lone electron pair of nitrogen atom on Lewis acid sites, through H-bonds with surface hydroxyl groups or through ammonia protonation generating NH_4^+ species. These species are rapidly oxidized to nitrates at high temperature and in the presence of oxygen.

- The reactivity of NH_3 adsorbed species is high over the whole temperature range, whereas NO adsorbed species are only reactive for NO reduction at high temperature. Consequently, a temperature-dependent reaction pathway has been proposed for SCR. At low temperature, SCR follows an

ER-type pathway in which adsorbed NH_3 reacts with NO from the gas phase. At high temperature, a LH-type pathway has been proposed in which two adsorbed NH_3 and one adsorbed NO react with a NO from the gas phase.

- o-DCB oxidation follows a Mars-van Krevelen pathway in which the adsorbed species are oxidized by surface oxygen of the catalyst. The first steps of this pathway are nucleophilic substitutions in which chlorine atoms are replaced by surface oxygen generating phenate species. The different distribution of adsorbed species with temperature has highlighted that:
  - Aromatic ring opening is easier at higher temperature.
  - A change in the reaction pathway occurs. At low temperature, maleate species, generated from a previous oxidation of phenate species, are rapidly oxidised to CO_2, whereas at high temperatures, the oxidation of maleate species are slower and involves a larger number of partial oxidations. This fact leads to the formation of CO and chlorinated organic compounds in addition to CO_2.

Improvement of catalytic performance by the modification of MnO_X-CeO_2 formulation.

- The two proposed strategies (supporting and doping the MnO_X-CeO_2 phase) have allowed to enhance the catalytic performance of the optimal bulk catalyst. This fact has been achieved by shifting the NO conversion profile towards higher temperature, where o-DCB conversion is also high and is not affected by catalyst deactivation.
- The modifications of the MnO_X-CeO_2 formulation have also greatly reduced the production of N_2O and NO_2. This is due to a reduction in the oxidative capability of MnO_X-CeO_2 phase, which has been achieved in supported catalysts by the high dispersion of Mn and Ce, which decreased the interaction between these active metals. In the case of doped catalysts, it was achieved by the chemical properties of dopant metal and the decrease of the activity of surface oxygen species due to the coverage of MnO_X-CeO_2 phase.

- The catalyst from each strategy that shows the best catalytic activity is the one supported on H-BETA and the one doped with W. Among them, the catalyst supported on H-BETA has been selected as optimal, as it exhibits the widest temperature range where NO and o-DCB conversion above 80% are obtained in the studied conditions, between 300-420 ^{o}C.

7.4. FUTURE WORKS.

This section provides several ideas in order to continue with the research started in this thesis and to complement the study of $dDiNO_X$ process with the MnO_X-CeO_2 formulation.

- A detailed analysis of catalytic activity by monitoring NH_3 concentration should be carried out, which would allow to know the selectivity of NO reduction towards N_2 and N_2O and NO_2 by-products.

  This type of analysis could not be performed in this work due to the interference of o-DCB on the analyser of NH_3. However, the optimal catalyst (85Mn15Ce) generated N_2O and NO_2. Therefore, it is important for the feasibility of $dDiNO_X$ process to know how selective the optimal catalyst is in NO reduction towards the desired product, that is, N_2.

  In addition, it would be interesting to assess the effect of several factors, such as o-DCB concentration, water concentration, etc., on the selectivity of NO reduction towards N_2.

- Transient experiments should be used to corroborate the proposed mechanisms, especially those related to SCR. These experiments would be similar to those discussed in Chapter 5, but performed in an experimental set-up that allows to quickly analyse all the reaction products (mass spectrometer).

  The results of these experiments would allow to relate the adsorbed species observed by FTIR to the reaction products.

- Mechanistic equations describing the kinetic behaviour of the studied reactions should be proposed, based on the reaction pathways proposed from the adsorbed species detected by FTIR.

- The use of PCDD/Fs model compounds containing functional groups with oxygen in their structure should be assessed. This fact is proposed because PCDD/Fs contain oxygen in their structure as a bond between the two aromatic rings.

- The best catalysts obtained in Chapter 6 should be optimised. In that chapter, the improvement of catalytic performance of MnO_X-CeO_2 formulation was addressed by means of two different strategies, which concluded that either supporting MnO_X-CeO_2 phase on H-BETA or surface doping MnO_X-CeO_2 phase with W allows to obtain high NO and o-DCB conversions in the conditions at which deactivation of the catalyst is not relevant.

  The catalytic activity of the supported catalyst can be improved by optimising the loading of MnO_X-CeO_2 phase and the deposition methodology. Similarly, in the case of doped catalyst, the loading of dopant metal can also be optimised. Moreover, it would be interesting to evaluate the combination of the two strategies by deposition on H-BETA of MnO_X-CeO_2 and WO_X phases.

Chapter 8

NOMENCLATURE

8. NOMENCLATURE

Variables and physical constants

$(r_A)_{obs}$	Experimental reaction rate (mol/g s)
A	Chromatographic peak area
A_s	Molecular cross-sectional area of adsorbate (nm^2)
B	Experimental FWHM
b	Instrumental contribution to peak width
BE	Binding Energy (eV)
C	BET constant
C_0	Initial concentration (mol/m^3)
C_{As}	Surface concentration of A (mol/m^3)
C_i	Concentration (mol/m^3)
d	Interplanar crystal spacing
D	Reactor diameter (m)
D_e	Effective diffusivity (m^2/s)
$D_{i,ax}$	Axial dispersion coefficient (m^2/s)
$D_{i,mix}$	Mixture dispersion coefficient (m^2/s)
D_k	Knudsen diffusivity (m^2/s)
d_p	Mean pore diameter (m)
d_{pt}	Particle diameter (m)
EK	Kinetic energy (eV)
hv	Energy of adsorbed photon (eV)
K	Shape factor
k_c	Mass transfer constant (m/s)
L	Catalytic bed length (m)
M	Mass of solid
n	Reaction order
N_A	Avogadro number
P	Pressure (Pa)
P_0	Saturation pressure of adsorbate (Pa)
PM	Molecular weight (mol/kg)

PM_c	Molecular weight of catalyst (mol/kg)
r	Catalyst particle radius (m)
R	Universal gas constant (J/mol K)
r_p	Porous radius (nm)
R_{split}	Split ratio
S_{BET}	BET surface (m^2/g)
S_i	Selectivity
SP	Calibration line slope
T	Adsorbate layer thickness (nm)
T	Temperature (K)
u	Flow speed (m/s)
V_{ads}	Volume adsorbed of adsorbate per mass unit of solid (cm^3/g)
V_{loop}	Loop Volume (ml)
V_m	Volume of adsorbate to form the monolayer (cm^3/g)
Vp	Pore volume (m^3/g)
X	Conversion
x_i	Molar fraction

Greek letters

β	Corrected broadening at FWHM
ε	Porosity of catalyst
ε_L	Porosity of catalytic bed
Θ	Glancing angle of incident X-ray
λ	X-Ray wavelength
μ	Gas viscosity (kg/m s)
ν	Dispersion volume
ρ	Gas density (kg/m^3)
ρ_a	Bulk density of catalyst (kg/m^3)
ρ_i	Analyte density at the conditions of injector
ρ_L	Density of catalytic bed (kg/m^3)
ρ_r	Real density of catalyst (kg/m^3)
σ	Angle contract of condense phase and surface of solid (rad)
τ	Tortuosity of catalyst
τ_L	Tortuosity of catalytic bed
Ψ	Surface tension of adsorbate (N/m)

Abbreviations and acronyms

BAT	Best Available Technology
BET	Brunauer, Emmett, Teller
CA	Chelating agent
CEM	Controller Evaporator Mixer
CEWEP	Confederation of European Waste-to-Energy Plants
dDiNOx	Simultaneous destruction of dioxins and NO_X
EDX	X-Ray Dispersive
EELS	Electron Energy Loss Spectroscopy
ER	Eley-Rideal
EU	European Union
FEG	Field Emission Gun
FGC	Flue Gas Cleaning
FTIR	Fourier Transform Infrared
FWHM	Full Width at Half Maximum
GC-MS	Gas Chromatography Mass Spectroscopy
HAADF	High Angle Annular Dark Field
HRTEM	High Resolution Transmission Electron Microscopy
ICDD	International Centre for Diffraction Data
ICP-AES	Inductively Coupled Plasma Atomic Emission Spectroscopy
IR	Infrared
IUPAC	International Union of Pure and Applied Chemistry
LH	Langmuir-Hinshelwood
MSWI	Municipal Solid Waste Incinerator
MSW	Municipal Solid Waste
NDIR	Non-Dispersive Infrared
NO_X	Nitrogen Oxides
NSCR	Non-Selective Catalytic Reduction
o-DCB	ortho-dichlorobenzene
PCB	Polychlorinated Biphenyl

PCDD	Polychlorinated dibenzo-p-dioxin
PCDF	Polychlorinated dibenzo-p-furan
PID	Proportional Integrator Derivative
PLC	Programmable Logic Controller
PTFE	Polytetrafluoroethylene
PY	Pyridine
SCADA	Supervisor Control and Data Acquisition
SCR	Selective Catalytic Reduction
SEM	Scanning Electron Microscopy
SNCR	Selective Non-Catalytic Reduction
STEM	Scanning Transmission Electron Microscopy
TCD	Thermal Conductivity Detector
TEM	Transmission Electron Microscopy
TE	Toxic Equivalent
TGA	Thermogravimetric Analysis
TOC	Total Organic Compounds
TOF	Turn Over Frequency
TOS	Time On Stream
TPD	Temperature Programmed Desorption
TPR	Temperature Programmed Reduction
TQSA	Chemical Technologies for Environmental Sustainability
UV-Vis-NIR DRS	Ultraviolet-Visible-Near Infrared Diffuse Reflectance Spectroscopy
VOC	Volatile Organic Compound
WDXRF	Wavelength Dispersive X-Ray Fluorescence
WtE	Waste to Energy
XRD	X-Ray Diffraction

Chapter 9

REFERENCES

9. REFERENCES

[1] A. Fazeli, F. Bakhtvar, L. Jahanshaloo, N. A. Che Sidik, A. E. Bayat, Malaysia's stand on municipal solid waste conversion to energy: A review, Renewable Sustainable Energy Rev. 58 (2016), 1007-1016, doi: https//doi.org/10.1016/j.rser.2015.12.270.

[2] L. Makarichi, W. Jutidamrongphan, K. Techato, The evolution of waste-to-energy incineration: A review, Renewable Sustainable Energy Rev. 91 (2018), 812-821, doi: https//doi.org/10.1016/j.rser.2018.04.088.

[3] F. Cucchiella, I. D'Adamo, M. Gastaldi, Sustainable waste management: Waste to energy plant as an alternative to landfill, Energy Convers. Manage. 131 (2017), 18-31, doi: https//doi.org/10.1016/j.enconman.2016.11.012.

[4] Statistical office of the European Union (Eurostat). https://ec.europa.eu/eurostat/web/waste/overview Access verification: 17-03-2022.

[5] D. Khan, A. Kumar, S.R. Samadder, Impact of socioeconomic status on municipal solid waste generation rate, Waste Manage. 49 (2016), 15-25, doi: https//doi.org/10.1016/j.wasman.2016.01.019.

[6] A. Kumar, S. R. Samadder, A review on technological options of waste to energy for effective management of municipal solid waste, Waste Manage. 69 (2017), 407-422, doi: https//doi.org/10.1016/j.wasman.2017.08.046.

[7] Directive 2008/98/CE of the European Parliament and of the Council of 19 November 2008.

[8] M. Pavlas, L. Bebar, J. Kropac, P. Stehlik, Waste to energy, an evaluation of the environmental impact, Chem. Eng. Trans. 18 (2009), 671-676, doi: https//doi.org/10.3303/CET0918109.

[9] A. Massarutto, Economic aspects of thermal treatment of solid waste in a sustainable WM system, Waste Manage. 37 (2015), 45-57, doi: https//doi.org/10.1016/j.wasman.2014.08.024.

[10] A. Bosmans, I. Vanderreydt, D. Geysen, L. Helsen, The crucial role of Waste-to-Energy technologies in enhanced landfill mining: A technology review, J. Clean. Prod. 55 (2013), 10-23, doi: https//doi.org/10.1016/j.jclepro.2012.05.032.

[11] H. Cheng, Y. Hu, Municipal solid waste (MSW) as a renewable source of energy: Current and future practices in China, Bioresour. Technol. 101 (2010), 3816-3824, doi: https//doi.org/10.1016/j.biortech.2010.01.040.

[12] O. Gohlke, J. Martin, Drivers for innovation in waste-to-energy technology, Waste Manage. Res. 25 (2007), 214-219, doi: https//doi.org/10.1177/0734242X07079146.

[13] P. H. Brunner, H. Rechberger, Waste to energy, key element for sustainable waste management, Waste Manage. 37 (2015), 3-12, doi: https//doi.org/10.1016/j.wasman.2014.02.003.

[14] Confederation of European Waste-to-Energy Plants (CEWEP). https://www.cewep.eu/wp-content/uploads/2017/08/FINAL_CEWEP_BROCHURE_04.pdf Access verification: 17-03-2022.

[15] F. Neuwahl, G. Cusano, J. Gómez Benavides, S. Holbrook, S. Roudier, Best Available Techniques (BAT) Reference Document for Waste Incineration; EUR 29971 EN; doi: 10.2760/761437.

[16] O. Reimann, CEWEP Energy Report III (2012). https://www.cewep.eu/wp-content/uploads/2017/10/1069_13_01_15_cewep_energy_report_iii.pdf Access verification: 17-03-2022.

[17] M. Grosso, A. Motta, L. Rigamonti, Efficiency of energy recovery from waste incineration, in the light of the new Waste Framework Directive, Waste Manage. 30 (2010), 1238-1243, doi: https//doi.org/10.1016/j.wasman.2010.02.036.

[18] Directive 2000/76/CE of the European Parliament and of the Council of 4 December 2000.

[19] Directive 2010/75/CE of the European Parliament and of the Council of 24 November 2010.

[20] Registro Estatal de Emisiones y Fuentes Contaminantes de España (PRTR). https://prtr-es.es/Particulas-PM10,15673,11,2007.html
Access verification: 17-03-2022.

[21] Registro Estatal de Emisiones y Fuentes Contaminantes de España (PRTR). https://prtr-es.es/Cloro-y-compuestos-inorganicos-como,15667,11,2007.html#:~:text=En%20condiciones%20normales%20y%20en,formar%20%C3%A1cido%20hipocloroso%20(HClO).
Access verification: 17-03-2022.

[22] Registro Estatal de Emisiones y Fuentes Contaminantes de España (PRTR). https://prtr-es.es/SOx-oxidos-de-azufre,15598,11,2007.html
Access verification: 17-03-2022.

[23] Registro Estatal de Emisiones y Fuentes Contaminantes de España (PRTR). https://prtr-es.es/Hg-Mercurio-y-compuestos,15608,11,2007.html#:~:text=El%20mercurio%20es%20un%20elemento,at%C3%B3mico%2080%20y%20s%C3%ADmbolo%20Hg.&text=En%20sus%20compuestos%2C%20el%20mercurio,(Hg2Cl2).
Access verification: 17-03-2022.

[24] Registro Estatal de Emisiones y Fuentes Contaminantes de España (PRTR). https://prtr-es.es/CO-Monoxido-de-carbono,15589,11,2007.html
Access verification: 17-03-2022.

[25] G. Wielgosiński, J. Czerwińska, O. Szymańska, J. Bujak, Simultaneous NO_X and dioxin removal in the SNCR process, Sustainability 12 (2020), 1-10, doi: https//doi.org/10.3390/su12145766.

[26] Registro Estatal de Emisiones y Fuentes Contaminantes de España (PRTR). https://prtr-es.es/NOx-oxidos-de-nitrogeno,15595,11,2007.html#:~:text=Los%20%C3%B3xidos%20de%20nitr%C3%B3geno%20son,de%20nitr%C3%B3geno%20(NO2).&text=Se%20ha%20hecho%20referencia%20a,principal%20de%20los%20NOX.
Access verification: 17-03-2022.

[27] Reimann, De-NO_X technologies including a comparison of SCR and SNCR, 2002.

[28] J. Lai, I.E. Wachs, A Perspective on the Selective Catalytic Reduction (SCR) of NO with NH_3 by Supported V_2O_5-WO_3/TiO_2 Catalysts, ACS Catalysis 8 (2018), 6537-6551, doi: https//doi.org/10.1021/acscatal.8b01357.

[29] G. Busca, L. Lietti, G. Ramis, F. Berti, Chemical and mechanistic aspects of the selective catalytic reduction of NO_X by ammonia over oxide catalysts: A review, Appl. Catal. B Environ. 18 (1998), 1-36, doi: https//doi.org/10.1016/S0926-3373(98)00040-X.

[30] M. J. F. Gutierrez, D. Baxter, C. Hunter, K. Svoboda, Nitrous oxide (N_2O) emissions from waste and biomass to energy plants, Waste Manage. Res. 23 (2005), 133-147, doi: https//doi.org/10.1177/0734242X05052803.

[31] E. Finocchio, G. Busca, M. Notaro, A review of catalytic processes for the destruction of PCDD and PCDF from waste gases, Appl. Catal. B Environ. 62 (2006), 12-20, doi: https//doi.org/10.1016/j.apcatb.2005.06.010.

[32] L. Han, S. Cai, M. Gao, J. Hasegawa, P. Wang, J. Zhang, L. Shi, D. Zhang, Selective Catalytic Reduction of NO_X with NH_3 by using Novel Catalysts: State of the art and future prospects, Chem. Rev. 119 (2019), 10916-10976, doi: https//doi.org/10.1021/acs.chemrev.9b00202.

[33] JRC (IoE), NO_X and dioxin emissions from waste incineration plants, EUR 20114 EN, 2001.

[34] M. Achternbosch, U. Richers, Material flows and investment costs of flue gas cleaning systems of municipal solid waste incinerators (MSWI), Institute of municipal waste incinerator, Institute for technical chemistry Karlsruhe, Germany, FZKA (2002).

[35] O. Gohlke, T. Weber, P. Seguin, Y. Laborel, A new process for NO_X reduction in combustion systems for the generation of energy from waste, Waste Manage. 30 (2010), 1348-1354, doi: https//doi.org/10.1016/j.wasman.2010.02.024.

[36] J. Møller, B. Munk, K. Crillesen, T. H. Christensen, Life cycle assessment of selective non-catalytic reduction (SNCR) of nitrous oxides in a full-scale municipal solid waste incinerator, Waste Manage. 31 (2011), 1184-1193, doi: https//doi.org/10.1016/j.wasman.2010.12.019.

[37] Registro Estatal de Emisiones y Fuentes Contaminantes de España (PRTR). https://en.prtr-es.es/Data/images/MTD_Incineracion_residuos_ES.pdf Access verification: 17-03-2022.

[38] Registro Estatal de Emisiones y Fuentes Contaminantes de España (PRTR). https://prtr-es.es/Dioxinas-y-Furanos-PCDDPCDF,15634,11,2007.html#:~:text=Las%20dioxinas%20y%20los%20furanos,el%20m%C3%A1s%20nocivo%20de%20todos. Access verification: 17-03-2022.

[39] World Health Organization (WHO). https://www.who.int/es/news-room/fact-sheets/detail/dioxins-and-their-effects-on-human-health Access verification: 17-03-2022.

[40] X. Guo, Y. Ma, X. Lin, X. Li, Y. Xiang, A. Wu, Reduction of Polychlorinated Dibenzo-p-dioxins and Dibenzofurans by Chemical Inhibition and Physisorption from a Municipal Solid Waste Incineration System, Energy Fuels 34 (2020) doi: https//doi.org/10.1021/acs.energyfuels.0c01918.

[41] C. Du, S. Lu, Q. Wang, A. G. Buekens, M. Ni, D. P. Debecker, A review on catalytic oxidation of chloroaromatics from flue gas, Chemical Engineering Journal 334 (2018), 519-544, doi: https://doi.org/10.1016/j.cej.2017.09.018.

[42] X. Lin, M. Yan, A. Dai, M. Zhan, J. Fu, X. Li, T. Chen, S. Lu, A. Buekens, J. Yan, Simultaneous suppression of PCDD/F and NO_X during municipal solid waste incineration, Chemosphere 126 (2015), 60-66, doi: https//doi.org/10.1016/j.chemosphere.2015.02.005.

[43] E. Abad, J. Caixach, J. Rivera, Improvements in dioxin abatement strategies at a municipal waste management plant in Barcelona, Chemosphere 50 (2003), 1175-1182, doi: https//doi.org/10.1016/S0045-6535(02)00483-6.

[44] K. H. Chi, S. H. Chang, C. H. Huang, H. C. Huang, M. B. Chang, Partitioning and removal of dioxin-like congeners in flue gases treated with activated carbon adsorption, Chemosphere 64 (2006), 1489-1498, doi: https//doi.org/10.1016/j.chemosphere.2005.12.072.

[45] P. C. Hung, S. H. Chang, M. B. Chang, Removal of chlorinated aromatic organic compounds from MWI with catalytic filtration, Aerosol Air Qual. Res. 14 (2014), 1215-1222, doi: https//doi.org/10.4209/aaqr.2013.02.0041.

[46] L. Wang, W. Lee, P. Tsai, W. Lee, G. Chang-Chien, Emissions of polychlorinated dibenzo-p-dioxins and dibenzofurans from stack flue gases of sinter plants, Chemosphere 50 (2003), 1123-1129, doi: https//doi.org/10.1016/S0045-6535(02)00702-6.

[47] K. Sam-Cwan, J.S. Hwan, J. Il-Rok, K. Ki-Hun, K. Myung-Hee, K. Jae-Hyung, Y. Jun-Heung, K. Seung-Jin, Y. Jae-Cheon, J. Dong-Hee, Removal efficiencies of PCDDs/PCDFs by air pollution control devices in municipal solid waste incinerators, Chemosphere 43 (2001), 773-776, doi: https//doi.org/10.1016/S0045-6535(00)00432-X.

[48] M. Goemans, P. Clarysse, J. Joannès, P. De Clercq, S. Lenaerts, K. Matthys, K. Boels, Catalytic NO_X reduction with simultaneous dioxin and furan oxidation, Chemosphere 54 (2004), 1357-1365, doi: https//doi.org/10.1016/S0045-6535(03)00255-8.

[49] G. T. Went, L. Leu, R. Rosin, A. Bell, The effects of structure on the catalytic activity and selectivity of V_2O_5/TiO_2 for the reduction of NO by NH_3, J. Catal. 134 (1992), 492-505, doi: https//doi.org/10.1016/0021-9517(92)90337-H.

[50] G. He, Z. Lian, Y. Yu, Y. Yang, K. Liu, X. Shi, Z. Yan, W. Shan, H. He, Polymeric vanadyl species determine the low-temperature activity of V-based catalysts for the SCR of NO_X with NH_3, Sci. Adv. 4 (2018) doi: https//doi.org/10.1126/sciadv.aau4637.

[51] I. Georgiadou, C. Papadopoulou, H.K. Matralis, G.A. Voyiatzis, A. Lycourghiotis, C. Kordulis, Preparation, characterization, and catalytic properties for the SCR of NO by NH_3 of V_2O_5/TiO_2 catalysts prepared by equilibrium deposition filtration, J. Phys. Chem. B 102 (1998), 8459-8468, doi: https//doi.org/10.1021/jp973187y.

[52] L. Lietti, I. Nova, G. Ramis, L. Dall'Acqua, G. Busca, E. Giamello, P. Forzatti, F. Bregani, Characterization and reactivity of V_2O_5-MoO_3/TiO_2 De-NO_X SCR catalysts, J. Catal. 187 (1999), 419-435, doi: https//doi.org/10.1006/jcat.1999.2603.

[53] L. Lietti, I. Nova, P. Forzatti, Selective catalytic reduction (SCR) of NO by NH_3 over TiO_2-supported V_2O_5-WO_3 and V_2O_5-MoO_3 catalysts, Top. Catal. 11-12 (2000), 111-122,.

[54] L. Casagrande, L. Lietti, I. Nova, P. Forzatti, A. Baiker, SCR of NO by NH_3 over TiO_2-supported V_2O_5-MoO_3 catalysts: Reactivity and redox behavior, Appl. Catal. B Environ. 22 (1999), 63-77, doi: https//doi.org/10.1016/S0926-3373(99)00035-1.

[55] A. Marberger, M. Elsener, D. Ferri, O. Kröcher, VO_X surface coverage optimization of V_2O_5/WO_3-TiO_2 SCR catalysts by variation of the V loading and by aging, Catalysts 5 (2015), 1704-1720, doi: https//doi.org/10.3390/catal5041704.

[56] G. Ramis, L. Yi, G. Busca, Ammonia activation over catalysts for the selective catalytic reduction of NO_X and the selective catalytic oxidation of NH_3. An FT-IR study, Catalysis Today 28 (1996), 373-380, doi: https//doi.org/10.1016/S0920-5861(96)00050-8.

[57] N. Topsøe, J. A. Dumesic, H. Topsøe, Vanadia-titania catalysts for selective catalytic reduction of nitric-oxide by ammonia. II. Studies of active sites and formulation of catalytic cycles, J. Catal. 151 (1995), 241-252, doi: https//doi.org/10.1006/jcat.1995.1025.

[58] L. Chen, Z. Si, X. Wu, D. Weng, R. Ran, J. Yu, Rare earth containing catalysts for selective catalytic reduction of NO_X with ammonia: A review, J. Rare Earth 32 (2014), 907-917, doi: https//doi.org/10.1016/S1002-0721(14)60162-9.

[59] K. Cheng, J. Liu, T. Zhang, J. Li, Z. Zhao, Y. Wei, G. Jiang, A. Duan, Effect of Ce doping of TiO_2 support on NH_3-SCR activity over V_2O_5-WO_3/CeO_2-TiO_2 catalyst, J. Environ. Sci. 26 (2014), 2106-2113, doi: https//doi.org/10.1016/j.jes.2014.08.010.

[60] X. Du, X. Gao, Y. Fu, F. Gao, Z. Luo, K. Cen, The co-effect of Sb and Nb on the SCR performance of the V_2O_5/TiO_2 catalyst, J. Colloid Interface Sci. 368 (2012), 406-412, doi: https//doi.org/10.1016/j.jcis.2011.11.026.

[61] A. Shi, X. Wang, T. Yu, M. Shen, The effect of zirconia additive on the activity and structure stability of V_2O_5/WO_3-TiO_2 ammonia SCR catalysts, Appl. Catal. B Environ. 106 (2011), 359-369, doi: https//doi.org/10.1016/j.apcatb.2011.05.040.

[62] F. Kapteijn, L. Singoredjo, A. Andreini, J. A. Moulijn, Activity and selectivity of pure manganese oxides in the selective catalytic reduction of nitric oxide with ammonia, Appl. Catal. B Environ. 3 (1994), 173-189, doi: https//doi.org/10.1016/0926-3373(93)E0034-9.

[63] X. Tang, J. Li, L. Sun, J. Hao, Origination of N_2O from NO reduction by NH_3 over β-MnO_2 and α-Mn_2O_3, Applied Catalysis B: Environmental 99 (2010), 156-162, doi: https//doi.org/https://doi.org/10.1016/j.apcatb.2010.06.012.

[64] L. Singoredjo, R. Korver, F. Kapteijn, J. Moulijn, Alumina supported manganese oxides for the low-temperature selective catalytic reduction of nitric oxide with ammonia, Appl. Catal. B Environ. 1 (1992), 297-316, doi: https//doi.org/10.1016/0926-3373(92)80055-5.

[65] J. Li, J. Chen, R. Ke, C. Luo, J. Hao, Effects of precursors on the surface Mn species and the activities for NO reduction over MnO_X/TiO_2 catalysts, Catal. Commun. 8 (2007), 1896-1900, doi: https//doi.org/10.1016/j.catcom.2007.03.007.

[66] S. Zhang, B. Zhang, B. Liu, S. Sun, A review of Mn-containing oxide catalysts for low temperature selective catalytic reduction of NO_X with NH_3. Reaction mechanism and catalyst deactivation, RSC Adv. 7 (2017), 26226-26242, doi: https//doi.org/10.1039/c7ra03387g.

[67] F. Gao, X. Tang, H. Yi, S. Zhao, C. Li, J. Li, Y. Shi, X. Meng, A review on selective catalytic reduction of NO_X by NH_3 over Mn–based catalysts at low temperatures: Catalysts, mechanisms, kinetics and DFT calculations, Catalysts 7 (2017) doi: https//doi.org/10.3390/catal7070199.

[68] G. Qi, R. T. Yang, Performance and kinetics study for low-temperature SCR of NO with NH_3 over MnO_X-CeO_2 catalyst, J. Catal. 217 (2003), 434-441, doi: https//doi.org/10.1016/S0021-9517(03)00081-2.

[69] K. Qi, J. Xie, Z. Zhang, D. Fang, D. Han, X. Liu, P. Gong, F. Li, F. He, Facile large-scale synthesis of Ce–Mn composites by redox-precipitation and its superior low-temperature performance for NO removal, Powder Technol. 338 (2018), 774-782, doi: https//doi.org/10.1016/j.powtec.2018.07.073.

[70] X. Yao, K. Ma, W. Zou, S. He, J. An, F. Yang, L. Dong, Influence of preparation methods on the physicochemical properties and catalytic performance of MnO_X-CeO_2 catalysts for NH_3-SCR at low temperature, Cuihua Xuebao Chin. J. Catalysis 38 (2017), 146-159, doi: https//doi.org/10.1016/S1872-2067(16)62572-X.

[71] G. Qi, R. T. Yang, Low-temperature selective catalytic reduction of NO with NH_3 over iron and manganese oxides supported on titania, Appl. Catal. B Environ. 44 (2003), 217-225, doi: https//doi.org/10.1016/S0926-3373(03)00100-0.

[72] G. Qi, R. T. Yang, R. Chang, MnO_X-CeO_2 mixed oxides prepared by co-precipitation for selective catalytic reduction of NO with NH_3 at low temperatures, Appl. Catal. B Environ. 51 (2004), 93-106, doi: https//doi.org/10.1016/j.apcatb.2004.01.023.

[73] S. Yang, Y. Liao, S. Xiong, F. Qi, H. Dang, X. Xiao, J. Li, N_2 selectivity of NO reduction by NH_3 over MnO_X-CeO_2: Mechanism and key factors, J. Phys. Chem. C 118 (2014), 21500-21508, doi: https//doi.org/10.1021/jp5062489.

[74] Z. Liu, Y. Yi, S. Zhang, T. Zhu, J. Zhu, J. Wang, Selective catalytic reduction of NO_X with NH_3 over Mn-Ce mixed oxide catalyst at low temperatures, Catal. Today 216 (2013), 76-81, doi: https//doi.org/10.1016/j.cattod.2013.06.009.

[75] J. Lichtenberger, M. D. Amiridis, Catalytic oxidation of chlorinated benzenes over V_2O_5/TiO_2 catalysts, J. Catal. 223 (2004), 296-308, doi: https//doi.org/10.1016/j.jcat.2004.01.032.

[76] D. P. Debecker, F. Bertinchamps, N. Blangenois, P. Eloy, E. M. Gaigneaux, On the impact of the choice of model VOC in the evaluation of V-based catalysts for the total oxidation of dioxins: Furan vs. chlorobenzene, Appl. Catal. B Environ. 74 (2007), 223-232, doi: https//doi.org/10.1016/j.apcatb.2007.02.016.

[77] S. Scirè, S. Minicò, The role of the support in the oxidative destruction of chlorobenzene on Pt/zeolite catalysts: An FT-IR investigation, Catal. Lett. 91 (2003), 199-205, doi: https//doi.org/10.1023/B:CATL.0000007155.59258.83.

[78] S. Scirè, S. Minicò, C. Crisafulli, Pt catalysts supported on H-type zeolites for the catalytic combustion of chlorobenzene, Appl. Catal. B Environ. 45 (2003), 117-125, doi: https//doi.org/10.1016/S0926-3373(03)00122-X.

[79] J. Giraudon, T. B. Nguyen, G. Leclercq, S. Siffert, J. Lamonier, A. Aboukaïs, A. Vantomme, B. Su, Chlorobenzene total oxidation over palladium supported on ZrO_2, TiO_2 nanostructured supports, Catal. Today 137 (2008), 379-384, doi: https//doi.org/10.1016/j.cattod.2008.02.019.

[80] H. L. Tidahy, S. Siffert, J. Lamonier, E. A. Zhilinskaya, A. Aboukaïs, Z. Yuan, A. Vantomme, B. Su, X. Canet, G. De Weireld, M. Frère, T. B. N'Guyen, J. Giraudon, G. Leclercq, New Pd/hierarchical macro-mesoporous ZrO_2, TiO_2 and ZrO_2-TiO_2 catalysts for VOCs total oxidation, Appl. Catal. A Gen. 310 (2006), 61-69, doi: https//doi.org/10.1016/j.apcata.2006.05.020.

[81] M. S. Kamal, S. A. Razzak, M. M. Hossain, Catalytic oxidation of volatile organic compounds (VOCs): A review, Atmos. Environ. 140 (2016), 117-134, doi: https//doi.org/10.1016/j.atmosenv.2016.05.031.

[82] J. A. Martín-Martín, M. Gallastegi-Villa, M.P. González-Marcos, A. Aranzabal, J.R. González-Velasco, Bimodal effect of water on V_2O_5/TiO_2 catalysts with different vanadium species in the simultaneous NO reduction and 1,2-dichlorobenzene oxidation, Chem. Eng. J. 417 (2021) doi: https//doi.org/10.1016/j.cej.2021.129013.

[83] J. L. Graham, C. B. Almquist, S. Kumar, S. Sidhu, An investigation of nanostructured vanadia/titania catalysts for the oxidation of monochlorobenzene, Catal. Today 88 (2003), 73-82, doi: https//doi.org/10.1016/j.cattod.2003.08.008.

[84] B. Schimmoeller, R. Delaigle, D. P. Debecker, E. M. Gaigneaux, Flame-made vs. wet-impregnated vanadia/titania in the total oxidation of chlorobenzene: Possible role of VO_X species, Catal. Today 157 (2010), 198-203, doi: https//doi.org/10.1016/j.cattod.2010.01.029.

[85] R. Weber, T. Sakurai, H. Hagenmaier, Low temperature decomposition of PCDD/PCDF, chlorobenzenes and PAHs by TiO_2-based V_2O_5-WO_3 catalysts, Appl. Catal. B Environ. 20 (1999), 249-256, doi: https//doi.org/10.1016/S0926-3373(98)00115-5.

[86] P. Liljelind, J. Unsworth, O. Maaskant, S. Marklund, Removal of dioxins and related aromatic hydrocarbons from flue gas streams by adsorption and catalytic destruction, Chemosphere 42 (2001), 615-623, doi: https//doi.org/10.1016/S0045-6535(00)00235-6.

[87] J. Corella, J. M. Toledo, A. M. Padilla, On the selection of the catalyst among the commercial platinum-based ones for total oxidation of some chlorinated hydrocarbons, Appl. Catal. B Environ. 27 (2000), 243-256, doi: https//doi.org/10.1016/S0926-3373(00)00154-5.

[88] C. Cho, S. Ihm, Development of new vanadium-based oxide catalysts for decomposition of chlorinated aromatic pollutants, Environmental Science and Technology 36 (2002), 1600-1606, doi: https//doi.org/10.1021/es015687h.

[89] A. R. Gandhe, J. S. Rebello, J. L. Figueiredo, J. B. Fernandes, Manganese oxide OMS-2 as an effective catalyst for total oxidation of ethyl acetate, Appl. Catal. B Environ. 72 (2007), 129-135, doi: https//doi.org/10.1016/j.apcatb.2006.10.017.

[90] Y. Liu, M. Luo, Z. Wei, Q. Xin, P. Ying, C. Li, Catalytic oxidation of chlorobenzene on supported manganese oxide catalysts, Appl. Catal. B Environ. 29 (2001), 61-67, doi: https//doi.org/10.1016/S0926-3373(00)00193-4.

[91] W. Tian, X. Fan, H. Yang, X. Zhang, Preparation of MnO_X/TiO_2 composites and their properties for catalytic oxidation of chlorobenzene, J. Hazard. Mater. 177 (2010), 887-891, doi: https//doi.org/10.1016/j.jhazmat.2009.12.116.

[92] M. R. Morales, B. P. Barbero, L. E. Cadús, Total oxidation of ethanol and propane over Mn-Cu mixed oxide catalysts, Appl. Catal. B Environ. 67 (2006), 229-236, doi: https//doi.org/10.1016/j.apcatb.2006.05.006.

[93] W. Tang, X. Wu, S. Li, W. Li, Y. Chen, Porous Mn-Co mixed oxide nanorod as a novel catalyst with enhanced catalytic activity for removal of VOCs, Catal. Commun. 56 (2014), 134-138, doi: https//doi.org/10.1016/j.catcom.2014.07.023.

[94] G. Picasso, M. Gutiérrez, M.P. Pina, J. Herguido, Preparation and characterization of Ce-Zr and Ce-Mn based oxides for n-hexane combustion: Application to catalytic membrane reactors, Chem. Eng. J. 126 (2007), 119-130, doi: https//doi.org/10.1016/j.cej.2006.09.005.

[95] H. Chen, A. Sayari, A. Adnot, F. Larachi, Composition-activity effects of Mn-Ce-O composites on phenol catalytic wet oxidation, Appl. Catal. B Environ. 32 (2001), 195-204, doi: https//doi.org/10.1016/S0926-3373(01)00136-9.

[96] D. Delimaris, T. Ioannides, VOC oxidation over MnO_X-CeO_2 catalysts prepared by a combustion method, Appl. Catal. B Environ. 84 (2008), 303-312, doi: https//doi.org/10.1016/j.apcatb.2008.04.006.

[97] H. Li, G. Lu, Q. Dai, Y. Wang, Y. Guo, Y. Guo, Efficient low-temperature catalytic combustion of trichloroethylene over flower-like mesoporous Mn-doped CeO_2 microspheres, Appl. Catal. B Environ. 102 (2011), 475-483, doi: https//doi.org/10.1016/j.apcatb.2010.12.029.

[98] X. Wang, L. Ran, Y. Dai, Y. Lu, Q. Dai, Removal of Cl adsorbed on Mn-Ce-La solid solution catalysts during CVOC combustion, J. Colloid Interface Sci. 426 (2014), 324-332, doi: https//doi.org/10.1016/j.jcis.2013.10.007.

[99] X. Liu, J. Wang, X. Wang, T. Zhu, Simultaneous removal of PCDD/Fs and NO_X from the flue gas of a municipal solid waste incinerator with a pilot plant, Chemosphere 133 (2015), 90-96, doi: https//doi.org/10.1016/j.chemosphere.2015.04.009.

[100] D. P. Debecker, R. Delaigle, P. C. Hung, A. Buekens, E. M. Gaigneaux, M. B. Chang, Evaluation of PCDD/F oxidation catalysts: Confronting studies on model molecules with tests on PCDD/F-containing gas stream, Chemosphere 82 (2011), 1337-1342, doi: https//doi.org/10.1016/j.chemosphere.2010.12.007.

[101] J. Jones, J. R. H. Ross, The development of supported vanadia catalysts for the combined catalytic removal of the oxides of nitrogen and of chlorinated hydrocarbons from flue gases, Catal. Today 35 (1997), 97-105, doi: https//doi.org/10.1016/S0920-5861(96)00148-4.

[102] G. Busca, M. Baldi, C. Pistarino, J. M. Gallardo Amores, V. Sanchez Escribano, E. Finocchio, G. Romezzano, F. Bregani, G. P. Toledo, Evaluation of V_2O_5-WO_3-TiO_2 and alternative SCR catalysts in the abatement of VOCs, Catal. Today 53 (1999), 525-533, doi: https//doi.org/10.1016/S0920-5861(99)00140-6.

[103] E. Finocchio, M. Baldi, G. Busca, C. Pistarino, G. Romezzano, F. Bregani, G. P. Toledo, Study of the abatement of VOC over V_2O_5-WO_3-TiO_2 and alternative SCR catalysts, Catal. Today 59 (2000), 261-268, doi: https//doi.org/10.1016/S0920-5861(00)00292-3.

[104] M. A. Larrubia, G. Busca, An FT-IR study of the conversion of 2-chloropropane, o-dichlorobenzene and dibenzofuran on V_2O_5 -MoO_3-TiO_2 SCR-deNOx catalysts, Appl. Catal. B Environ. 39 (2002), 343-352, doi: https//doi.org/10.1016/S0926-3373(02)00116-9.

[105] S. Krishnamoorthy, J. P. Baker, M. D. Amiridis, Catalytic oxidation of 1,2-dichlorobenzene over V_2O_5/TiO_2-based catalysts, Catalysis Today 40 (1998), 39-46, doi: https://doi.org/10.1016/S0920-5861(97)00117-X.

[106] S. Krishnamoorthy, M. D. Amiridis, Kinetic and in situ FTIR studies of the catalytic oxidation of 1,2-dichlorobenzene over V_2O_5/Al_2O_3 catalysts, Catal. Today 51 (1999), 203-214, doi: https//doi.org/10.1016/S0920-5861(99)00045-0.

[107] S. Krishnamoorthy, J. A. Rivas, M. D. Amiridis, Catalytic Oxidation of 1,2-Dichlorobenzene over Supported Transition Metal Oxides, Journal of Catalysis 193 (2000), 264-272, doi: https//doi.org/10.1006/jcat.2000.2895.

[108] K. Poplawski, J. Lichtenberger, F. J. Keil, K. Schnitzlein, M. D. Amiridis, Catalytic oxidation of 1,2-dichlorobenzene over ABO_3-type perovskites, Catalysis Today 62 (2000), 329-336, doi: https//doi.org/10.1016/S0920-5861(00)00434-X.

[109] C. E. Hetrick, F. Patcas, M. D. Amiridis, Effect of water on the oxidation of dichlorobenzene over V_2O_5/TiO_2 catalysts, Appl. Catal. B Environ. 101 (2011), 622-628, doi: https//doi.org/10.1016/j.apcatb.2010.11.003.

[110] S. Lomnicki, J. Lichtenberger, Z. Xu, M. Waters, J. Kosman, M. D. Amiridis, Catalytic oxidation of 2,4,6-trichlorophenol over vanadia/titania-based catalysts, Applied Catalysis B: Environmental 46 (2003), 105-119, doi: https//doi.org/10.1016/S0926-3373(03)00215-7.

[111] C. E. Hetrick, J. Lichtenberger, M. D. Amiridis, Catalytic oxidation of chlorophenol over V_2O_5/TiO_2 catalysts, Appl. Catal. B Environ. 77 (2008), 255-263, doi: https//doi.org/10.1016/j.apcatb.2007.07.022.

[112] S. Albonetti, G. Baldi, A. Barzanti, A. L. Costa, J. E. Mengou, F. Trifirò, A. Vaccari, Chlorinated organics total oxidation over V_2O_5/TiO_2 catalysts prepared by polyol-mediated synthesis, Appl. Catal. A Gen. 325 (2007), 309-315, doi: https//doi.org/10.1016/j.apcata.2007.02.031.

[113] D. P. Debecker, K. Bouchmella, R. Delaigle, P. Eloy, C. Poleunis, P. Bertrand, E. M. Gaigneaux, P. H. Mutin, One-step non-hydrolytic sol-gel preparation of efficient V_2O_5-TiO_2 catalysts for VOC total oxidation, Appl. Catal. B Environ. 94 (2010), 38-45, doi: https//doi.org/10.1016/j.apcatb.2009.10.018.

[114] D. P. Debecker, R. Delaigle, K. Bouchmella, P. Eloy, E. M. Gaigneaux, P. H. Mutin, Total oxidation of benzene and chlorobenzene with MoO_3 and WO_3 promoted V_2O_5/TiO_2 catalysts prepared by a nonhydrolytic sol-gel route, Catal. Today 157 (2010), 125-130, doi: https//doi.org/10.1016/j.cattod.2010.02.010.

[115] F. Bertinchamps, M. Treinen, N. Blangenois, E. Mariage, E. M. Gaigneaux, Positive effect of NO_X on the performances of VO_X/TiO_2-based catalysts in the total oxidation abatement of chlorobenzene, J. Catal. 230 (2005), 493-498, doi: https//doi.org/10.1016/j.jcat.2005.01.009.

[116] F. Bertinchamps, M. Treinen, P. Eloy, A. Dos Santos, M. M. Mestdagh, E. M. Gaigneaux, Understanding the activation mechanism induced by NO_X on the performances of VO_X/TiO_2 based catalysts in the total oxidation of chlorinated VOCs, Appl. Catal. B Environ. 70 (2007), 360-369, doi: https//doi.org/10.1016/j.apcatb.2005.11.022.

[117] M. Gallastegi-Villa, A. Aranzabal, Z. Boukha, J. A. González-Marcos, J. R. González-Velasco, M. V. Martínez-Huerta, M. A. Bañares, Role of surface vanadium oxide coverage support on titania for the simultaneous removal of o-dichlorobenzene and NO_X from waste incinerator flue gas, Catal. Today 254 (2015), 2-11, doi: https//doi.org/10.1016/j.cattod.2015.02.029.

[118] M. Gallastegi-Villa, A. Aranzabal, J. A. González-Marcos, J. R. González-Velasco, Tailoring dual redox-acid functionalities in VO_X/TiO_2/ZSM5 catalyst for simultaneous abatement of PCDD/Fs and NO_X from municipal solid waste incineration, Appl. Catal. B Environ. 205 (2017), 310-318, doi: https//doi.org/10.1016/j.apcatb.2016.12.020.

[119] M. Gallastegi-Villa, $VO_X/WO_X/TiO_2$ and alternative catalysts for the simultaneous abatement of NO_X and PCDD/Fs from MWS treatment plants, 2016.

[120] F. Izquierdo, M. S. Goberna Selca, C. E., Técnicas de análisis y caracterización de materiales, 2º ed. rev. y aum. ed. ed., CSIC, Madrid, 2019.

[121] S. Brunauer, L. S. Deming, W. E. Deming, E. Teller, On a theory of the van der Waals Adsorption of Gases, J. Am. Chem. Soc. 62 (1940), 1723-1732, doi: https//doi.org/10.1021/ja01864a025.

[122] S. Brunauer, P. H. Emmett, E. Teller, Adsorption of Gases in Multimolecular Layers, J. Am. Chem. Soc. 60 (1938), 309-319, doi: https//doi.org/10.1021/ja01269a023.

[123] E. P. Barrett, L. G. Joyner, P. P. Halenda, The determination of pore volume and area Distributions in porous substances. I. Computations from nitrogen isotherms, J. Am. Chem. Soc. 73 (1951), 373-380, doi: https//doi.org/10.1021/ja01145a126.

[124] J. H. de Boer, B. G. Linsen, T. J. Osinga, Studies on pore systems in catalysts. VI. The universal t curve, J. Catal. 4 (1965), 643-648, doi: https//doi.org/10.1016/0021-9517(65)90263-0.

[125] R. López Fonseca, Zeolitas protónicas (H-Y, H-ZSM5 y H-MOR) para la destrucción catalítica de compuestos orgánicos volátiles clorados, 2001.

[126] I. E. Wachs, In situ Raman spectroscopy studies of catalysts, Top. Catal. 8 (1999), 57-63, doi: https//doi.org/10.1023/a:1019100925300.

[127] M. Fadoni, L. Lucarelli, Temperature programmed desorption, reduction, oxidation and flow chemisorption for the characterisation of heterogeneous catalysts. Theoretical aspects, instrumentation and applications, Stud. Surf. Sci. Catal. 120 A (1999) 49, doi: https//doi.org/10.1016/s0167-2991(99)80553-9

[128] H. Knozinger, Handbook of Heterogeneous catalysis, Vol 2º ed., 1997.

[129] G. Busca, Spectroscopic characterization of the acid properties of metal oxide catalysts, Catal. Today 41 (1998), 191-206, doi: https//doi.org/10.1016/S0920-5861(98)00049-2.

[130] A. Bassetti, M. Bodini, M. Donega, R. Miglio, W. Tirler, G. Voto, Dioxin and NO_X low temperature catalytic degradation, Organohalogen Compd. (2001), 98-101.

[131] S. Albonetti, S. Blasioli, R. Bonelli, J. E. Mengou, S. Scirè, F. Trifirò, The role of acidity in the decomposition of 1,2-dichlorobenzene over TiO_2-based V_2O_5/WO_3 catalysts, Appl. Catal. A: Gen. 341 (2008), 18-25, doi: https//doi.org/10.1016/j.apcata.2007.12.033.

[132] Q. Wang, X. Huang, Y. Feng, J. Zhou, H. Shi, J. Jin, Interaction Mechanism Study on Simultaneous Removal of 1,2-Dichlorobenzene and NO over MnO_X-CeO_2/TiO_2 Catalysts at Low Temperatures, Ind. Eng. Chem. Res. 60 (2021), 4820-4830, doi: https//doi.org/10.1021/acs.iecr.0c05862.

[133] P. Andrigo, R. Bagatin, G. Pagani, Fixed bed reactors, Catal. Today 52 (1999), 197-221, doi: https//doi.org/10.1016/S0920-5861(99)00076-0.

[134] R. J. Berger, J. Pérez-Ramírez, F. Kapteijn, J. A. Moulijn, Catalyst performance testing: The influence of catalyst bed dilution on the conversion observed, Chem. Eng. J. 90 (2002), 173-183, doi: https//doi.org/10.1016/S1385-8947(02)00078-5.

[135] E. N. Fuller, P. D. Schettler, J. C. Giddings, A new method for prediction of binary gas-phase diffusion coefficients, Ind. Eng. Chem. 58 (1966), 18-27, doi: https//doi.org/10.1021/ie50677a007.

[136] M. Punčochář, J. Drahoš, The tortuosity concept in fixed and fluidized bed, Chem. Eng. Sci. 48 (1993), 2173-2175, doi: https//doi.org/10.1016/0009-2509(93)80092-5.

[137] F. Bertinchamps, C. Grégoire, E.M. Gaigneaux, Systematic investigation of supported transition metal oxide based formulations for the catalytic oxidative elimination of (chloro)-aromatics: Part I: Identification of the optimal main active phases and supports, Applied Catalysis B: Environmental 66 (2006), 1-9, doi: https//doi.org/https://doi.org/10.1016/j.apcatb.2006.02.011.

[138] S. Ramana, B. G. Rao, P. Venkataswamy, A. Rangaswamy, B. M. Reddy, Nanostructured Mn-doped ceria solid solutions for efficient oxidation of vanillyl alcohol, J. Mol. Catal. A Chem. 415 (2016), 113-121, doi: https//doi.org/10.1016/j.molcata.2016.01.028.

[139] X. Du, D. Zhang, L. Shi, R. Gao, J. Zhang, Morphology dependence of catalytic properties of Ni/CeO_2 nanostructures for carbon dioxide reforming of methane, J. Phys. Chem. C 116 (2012), 10009-10016, doi: https//doi.org/10.1021/jp300543r.

[140] C. Tang, J. Li, X. Yao, J. Sun, Y. Cao, L. Zhang, F. Gao, Y. Deng, L. Dong, Mesoporous NiO-CeO_2 catalysts for CO oxidation: Nickel content effect and mechanism aspect, Appl. Catal. A Gen. 494 (2015), 77-86, doi: https//doi.org/10.1016/j.apcata.2015.01.037.

[141] C. M. Julien, M. Massot, C. Poinsignon, Lattice vibrations of manganese oxides: Part I. Periodic structures, Spectrochim. Acta Part A Mol. Biomol. Spectrosc. 60 (2004), 689-700, doi: https//doi.org/10.1016/S1386-1425(03)00279-8.

[142] P. Venkataswamy, D. Jampaiah, C. U. Aniz, B. M. Reddy, Investigation of physicochemical properties and catalytic activity of nanostructured $Ce_{0.7}M_{0.3}O_2$ (M = Mn, Fe, Co) solid solutions for CO oxidation, J. Chem. Sci. 127 (2015), 1347-1360, doi: https//doi.org/10.1007/s12039-015-0897-8.

[143] J. C. Groen, L. A. A. Peffer, J. Pérez-Ramírez, Pore size determination in modified micro and mesoporous materials. Pitfalls and limitations in gas adsorption data analysis, Microporous Mesoporous Mater. 60 (2003), 1-17, doi: https//doi.org/10.1016/S1387-1811(03)00339-1.

[144] E. R. Stobbe, B. A. De Boer, J. W. Geus, The reduction and oxidation behaviour of manganese oxides, Catal. Today 47 (1999), 161-167, doi: https//doi.org/10.1016/S0920-5861(98)00296-X.

[145] W. Xingyi, K. Qian, L. Dao, Catalytic combustion of chlorobenzene over MnO_X-CeO_2 mixed oxide catalysts, Appl. Catal. B Environ. 86 (2009), 166-175, doi: https//doi.org/10.1016/j.apcatb.2008.08.009.

[146] Q. Shen, L. Zhang, N. Sun, H. Wang, L. Zhong, C. He, W. Wei, Y. Sun, Hollow MnO_X-CeO_2 mixed oxides as highly efficient catalysts in NO oxidation, Chem. Eng. J. 322 (2017), 46-55, doi: https//doi.org/10.1016/j.cej.2017.02.148.

[147] Z. Wu, N. Tang, L. Xiao, Y. Liu, H. Wang, MnO_X/TiO_2 composite nanoxides synthesized by deposition-precipitation method as a superior catalyst for NO oxidation, J. Colloid Interface Sci. 352 (2010), 143-148, doi: https//doi.org/10.1016/j.jcis.2010.08.031.

[148] S. Ren, J. Yang, T. Zhang, L. Jiang, H. Long, F. Guo, M. Kong, Role of cerium in improving NO reduction with NH_3 over Mn–Ce/ASC catalyst in low-temperature flue gas, Chem. Eng. Res. Des. 133 (2018), 1-10, doi: https//doi.org/10.1016/j.cherd.2018.02.041.

[149] C. Wang, F. Yu, M. Zhu, C. Tang, K. Zhang, D. Zhao, L. Dong, B. Dai, Highly selective catalytic reduction of NO_X by MnO_X–CeO_2–Al_2O_3 catalysts prepared by self-propagating high-temperature synthesis, J. Environ. Sci. 75 (2019), 124-135, doi: https//doi.org/10.1016/j.jes.2018.03.011.

[150] Q. Ye, B. Xu, Textural and structure characterizations of $Ce_{1-x}Mn_xO_2$ prepared by citric acid sol-gel method, Acta Phys. Chim. Sin. 22 (2006), 345-349.

[151] V. Sánchez Escribano, E. Fernández López, M. Panizza, C. Resini, J. M. Gallardo Amores, G. Busca, Characterization of cubic ceria-zirconia powders by X-ray diffraction and vibrational and electronic spectroscopy, Solid State Sci. 5 (2003), 1369-1376, doi: https//doi.org/10.1016/j.solidstatesciences.2003.07.001.

[152] I. Ambat, V. Srivastava, E. Haapaniemi, M. Sillanpää, Nano-magnetic potassium impregnated ceria as catalyst for the biodiesel production, Renew. Energy 139 (2019), 1428-1436, doi: https//doi.org/10.1016/j.renene.2019.03.042.

[153] J. T. Philip, C. P. Koshy, M. D. Mathew, Advanced characterization of precipitation synthesized ceria and ceria-zirconia hybrid nanoparticles, Mater. Res. Express 6 (2019) doi: https//doi.org/10.1088/2053-1591/ab4fd5.

[154] Y. Dai, X. Wang, Q. Dai, D. Li, Effect of Ce and La on the structure and activity of MnO_X catalyst in catalytic combustion of chlorobenzene, Appl. Catal. B Environ. 111-112 (2012), 141-149, doi: https//doi.org/10.1016/j.apcatb.2011.09.028.

[155] S. Ponce, M. A. Peña, J. L. G. Fierro, Surface properties and catalytic performance in methane combustion of SR-substituted lanthanum manganites, Appl. Catal. B Environ. 24 (2000), 193-205, doi: https//doi.org/10.1016/S0926-3373(99)00111-3.

[156] J. Chen, M. Shen, X. Wang, G. Qi, J. Wang, W. Li, The influence of nonstoichiometry on $LaMnO_3$ perovskite for catalytic NO oxidation, Appl. Catal. B Environ. 134-135 (2013), 251-257, doi: https//doi.org/10.1016/j.apcatb.2013.01.027.

[157] Y. Wang, X. Li, L. Zhan, C. Li, W. Qiao, L. Ling, Effect of SO_2 on activated carbon honeycomb supported CeO_2-MnO_X catalyst for NO removal at low temperature, Ind. Eng. Chem. Res. 54 (2015), 2274-2278, doi: https//doi.org/10.1021/ie504074h.

[158] M. D. H. Chowdhury, J. G. Um, J. Jang, Remarkable changes in interface O vacancy and metal-oxide bonds in amorphous indium-gallium-zinc-oxide thin-film transistors by long time annealing at 250°C, Appl. Phys. Lett. 105 (2014) doi: https//doi.org/10.1063/1.4903874.

[159] C. Bozo, N. Guilhaume, J. Herrmann, Role of the ceria-zirconia support in the reactivity of platinum and palladium catalysts for methane total oxidation under lean conditions, J. Catal. 203 (2001), 393-406, doi: https//doi.org/10.1006/jcat.2001.3320.

[160] F. Saad, J. D. Comparot, R. Brahmi, M. Bensitel, L. Pirault-Roy, Influence of acid-base properties of the support on the catalytic performances of Pt-based catalysts in a gas-phase hydrogenation of acetonitrile, Appl. Catal. A Gen. 544 (2017), 1-9, doi: https//doi.org/10.1016/j.apcata.2017.06.038.

[161] C. Ravindra Reddy, G. Nagendrappa, B. S. Jai Prakash, Surface acidity study of Mn-montmorillonite clay catalysts by FT-IR spectroscopy: Correlation with esterification activity, Catal. Commun. 8 (2007), 241-246, doi: https//doi.org/10.1016/j.catcom.2006.06.023.

[162] C. Binet, M. Daturi, J. Lavalley, IR study of polycrystalline ceria properties in oxidised and reduced states, Catal. Today 50 (1999), 207-225, doi: https//doi.org/10.1016/S0920-5861(98)00504-5.

[163] E. Finocchio, G. Busca, Characterization and hydrocarbon oxidation activity of coprecipitated mixed oxides Mn_3O_4/Al_2O_3, Catal. Today 70 (2001), 213-225, doi: https//doi.org/10.1016/S0920-5861(01)00419-9.

[164] H. A. Prescott, Z. Li, E. Kemnitz, A. Trunschke, J. Deutsch, H. Lieske, A. Auroux, Application of calcined Mg-Al hydrotalcites for Michael additions: An investigation of catalytic activity and acid-base properties, J. Catal. 234 (2005), 119-130, doi: https//doi.org/10.1016/j.jcat.2005.06.004.

[165] T. S. Park, S. K. Jeong, S. H. Hong, S. C. Hong, Selective catalytic reduction of nitrogen oxides with NH_3 over natural manganese at low temperature, Ind. Eng. Chem. Res. 40 (2001), 4491-4495, doi: https//doi.org/10.1021/ie010218+.

[166] X. Tang, J. Hao, W. Xu, J. Li, Low temperature selective catalytic reduction of NO_X with NH_3 over amorphous MnO_X catalysts prepared by three methods, Catal. Commun. 8 (2007), 329-334, doi: https//doi.org/10.1016/j.catcom.2006.06.025.

[167] M. Kang, E. D. Park, J. M. Kim, J. E. Yie, Cu-Mn mixed oxides for low temperature NO reduction with NH_3, Catal. Today 111 (2006), 236-241, doi: https//doi.org/10.1016/j.cattod.2005.10.032.

[168] M. Kang, E. D. Park, J. M. Kim, J. E. Yie, Manganese oxide catalysts for NO_X reduction with NH_3 at low temperatures, Appl. Catal. A Gen. 327 (2007), 261-269, doi: https//doi.org/10.1016/j.apcata.2007.05.024.

[169] Z. Pu, H. Zhou, Y. Zheng, W. Huang, X. Li, Enhanced methane combustion over Co_3O_4 catalysts prepared by a facile precipitation method: Effect of aging time, Appl. Surf. Sci. 410 (2017), 14-21, doi: https//doi.org/10.1016/j.apsusc.2017.02.186.

[170] M. Aghazadeh, Electrochemical preparation and characterization of Mn_5O_8 nanostructures, J. Nanostructures 8 (2018), 67-74, doi: https//doi.org/10.22052/JNS.2018.01.008.

[171] F. Milella, J. M. Gallardo-Amores, M. Baldi, G. Busca, A study of Mn-Ti oxide powders and their behaviour in propane oxidation catalysis, J. Mater. Chem. 8 (1998) 2525-2531, doi: https//doi.org/10.1039/a803994a

[172] G. Wu, Y. Gao, F. Ma, B. Zheng, L. Liu, H. Sun, W. Wu, Catalytic oxidation of benzyl alcohol over manganese oxide supported on MCM-41 zeolite, Chem. Eng. J. 271 (2015), 14-22, doi: https//doi.org/10.1016/j.cej.2015.01.119.

[173] E. Fernández López, V. Sánchez Escribano, J. M. Gallardo-Amores, C. Resini, G. Busca, Structural and morphological characterization of Mn-Zr mixed oxides prepared by a sol-gel method, Solid State Sci. 4 (2002) 951-961, doi: https//doi.org/10.1016/S1293-2558(02)01350-X.

[174] H. Wan, D. Li, Y. Dai, Y. Hu, B. Liu, L. Dong, Catalytic behaviors of CuO supported on Mn_2O_3 modified γ-Al_2O_3 for NO reduction by CO, J. Mol. Catal. A Chem. 332 (2010), 32-44, doi: https//doi.org/10.1016/j.molcata.2010.08.016.

[175] A. Choya, B. de Rivas, J. I. Gutiérrez-Ortiz, R. López-Fonseca, Effect of residual Na^+ on the combustion of methane over Co_3O_4 bulk catalysts prepared by precipitation, Catalysts 8 (2018) doi: https//doi.org/10.3390/catal8100427.

[176] J. Li, H. Chang, L. Ma, J. Hao, R. T. Yang, Low-temperature selective catalytic reduction of NO_X with NH_3 over metal oxide and zeolite catalysts. A review, Catal. Today. 175 (2011), 147-156, doi: https//doi.org/10.1016/j.cattod.2011.03.034.

[177] C. Li, M. Shen, J. Wang, J. Wang, Y. Zhai, New Insights into the Role of WO_3 in Improved Activity and Ammonium Bisulfate Resistance for NO Reduction with NH_3 over V-W/Ce/Ti Catalyst, Ind. Eng. Chem. Res. 57 (2018), 8424-8435, doi: https//doi.org/10.1021/acs.iecr.8b01031.

[178] C. Yu, B. Huang, L. Dong, F. Chen, X. Liu, In situ FT-IR study of highly dispersed MnO_X/SAPO-34 catalyst for low-temperature selective catalytic reduction of NO_X by NH_3, Catal. Today 281 (2017) 610-620, doi: https//doi.org/10.1016/j.cattod.2016.06.025

[179] F. Lin, Q. Wang, J. Zhang, J. Jin, S. Lu, J. Yan, Mechanism and Kinetics Study on Low-Temperature NH_3-SCR over Manganese-Cerium Composite Oxide Catalysts, Ind. Eng. Chem. Res. 58 (2019), 22763-22770, doi: https//doi.org/10.1021/acs.iecr.9b04780.

[180] S. Yang, C. Wang, J. Li, N. Yan, L. Ma, H. Chang, Low temperature selective catalytic reduction of NO with NH_3 over Mn-Fe spinel: Performance, mechanism and kinetic study, Appl. Catal. B Environ. 110 (2011), 71-80, doi: https//doi.org/10.1016/j.apcatb.2011.08.027.

[181] M. Casapu, O. Kröcher, M. Mehring, M. Nachtegaal, C. Borca, M. Harfouche, D. Grolimund, Characterization of Nb-containing MnO_X-CeO_2 catalyst for low-temperature selective catalytic reduction of NO with NH_3, J. Phys. Chem. C 114 (2010), 9791-9801, doi: https//doi.org/10.1021/jp911861q.

[182] Z. Kong, C. Wang, Z. Ding, Y. Chen, Z. Zhang, Enhanced activity of $Mn_XW_{0.05}Ti_{0.95-X}O_2$ for selective catalytic reduction of NO_X with ammonia by self-propagating high-temperature synthesis, Catal. Commun. 64 (2015), 27-31, doi: https//doi.org/10.1016/j.catcom.2015.01.028.

[183] M. Wu, X. Wang, Q. Dai, Y. Gu, D. Li, Low temperature catalytic combustion of chlorobenzene over Mn-Ce-O/γ-Al_2O_3 mixed oxides catalyst, Catal. Today 158 (2010), 336-342, doi: https//doi.org/10.1016/j.cattod.2010.04.006.

[184] J. R. González-Velasco, J. A. Botas, J. A. González-Marcos, M. A. Gutiérrez-Ortiz, Influence of water and hydrocarbon processed in feedstream on the three-way behaviour of platinum-alumina catalysts, Appl. Catal. B Environ. 12 (1997), 61-79, doi: https//doi.org/10.1016/S0926-3373(96)00058-6.

[185] A. Buzková Arvajová, J. Březina, R. Pečinka, P. Kočí, Modeling of two-step CO oxidation light-off on Pt/Γ-Al_2O_3 in the presence of C_3H_6 and NO_X, Appl. Catal. B Environ. 233 (2018), 167-174, doi: https//doi.org/10.1016/j.apcatb.2018.03.081.

[186] J. Brunet, E. Genty, C. Barroo, F. Cazier, C. Poupin, S. Siffert, D. Thomas, G. De Weireld, T.V. de Bocarmé, R. Cousin, The CoAlCeO mixed oxide: An alternative to palladium-based catalysts for total oxidation of industrial VOCs, Catalysts 8 (2018) doi: https//doi.org/10.3390/catal8020064.

[187] Z. Xu, S. Deng, Y. Yang, T. Zhang, Q. Cao, J. Huang, G. Yu, Catalytic destruction of pentachlorobenzene in simulated flue gas by a V_2O_5-WO_3/TiO_2 catalyst, Chemosphere 87 (2012), 1032-1038, doi: https//doi.org/10.1016/j.chemosphere.2012.01.004.

[188] B. Yang, Q. Jin, Q. Huang, M. Chen, L. Xu, Y. Shen, H. Xu, S. Zhu, X. Li, Synergetic catalytic removal of chlorobenzene and NO_X from waste incineration exhaust over $MnNb_{0.4}Ce_{0.2}O_X$ catalysts: Performance and mechanism study, J. Rare Earth 38 (2020), 1178-1189, doi: https//doi.org/10.1016/j.jre.2020.06.013.

[189] L. Gan, W. Shi, K. Li, J. Chen, Y. Peng, J. Li, Synergistic Promotion Effect between NO_X and Chlorobenzene Removal on MnO_X-CeO_2 Catalyst, ACS Appl. Mater. Interfaces 10 (2018), 30426-30432, doi: https//doi.org/10.1021/acsami.8b10636.

[190] Q. Jin, Z. Xue, X. Zhi, W. Ji, Y. Shen, Y. Zeng, Catalytic removal of NO and chlorobenzene over Ce-Mn-W-Zr-O_X/TiO_2: Performance study of hollow spheres effect, Fuel 305 (2021), doi: https//doi.org/10.1016/j.fuel.2021.121534.

[191] Q. Wang, P. C. Hung, S. Lu, M. B. Chang, Catalytic decomposition of gaseous PCDD/Fs over V_2O_5/TiO_2-CNTs catalyst: Effect of NO and NH_3 addition, Chemosphere 159 (2016), 132-137, doi: https//doi.org/10.1016/j.chemosphere.2016.05.072.

[192] M. D. Amiridis, I. E. Wachs, G. Deo, J. Jehng, D. S. Kim, Reactivity of V_2O_5 catalysts for the selective catalytic reduction of NO by NH_3: Influence of vanadia loading, H_2O, and SO_2, J. Catal. 161 (1996), 247-253, doi: https//doi.org/10.1006/jcat.1996.0182.

[193] Z. Huang, Z. Liu, X. Zhang, Q. Liu, Inhibition effect of H_2O on V_2O_5/AC catalyst for catalytic reduction of NO with NH_3 at low temperature, Appl. Catal. B: Environmental 63 (2006), 260-265, doi: https//doi.org/10.1016/j.apcatb.2005.10.011.

[194] X. You, Z. Sheng, D. Yu, L. Yang, X. Xiao, S. Wang, Influence of Mn/Ce ratio on the physicochemical properties and catalytic performance of graphene supported MnO_X-CeO_2 oxides for NH_3-SCR at low temperature, Appl. Surf. Sci. 423 (2017), 845-854, doi: https//doi.org/10.1016/j.apsusc.2017.06.226.

[195] M. Gallastegi-Villa, A. Aranzabal, M. Romero-Sáez, J. A. González-Marcos, J. R. González-Velasco, Catalytic activity of regenerated catalyst after the oxidation of 1,2-dichloroethane and trichloroethylene, Chem. Eng. J. 241 (2014), 200-206, doi: https//doi.org/10.1016/j.cej.2013.12.008.

[196] J. R. González-Velasco, A. Aranzabal, R. López-Fonseca, R. Ferret, J. A. González-Marcos, Enhancement of the catalytic oxidation of hydrogen-lean chlorinated VOCs in the presence of hydrogen-supplying compounds, Applied Catalysis B: Environmental 24 (2000), 33-43, doi: https//doi.org/10.1016/S0926-3373(99)00087-9.

[197] V. Sanchez Escribano, G. Garbarino, E. Finocchio, G. Busca, γ-Alumina and Amorphous Silica–Alumina: Structural Features, acid Sites and the role of Adsorbed water, Top. Catal. 60 (2017), 1554-1564, doi: https//doi.org/10.1007/s11244-017-0838-5.

[198] X. Yu, X. Wu, Z. Chen, Z. Huang, G. Jing, Oxygen vacancy defect engineering in Mn-doped CeO_2 nanostructures for nitrogen oxides emission abatement, Mol. Cat. 476 (2019) doi: https//doi.org/10.1016/j.mcat.2019.110512.

[199] L. Xu, X. Li, M. Crocker, Z. Zhang, A. Zhu, C. Shi, A study of the mechanism of low-temperature SCR of NO with NH_3 on MnO_X/CeO_2, J. Mol. Catal. A Chem. 378 (2013), 82-90, doi: https//doi.org/10.1016/j.molcata.2013.05.021.

[200] M. Kantcheva, A. Agiral, O. Samarskaya, M. Stranzenbach, B. Saruhan, Characterization of $LaMnAl_{11}O_{19}$ by FT-IR spectroscopy of adsorbed NO and NO/O 2, Appl. Surf. Sci. 252 (2005), 1481-1491, doi: https//doi.org/10.1016/j.apsusc.2005.02.139.

[201] M. Kantcheva, Identification, stability, and reactivity of NO_X species adsorbed on titania-supported manganese catalysts, J. Catal. 204 (2001) 479-494, doi: https//doi.org/10.1006/jcat.2001.3413.

[202] Z. Wu, B. Jiang, Y. Liu, H. Wang, R. Jin, DRIFT study of manganese/titania-based catalysts for low-temperature selective catalytic reduction of NO with NH_3, Environ. Sci. Technol. 41 (2007) 5812-5817, doi: https//doi.org/10.1021/es0700350.

[203] K. Hadjiivanov, Use of overtones and combination modes for the identification of surface NO_X anionic species by IR spectroscopy, Catal. Lett. 68 (2000), 157-161, doi: https//doi.org/10.1023/a:1019087521084

[204] Y. Geng, W. Shan, F. Liu, S. Yang, Adjustment of operation temperature window of Mn-Ce oxide catalyst for the selective catalytic reduction of NO_X with NH_3, J. Hazard. Mater. 405 (2021) doi: https//doi.org/10.1016/j.jhazmat.2020.124223.

[205] Y. Liu, T. Gu, X. Weng, Y. Wang, Z. Wu, H. Wang, DRIFT studies on the selectivity promotion mechanism of Ca-modified Ce-Mn/TiO_2 catalysts for low-temperature NO reduction with NH_3, J. Phys. Chem. C 116 (2012), 16582-16592, doi: https//doi.org/10.1021/jp304390e.

[206] G. Gao, J. Shi, C. Liu, C. Gao, Z. Fan, C. Niu, Mn/CeO_2 catalysts for SCR of NO_X with NH_3 comparative study on the effect of supports on low-temperature catalytic activity, Appl. Surf. Sci. 411 (2017), 338-346, doi: https//doi.org/10.1016/j.apsusc.2017.03.164.

[207] G. Qi, R. T. Yang, Characterization and FTIR studies of MnO_X-CeO_2 catalyst for low-temperature selective catalytic reduction of NO with NH_3, J. Phys. Chem. B 108 (2004), 15738-15747, doi: https//doi.org/10.1021/jp048431h.

[208] K. I. Hadjiivanov, Identification of neutral and charged N_XO_y surface species by IR spectroscopy, Catal. Rev. Sci. Eng. 42 (2000), 71-144, doi: https//doi.org/10.1081/CR-100100260.

[209] W. S. Kijlstra, D. S. Brands, E. K. Poels, A. Bliek, Mechanism of the selective catalytic reduction of NO by NH_3 over MnO_X/Al_2O_3: I. Adsorption and desorption of the single reaction components, J. Catal. 171 (1997), 208-218, doi: https//doi.org/10.1006/jcat.1997.1788.

[210] B. Q. Jiang, Z. B. Wu, Y. Liu, S. C. Lee, W. K. Ho, DRIFT study of the SO_2 effect on low-temperature SCR reaction over Fe-Mn/TiO_2, J. Phys. Chem. C 114 (2010), 4961-4965, doi: https//doi.org/10.1021/jp907783g.

[211] L. Qiu, D. Pang, C. Zhang, J. Meng, R. Zhu, F. Ouyang, In situ IR studies of Co and Ce doped Mn/TiO_2 catalyst for low-temperature selective catalytic reduction of NO with NH_3, Appl. Surf. Sci. 357 (2015), 189-196, doi: https//doi.org/10.1016/j.apsusc.2015.08.259.

[212] J. Liu, X. Li, Q. Zhao, J. Ke, H. Xiao, X. Lv, S. Liu, M. Tadé, S. Wang, Mechanistic investigation of the enhanced NH_3-SCR on cobalt-decorated Ce-Ti mixed oxide: In situ FTIR analysis for structure-activity correlation, Appl. Catal. B Environ. 200 (2017), 297-308, doi: https//doi.org/10.1016/j.apcatb.2016.07.020.

[213] Q. Zhang, H. Wang, P. Ning, Z. Song, X. Liu, Y. Duan, In situ DRIFTS studies on CuO-Fe_2O_3 catalysts for low temperature selective catalytic oxidation of ammonia to nitrogen, Appl. Surf. Sci. 419 (2017), 733-743, doi: https//doi.org/10.1016/j.apsusc.2017.05.056.

[214] D. Song, X. Shao, M. Yuan, L. Wang, W. Zhan, Y. Guo, Y. Guo, G. Lu, Selective catalytic oxidation of ammonia over MnO_X-TiO_2 mixed oxides, RSC Adv. 6 (2016), 88117-88125, doi: https//doi.org/10.1039/c6ra20999h.

[215] F. Gao, X. Tang, H. Yi, J. Li, S. Zhao, J. Wang, C. Chu, C. Li, Promotional mechanisms of activity and SO_2 tolerance of Co- or Ni-doped MnO_X-CeO_2 catalysts for SCR of NO_X with NH_3 at low temperature, Chem. Eng. J. 317 (2017), 20-31, doi: https//doi.org/10.1016/j.cej.2017.02.042.

[216] S. Yang, F. Qi, Y. Liao, S. Xiong, Y. Lan, Y. Fu, W. Shan, J. Li, Dual effect of sulfation on the selective catalytic reduction of NO with NH_3 over MnO_X/TiO_2: Key factor of NH_3 distribution, Ind. Eng. Chem. Res. 53 (2014), 5810-5819, doi: https//doi.org/10.1021/ie5001357.

[217] S. Xiong, Y. Liao, H. Dang, F. Qi, S. Yang, Promotion mechanism of CeO_2 addition on the low temperature SCR reaction over MnO_X/TiO_2: A new insight from the kinetic study, RSC Adv. 5 (2015), 27785-27793, doi: https//doi.org/10.1039/c5ra01767j.

[218] N. Topsøe, Mechanism of the selective catalytic reduction of nitric oxide by ammonia elucidated by in situ on-line Fourier transform infrared spectroscopy, Science 265 (1994), 1217-1219, doi: https//doi.org/10.1126/science.265.5176.1217.

[219 L. Lietti, I. Nova, E. Tronconi, P. Forzatti, Transient kinetic study of the SCR-DeNOx reaction, Catal. Today 45 (1998), 85-92, doi: https//doi.org/10.1016/S0920-5861(98)00253-3.

[220] N. Topsøe, H. Topsøe, J. A. Dumesic, Vanadia/titania catalysts for selective catalytic reduction (SCR) of nitric-oxide by ammonia. I. Combined temperature-programmed in-situ ftir and on-line mass-spectroscopy studies, J. Catal. 151 (1995), 226-240, doi: https//doi.org/10.1006/jcat.1995.1024.

[221] Y. He, M. E. Ford, M. Zhu, Q. Liu, U. Tumuluri, Z. Wu, I. E. Wachs, Influence of catalyst synthesis method on selective catalytic reduction (SCR) of NO by NH_3 with V_2O_5-WO_3/TiO_2 catalysts, Appl. Catal. B Environ. 193 (2016), 141-150, doi: https//doi.org/10.1016/j.apcatb.2016.04.022.

[222] E. Finocchio, G. Ramis, G. Busca, A study on catalytic combustion of chlorobenzenes, Catal. Today 169 (2011), 3-9, doi: https//doi.org/10.1016/j.cattod.2010.10.097.

[223] L. Li, J. Shi, M. Tian, C. Chen, B. Wang, M. Ma, C. He, In situ fabrication of robust three dimensional ordered macroporous γ-MnO_2/$LaMnO_3$ catalyst for chlorobenzene efficient destruction, Appl. Catal. B Environ. 282 (2021) doi: https//doi.org/10.1016/j.apcatb.2020.119565.

[224] J. Zeng, X. Liu, J. Wang, H. Lv, T. Zhu, Catalytic oxidation of benzene over MnO_X/TiO_2 catalysts and the mechanism study, J. Mol. Catal. A Chem. 408 (2015), 221-227, doi: https//doi.org/10.1016/j.molcata.2015.07.024.

[225] X. Weng, P. Sun, Y. Long, Q. Meng, Z. Wu, Catalytic Oxidation of Chlorobenzene over $Mn_XCe_{1-x}O_2$/HZSM-5 Catalysts: A Study with Practical Implications, Environ. Sci. Technol. 51 (2017), 8057-8066, doi: https//doi.org/10.1021/acs.est.6b06585.

[226] Y. Gu, T. Cai, X. Gao, H. Xia, W. Sun, J. Zhao, Q. Dai, X. Wang, Catalytic combustion of chlorinated aromatics over WO_X/CeO_2 catalysts at low temperature, Appl. Catal. B Environ. 248 (2019), 264-276, doi: https//doi.org/10.1016/j.apcatb.2018.12.055.

[227] Z. Zhang, J. Huang, H. Xia, Q. Dai, Y. Gu, Y. Lao, X. Wang, Chlorinated volatile organic compound oxidation over SO_4^{2-}/Fe_2O_3 catalysts, J. Catal. 360 (2018), 277-289, doi: https//doi.org/10.1016/j.jcat.2017.11.024.

[228] J. Zhao, W. Xi, C. Tu, Q. Dai, X. Wang, Catalytic oxidation of chlorinated VOCs over Ru/Ti_XSn_{1-x} catalysts, Appl. Catal. B Environ. 263 (2020) doi: https//doi.org/10.1016/j.apcatb.2019.118237.

[229] J. Wang, X. Wang, X. Liu, T. Zhu, Y. Guo, H. Qi, Catalytic oxidation of chlorinated benzenes over V_2O_5/TiO_2 catalysts: The effects of chlorine substituents, Catal. Today 241 (2015), 92-99, doi: https//doi.org/10.1016/j.cattod.2014.04.002.

[230] Y. Gu, S. Shao, W. Sun, H. Xia, X. Gao, Q. Dai, W. Zhan, X. Wang, The oxidation of chlorinated organic compounds over W-modified Pt/CeO_2 catalysts, J. Catal. 380 (2019), 375-386, doi: https//doi.org/10.1016/j.jcat.2019.06.041.

[231] Z. Zhang, H. Xia, Q. Dai, X. Wang, Dichloromethane oxidation over Fe_XZr_{1-x} oxide catalysts, Appl. Catal. A Gen. 557 (2018), 108-118, doi: https//doi.org/10.1016/j.apcata.2017.12.003.

[232] G. Wang, Y. Wang, L. Qin, B. Zhao, L. Guo, J. Han, Efficient and stable degradation of chlorobenzene over a porous iron-manganese oxide supported ruthenium catalyst, Catal. Sci. Technolog. 10 (2020), 7203-7216, doi: https//doi.org/10.1039/d0cy01148g.

[233] M. Gallastegi-Villa, A. Aranzabal, M. P. González-Marcos, B. Markaide-Aiastui, J. A. González-Marcos, J. R. González-Velasco, Effect of vanadia loading on acidic and redox properties of VO_X/TiO_2 for the simultaneous abatement of PCDD/Fs and NO_X, Journal of Industrial and Engineering Chemistry 81 (2020), 440-450, doi: https//doi.org/10.1016/j.jiec.2019.09.034.

[234] J. A. Martín-Martín, J. Sánchez-Robles, M. P. González-Marcos, A. Aranzabal, J. R. González-Velasco, Effect of preparation procedure and composition of catalysts based on Mn and Ce oxides in the simultaneous removal of NO_X and o-DCB, Mol. Cat. 495 (2020) doi: https//doi.org/10.1016/j.mcat.2020.111152.

[235] C. Liu, J. Shi, C. Gao, C. Niu, Manganese oxide-based catalysts for low-temperature selective catalytic reduction of NO_X with NH_3: A review, Appl. Catal. A Gen. 522 (2016), 54-69, doi: https//doi.org/10.1016/j.apcata.2016.04.023.

[236] F. Cao, J. Xiang, S. Su, P. Wang, L. Sun, S. Hu, S. Lei, The activity and characterization of MnO_X-CeO_2-ZrO_2/γ-Al_2O_3 catalysts for low temperature selective catalytic reduction of NO with NH_3, Chem. Eng. J. 243 (2014), 347-354, doi: https//doi.org/10.1016/j.cej.2014.01.034.

[237] F. Cao, S. Su, J. Xiang, P. Wang, S. Hu, L. Sun, A. Zhang, The activity and mechanism study of Fe-Mn-Ce/γ-Al_2O_3 catalyst for low temperature selective catalytic reduction of NO with NH_3, Fuel 139 (2015), 232-239, doi: https//doi.org/10.1016/j.fuel.2014.08.060.

[238] T. Boningari, P. R. Ettireddy, A. Somogyvari, Y. Liu, A. Vorontsov, C. A. McDonald, P. G. Smirniotis, Influence of elevated surface texture hydrated titania on Ce-doped Mn/TiO_2 catalysts for the low-temperature SCR of NO_X under oxygen-rich conditions, J. Catal. 325 (2015), 145-155, doi: https//doi.org/10.1016/j.jcat.2015.03.002.

[239] Z. Wu, R. Jin, Y. Liu, H. Wang, Ceria modified MnO_X/TiO_2 as a superior catalyst for NO reduction with NH_3 at low-temperature, Catal. Commun. 9 (2008), 2217-2220, doi: https//doi.org/10.1016/j.catcom.2008.05.001.

[240] R. Jin, Y. Liu, Z. Wu, H. Wang, T. Gu, Low-temperature selective catalytic reduction of NO with NH_3 over Mn-Ce oxides supported on TiO_2 and Al_2O_3: A comparative study, Chemosphere 78 (2010), 1160-1166, doi: https//doi.org/10.1016/j.chemosphere.2009.11.049.

[241] W. Pan, J. Hong, R. Guo, W. Zhen, H. Ding, Q. Jin, C. Ding, S. Guo, Effect of support on the performance of Mn-Cu oxides for low temperature selective catalytic reduction of NO with NH_3, J. Ind. Eng. Chem. 20 (2014), 2224-2227, doi: https//doi.org/10.1016/j.jiec.2013.09.054.

[242] E. Sarkadi-Pribóczki, N. Kumar, T. Salmi, Z. Kovácz, D. Y. Murzin, A novel radioisotope method for studying catalytic transformations over alumina, H-ZSM-5 and H-beta zeolite catalysts: Investigation of conversion of 11C-labeled methanol to 11C-labeled dimethyl ether and hydrocarbons, Catal. Lett. 93 (2004), 101-107, doi: https//doi.org/10.1023/b:catl.0000016956.04114.22.

[243] W. Xu, G. Zhang, H. Chen, G. Zhang, Y. Han, Y. Chang, P. Gong, Mn/beta and Mn/ZSM-5 for the low-temperature selective catalytic reduction of NO with ammonia: Effect of manganese precursors, Cuihua Xuebao Chin. J. Catalysis 39 (2018), 118-127, doi: https//doi.org/10.1016/S1872-2067(17)62983-8.

[244] G. Carja, Y. Kameshima, K. Okada, C.D. Madhusoodana, Mn-Ce/ZSM5 as a new superior catalyst for NO reduction with NH_3, Appl. Catal. B Environ. 73 (2007), 60-64, doi: https//doi.org/10.1016/j.apcatb.2006.06.003.

[245] M. Taralunga, J. Mijoin, P. Magnoux, Catalytic destruction of 1,2-dichlorobenzene over zeolites, Catal. Commun. 7 (2006), 115-121, doi: https//doi.org/10.1016/j.catcom.2005.09.006.

[246] J. A. Botas, D. P. Serrano, A. García, J. De Vicente, R. Ramos, Catalytic conversion of rapeseed oil into raw chemicals and fuels over Ni- and Mo-modified nanocrystalline ZSM-5 zeolite, Catal. Today 195 (2012), 59-70, doi: https//doi.org/10.1016/j.cattod.2012.04.061.

[247] X. Zeng, Z. Wang, J. Ding, L. Wang, Y. Jiang, C. Stampfl, M. Hunger, J. Huang, Catalytic arene alkylation over H-Beta zeolite: Influence of zeolite shape selectivity and reactant nucleophilicity, J. Catal. 380 (2019), 9-20, doi: https//doi.org/10.1016/j.jcat.2019.09.035.

[248] V. Bratan, C. Munteanu, C. Hornoiu, A. Vasile, F. Papa, R. State, S. Preda, D. Culita, N. I. Ionescu, CO oxidation over Pd supported catalysts. In situ study of the electric and catalytic properties, Appl. Catal. B Environ. 207 (2017), 166-173, doi: https//doi.org/10.1016/j.apcatb.2017.02.017.

[249] Y. Zhang, Y. Zheng, X. Wang, X. Lu, Preparation of Mn-FeO_X/CNTs catalysts by redox co-precipitation and application in low-temperature NO reduction with NH_3, Catal. Commun. 62 (2015), 57-61, doi: https//doi.org/10.1016/j.catcom.2014.12.023.

[250] C. Zhang, T. Chen, H. Liu, D. Chen, B. Xu, C. Qing, Low temperature SCR reaction over Nano-Structured Fe-Mn Oxides: Characterization, performance, and kinetic study, Appl. Surf. Sci. 457 (2018), 1116-1125, doi: https//doi.org/10.1016/j.apsusc.2018.07.019.

[251] P. Lu, L. Ye, X. Yan, X. Chen, P. Fang, D. Chen, D. Chen, C. Cen, N_2O inhibition by toluene over Mn-Fe spinel SCR catalyst, J. Hazard. Mater. 414 (2021) doi: https//doi.org/10.1016/j.jhazmat.2021.125468.

[252] P. Maitarad, D. Zhang, R. Gao, L. Shi, H. Li, L. Huang, T. Rungrotmongkol, J. Zhang, Combination of experimental and theoretical investigations of $MnO_X/Ce_{0.9}Zr_{0.1}O_2$ nanorods for selective catalytic reduction of NO with ammonia, J. Phys. Chem. C 117 (2013), 9999-10006, doi: https//doi.org/10.1021/jp400504m.

[253] R. Gao, D. Zhang, P. Maitarad, L. Shi, T. Rungrotmongkol, H. Li, J. Zhang, W. Cao, Morphology-dependent properties of MnO_X/ZrO_2-CeO_2 nanostructures for the selective catalytic reduction of NO with NH_3, J. Phys. Chem. C 117 (2013), 10502-10511, doi: https//doi.org/10.1021/jp400984z.

[254] Y. Zhu, X. Xiao, J. Wang, C. Ma, X. Jia, W. Qiao, L. Ling, Enhanced activity and water resistance of hierarchical flower-like Mn-Co binary oxides for ammonia-SCR reaction at low temperature, Appl. Surf. Sci. 569 (2021) doi: https//doi.org/10.1016/j.apsusc.2021.150989.

[255] N. Akter, S. Zhang, J. Lee, D. H. Kim, J. A. Boscoboinik, T. Kim, Selective catalytic reduction of NO by ammonia and NO oxidation Over CoO_X/CeO_2 catalysts, Mol. Cat. 482 (2020) doi: https//doi.org/10.1016/j.mcat.2019.110664.

[256] Q. Zhang, C. Qiu, H. Xu, T. Lin, M. Gong, Y. Chen, Novel promoting effects of tungsten on the selective catalytic reduction of NO by NH_3 over MnO_X-CeO_2 monolith catalyst, Catal. Commun. 16 (2011), 20-24, doi: https//doi.org/10.1016/j.catcom.2011.08.036.

[257] L. Peng, L. Huan, L. Huayan, C. Yinfei, Z. Zekai, Influence of tungsten on the NH_3-SCR activity of $MnWO_X/TiO_2$ catalysts, RSC Adv. 7 (2017), 19771-19779, doi: https//doi.org/10.1039/c7ra00427c.

[258] F. Liu, W. Shan, Z. Lian, L. Xie, W. Yang, H. He, Novel $MnWO_X$ catalyst with remarkable performance for low temperature NH_3-SCR of NO_X, Catal. Sci. Technolog. 3 (2013), 2699-2707, doi: https//doi.org/10.1039/c3cy00326d.

[259] Z. Ma, X. Wu, Y. Feng, Z. Si, D. Weng, Effects of WO_3 doping on stability and N_2O escape of MnO_X-CeO_2 mixed oxides as a low-temperature SCR catalyst, Catal. Commun. 69 (2015), 188-192, doi: https//doi.org/10.1016/j.catcom.2015.06.014.

[260] A. Choya, B. de Rivas, J.R. González-Velasco, J.I. Gutiérrez-Ortiz, R. López-Fonseca, Oxidation of residual methane from VNG vehicles over Co_3O_4-based catalysts: Comparison among bulk, Al_2O_3-supported and Ce-doped catalysts, Appl. Catal. B Environ. 237 (2018), 844-854, doi: https//doi.org/10.1016/j.apcatb.2018.06.050.